

**CHARACTERISATION OF CYTOCHROME P450 AZOLE DRUG-RESISTANT
STEROL DEMETHYLASE CYP51B1 AND EXPRESSION OF CYP123 AND
CYP136 FROM *MYCOBACTERIUM TUBERCULOSIS***

A thesis submitted to the University of Manchester for the degree of
Doctor of Philosophy
in the Faculty of Life Sciences

2011

CHRISTINE CHERYL FERNANDEZ

TABLE OF CONTENTS

TABLE OF CONTENTS	2	
LIST OF FIGURES	5	
LIST OF TABLES	7	
LIST OF EQUATIONS	8	
LIST OF ABBREVIATIONS	9	
SCIENTIFIC ABSTRACT	10	
LAY ABSTRACT	11	
DECLARATION	12	
COPYRIGHT STATEMENT	12	
BIOGRAPHY	13	
ACKNOWLEDGEMENTS	14	
DEDICATION	15	
CHAPTER		
1	INTRODUCTION	16
1.1	Tuberculosis – A Global Emergency	17
1.2	Fungal Infections and Azole Antifungals	18
1.3	<i>Candida albicans</i> and Azole Drug-Resistance	22
1.4	<i>Mycobacterium tuberculosis</i> and Antitubercular Drugs	23
1.5	Cytochrome P450	29
1.6	P450 Catalytic Cycle	34
1.7	P450 Systems in Mtb	39
1.8	Mtb P450 as Drug Targets	42
1.9	Background on Sterol Demethylase (CYP51)	45
1.10	Evidence of Multiple CYP51 Systems	54
1.11	Characterisation of CYP51B1	57
1.12	Scope of Research	58
1.13	Objectives of Research	62
2	GENERAL MATERIALS AND METHODS	64
2.1	Materials	65
2.1.1	<i>E. coli</i> strains and Plasmid Vectors	65
2.1.2	Growth and Strain Maintenance Media	67
2.1.3	Expression Media	68
2.1.4	Antibiotics and Other Reagents	68
2.1.5	Buffers for Purification and Assays	69
2.2	Methods	70
2.2.1	Agarose Gel Electrophoresis	70
2.2.2	Sodium-Dodecyl-Sulphate-Polyacrylamide Gel Electrophoresis (SDS-PAGE)	70
2.2.3	Protein Engineering and Primer Design	71
2.2.4	Expression Trials	72
2.2.5	Protein Purification	73
2.2.6	Protein Identification – MALDI-TOF and Western Blotting	74
2.2.7	Spectroscopic P450 Characterisation	75
2.2.8	Kinetic Spectroscopic Analysis	76
2.2.9	Hemoprotein Estimation by Pyridine Hemochromogen Technique	80
2.2.10	Biophysical Analysis	81
2.2.11	Crystallogensis	83
2.2.12	Potentiometric Studies	84

2.2.13	Redox Cycling of CYP51B1	85
2.2.14	Stabilisation of the P450 Species by CO Trapping with Redox Partners	86
2.2.15	CYP51B1 Reconstitution of Catalysis	88
3	BIOCHEMICAL CHARACTERISATION OF CYP51B1 AND FLUCONAZOLE-RESISTANT MUTANTS	90
3.1	Mapping Fluconazole-Resistant Point Mutants from <i>Candida albicans</i>	91
3.2	Site-Directed Mutagenesis on CYP51B1	94
3.3	Expression and Purification of Mutants	95
3.4	The Effect of Drug Solvent DMSO Concentration on CYP51B1	102
3.5	Understanding the Molecular Mechanisms and Mode of Action/ Physiological Roles of Mtb CYP51B1	105
3.5.1	Quantification of Heme <i>b</i> in WT CYP51B1 and Mutants	105
3.5.2	CYP51B1 Heme-Coordination by NO and CO	106
3.5.2.1	NO-Ferric-Heme Coordination	106
3.5.2.2	CO-Ferrous-Heme Coordination	109
3.5.3	Formation of CO-Free Ferrous-Thiol Species	114
3.5.4	Stabilisation of the P450 Form in the Presence of Estriol and Redox Partners	118
3.5.5	Redox Potentials of CYP51B1 Ligand- Free Form	129
3.5.6	Redox Cycling with Chemical Reducing and Oxidising Agents	138
3.6	Understanding the Mechanisms of Azole-Resistance in CYP51ca Using CYP51B1 as a Template	141
3.6.1	CYP51B1 UV-Visible Spectral Ligand Binding Properties	141
3.6.1.1	Photo-Diode Array Analysis of Estriol and Fluconazole Binding	141
3.6.1.2	Equilibrium Titration of Azole Drugs and Estriol	145
3.6.1.3	Stopped-Flow Analysis of Azole Drugs	157
3.6.2	Reconstitution of CYP51B1 Enzyme Catalysis with Lanosterol and Dihydrolanosterol	163
3.7	Summary and Critical Assessment	165
4	BIOPHYSICAL AND STRUCTURAL CHARACTERISATION OF CYP51B1 AND FLUCONAZOLE-RESISTANT MUTANTS	171
4.1	Available Crystal Structures of CYP51B1	172
4.2	Circular Dichroism (CD) Comparative Analysis	175
4.3	Dynamic Light Scattering Analysis	178
4.4	Differential Scanning Calorimetry (DSC) of Ligand-Free and Bound Forms	181
4.5	Analysis of Ferric-Heme Coordination by Electron Paramagnetic Resonance (EPR)	183
4.5.1	EPR of CYP51B1 Ligand-Free and Bound Forms	183
4.5.2	EPR of CYP51B1 Post-Redox Cycling of the Enzyme	190
4.6	CYP51B1 Crystallisation	192
4.7	CYP51B1 Crystal Structure Features in Ligand-Bound Forms	194
4.8	Summary and Critical Assessment	200
5	MOLECULAR BIOLOGY STUDIES OF CYP123 AND CYP136	203
5.1	Pseudogenes, Paralogues or New Enzymes	204
5.2	Gene and Protein Engineering	208
5.2.1	CYP123	208
5.2.2	CYP136	209
5.3	Expression Systems	211
5.3.1	CYP123	211
5.3.2	CYP136	213

5.4	Purification with Native and Tagged Proteins	215
5.5	Chaperone Proteolysis	216
5.6	MALLS and CD Analysis	220
5.7	Discussions from Bioinformatics Analysis	222
5.8	Summary, Critical Assessment and Future Work	225
6	CONCLUSIONS AND FUTURE WORK	227
6.1	Azole-Resistance in CYP51	228
6.2	Importance of Studying CYP123 and CYP136 from Mtb	234
6.3	P450s in Mtb and Host Cholesterol Relationship	236
7	REFERENCES	239
8	APPENDICES	253
A	Summary of CYP51B1 WT and Mutants Experimental Analysis	253
B	Brief Genomics and Proteomics Summary of CYP51B1, CYP123 and CYP136	255
C	DSC Data for CYP51B1 Variants	257
D	Multiple Sequence Alignment of CYP51 Enzymes, CYP123 and CYP136	258
E	Membrane Protein Topology Prediction of CYP123, CYP136 and CYP51B1 from Mtb	259
F	EPR g Values for CYP51B1	260
G	Choice of Model Parameters in the DSC Software	261
H	Crystallographic Data Statistics of CYP51B1 Variants	262

Final word count: 88 184 (78 913 excluding Chapter 7 References)

LIST OF FIGURES

FIGURE	TITLE	PAGE NO.
1.1	Map of the distribution of countries reporting XDR-TB incidences.	18
1.2	Morphology of <i>Mycobacterium tuberculosis</i> .	24
1.3	A schematic diagram of the <i>Mycobacterium tuberculosis</i> cell wall.	25
1.4	Spectral properties and spin state changes of ferric-heme P450.	31
1.5	The catalytic cycle of cytochrome P450, showing known intermediates and the rebound mechanism.	37
1.6	Structures of crystallised Cytochromes P450 from <i>Mycobacterium tuberculosis</i> .	41
1.7	Crystal structures of Mtb P450s CYP51B1 and CYP121.	43
1.8	Phylogenetic comparison of CYP51 across families and phyla.	46
1.9	The CYP51 three-step reaction scheme.	49
1.10	CYP51B1 substrate recognition sites (SRS), substrate binding sites (SBS) and mutations-prone residues by comparison with <i>C. albicans</i> CYP51.	53
1.11	Multiple sequence alignment of CYP51 isoforms identified as drug targets with their respective host organisms shown.	57
1.12	Example of Mtb CYP51B1 P450 complex collapse to P420	60
1.13	Example of spectral binding data for the interaction of an azole drug (miconazole) with a bacterial P450 (<i>Bacillus subtilis</i> P450 BioI).	61
2.1	Plasmid maps of vectors used for the expression of CYP51B1 WT and mutants, CYP123 and CYP136.	66
2.2	Derivation of second order rate constants from stopped flow kinetics.	79
3.1	Fluconazole-resistant point mutations from <i>Candida albicans</i> CYP51.	93
3.2	Sequencing results spectra for site-directed mutagenesis.	94
3.3	Purification chromatogram of CYP51B1 WT and G388S.	96
3.4	Expression of CYP51B1 WT and mutants.	99
3.5	Immunoblot and Soret band spectrum for the S348F CYP51B1 mutant.	101
3.6	Heme perturbation profile of CYP51B1 titrated with DMSO.	104
3.7	Heme <i>b</i> quantification by the pyridine hemochromogen technique.	106
3.8	Spectral characterisation of CYP51B1 ferric-heme nitrosyl complexes.	108
3.9	Spectral properties of Fe(II)-CO adduct complexes for CYP51B1 enzymes with B-C loop mutations.	111
3.10	Fe(II)-CO adduct complexes and their conversions in CYP51B1 cysteinyl loop mutants.	113
3.11	Formation of Fe(II)-thiolate and Fe(II)-thiol species in CYP51B1 enzymes.	117
3.12	P450 species formation in CYP51B1 WT with various Mtb redox partners.	122
3.13	Electron transfer scheme between Mtb redox partner enzymes and CYP51B1.	124
3.14	P450 species formation and stabilisation in CYP51B1 mutants with Fdr and Fd2.	126
3.15	Redox potentials of ligand-free WT CYP51B1 and cysteinyl loop mutant enzymes.	130
3.16	Residues at the β -bulge of the cysteinyl loop trans to the substrate	133

	binding site.	
3.17	Redox potentials of ligand-free CYP51B1 B-C loop mutant enzymes.	137
3.18	Redox-cycled CYP51B1 WT and mutants.	140
3.19	Estriol binding to WT and F89H CYP51B1 analysed by stopped-flow PDA analysis.	143
3.20	Fluconazole binding to CYP51B1 enzymes using stopped-flow global analysis.	145
3.21	Spectral changes in CYP51B1 displaying type I and type II Soret band shifts.	147
3.22	Structures of selected azole drugs and the substrate analogue estriol used in CYP51B1 ligand binding studies.	150
3.23	Optical titrations of CYP51B1 enzymes with the substrate-like analogue estriol.	153
3.24	Optical titrations of the G388S CYP51B1 mutant with azole inhibitors.	155
3.25	Optical titrations of L100F and R391K CYP51B1 mutants with azole inhibitors.	156
3.26	Plots of apparent azole drug-CYP51B1 binding rates (k_{obs}) versus azole concentration.	158
3.27	Apparent CYP51B1 enzyme azole drug-binding reaction rates obtained from stopped-flow binding studies.	160
3.28	Structures of substrates and products of CYP51B1 catalysis, and comparison with the substrate analogue estriol.	164
4.1	CYP51 from Mtb, human and <i>Trypanosoma brucei</i>.	175
4.2	Far UV and near UV-visible circular dichroism spectra of CYP51B1 WT and mutants.	177
4.3	Multi-angle laser light scattering spectra of CYP51B1 WT and mutants.	180
4.4	Protein unfolding transition thermograms for ligand-free and inhibitor-bound CYP51B1.	182
4.5	EPR spectra of ligand-free mutants and WT CYP51B1.	184
4.6	EPR spectra of the CYP51B1 L100F mutant enzyme bound to azole-inhibitors.	188
4.7	EPR spectra of WT and mutant CYP51B1 enzymes in resting and azole-bound forms.	189
4.8	EPR spectra of redox-cycled WT and mutant CYP51B1 enzymes.	190
4.9	Protein crystals obtained and a representative diffraction pattern for CYP51B1 WT and mutant forms.	193
4.10	Crystal structures of CYP51B1 mutants.	194
4.11	Dynamics of the highly mobile CYP51B1 B-C loop.	196
4.12	Comparison of WT and R391K mutant structures.	197
4.13	Mobile regions of CYP51B1.	198
4.14	Structural differences induced by 4PI and EPBA ligation in CYP51B1.	199
5.1	Amino-terminal sequence alignment of CYP51s, CYP123 and CYP136.	207
5.2	Plasmid and gene isolation for <i>CYP123</i> vector construction.	208
5.3	Primer design for reading frame correction for the <i>Rv0776c</i> (<i>CYP123</i>) gene constructs.	209
5.4	Plasmid and DNA isolation for <i>CYP136</i> vector construction.	210
5.5	Multiple cloning sites in pCOLD TM TF vector and position of <i>Rv3059</i> gene.	211

5.6	Expression of <i>CYP123</i> in non-tagged pET20b and pET24b constructs with Rosetta2 (DE3) expression host.	212
5.7	Expression of His ₆ -tagged CYP136 in the pET15b construct with various expression hosts.	213
5.8	Expression of CYP136 in pET15b with a HMS174 (DE3) expression host.	214
5.9	Expression of CYP136 in various vectors with a HMS174 (DE3) expression host.	214
5.10	Purification protocol for His ₆ -tagged CYP136 fused to trigger factor chaperone expressed from the pCOLDt _f vector.	215
5.11	Trigger factor chaperone proteolysis trials by HRV3C protease.	217
5.12	Scale-up of trigger factor chaperone proteolysis from CYP136.	218
5.13	Light scattering results from analysis of the CYP136-trigger factor chaperone fusion protein.	220
5.14	Far UV CD spectra of CYP136 _{tf} and CYP51B1.	222
5.15	Transmembrane protein predictions for CYP136 and CYP51B1.	224
6.1	The sterol biosynthetic pathway.	236
8.1	Topology prediction of membrane proteins.	259
8.2	Purification results for native non-His ₆ -tagged CYP136 from the pET20b vector.	259

LIST OF EQUATIONS

EQUATION	NAME	PAGE NO.
1.1	Cytochrome P450 catalysis reaction	33
2.1	Single exponential function	76 & 80
2.2	Quadratic function	77
2.3	Double exponential function	80
2.4	Single electron Nernst equation	85

LIST OF TABLES

TABLE	TITLE	PAGE NO.
1.1	Estimated number of MDR-TB cases.	17
1.2	Antifungal drugs used in oral and topical treatment of aspergillosis and candidiasis in humans.	20
1.3	Upcoming and classical antitubercular drugs targeting various systems in Mtb.	27
2.1	Antibiotics and reagents used throughout experiments.	68
2.2	Composition of all buffers used in experiments.	69
2.3	Constituents of stacking and separating gels for 12.5% gel in SDS-PAGE.	71
2.4	Mediators used in redox potential determination.	84
2.5	<i>Mycobacterium tuberculosis</i> redox partner proteins and components for CO trapping experiment.	87
2.6	Components of CYP51B1 catalysis reaction mixture.	89
3.1	Recurring point mutations in the <i>ERG11</i> gene encoding for sterol demethylase of fluconazole-resistant <i>Candida albicans</i>.	92
3.2	Rate constants for CYP51B1 ferrous thiolate to thiol conversion upon reduction with dithionite.	113
3.3	Summary of P450 species formation in WT CYP51B1 with various Mtb redox partners and coenzymes.	119
3.4	Rate constants for P450 species formation of CYP51B1 mutants with Mtb Fdr and Fd2 redox partners.	124
3.5	Dissociation constants of CYP51B1 WT and mutants from equilibrium binding analysis at pH 7.5.	150
3.6	Summary of K_d values obtained through stopped-flow analysis of azole drug binding with CYP51B1 WT and mutants.	161
4.1	Melting temperatures or transition midpoints (T_m) for WT and mutant CYP51B1 enzymes.	183
4.2	Examples of various ligation and spin states of ferric heme in proteins.	186
6.1	Mutant CYP51B1 fluconazole resistance and susceptibility based on K_d values from SF and EB measurements.	232
8.1	Summary of experimental analysis on WT and fluconazole-resistant CYP51B1 mutants performed in this PhD thesis.	253
8.2	Potential P450 drug target proteins from Mtb worked on 2008-2011 in this thesis.	255
8.3	Melting temperatures or transition midpoints (T_m), enthalpy or calorimetric heat change (ΔH) and van't Hoff heat change (ΔH_v) values.	257
8.4	Crystallography statistics of CYP51B1 WT and mutants.	262

LIST OF ABBREVIATIONS

2YT	2 x yeast and tryptone medium	LS	Low spin
4PI	4-Phenylimidazole	mAGP	Mycolyarabinogalactan peptidoglycan
ABC	ATP-binding cassette	MALDI-TOF	Matrix-assisted laser desorption/ionization with time of flight
Ara f	Arabinomannan	MALLS	Multi-angle laser light scattering
ATP	Adenosine triphosphate	Man p	Mannan
BCG	Bacille Calmette–Guérin	MDR	Multi-drug resistant
BV	Benzyl viologen	MIC	Minimal inhibitory concentration
CD	Circular dichroism	MSA	Multiple sequence alignment
CDC	Centers for Disease Control	Mtb	<i>Mycobacterium tuberculosis</i>
CO	Carbon monoxide	MV	Methyl viologen
CPR	Cytochrome P450 reductase	Mw	Molecular weight
DEAE	Diethylaminoethyl cellulose	NADH	Nicotinamide adenine dinucleotide
DMSO	Dimethyl sulfoxide	NADPH	Nicotinamide adenine dinucleotide phosphate
DNA	Deoxyribonucleic acid	NIH	National Institutes of Health
DOTS	Directly observed treatment, short-course	Ni-NTA	Nickel-nitriloacetic acid
DSC	Differential scanning calorimetry	NO	Nitric oxide
EB	Equilibrium binding	P450	Cytochrome P450
EDTA	Ethylenediaminetetraacetic acid	PCR	Polymerase chain reaction
EMB	Ethambutol	PDA	Photo-diode array
ENDOR	Electron nuclear double resonance	PDB	Protein data bank
EPBA	α -Ethyl-N-4-pyridinyl-benzeneacetamide	PDI	Protein disulfide isomerase
EPR	Electron paramagnetic resonance	PIMS	Phosphatidylinositol-mannan
ETH	Ethionamide	PMS	Phenazine methosulfate
Fd1	Ferredoxin 1 Rv0763c	PMSF	Phenylmethanesulfonyl fluoride
Fd2	Ferredoxin 2 Rv1786	PVDF	Polyvinylidene fluoride
Fdr	Ferredoxin reductase Rv0688	PZA	Pyrazinamide
Fdx	<i>Mycobacterium tuberculosis</i> ferredoxin	QELS	Quasi-elastic light scattering
Fld	<i>E. coli</i> flavodoxin	rmsd	Root mean square distance
Fldr	<i>E. coli</i> flavodoxin reductase	RNA	Ribonucleic acid
Fnr	Spinach ferredoxin reductase	RTF	Universal gas constant*temperature of experiment*Faraday constant
FprA	Flavoprotein reductase A Rv3106	RT-PCR	Reverse transcription polymerase chain reaction
Gal f	Glycogen	RZ	Reinheitszahl
GalN	Galactosamine	SBS	Substrate binding site
GAPDH	D-glyceraldehyde-3-phosphate dehydrogenase	SDS-PAGE	Sodium dodecyl sulphate – polyacrylamide gel electrophoresis
GCMS	Gas chromatography mass spectrometry	SEC	Size exclusion chromatography
HA	Hydroxyapatite	SF	Stopped-flow
HEPES	4-(2-hydroxyethyl)-1-piperazineethanesulphonic acid	SHE	Standard hydrogen electrode
HIV	Human immunodeficiency virus	So	Soluble
HNQ	2-Hydroxy-1,4-naphthoquinone	SOC	Super optimal broth with catabolite repression
HRV-3C	Human Rhino Virus 3C protease	SRS	Substrate recognition site
HS	High spin	TAE	Tris-acetate
HSP	Heat shock protein	TB	Tuberculosis or Terrific broth medium
IB	Inclusion bodies	TCE	Trichloroethylene
INH	Isoniazid	tf	Trigger factor
IPTG	Isopropyl β -D-1-thiogalactopyranoside	TM	Transmembrane
kbp	Kilo-base pair	TU	<i>Escherichia coli</i> elongation factor
K_d	Dissociation constant	UV-Vis	Ultra violet-visible
kDa	Kilo-Dalton	WC	Whole cell
k_{obs}	Observed rate constant	WHO	World Health Organisation
k_{off}	Apparent de-binding rate constant	WT	Wild type
k_{on}	Second order ligand binding rate constant	XDR	Extensively -drug resistant
LAM	Lipoarabinomannan	α	Alpha Helix
LB	Luria Bertani agar or broth	δ -ala	Delta-aminolevulinic acid
LCMS	Liquid chromatography mass spectrometry		

The University of Manchester

Christine Cheryl Fernandez

Doctor of Philosophy

Characterisation of Cytochrome P450 Azole Drug-Resistant Sterol Demethylase CYP51B1 and Expression of CYP123 and CYP136 from *Mycobacterium tuberculosis*.

July 2011

Scientific Abstract

Tuberculosis (TB) affects nearly a third of the world's population and has been termed a 'Global Emergency' by the WHO. The emergence of multi/extensively drug resistant (M/XDR) strains of *Mycobacterium tuberculosis* (Mtb), the causative agent of TB, and the increasing incidences of azole drug resistant sterol demethylases (CYP51) from pathogenic fungi has propelled studies to understand mechanisms of azole drug resistance on the drug target CYP51. Since Mtb is devoid of a sterol biosynthetic pathway, the presence and study of CYP51B1 and 19 other Cytochrome P450s in its genome is important to clarify host-pathogen mechanism of infection and the potential of using azole drugs to treat TB. In this study, CYP51B1 from Mtb was used as the model enzyme to study CYP51 mutants from *Candida albicans* fluconazole-resistant clinical strains. By protein engineering methods, F89H, L100F, S348F, G388S and R391K CYP51B1 mutants were made and azole drug binding properties were investigated using stopped-flow kinetics and static equilibrium methods. Dissociation constant (K_d) values were derived for a range of commercially available azole drugs by fitting the equilibrium binding data to a hyperbolic equation. K_d values for stopped-flow kinetics were derived by plotting observed binding rates (k_{obs}) across different azole drug concentrations against time, followed by fitting multiple k_{obs} data to a linear equation to derive azole drug de-binding (k_{off}) and binding (k_{on}) rate constants – the K_d was obtained by k_{off}/k_{on} . Extinction coefficient for heme *b* content in mutants and Wild Type (WT) CYP51B1 were an average of $\epsilon_{419} = 96.1 \text{ mM}^{-1} \text{ cm}^{-1}$. Biochemical characterisation of the mutants were carried out using established experiments on CYP51 – reduction of Fe(III)-heme to Fe(II)-heme, NO binding to Fe(III)-heme, rates of CO-Fe(II) adduct formation and rates of collapse of the P450 to P420 species in the presence of CO and estriol with redox partners from Mtb. In order to elucidate the effects of the above mutations on the iron-heme catalytic region, electron paramagnetic resonance (EPR) experiments were carried out with and without azole drugs. Circular dichroism (CD), differential scanning calorimetry (DSC) and multi-angled laser light scattering (MALLS) analysis confirmed that F89H, R391K and L100F mutants were stable and homogeneous. Crystallogenesis was successful for the above mentioned mutants and atomic structures were obtained for all mutants and WT CYP51B1 (in ligand-bound and substrate-free forms), except for S348F and G388S mutants which were expressed as inclusion bodies and 60% holoenzyme, respectively. Reconstituted catalytic assays to determine the sterol demethylating propensity of the mutants were carried out using redox partners from Mtb or *E. coli*, and with lanosterol and dihydrolanosterol as the surrogate substrates. Redox potentiometry showed similar potentials to WT for all mutants except for the G388S mutant which was relatively positive (–102 mV). Redox cycling experiments followed by EPR analysis for mutants and WT resulted in a novel P450 high-spin species at g value 5.84 (80 %) which gradually collapsed to the initial low spin state over 48 h. Expression trials were concurrently carried out on two other Mtb P450 genes – *CYP123* (*Rv0744c*) and *CYP136* (*Rv3059*) products of which may have similar functions to CYP51B1 or may share similar redox partners. *CYP123* is located on the same operon as *CYP51B1* while *CYP136* has a 29% sequence identity to another CYP51 from a marine slime bacterium. Although further work is necessary, in this study CYP123 was expressed totally as inclusion bodies while CYP136 was expressed as soluble apoprotein fused with trigger factor chaperone.

The University of Manchester

Christine Cheryl Fernandez

Doctor of Philosophy

Characterisation of Cytochrome P450 Azole Drug-Resistant Sterol Demethylase CYP51B1 and Expression of CYP1236 and CYP136 from *Mycobacterium tuberculosis*.

July 2011

Lay Abstract

Tuberculosis (TB) is an airborne infectious disease caused by *Mycobacterium tuberculosis* (Mtb) which has been called a 'Global Emergency' by the World Health Organisation because of increasing numbers of multi-drug resistant (MDR) or extreme multi-drug resistant (XDR) cases. Mtb is a bacterium which contains a relatively large number of proteins from the P450 superfamily which are innately red in colour due to the presence of a catalytically important heme centre anchored within the proteins. One of the 20 P450s in Mtb is called a sterol demethylase (CYP51), an enzyme which is necessary to produce cholesterol in humans, phytosterol in plants and ergosterol in fungi. Amazingly, CYP51B1 does not have a known function in Mtb, since this bacterium does not produce sterols, and yet its molecular structure has been solved. CYP51 however, is the main target for azole-antifungal drugs in patients with fungal infections (candidiasis or aspergillosis caused by *Candida albicans* and *Aspergillus fumigatus*, respectively). Concurrently with TB, drug resistant cases in patients with candidiasis are on the rise and researchers have identified important locations at the surface and near the heme in the CYP51 drug target from resistant *C. albicans* that have changed or mutated. These mutated points have been mapped out onto CYP51B1 of Mtb, which is the only soluble version of this enzyme and therefore can be easily studied. These azole drug resistant mutants have been designated F89H and L100F at the surface (which are also flexible regions), S348F buried in the enzyme, and G388S and R391K near the heme centre. By using various methods, these mutants have been compared to its original non-mutated enzyme (WT) and studied in terms of their biochemical behaviour and binding to azole drugs and a substrate-mimic (estriol). The azole drugs and substrate-mimic interactions with these mutants have been recorded using two methods, one being time-dependent (stopped-flow kinetics) and the other time-independent (equilibrium binding). The values for drug/substrate binding from these two methods were very different from one another. The affinities from stopped-flow values were substantially greater (i.e. weaker binding) than from equilibrium binding values. These values were compared across the different drugs and substrate-mimic to understand the extent of their interactions with the mutants. The heme quantity for each mutant was also measured and the G388S mutant was shown to gradually lose its heme and to exist in two forms, with heme and without heme. This heme loss event substantially influenced G388S mutant biochemical behaviour and interactions with the drugs and substrate-mimic. Mutants at the surface flexible regions and R391K near the heme centre were successfully crystallised in order to solve their molecular structures. These high quality crystals, though small, produced good molecular structures which proved crucial toward understanding the drug interactions near the heme centre and how the azole drug resistant mutations affected these interactions. At the same time, preliminary studies were done for two more P450 proteins from Mtb, which may have similar roles to CYP51B1. They are CYP123 and CYP136, whose functions are also unknown. CYP123 was highly insoluble while CYP136 was partially soluble with heme incorporation problems. Results from this study will eventually help researchers define the function of CYP51B1 in Mtb, explain the mechanism of azole drug resistance in *C. albicans* and identify potential drugs to address antifungal and TB MDR and XDR problems.

DECLARATION

No part of this thesis has been submitted in support of an application for any degree or qualification of The University of Manchester or any other University or Institute of learning.

COPYRIGHT STATEMENT

- i. The author of this thesis (including any appendices and/or schedules to this thesis) owns certain copyright or related rights in it (the “Copyright”) and s/he has given The University of Manchester certain rights to use such Copyright, including for administrative purposes.
- ii. Copies of this thesis, either in full or in extracts and whether in hard or electronic copy, may be made only in accordance with the Copyright, Designs and Patents Act 1988 (as amended) and regulations issued under it or, where appropriate, in accordance with licensing agreements which the University has from time to time. This page must form part of any such copies made.
- iii. The ownership of certain Copyright, patents, designs, trade marks and other intellectual property (the “Intellectual Property”) and any reproductions of copyright works in the thesis, for example graphs and tables (“Reproductions”), which may be described in this thesis, may not be owned by the author and may be owned by third parties. Such Intellectual Property and Reproductions cannot and must not be made available for use without the prior written permission of the owner(s) of the relevant Intellectual Property and/or Reproductions.
- iv. Further information on the conditions under which disclosure, publication and commercialisation of this thesis, the Copyright and any Intellectual Property and/or Reproductions described in it may take place is available in the University IP Policy (see <http://www.campus.manchester.ac.uk/medialibrary/policies/intellectual-property.pdf>), in any relevant Thesis restriction declarations deposited in the University Library, The University Library’s regulations (see <http://www.manchester.ac.uk/library/aboutus/regulations>) and in The University’s policy on presentation of Theses

BIOGRAPHY

The author was born in Melaka, Malaysia and is the eldest of two siblings. She is also known as Mariam Aisha Fatima or Mariam-Aisha Jamal. She received her primary education from the Sacred Heart Convent National Primary Girls' School and secondary education from the Infant Jesus Convent National Secondary Girls' School, both in Melaka.

Upon achieving distinctions in all her government examinations, she pursued her Bachelor's degree in 2001 at the Faculty of Science, Universiti Teknologi Malaysia, Skudai, Johor under the Department of Public Services study scholarship and the Charles E. Spork scholarship program sponsored by the National Semiconductor Corporation in which she actively participated in academic and extracurricular activities. During her final year project under the supervision of Professor Dr. Noor Aini Abdul Rashid, she published her first journal publication in the Pakistan Journal of Biological Sciences on phenol degradation enzyme kinetics.

Graduating with a BS (Hons) and Dean's Award in Industrial Biology in 2005 she continued her postgraduate studies by research at the Institute of Bioscience, Universiti Putra Malaysia in May 2005 under the supervision of Assoc. Prof. Dr. Suraini Abdul Aziz. Throughout her tenure as MS student she participated in several international and local conferences and symposia as well as workshops, and contributed as a demonstrator for the Bioreactor Operations Workshop organised by the then Laboratory of Enzyme and Microbial Technology, Institute of Bioscience in 2006. She was the committee member and vice president of the Bioscience Postgraduate Club in 2005 and 2006 respectively. Until 2008 she was the committee member for the same club. In 2006 till June 2007 she was the research assistant of Assoc. Prof. Dr. Suraini Abdul Aziz.

Following her completion of MS (Enzyme Technology) in 2007, she was awarded the prestigious scholarship: Biasiswa Yang Di-Pertuan Agong 2007 (BYDPA 2007) (The King's Scholarship) to pursue her PhD (Biotechnology) at the University of Manchester, United Kingdom. Since January 2008 to July 2011 she has been working at the Manchester Interdisciplinary Biocentre on an EU funded project called New Medicines for Tuberculosis (NM4TB) under the excellent supervision of Professor Andrew W. Munro. At the same time, she spent her free time working as a graduate teaching assistant for the Faculty of Life Sciences, UoM (2008-2010) and as a part-time internet networking representative for University halls of residences (2008-2010).

She is presently a contributor for Vitae's postgraduate researchers' 'What's Up Doc?' blog where she contributes articles monthly on a voluntary basis.

A list of scientific publications by the author can be found at <http://www.christinefernandez.blogspot.com>

ACKNOWLEDGEMENTS

I am truly in debt to the following persons who were instrumental in my doctoral training:

Professor Andrew Munro: for the best research supervision I have had to date, for the opportunities to attend international scientific meetings overseas, fully funded, and for all the hawk-eyed reading and corrections he has done in impressive detail and timescales of this work and more!

Dr. Kirsty McLean: for all her patience and expert help in guiding me through new techniques in the laboratory for P450 research and much more.

Professor David Leys: for solving my crystal structures and for crystallographic advice.

Dr. Karl Fisher: for proofreading this thesis, for EPR assistance, GCMS vials and motivation in time of need.

Marina Golovanova, Michiyo Sakuma, Dr. Binu Raj and Dr. Adrian Dunford: for guidance with AKTA purification systems, centrifuges, media services and advice.

Arshad Jamal: my significant other and the one who made it possible for me to finish my 4th year writing-up in comfort and serenity.

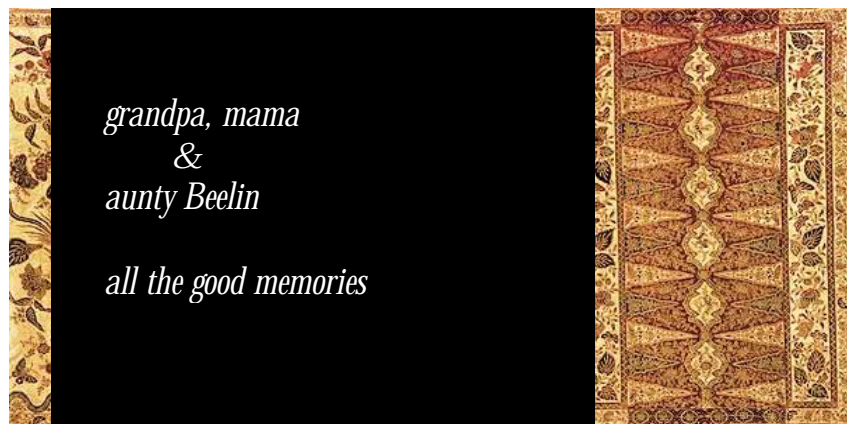
The Malaysian government: for sponsoring the first 3 years of my PhD studies in the UK.

I thank Marj Howard, Dr. Tom Jowitt, Dr. Steve Rigby, Paul Williams, Dr. Patrick Bryant for technical help and advice with MALLS, DSC, EPR, LCMS and Crystal Phoenix instruments, respectively. Finally, thanks to the Munro group for their unending support.

DEDICATION

“As with scientific research, *batik*, a traditional Malaysian art is unique, yet unlike science, *batik* is never reproducible.”

In this thesis you will find *batik* motifs indigenous to the Malay community of South East Asia at chapter pages as a commemoration to the novelty of science and as a remembrance of my late grandmother who was from the unique Straits-born Chinese-Malay community of Malaysia. The women-folk of this community wear traditional *batik* cloth as a daily garment.





Chapter 1 | Introduction

- 1.1 Tuberculosis – A Global Emergency*
- 1.2 Fungal Infections and Azole Antifungals*
- 1.3 Candida albicans and Azole Drug-Resistance*
- 1.4 Mycobacterium tuberculosis (Mtb) and Antitubercular Drugs*
- 1.5 Cytochrome P450*
- 1.6 P450 Catalytic Cycle*
- 1.7 P450 Systems in Mtb*
- 1.8 Mtb P450 as Drug Targets*
- 1.9 Background on Sterol Demethylase (CYP51)*
- 1.10 Evidence of Multiple CYP51 Systems*
- 1.11 Characterisation of CYP51B1*
- 1.12 Scope of Research*
- 1.13 Objectives of Research*

1 INTRODUCTION

1.1 Tuberculosis – A Global Emergency

Tuberculosis (TB), an airborne bacterial disease, has emerged as a primary global infectious disease with the development of drug resistant *Mycobacterium tuberculosis* (Mtb) strains. The World Health Organisation (WHO) has engaged a Stop TB Strategy Global Plan (2006 – 2015) to dramatically curb TB spread by 2015. According to the WHO, 8.8 million new TB cases were estimated in 2005 alone, with 18.2% of the patients dying of the disease including those infected with the human immunodeficiency virus (HIV) (NIH 1996; WHO 2007). The WHO reported recently that 9.2 million new cases of TB occurred in 2006, an alarming increase. In 2008 and 2009, as a manifestation of the efficacy from Stop TB Strategy Global Plan, the total number of new TB cases stabilised at 9.4 million. Incidences of new TB cases are slowly declining with respect to population growth, but not fast enough to eradicate TB from the world in our lifetime (WHO 2010b). This problem intensifies by the synergistic effect of the HIV virus and AIDS especially when TB is manifested in people who are immunosuppressed/immunodepressed, undernourished/malnourished, in the very young and the elderly and in those with increased exposure to atypical mycobacteria (Andrews *et al.* 2007; Llerena *et al.* 2010; Marais 2008; Salvado *et al.* 2010; Scullion 2003; Zandoni *et al.* 2011). The emergence of multidrug-resistant (MDR) and extensively drug-resistant (XDR) Mtb strains has aggravated the disease mostly in the Americas, Europe and Asia (Figure 1.1 and Table 1.1), with India and China alone accounting for more than 50% of the cases (Cox *et al.* 2010; Kumar *et al.* 2010; WHO 2010a; Zager and McNerney 2008).

Table 1.1: Estimated number of MDR-TB cases.

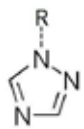
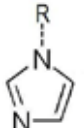
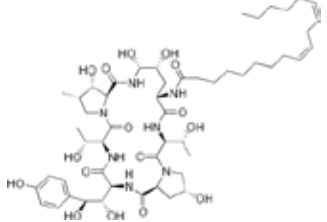
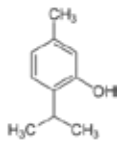
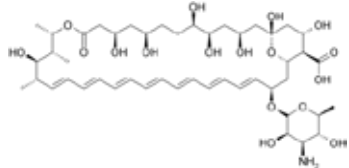
WHO region	Estimated number of MDR-TB cases in 2008 by thousands	No. of countries resistant to second-line anti-TB drugs (%)
African	69	3 (7)
Americas	8.2	3 (9)
East Mediterranean	24	1 (5)
European	81	31 (58)
South East Asia	130	2 (18)
Western Pacific	120	6 (22)
Total	432.2	46 (24)

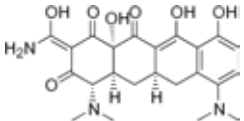
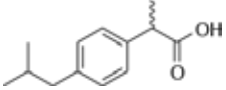
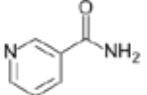
Note: These cases include primary and acquired TB in 2008, and from countries reporting bacterial resistance to second-line anti-TB drugs (WHO 2010a).

Aspergillus spp. on infected crops has had serious repercussions on animals and humans which has led to death (Edlayne *et al.* 2009). Since 1920, *Aspergillus flavus* has been a well known crop pathogen and the main producer of the carcinogenic aflatoxins which can be transferred through the food chain via cows' milk (when eaten by ruminant animals) to humans and from mothers' milk to newborns (Al-Abdalall 2010; Machida and Gomi 2010). Once thought to be a crop pathogen, now concurrently with *A. fumigatus* and *A. terreus* as opportunistic pathogens, *A. flavus* has emerged as a causative agent for aspergillosis in humans (Barnes and Marr 2006; Sales 2009; Soubani and Chandrasekar 2002).

In humans, unlike TB, fungal infections spread by different means depending on the particular type of fungus involved. High risk individuals who can easily contract fungal infections are immunosuppressed/immunodepressed, post-organ transplant patients/donors, babies, the elderly and those practicing unhygienic conditions and unprotected sex (Achkar and Fries 2010; Al Sogair and Hay 2000; Dorko *et al.* 2003; Gupta 2001; Yamanouchi *et al.* 2010). Yeasts are the most common cause of fungal infections among the young and old, emerging as regular as dandruff, eczema, diaper rash and thrush (Achkar and Fries 2010; Cernicka and Subik 2006; Dorko *et al.* 2003; Leibovici *et al.* 2008; Massone *et al.* 2006; Xu *et al.* 2007). The most reoccurring isolate is *Candida albicans*, the main culprit for the rising urethrovaginal candidiasis cases among women (Achkar and Fries 2010). A widely used treatment for this infection is by azole antifungal drugs. Clinical *C. albicans* strains isolated from infected patients demonstrated resistance towards fluconazole, a derivative of the azole antifungal drugs, in microbial inhibitory concentration (MIC) tests. Fluconazole, voriconazole and other derivatives of azole drugs and antifungals in Table 1.2 are used to treat *C. albicans* infections both orally and topically in patients with candidiasis. Although fluconazole is a safe and compatible oral and intravenous treatment with other drugs (HIV/AIDS and cancer), the latest azole antifungal drugs on the market, voriconazole, posaconazole, itraconazole, isavuconazole and ravuconazole showed adverse effects and drug interactions with patients on other medications (Cronin and Chandrasekar 2010; Pasqualotto *et al.* 2010). To address the problem of drug resistance and cross-drug compatibility issues, antifungal drugs from different classes (echinocandins, tetracycline derivatives, ibuprofen, thymol and nicotinamide) have recently been introduced, with ongoing laboratory and clinical studies targeting patients on treatment with a cocktail of other drugs as shown in Table 1.2.

Table 1.2: Antifungal drugs used in oral and topical treatment of aspergillosis and candidiasis in humans.

Causative agent	Drug class	Representative structure	Drug name	Drug target or mechanism	Ref.
Filamentous fungi: <i>Aspergillus</i> spp. - <i>A. flavus</i> - <i>A. fumigatus</i> - <i>A. terreus</i>	Triazoles		Fluconazole, Voriconazole, Isavuconazole, Itraconazole, Posaconazole	All azoles – Inhibition of sterol 14 alpha demethylase. – Disruption of the ergosterol biosynthetic pathway and cell wall/membrane integrity.	(Musaji 2010; Pasqualotto <i>et al.</i> 2010)
	Imidazoles		Miconazole, Clotrimazole, Ravuconazole, Albaconazole, Ketoconazole	Miconazole – Inhibition of sterol 14 alpha demethylase, peroxidase and catalase. – Increase in cellular reactive oxygen species, disruption of the ergosterol biosynthetic pathway and cell membrane integrity.	
	Echinocandins		Caspofungin, Micafungin, Anidulafungin	Inhibition of beta (1, 3)-D-glucan synthase and the disruption of cell membrane integrity.	(Grover 2010; Hoehamer <i>et al.</i> 2010; Liu <i>et al.</i> 2005; Munoz <i>et al.</i> 2010)
Yeast: <i>Candida</i> spp. - <i>C. albicans</i> - <i>C. glabrata</i>	Natural isopropyl cresols/ monoterpenoids		Thymol (5-methyl-2-(1-methyl ethyl) phenol), Carvacrol	Chemosensitisation and disruption of oxidative stress response system in synergy with azoles and amphotericin B, and inhibition of ergosterol biosynthesis and the disruption of cell membrane integrity.	(Ahmad <i>et al.</i> 2011a; Guo <i>et al.</i> 2009; Kim <i>et al.</i> 2010; Kumbhar and Dewang 2001)
	Polyene antimycotics		Amphotericin B	Binds to ergosterol, creating inter-membrane aqueous pores. This leads to efflux of Na ⁺ and Ca ²⁺ and other ions out of cytoplasm. Disruption of cell membrane integrity results in cell death.	(Cohen 2010; Hoehamer <i>et al.</i> 2010; Liu <i>et al.</i> 2005)

Tetracycline derivatives		Minocycline	Broad range antimicrobial properties on <i>Candida</i> spp. biofilms in synergy with azole drugs	(Shi <i>et al.</i> 2010)
Ibuprofen		Ibuprofen	Fungicidal with synergistic effect with azole drugs	(Li <i>et al.</i> 2010)
Nicotinamide treatment		Nicotinamide	Broad range antifungal properties targeting histone acetylation	(Harrison 2010; Wurtele <i>et al.</i> 2010)

1.3 *Candida albicans* and Azole Drug-Resistance

Recent studies showed various forms of azole drug-resistance mechanisms in both the *Aspergillus* and *Candida* pathogenic strains. These are: (i) the up-regulation and over-expression of ATP-dependent cross (ABC) membrane efflux pumps in *Candida krusei* and *Candida glabrata* (Lamping *et al.* 2009; Mansfield *et al.* 2010; Niimi 2010) (ii) amino acid modifications across the azole drug target, sterol demethylase (CYP51), *ERG11* gene (Marichal *et al.* 1999; Mellado *et al.* 2007; Sanglard *et al.* 1998); (iii) possible existence of complementary or alternative CYP51s in the genome (Martel *et al.* 2010c; Mellado *et al.* 2001; Warrilow *et al.* 2010b); (iv) modifications of other enzymes in the fungal ergosterol biosynthetic pathway, i.e. *ERG3* gene coding for sterol C-5 desaturase and *ERG5* gene coding for sterol C-22 desaturase (Lo *et al.* 2005; Martel *et al.* 2010a; Martel *et al.* 2010b). Of particular interest are clinical *C. albicans* azole drug-resistant strains isolated from infected patients with oral or vaginal candidiasis who demonstrated mutation-prone regions in the gene for the azole drug target CYP51 from the cytochrome P450 superfamily of proteins (Marichal *et al.* 1999; Sanglard *et al.* 1998). Similar cases were recently reported for CYP51A from *A. fumigatus*, the opportunistic pathogen causing aspergillosis or aspergillomas in the lungs and respiratory tract (Mellado *et al.* 2007).

Fluconazole, the front line drug which targets CYP51 of *C. albicans* has been used for over 20 years as both oral and intravenous treatments for candidiasis (Cronin and Chandrasekar 2010). Over the years numerous cases of resistance towards this azole drug have been reported. With this, reoccurring incidences of modifications towards the azole drug target have been isolated from clinical and laboratory strains of fluconazole resistant *C. albicans*. Microarray and RT-PCR studies identified specific mutation-prone regions at conserved substrate recognition sites (SRS) throughout the CYP51 fluconazole resistant enzymes (Marichal *et al.* 1999). The SRS regions are parts of a P450 protein sequence that line the active site towards the N-terminal regions with conserved amino acid residues (albeit often having very different functions from one P450 protein to another) coming into contact to the bound substrate, as proposed in early studies by Gotoh *et al.* (1985) using structural information from the P450cam camphor hydroxylase from *Pseudomonas putida* (Gotoh *et al.* 1985). The retention of the SRS region was confirmed and defined over a larger P450 library from the protein database in 1992 (Gotoh 1992). Due to the popularity of azole drugs as a wide spectrum antifungal treatment in humans and as fungicides for plants targeting sterol demethylase of fungi (Stergiopoulos *et al.* 2003; Zarn *et al.* 2003; Zwiers *et al.* 2002), and with the high tolerability of fluconazole as a systemic drug treatment and to address azole drug-resistance issues, derivatives of these azole antifungals

are being actively designed (Bueid *et al.* 2010; Cecil and Wenzel 2009; Lipp 2011; Pasqualotto *et al.* 2010; Sakagami 2010). Recently, as additional antifungal agents, the azole drug econazole and nitroimidazole derivatives which have entered the second phase (out of three phases before being approved as a new drug) of clinical trials have been successfully reported to curb the infection of *Mycobacterium tuberculosis* (Mtb), the causative agent of TB, in murine TB cases (Ahmad *et al.* 2008; Ahmad *et al.* 2011b; Ahmad 2006). The potency of econazole against the infectivity of Mtb has been further analysed in studies of its mechanism of binding to CYP130, a gene which is important for Mtb virulence and which is deleted from the *Mycobacterium bovis* strain used in the BCG vaccine (Ouellet *et al.* 2008).

1.4 *Mycobacterium tuberculosis* (Mtb) and Antitubercular Drugs

The causative agent of TB is the gram positive Mtb (Figures 1.2 A and B). It has the properties of both gram negative and gram positive bacteria, being acid-fast, slow-growing, and with a G+C-rich genome (Cole *et al.* 1998; Crick 2001). The bacterium was first identified and described by Robert Koch in 1882 and, after 39 years, the BCG vaccination was introduced to infants to curb the spread of tuberculosis in humans (Ducati *et al.* 2006; Tala-Heikkila 2002; Wang and Xing 2002). Mtb has an extended generation time of 24 hours in normal media and, in the infected host, nearly 50 times longer than the normal time for *Escherichia coli* (Cole *et al.* 1998). Even before its discovery, Mtb had made a dramatic spread throughout the world. Recently, and specifically within the past decade, drug- and multidrug-resistant strains have become widespread and the WHO has declared the situation a 'global emergency'. This has pushed the WHO, the National Institutes of Health (NIH), and the Centre for Disease Control (CDC) to work towards a solution for MDR and XDR Mtb strains (Centers for Disease Control and Prevention 2006; NIH 2007; WHO 2010a). New drug strategies including chemotherapy in the directly observed therapy short course (DOTS) scheme are desperately required to deal with the increased threat from Mtb, particular since the major drugs (including rifampicin, isoniazid and ethambutol) are becoming ineffective against many clinical strains (Ducati *et al.* 2006; Tomioka and Namba 2006).

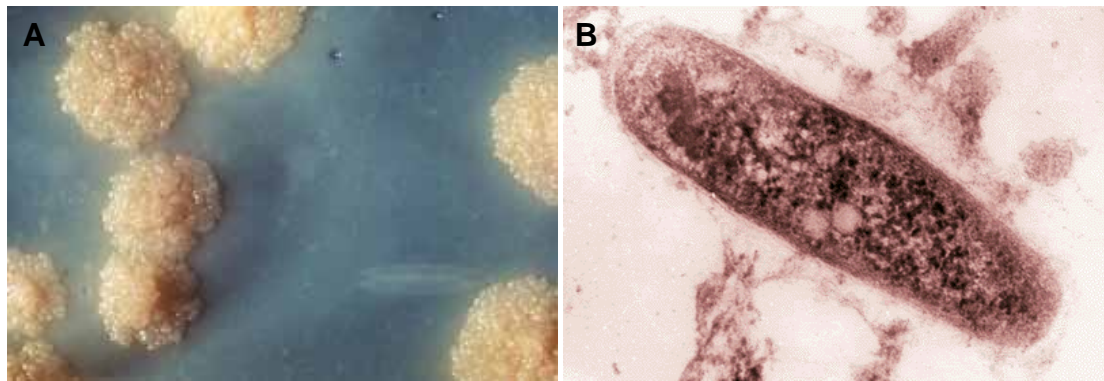


Figure 1.2: Morphology of *Mycobacterium tuberculosis*. A) Colony forming units on an agar plate which shows typical colourless rough surface of *Mycobacterium tuberculosis* colonies (Kubica 1976), B) transmission electron micrograph of *Mycobacterium tuberculosis* (Wadsworth 2008).

Mycobacteria produce an extremely unusual cell wall structure; the peptidoglycan contains N-glycolylmuramic acid instead of the usual N-acetylmuramic acid found amongst most other bacteria (Chatterjee 1997). Up to 60% of the mycobacterial cell wall is composed of lipids that consist basically of uncommon long-chain fatty acids with 60 to 90 carbons, dominated by mycolic acids. Mycolic acids are branched fatty acids that have a short and a long branch, with 22 to 24 and 40 to 64 carbons, respectively, they are covalently linked to the polysaccharide that composes the cell wall, the arabinogalactan, which in turn is attached to peptidoglycan by a phosphodiester link (Figure 1.3) (Chatterjee 1997). Amongst mycobacterial species, Mtb is one of the more permeable to hydrophilic antimycobacterial agents and, thereby, less resistant to hydrophilic drugs, ethambutol for instance (Sabri 2007). However, due to its increasing resistance to first-line TB drugs, TB has become a leading cause of mortality next to AIDS and malaria (WHO 2010b).

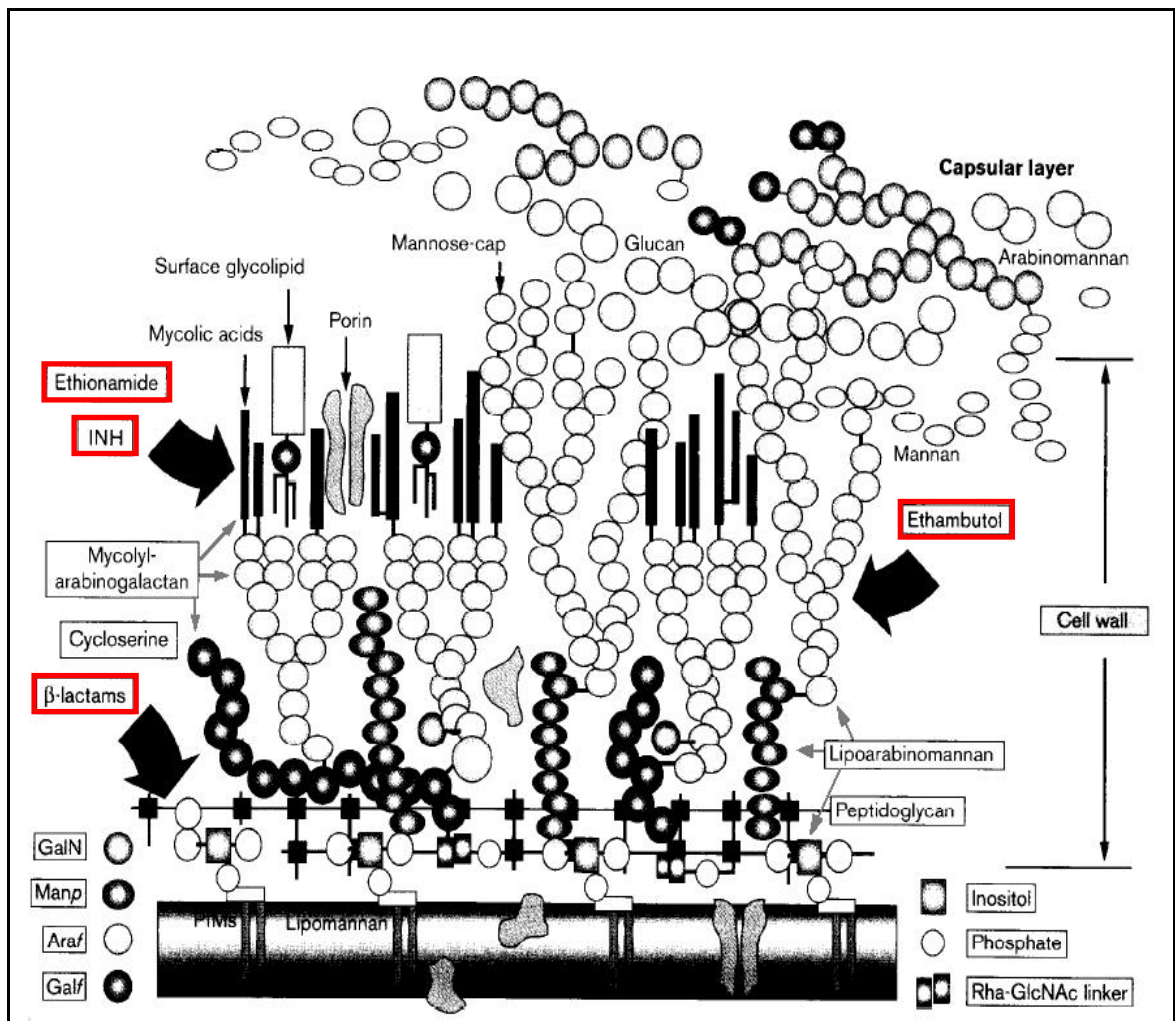


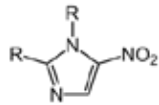
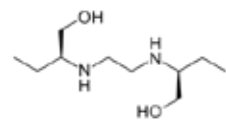
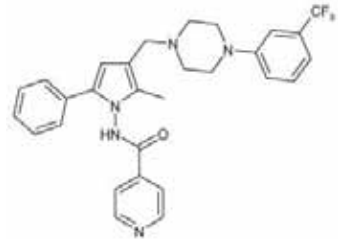
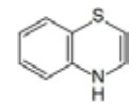
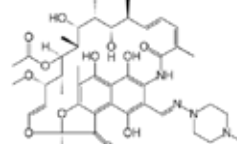
Figure 1.3: A schematic diagram of the *Mycobacterium tuberculosis* cell wall. The three-dimensional and spatial arrangements of the key molecules are largely unknown. Mycobacterial cell walls conform to this model, whereby mycolylarabinogalactan peptidoglycan (mAGP) and lipoarabinomannan (LAM) are the two principal constituents. A capsular-like substance surrounds the bacillus and is rich in polysaccharides. These extracellular polysaccharides are usually glycogen (glucan) (*GalF*), galactosamine (*GalN*), arabinomannan (*AraF*) and mannan (*Manp*). The surface glycolipids include a variety of species- and strain-specific glycopeptidolipids, lipooligosaccharides, and phenolic glycolipid, the chemical identity and amount of which varies from one species to another. The sites of action of some known antimycobacterial drugs are also depicted (grey arrow) in the model. Diagram is taken from Chatterjee (1997) (Chatterjee 1997) to illustrate the site of action of classical antitubercular drug targets on the mycobacterial cell wall used more than a decade ago in DOTS chemotherapy for TB. INH – Isoniazid, PMS – phosphatidylinositol-mannan.

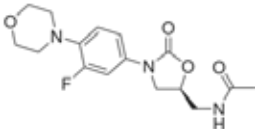
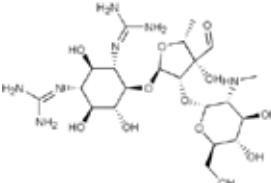
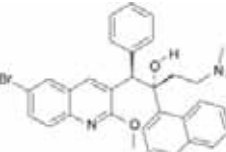
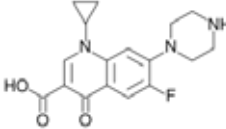
Taking advantage of *Mtb*'s unique cell wall composition, the majority of antitubercular drugs available target a component of the cell wall as illustratively described by Chatterjee in his review for drug activity in the cell wall of *Mtb* (Chatterjee 1997). However, in order to address the *Mtb* MDR/XDR concern, present and up-coming antitubercular drugs are actively aiming at different enzymes and systems involved in *Mtb*'s metabolic pathways, as was comprehensively discussed by Koul *et al.* and others (Cole and Alzari 2005; Koul *et al.* 2011; Zhang *et al.* 2006) and as summarised in Table 1.3. It is highly

encouraging that there are new drugs from different classes being developed and aiming not only at the Mtb's unique cell wall, but also targeting Mtb strains whether drug-resistant (MDR) or susceptible, and acting at other sites beyond the cell wall. Prominent among these are the new diarylquinolines which are in development by Johnson and Johnson (Cole and Alzari 2005). Diarylquinolines target particularly the mycobacterial ATP synthases and showed higher antimycobacterial performance compared to the well established isoniazid (INH), pyrazinamide (PZA) and other prodrugs in this class (Andries *et al.* 2005). Newer drugs from the nitroimidazole derivative class targeting mycolic acids in Mtb's cell wall and cell respiration are also under development (Koul *et al.* 2011). One could observe by comparing both tables 1.2 and 1.3 that the drug classes for fungal infections and TB are almost overlapping with the introduction of azole drug derivatives in antitubercular treatment e.g. nicotinamide and azole drug derivatives.

The determination of the genome sequence of Mtb provided an important boost in this area, and enabled some crucial observations relating to the physiology of the bacterium (Cole *et al.* 1998). Among these was the finding that an extraordinarily large number of Mtb genes are involved in biosynthesis and metabolism of lipids – in accord with the complex lipid composition of Mtb, which contains some extremely long and intricate lipid structures (e.g. the mycolipids) (Brennan 2007; McLean *et al.* 2007a). In addition, it was found that Mtb encodes a very large number of cytochrome P450 enzymes (or P450s): 20 in all (McLean *et al.* 2006a). The genome of the model organism *Escherichia coli* is of similar size – but contains no P450 genes – while the human genome contains 57 P450s (McLean *et al.* 2006a; Nelson 2009). The large number of P450s must indicate their importance to the biochemistry and physiology of Mtb, and likely points to their potential as novel drug target enzymes.

Table 1.3: Upcoming and classical antitubercular drugs targeting various systems in Mtb.

Drug target	Drug class	Drug name	Mechanism of action	Representative drug structure
Cell membrane	Azole – nitroimidazoles	PA 824, OPC 67683	Novel and complex mechanism of inhibition of mycolic acids in cell wall, and inhibits cell respiration.	
	1,2-ethylene diamine	Ethambutol (EMB) since 1962	Interferes with the polymerisation of cell wall arabinan and of lipoarabinomannan by targeting arabinosyltransferase.	
		SQ 109	Derivative of EMB. Inhibition of cell membrane synthesis.	
	Nicotinamide derivatives	Isoniazid (INH) since 1952	Prodrug activated by catalase peroxidase to form an isonicotinic acyl radical which binds to NAD ⁺ . Inhibits mycolic acid (long chain C ₇₀ -C ₉₀ α-branched β-hydroxy fatty acids) synthesis leading to disruption of cell membrane and cell death.	
		Sudoterb (Rivers and Mancera 2008)	Derivative of INH.	
		Pyrazinamide (PZA) since 1952	Prodrug activated by pyrazinamidase/nicotinamidase to form pyrazinoic acid which gets charged and accumulates in the cytoplasm under acidic conditions, making intracellular conditions acidic. This inhibits activity of other enzymes vital for membrane synthesis and affects membrane transport leading to cell death.	
Ethionamide (ETH) since 1956		Prodrug. Disrupts the synthesis of mycolic acids leading to disruption of cell membrane integrity.		
	Benzothiazinones	BTZ043	Targets essential cell membrane arabinan synthesis.	
RNA synthesis	Rifampin since 1957 (McLean and Munro 2008)	Rifamycin, Rifabutin, Rifapentin, Rifalazil	Broad spectrum antibacterial which inhibits RNA synthesis by binding to RNA polymerase.	

Protein synthesis	Oxazolidinones	PNU 100480	Targets ribosomes and inhibits protein synthesis.	
		AZD 5847		
	Macrolides since 1943	Streptomycin	Targets ribosomal S12 protein and 16S rRNA	
		Kanamycin	Targets 16S rRNA	
Capreomycin		Targets 16S rRNA, 50S ribosome, rRNA methyltransferase (TlyA)		
ATP synthase	Diarylquinolines (Andries <i>et al.</i> 2005; Cole and Alzari 2005)	TMC 207	Highly efficient mycobacteria-cidal effect. Best substitute for prodrug-MDR Mtb. It inhibits the synthesis of the mobile disk subunit of mycobacterial ATP synthase, a membrane-bound enzyme, which results in insufficient proton translocation and drastic pH changes in the cytoplasm leading to cell death.	
DNA gyrase	Fluoroquinolones	Ciprofloxacin, Gatifloxacin, Moxifloxacin	Broad-spectrum antibacterial. Inhibits DNA gyrase enzymes which are necessary to separate bacterial DNA, leading to disruption in cell division and cell death.	

Note: Table was adapted from data and reviews of Zhang *et al.* (2006), Koul *et al.* (2011), the National Institute of Allergy and Infectious Diseases (NIAID) (NIH 2007), and cited references. Drugs shaded in grey are undergoing development. Drugs shaded in red are first-line antitubercular drugs introduced in the mid-1900s and are now susceptible to resistance mechanisms.

1.5 Cytochrome P-450 – Background and Physicochemical Properties

The cytochrome P-450 (EC 1.14.14.1) are a superfamily of heme-containing mono-oxygenase enzymes which are classified into families and sub-families based on the extent of amino acid sequence identity. They were first described as mixed-function oxidases (Mason *et al.* 1955) and then mono-oxygenases (Hayaishi *et al.* 1957). They were first indentified in the early 1950s and before the term cytochrome P-450 was first coined in 1962 when Omura and Sato (Omura and Sato 1962) repeatedly observed a spectroscopic signature species at 450 nm (Soret band or absorption maximum) upon binding dithionite-reduced pigments in rat liver microsomes to carbon monoxide (CO). This was when they made the pivotal distinction between other membranous cytochromes and the P450 pigments (cytochrome P-450) containing heme type *b*. A new classification system was soon established for what became a hemoprotein superfamily of more than 11 512 members (and growing) (Nelson 2009). Cytochromes P-450, more routinely called CYPs or P450s are classified in the same family when they meet $\geq 40\%$ amino acid sequence identity and members of the same family often exhibit similar substrate selectivity (McLean *et al.* 2006a; McLean *et al.* 2007a; Nelson *et al.* 1996). Subsequently, P450s were characterised by their low spin oxidised ferric-heme resting state Soret band at approximately 418-419 nm and by their conserved cysteinyl proximal heme iron ligand which can exist either as a thiol (Cys-SH) or thiolate (Cys-S⁻) proximal ligand, with the latter being the catalytically active state (Poulos *et al.* 1987). Previously, the thiol and thiolate states of the cysteinyl proximal ligand have been the subject of much debate with respect to the formation of the 'inactive' P420 species with its CO complex spectral maximum close to 420 nm (Perera *et al.* 2003; Wells *et al.* 1992). It was thought that the P420 species is a portrayal of irreversibly denatured P450 with a Soret band at ~ 420 nm (hence its name P420) and with its proximal cysteine ligand displaced by a histidine, often due to interactions with denaturants or a result of high pressure treatments (Hui Bon Hoa *et al.* 2002; Perera *et al.* 2003; Wells *et al.* 1992). However, it was demonstrated by Dunford *et al.* (Dunford *et al.* 2007) that two states of the cysteinyl axial ligand (the thiolate and thiol, the latter formed cysteinate proximal ligand protonation) can also be manifested in a reversible spectral shift of the Soret band from ~ 448 nm (thiolate P450 species) to ~ 426 nm (thiol P420 species) and back to ~ 448 nm according to pH adjustments during studies of the reduced/CO bound form of CYP121 heme iron, and these data will be discussed simultaneously with my results in Chapter 3. The capability of the P450 Soret band to shift towards a lower or higher wavelength in accordance to different ligand (substrates/inhibitors) binding at the heme

pocket, its heme iron redox states and the different heme iron spin states is of fundamental importance in P450 characterisation (Lewis 2001).

Presently, these P450 spectral changes can be categorised in three major ways which are the type I, type II and the reverse type I (modified type II) spectral changes (Schenkma 1970; Schenkma *et al.* 1972). The type I shift or blue shift (hypsochromic shift), when the Soret band (which is the spectral signature of the major heme species) moves to a shorter wavelength, is accompanied by a spin state change of the heme iron from low spin (LS) to high spin (HS) when the distally bound water molecule of the resting (oxidised) ferric-heme is displaced upon substrate/substrate analogue coordination at the catalytic pocket near the heme (Lewis 2001). This is reflected by the Soret absorbance shifting from ~ 420 nm to ~ 390 nm, seen for example in the binding of substrate cholest-4-en-3-one to the Mtb CYP142 (cholesterol 27-hydrolase), shifting the Soret band from 418 nm to 394 nm (Driscoll *et al.* 2010). This spectrally observable spin state shift is attributed to the change in electron pairing arrangements in the five *d* orbitals of the ferric-heme (Gibson and Skett 2001). Inherently, P450 ferric-heme iron binds to the four pyrrole nitrogen atoms of its protoporphyrin IX skeleton and its five *d* orbitals have different energy states which will change according to the number and type of ligands to the heme iron e.g. whether it has penta-coordinated HS (Figure 1.4 A) or hexa-coordinated LS (Figure 1.4 B) heme iron with a cysteinate ligand (Gibson and Skett 2001). The protoporphyrin IX serves as a good electron donor and acceptor for iron in P450s thus conferring its specific redox properties in its various biological functions. Simultaneously, iron with its unique chemistry is able to exist in different oxidation states; and the ferric, ferrous and ferryl forms are the backbone to the P450 catalytic cycle (Lewis 1996). Ferrous iron has six electrons in the 3*d* shell and two 4*s* electrons in the valence shell. In the conversion between its ferric (Fe^{3+} or Fe(III)) and ferrous (Fe^{2+} or Fe(II)) forms, a 3*d* electron is added which results in the 3*d*⁶ (ferric) and 3*d*⁵ (ferrous) forms, respectively (Lewis 1996).

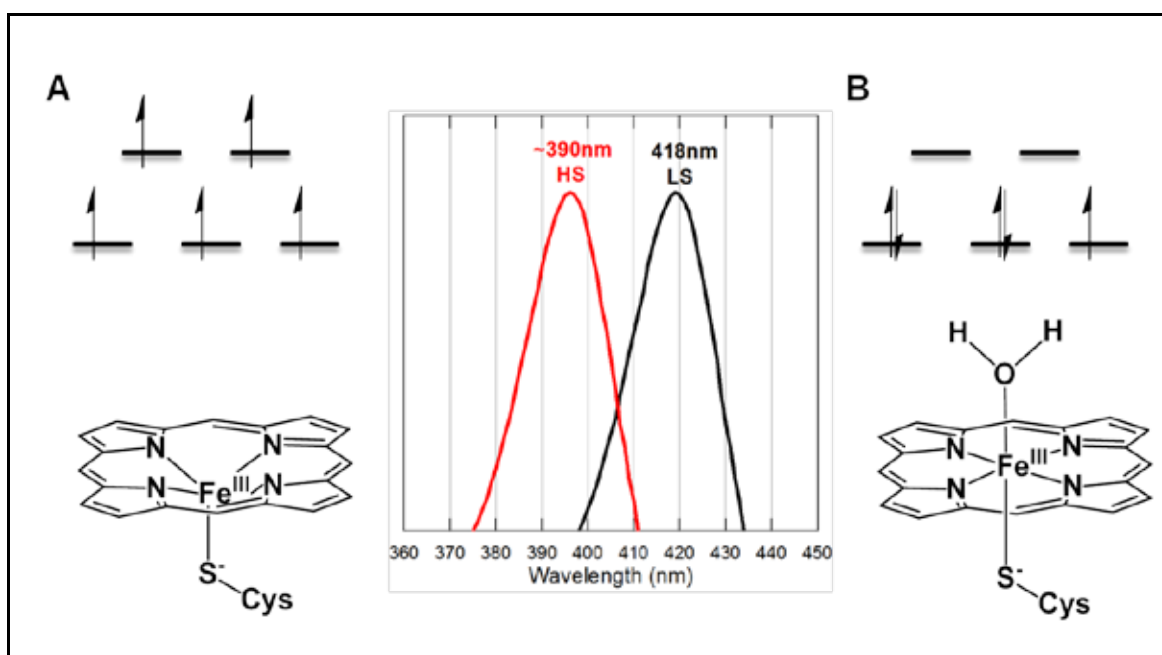


Figure 1.4: Spectral properties and spin state changes of ferric-heme P450. *d* orbital electron distribution for high spin (HS) 5/2 (A) and low spin (LS) 1/2 (B) states of ferric-heme P450 are shown correspondingly to their spectral properties at ~390 nm and 418 nm of the Soret band respectively. Panel A) Upon coordination to type I substrates, the penta-coordinated HS species form with an out-of-plane iron atom which descends axially beneath the porphyrin ring as the central cavity is too small to accommodate a larger cationic radius and the energy equilibrium of the paired electrons of ferric-heme changes to achieve a higher energy rearrangement to fill the two empty higher energy *d* orbitals, which means five electrons singly occupying five *d* orbitals, hence a paramagnetic configuration of $S=5/2$, resulting in a HS state (Gibson and Skett 2001). Panel B) In the LS resting state when a water molecule occupies the sixth distal ligand space of ferric-heme, five electrons fill the three lower energy *d* orbitals with one unpaired electron, hence a configuration of $S=1/2$, and two empty *d* orbitals (Gibson and Skett 2001). This LS hexa-coordinated ferric heme is stabilised by a ligand making the iron in-plane with the porphyrin ring.

In the LS resting ferric heme iron state when a water molecule occupies the sixth distal ligand position, five electrons fill the three lower energy *d* orbitals (t_{2g}) with one unpaired electron, and hence an overall spin of $S=1/2$, and the two higher energy *eg* *d* orbitals are empty (Gibson and Skett 2001). This LS hexa-coordinated ferric heme is stabilised by a sixth axial ligand (water), making the iron in-plane with the porphyrin ring. When the water molecule is displaced by an incoming substrate/substrate analogue, which locates itself in the heme iron catalytic space without physically binding to the cofactor, the electronic organisation of the 3*d* electrons of the ferric-heme iron changes to achieve a higher energy rearrangement, populating the two previously empty higher energy *eg* *d* orbitals, which means five electrons singly occupying each of the five *d* orbitals, hence a paramagnetic configuration of $S=5/2$, resulting in a HS state (Gibson and Skett 2001) with a spectral Soret band signature at ~390 nm, an EPR signal at $g_z = \sim 7.80$ and a resonance Raman ν_3 band at 1487 cm^{-1} for the Mtb cholesterol hydroxylase CYP125, and also for most P450s which exist in a HS state or in a mixture of LS and HS forms in their resting

state (Lewis 1996; McLean *et al.* 2009). This HS penta-coordinated ferric heme exhibits an out-of-plane iron atom which descends axially beneath the porphyrin ring (Figure 1.4 A) as the central cavity is too small to accommodate a larger cationic radius (Gibson and Skett 2001). Type I shifts are produced by the binding of type I ligands at the catalytic pocket near the heme, these usually being the indigenous substrates e.g. camphor to P450cam (CYP101A1) of *Pseudomonas putida* (Schlichting *et al.* 2000) and the fatty acid palmitate to P450 BM3 (CYP102A1) of *Bacillus megaterium*. Alternatively, type I shifts can be induced by substrate-like inhibitors which mimic the substrate binding in the catalytic pocket but which do not undergo oxidation to form product e.g. metyrapone to P450 BM3 (Macdonald *et al.* 1996).

Type II spectral changes are observed when the heme iron is bound to type II ligands which are essentially heme iron binding inhibitors which have lone electron pairs to directly ligate to the heme iron (Lewis 1996). Type II or red shifts (bathochromic shifts), when the Soret band moves to a longer wavelength, happens when the axial ligating water molecule is displaced by an inhibitor with a free pair of electrons from its donating (often nitrogen) atom which distally ligates directly to the heme iron, enhancing or stabilising the LS hexa-coordinated form of the ferric iron, as it binds more tightly than water, and bringing the iron in-plane with the porphyrin ring (Gibson and Skett 2001; Schenkma.Jb 1970), particularly in the case of HS P450s when the iron is out-of-plane prior to inhibitor binding. For example, the Mtb CYP125 is predominantly HS in its resting state and upon binding to azole drug inhibitors at the distal position a dominant hexa-coordinated LS species is formed (McLean *et al.* 2009). Spectrally, the Soret band shift is observed from ~390-405 nm to ~425-435 nm (Lewis 2001), and such changes have been reported in all imidazole and triazole drug binding experiments on P450s from Mtb (Driscoll *et al.* 2011; McLean *et al.* 2007a) and also for the azole-antifungal drug target CYP51 in *Candida* spp., *Aspergillus* spp., humans and plants (Lamb *et al.* 2000; Strushkevich *et al.* 2010; Warrilow *et al.* 2010a; Warrilow *et al.* 2010b). The third spectral change event is the reverse type I or modified type II shift (Schenkma *et al.* 1972). A reverse type I shift is characterised by an increase in absorption at ~420 nm and a decrease at ~390 nm when a substrate/substrate analogue/ inhibitor binds to the active site close to the heme iron causing a mirror-image of the type I substrate binding. Initial studies on this modified type II shift did not reach an evidential consensus on the manner by which the heme iron is ligated in response to the incoming reverse type I ligand, e.g. whether by replacement of the distal water molecule, by indirect substrate ligation to the heme iron via the distal water molecule, or by coordination of the modified type I substrate to a hydrophobic region of the heme pocket (Lewis 2001).

Recently, structural studies have complemented spectroscopic observations of modified type I substrates coordination to the heme iron of CYP125 from Mtb (McLean *et al.* 2002a; McLean *et al.* 2009; Ouellet *et al.* 2011; Seward *et al.* 2006). The structure of CYP125 of Mtb was solved with a modified type I substrate (LP10 or α -[(4-methylcyclohexyl)carbonyl amino]-N-4-pyridinyl-1H-indole-3-propanamide) and the heme iron was shown to ligate the substrate via the distal water ligand, creating the predominant LS hexa-coordinate heme iron ligand complex upon ligand binding in this P450 (McLean *et al.* 2009; Ouellet *et al.* 2011; Seward *et al.* 2006). Essentially, these spectral properties of P450 heme iron and the various spectral Soret band shifts are sensitive characterisation methods using convenient UV-visible spectroscopic analyses to monitor ligand binding events qualitatively or for quantitative measurements of dissociation constants (K_d) of substrates and inhibitors, both kinetically and statically. These techniques are systematically employed in this study of fluconazole-resistant CYP51B1 mutants.

In terms of its catalytic cycle, the vast majority of P450s catalyse the reductive breakage of the bond between oxygen atoms in dioxygen (i.e. atmospheric oxygen) when this is bound to the ferrous form of their heme iron. Electrons for this process are usually supplied from NADPH or NADH, and transferred to the P450 by one or more redox partner enzymes (Denisov 2005; Munro *et al.* 2007a; Munro *et al.* 2007b). The mechanism of P450 catalysis can be surmised by Equation 1.1 and will be elaborated in the following subchapter. RH is the substrate which binds to the heme iron catalytic site with the contribution of 2 electrons from NADPH via redox partner proteins and 2 protons from aqueous solution to form product ROH and a water molecule.



The roles of human adrenal P450s in steroid synthesis and of multiple hepatic isoforms of P450s in xenobiotic metabolism have been intensively studied, and the importance of P450-dependent metabolism in human physiology is well characterized (Guengerich 2006; Guengerich 2008; Guengerich and Rendic 2010; Rendic and Guengerich 2010). Major reviews have been published on human P450s, their characterisation and roles by Guengerich and co-workers (Guengerich 2008; Guengerich *et al.* 2011; Guengerich *et al.* 2010) and de Montellano and co-workers (Ortiz de Montellano 2005; Ortiz de Montellano 2010) but will not be discussed in detail here as I approach the mechanisms of P450 monooxygenation.

1.6 P450 Catalytic Cycle

The irony in P450 heme *b* structural diversity is reflected in their common catalytic mechanism (Omura 2010). The P450s catalyse the reduction of molecular oxygen at the ferric ion of the heme that results in the mono-oxygenation of an adjacent bound substrate, and produces a molecule of water from the second oxygen atom. The whole mechanism requires two electrons, delivered by NAD(P)H from one (or few) redox partners which are either from flavoproteins or iron-sulfur proteins, and two protons contributed by the bulk solvent. These protonation reactions are likely mediated by the active site amino acid side chains. The existence of multiple reactive intermediates which are catalytically relevant oxidative radicals that attack the substrate within the P450 catalytic cycle as outlined by the dotted boxes in Figure 1.5 (A) is typically transient. The sequential formation of these relatively reactive and transient intermediate species from steps (iv-vi) have been intensively researched with few direct measurements due to the high reactivity and the low accumulation of these intermediates in kinetic studies (Denisov 2005; Guengerich and Isin 2008; McLean and Munro 2008).

The most reactive yet transient species in the cycle is Compound I or the ferryl-oxo porphyrin radical intermediate which has been actively studied since the 1970s by Klaus Ruckpaul's group (Jung 2011) and subsequently by Steve Sligar's (Newcomb *et al.* 2006), John Dawson's, Brian Hoffman's and Mike Green's groups. Compound I, or the ferryl-oxo intermediate is the most reactive compound in the P450 catalytic cycle which transfers an oxygen atom to the substrate to form the product. The four research groups above, reported important sightings of transient unstable intermediates (iv-vi) (Figure 1.5 A) at cryogenic temperatures. Co-60 gamma-irradiation and thermal annealing steps gave evidential EPR/ENDOR spectra for formation of intermediates (iv), (v) leading to product formation (Davydov *et al.* 2001; Davydov *et al.* 2005). Laser flash photolysis (Newcomb *et al.* 2006) and stopped-flow spectrophotometry (Kellner *et al.* 2002) analysis proved spectrally the formation of Compound I prior to product release, and very recently, Rittle and Green (2010) successfully reported the isolation and characterisation of the elusive Compound I, the final transient P450 catalytic cycle intermediate to be characterised (Rittle and Green 2010) and isolated from CYP119 of the thermophilic archaeon *Sulfolobus solfataricus* (Denisov 2005; Isin and Guengerich 2008; Rittle and Green 2010; Rittle *et al.* 2010; Sligar 2010; Yano *et al.* 2000). The intermediate (v) has only been observed at cryogenic temperatures (Denisov *et al.* 2008) and has been defined as the rate limiting step in P450 hydrocarbon hydroxylation reactions (Bach 2010). The generally accepted mechanism for cytochrome P450 hydrocarbon oxidation was proposed by Groves *et al.* in

the late 1970s involving steps shown in the yellow box of Figure 1.5 (A). This concept, termed the ‘oxygen rebound’ mechanism, introduces the last marginally stable intermediate – Compound 0 (protonated intermediate (iii)) following the activation of molecular oxygen to ferrous-heme-substrate complex (ii), which becomes intermediate (iii) in Figure 1.5 (A). The protonation of Compound 0 leads to loss of a water molecule and the formation of the catalytically active Compound I which abstracts a hydrogen from the substrate to yield a one-electron reduced ferryl-oxo species or a protonated-ferryl-oxo species (Compound II) and a carbon radical intermediate (R-C[•]) from the substrate as shown in Figure 1.5 (B) (Green 2009). This carbon radical group then recombines with Compound II to give an enzyme–product complex; the final alcohol product is then released. This mechanism is also called the ‘alkyl rebound’ state by Shaik *et al.* (Shaik *et al.* 2007; Shaik *et al.* 2005) who proposed multi-state C-H activation and alkyl group dissociation forms prior to product release from (at step (vii)) Compound II. While the presence of Compound II, the oxygen rebound consensus mechanism and the role of thiolate ligand enhancing the oxidative potential of Compound I in cytochrome P450 has been reaffirmed by Green *et al.* (Green *et al.* 2004) and Rittle and Green (Rittle and Green 2010), theoretical work, describing by quantum mechanical dynamics that the distal oxygen atom in Compound 0 is less likely to be protonated and that P450 hydrocarbon hydroxylation occurs by another mechanism involving Compound I and II via a ‘somersault’ rearrangement mechanism, is argued by Bach (Bach 2010; Bach and Dmitrenko 2006).

Essentially, the P450 reaction begins with the binding of substrate at the catalytic pocket (i) and the immediate dissociation of the loosely bound distal water molecule (as the sixth ligand to the heme-iron) making it a five-ligated high spin (HS) heme-iron. Next, the five-ligated HS ferric-heme will be reduced by the first electron from NADH/NADPH via a redox partner enzyme (in which case the redox partner enzyme(s) depends on the class of P450 – mammalian, fungal or bacterial) to become ferrous-heme (ii) with the Soret band at 418 nm, a β -band at 555 nm, and a weak α -band at 580 nm shifting to \sim 410 nm and the α and β -bands merging at \sim 558 nm for P450cam (Ortiz de Montellano 2010). The oxy-P450 complex ($\text{Fe}^{3+}\text{-O}_2$) is the last ‘stable’ intermediate following the (iii) step of molecular oxygen binding (Denisov 2005; Guengerich and Isin 2008). After the reduction of the oxy-P450 complex by the second electron from NADH/NADPH via the redox partner enzyme, there is a sequential formation of a peroxo-ferric intermediate (iv), then the protonated form called the hydroperoxo-ferric intermediate (v), followed by the second protonation at the distal oxygen atom with subsequent heterolysis of the stable O_2 bond resulting in the Compound I ferryl-oxo (vi) species and formation of a water molecule.

Finally, this is followed by the oxidation of Compound I to form a product complex after step (vii), before the dissociation of the final substrate ROH (viii) and the return of the heme to its initial resting state (de Montellano and De Voss 2002; Denisov 2005; Poulos 2005). Due to the reactivity of some of the intermediates in the P450 cycle, some side reactions may occur at the expense of cellular energy (Ortiz de Montellano 2010; Poulos 2005) (Figure 1.5 (A) dashed arrows **1-3**). These are – **1**) the autooxidation of the last stable intermediate (Denisov *et al.* 2007) (iii), the oxy-P450 complex, where the bound oxygen leaves as a superoxide ion and the P450 returns to its ferric-heme state. **2**) The reverse peroxide shunt at the hydroperoxo-ferric intermediate (v) happens when the inner oxygen atom is protonated instead of the outer oxygen bound to hydrogen, resulting in the release of a hydrogen peroxide molecule and the return of intermediate (v) to the ferric-heme state. **3**) The oxidase shunt at the Compound I ferryl-oxo intermediate (vi) happens when the oxygen atom is reduced to a water molecule and Compound I again returns to the ferric-heme state. These reactions occur largely in mammalian drug metabolising P450 systems when the P450s are inefficiently coupled to their electron donors resulting in these autooxidation pathways because the monooxygenase systems are imperfect for substrate turnover (Poulos 2005).

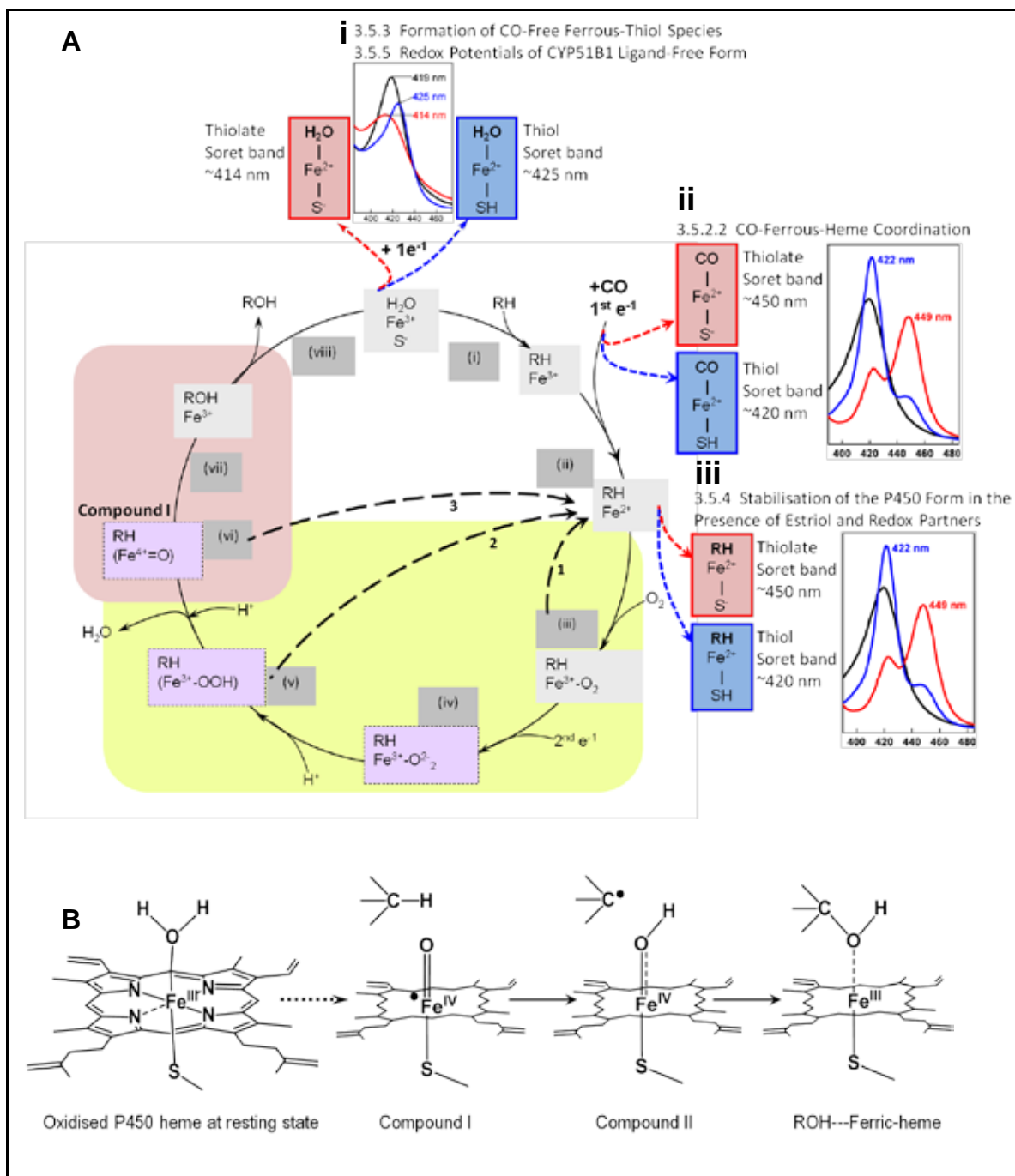
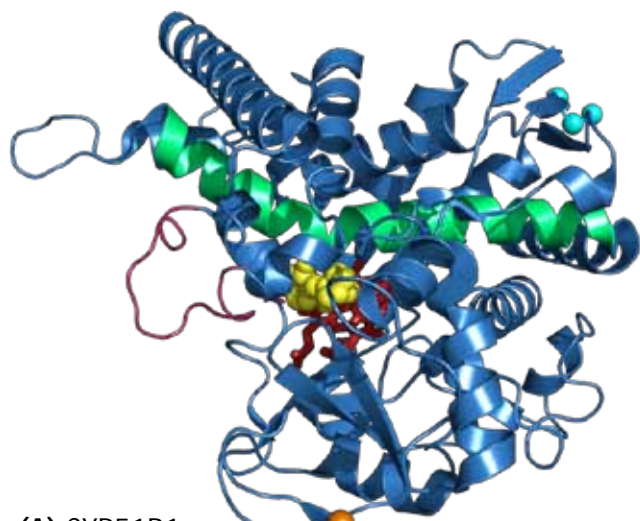


Figure 1.5: The catalytic cycle of cytochrome P450, showing known intermediates and the rebound mechanism. Panel A The classical catalytic cycle of P450s begins with (i) Substrate binding, (ii) Reduction, (iii) O₂ binding, (iv) Reaction of the FeO₂²⁺ complex, (v – vii) with delivery of 2nd e⁻¹ from redox partners and 2 protons, (viii) Dissociation of final product ROH and return to low spin state of the Fe³⁺ at the heme catalytic centre (Denisov 2005; McLean *et al.* 2006a). The dashed arrows show alternative pathways which may occur due to the reactivity of some intermediates which by-passes the cycle (Poulos 2005). **A i to iii** as shown by the coloured (red/blue) dotted arrows are pathways in the P450 catalytic cycle which were being exploited/used in the characterisation of CYP51B1 variants in this work as designated accordingly to the section title in Chapter 3 results. **Panel B** details the rebound mechanism in the P450 catalytic cycle shaded in red. P450 intermediates are shown and substrate and heme porphyrin radical are indicated by (•) adjacent. Compound I – is the ferryl-oxo reactive intermediate which transfers an oxygen atom to the substrate according to the consensus oxygen rebound mechanism described by Groves and McClusky (1976) by H abstraction from substrate to form the transient Compound II (a protonated ferryl-oxo species and substrate-C radical) before these species recombine to dissociate an alcohol product and complete the monooxygenase reaction in the P450 catalytic cycle (Green 2009; Ortiz de Montellano 2010).

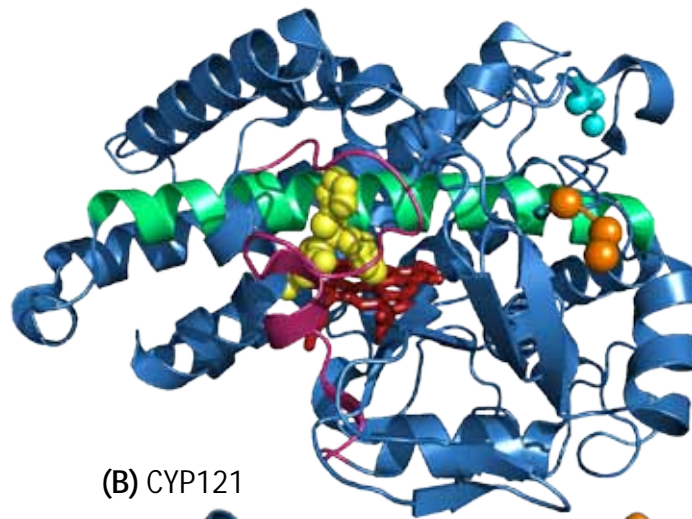
In addition to monooxygenation of substrates, P450s have also been found to participate in other chemical reactions; desaturation reactions to increase the production of penicillin by a mutation in CYP504 of *Aspergillus nidulans* which suppresses the hydroxylation of phenylacetate (Mingot *et al.* 1999), for instance. Also, the reduction of some substrates e.g. reductive dehalogenation of alkyl halides, reductive ring-cleavage of the anticonvulsant drug zonisamide and the reduction of 4-nitropyrene, oxidative cleavage of ester and amide bonds, as well as catalysing subsequent rearrangement reactions which may form an unexpected reactive product that may then undergo another spontaneous rearrangement reaction (Guengerich and Isin 2008; Ortiz de Montellano 2005; Ortiz de Montellano 2010). An example is in the case of murine CYP2B1 involving unusual isomerase activity of the hydroperoxide-substrate complex at steps (iv) – (v) in Figure 1.5 (A) when another methylene group (next to the primary CH₂R group but closer in proximity to the ferryl radical) was hydroxylated instead, resulting in the transfer of the reactive oxygen of Compound I into the secondary methylene group (Kupfer *et al.* 2001). This spontaneous rearrangement of groups in substrates of some P450s, i.e. an isomerase activity, is attributed to substrate intramolecular stereoselectivity coupled with the high reactivity of the transient intermediates, especially the Compound I radical (Ortiz de Montellano and De Voss 2002). Another unusual P450 mechanism which describes the diversity of P450 reactions takes place during the last step of estrogen production by human CYP19 aromatase when the sequential production of hydroperoxy-ferric intermediate (v) was not detected, directly forming the ferryl-oxo Compound I and enabling nucleophilic competition between the other reactive intermediates (Gantt *et al.* 2009). There have been cases where metabolism of xenobiotic compounds by P450s produces more toxic side products which may be carcinogenic to cells (Myasoedova 2008). This occurs especially by human hepatic CYP3A4 and 2C9, where 70% of ingested xenobiotic compounds are metabolised, including the toxic trichloroethylene (TCE) compound via epoxidation and rearrangement reactions to its oxide and toxic intermediates which then fuse to important enzymes (CYP2E1, CYP2B1 and P450 reductase) by covalently modifying the polypeptides in the enzymes with formyl or chlorinated groups, irreversibly deactivating them (Cai and Guengerich 2001). Also the activation of benzo[a]pyrene (a carcinogenic product from combusted organic material) from cigarette smoke to its carcinogenic epoxide form by CYP1A1-dependent catalysis have been reported (McLean *et al.* 2007b). Other P450-dependent xenobiotic metabolism includes heteroatom dealkylation to deactivate caffeine and heteroatom oxygenation of toxic solvent pyridine which all share the same P450 catalytic cycle (Furge and Guengerich 2006).

1.7 P450 Systems in Mtb

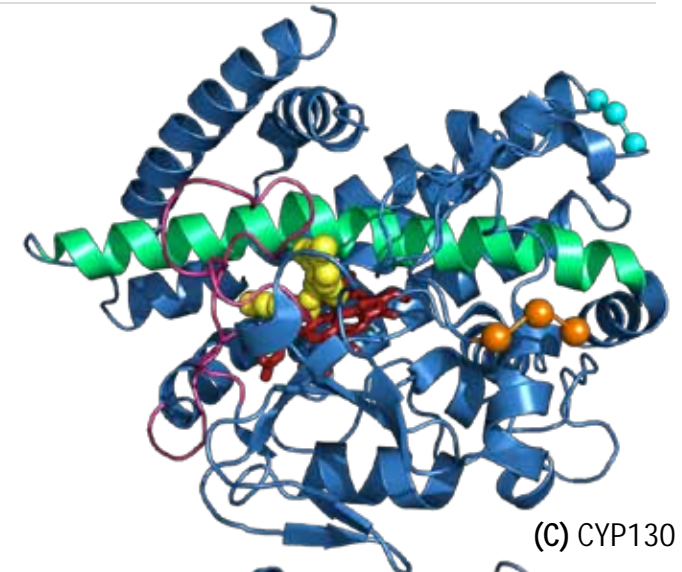
The P450s are widespread in nature (humans have 57 isoforms), but are generally present in rather small numbers in bacteria (Lewis 2004). Their presence in such large numbers (20 P450s) in Mtb is almost certainly related to the complicated lipid biochemistry of the pathogenic bacterium, which (in turn) is known to be essential to viability and infectivity of Mtb (Ehrt 2007; McLean *et al.* 2010). Similar to Mtb, other actinomycetes (e.g. *Mycobacterium bovis* and *Streptomyces coelicolor*) also possess a large number of P450s in their genome (Lamb *et al.* 2002; McLean *et al.* 2006a). Studies on some P450s in Mtb has revealed their importance for metabolic purposes and their response systems to external stimuli, immune response or chemical exposure (Betts *et al.* 2003; Sassetti *et al.* 2003). CYP121 was induced when the bacilli were exposed to antibiotics (isoniazid and thiolactomycin) which inhibit mycolic acid synthesis in Mtb, while CYP123 and CYP138 were induced at higher temperatures (Betts *et al.*). In addition, both CYP123 and CYP138 may share an operon with CYP51B1 and its related ferredoxin redox partner (McLean *et al.* 2006c). CYP128 was shown to be important for growth *in vitro* when it was induced during cell starvation (Sassetti). CYP144, although not necessary for growth, may be essential for azole drug resistance as deletion strains showed increased susceptibility to azole drugs (Driscoll *et al.* 2011). CYP124 has an unusual hydroxylase activity toward methyl-branched lipids which may prove a unique drug target once its function is understood (Johnston *et al.* 2009). Further evidence for the importance of P450 chemistry to Mtb is the fact that azole drugs (known inhibitors of the fungal sterol demethylase CYP51 P450 and widely used antifungal antibiotics) are potent anti-Mtb drugs with typical MIC values of ~5 mg/mL (McLean *et al.* 2002b). Agents such as clotrimazole and econazole are particularly effective as antituberculars, and econazole was also reported to clear Mtb bacteria from infected mice (Ahmad *et al.* 2008; Ahmad 2006). The same azoles are essentially inactive against *E. coli*, reinforcing the importance of the P450s as targets in Mtb (McLean *et al.* 2002b). Figure 1.6 shows the crystal structures of Mtb P450 enzymes solved to date either ligand-free or bound to azole drug inhibitors.



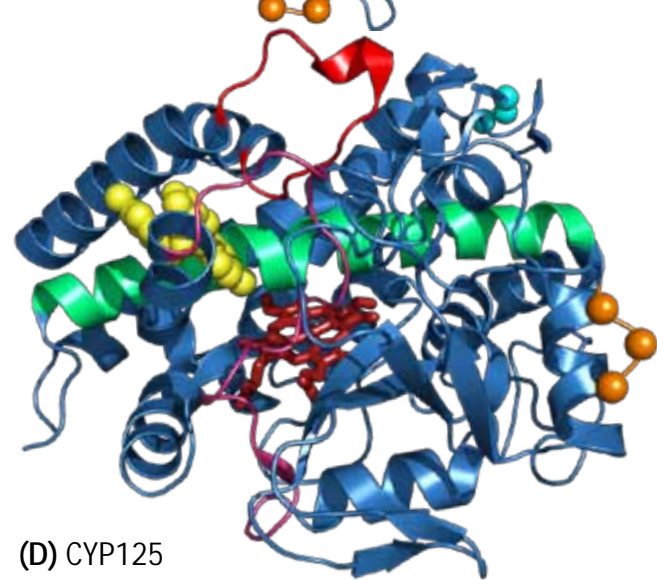
(A) CYP51B1



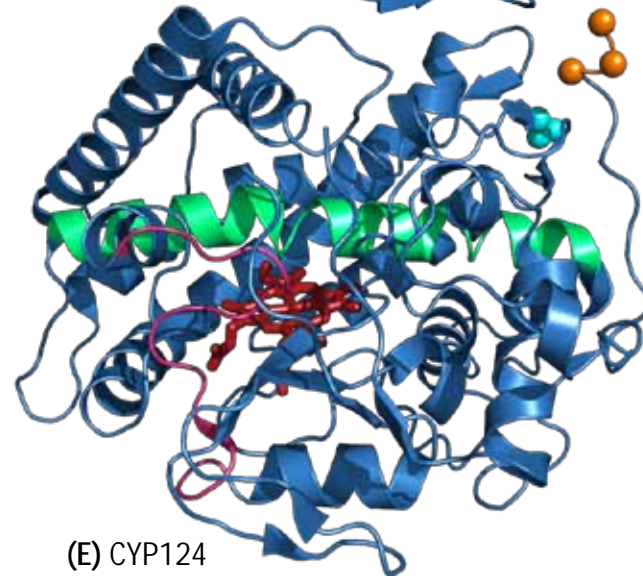
(B) CYP121



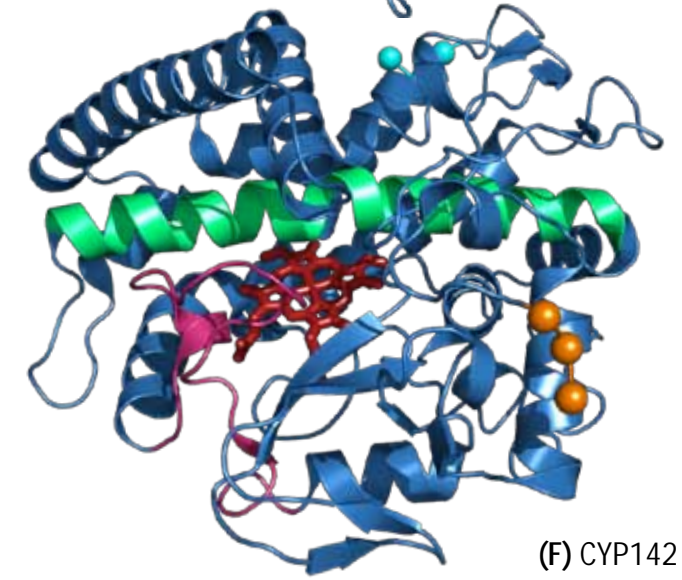
(C) CYP130



(D) CYP125



(E) CYP124



(F) CYP142

Figure 1.6: Structures of crystallised Cytochromes P450 from *Mycobacterium tuberculosis*. Green helix – I-helix, pink loop/helix – BC-loop region, orange spheres – N-terminal, blue spheres – C-terminal, red sticks – iron-heme porphyrin, yellow spheres – azole drug ligand. (A) CYP51 (PDB: 1ea1) also known as sterol 14 α -demethylase (Podust *et al.* 2001a) and (B) CYP121 (PDB: 2ij7) in complex with the inhibitor fluconazole (yellow spheres) which is bound to the iron of the heme active site. Fluconazole forms the sixth axial ligand to the Fe³⁺ of the heme replacing a water molecule in their ligand-free forms. CYP51 is the only cytochrome P450 structure that has a characteristic kink in the middle of the I α -helix (green), and near its N terminus (Leys *et al.* 2003; McLean *et al.* 2006b; Podust *et al.* 2004). (C) CYP130 (PDB: 2uvn) in complex with econazole (yellow spheres) (Ouellet *et al.* 2008). (D) CYP125 (PDB: 3iw2) in complex with econazole (yellow spheres) distally coordinated to the iron-heme, shown here at the ‘letter box’ (denoted by the red FG-loop and BC-loop opening) entry channel to the iron-heme catalytic pocket. As with fluconazole, econazole forms the sixth axial ligand to ferric-heme replacing a water molecule (McLean *et al.* 2009). (E) CYP124 (PDB: 2wm5) in the ligand-free form is a methyl-branched lipid omega-hydroxylase (Johnston *et al.* 2009). (F) CYP142 (PDB: 2xkr) is a novel cholesterol oxidase (ligand-free form) which catalyses the 27-hydroxylation of cholesterol and cholest-4-en-3-one to their 27-hydroxy derivatives and on to 5-cholestenoic acid and cholest-4-en-3-one-27-oic acid, respectively, which may be important for host-cholesterol metabolism (Driscoll *et al.* 2010). All models were drawn using PyMol™ software (DeLano Scientific, 2005) based on published pdb files.

CYP126 and CYP144 have also recently been solved (Professor Andrew Munro, pers. comm.). Out of these eight structurally solved P450s from Mtb, two, CYP125 and CYP142 demonstrated catalytic activity on intermediates in cholesterol oxidation and are important for host-cholesterol metabolism (Driscoll *et al.* 2010; McLean *et al.* 2009). CYP125 was shown to be important for infectivity when Mtb break down host cholesterol when engulfed in macrophages in TB infected mice (Kendall 2004). CYP51B1, encoded by the gene *Rv0764c*, was the first P450 structurally solved from Mtb and the first sterol demethylase found in a prokaryote (Aoyama *et al.* 1998). Although its sterol demethylating activity on lanosterol, 24, 25-dihydrolanosterol and the plant sterol obtusifoliol has been proven (Bellamine *et al.* 1999), the absence of a sterol biosynthetic pathway (specifically the absence of squalene monooxygenase and oxidosqualene cyclase genes, required to form the initial sterol) in Mtb suggest that CYP51B1 may utilise host sterol substrate upon host infection of the pathogen making it one of the antitubercular drug targets next to CYP121, CYP125 and CYP142 (Munro *et al.* 2003). Of these, CYP51B1 and four azole-resistant mutants mapped from *Candida albicans* CYP51 fluconazole-antifungal resistant strains (Aoyama *et al.* 2000; Kudo *et al.* 2005; Marichal *et al.* 1999; Sanglard *et al.* 2003) will be studied in detail in Chapters 3 and 4 with regards to its azole drug binding kinetics, biophysical characterisation and structural elucidation.

1.8 Mtb P450 as Drug Targets

Recent work has highlighted the importance of certain Mtb P450 isoforms as likely azole drug targets. Initially, P450s make good drug targets because they are specifically involved in an essential pathway for the viability of fungal cells (i.e. cell wall biosynthesis) or in pathogenicity. In Mtb, an increasing number of P450s were found to be involved in cholesterol metabolism (McLean *et al.* 2009; Driscoll *et al.* 2010). Cholesterol is the substrate of the product of two essential genes for pathogenicity in Mtb while Mtb itself does not have a *de novo* cholesterol biosynthetic pathway (McLean *et al.* 2009; Driscoll *et al.* 2010; Cole *et al.* 1998, Sasseti *et al.* 2003; Lamichhane *et al.* 2003). Azole drugs were chosen based on their high affinity towards P450 proteins, making them obvious candidate for antitubercular drugs especially when this class of drugs have been widely established as antifungal drugs (Munro *et al.* 2003). The major P450 drug targets are likely to be (i) CYP121, which was recently demonstrated to be essential for Mtb viability *in vitro* (McLean *et al.* 2008). CYP121 has been structurally characterised to high resolution, and recent work demonstrated a novel mode of binding of an azole drug (fluconazole) to the P450, with heme iron interaction occurring via a bridging water molecule (Leys *et al.* 2003; Seward *et al.* 2006) (Figure 1.7 **B, D**); (ii) CYP128, which was shown to be an essential gene for Mtb viability through analysis of libraries of transposon insertion mutants (McLean *et al.* 2006a); (iii) CYP125, which is located in a cluster of genes associated with catabolism/metabolism of cholesterol and which is essential for the ability of Mtb to establish an infective state in humans (McLean *et al.* 2009); (iv) CYP142, which is located in the gene cluster for host cholesterol metabolism and is known as a cholesterol 27-oxidase required for initiation of cholesterol breakdown (Driscoll *et al.* 2010) and (v) CYP51B1, which is a sterol demethylase, has orthologues in fungi, humans, plants, and trypanosomes, and for which the major difference with eukaryotic forms is the absence of an N-terminal membrane anchor in the Mtb CYP51B1 enzyme. It is the only P450 in Mtb whose structure is in the open conformation and with a characteristic 'kink' in its I-helix (Figure 1.7 **A**), thus enabling accommodation of a large range of ligands at its catalytic pocket (Lepesheva and Waterman 2007; McLean *et al.* 2006a; Stout 2004; Waterman and Lepesheva 2002). Lack of a membrane anchor is a typical feature of prokaryotic P450s, virtually all of which are soluble, cytoplasmic enzymes (Lamb *et al.* 1998; Warrilow *et al.* 2010b; Yoshida *et al.* 2000). Due to the difficulties in expressing, purifying and performing detailed kinetic and spectroscopic analysis of membranous yeast and filamentous fungi CYP51 enzymes, the soluble nature of the CYP51B1 isoform from Mtb (due to the absence of the N-terminal membrane anchor in bacterial CYP51) and that its redox partners are also soluble (McLean

et al. 2003a; McLean *et al.* 2003b; McLean *et al.* 2006c) makes it a better candidate. This is unlike eukaryotic CYP51 systems, whose components are membrane bound rendering the expression and purification of the eukaryotic CYP51 systems more problematic. Therefore, CYP51B1 from *Mtb* could easily facilitate its use as a model enzyme and for structural analysis and examination of the mode of interaction between CYP51 enzymes and azole drugs, as demonstrated in Figure 1.7 (C).

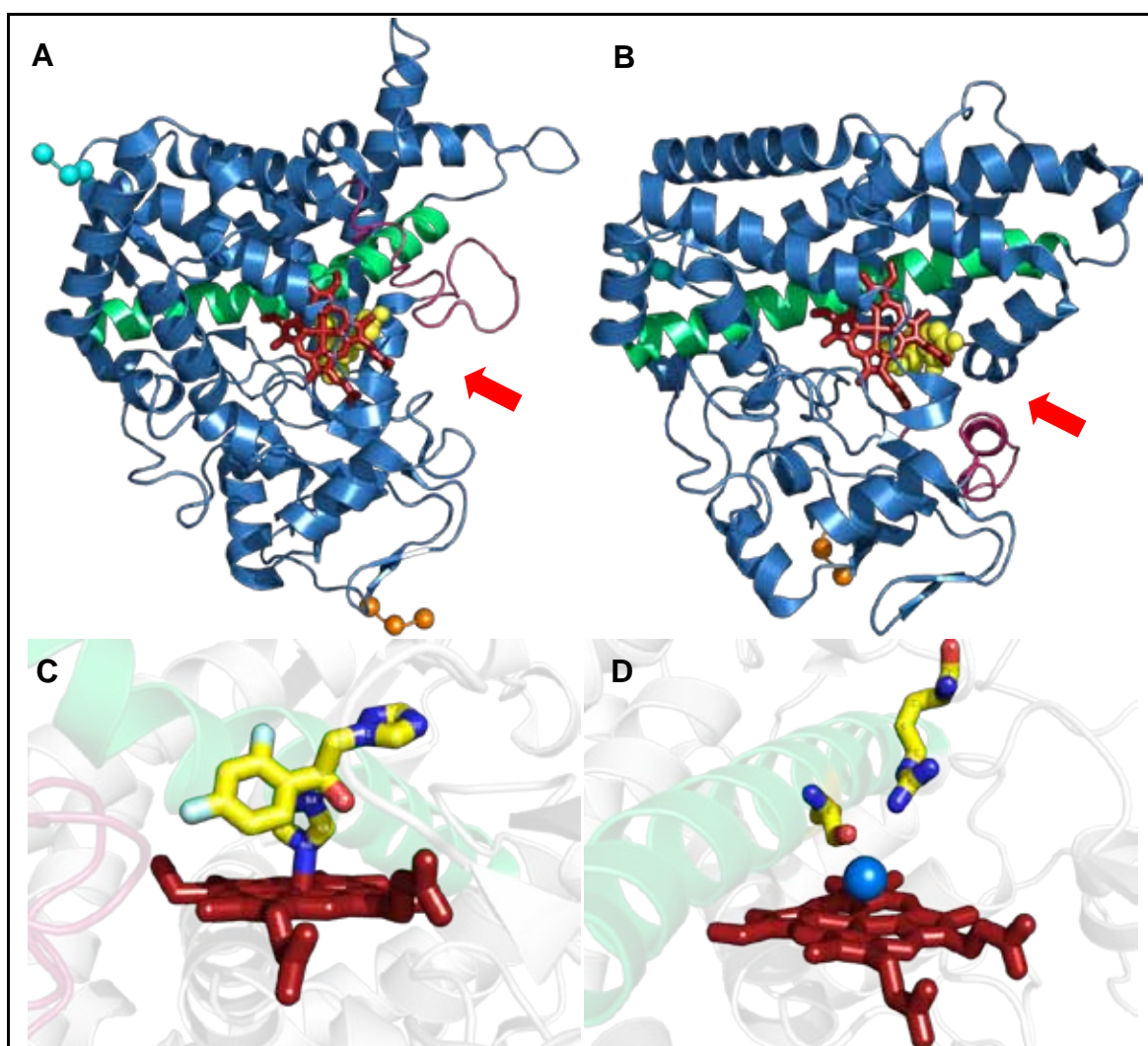


Figure 1.7: Crystal structures of *Mtb* P450s CYP51B1 and CYP121. (A) and (B) are distal views of CYP51B1 and CYP121 with the N-terminal (orange) and C-terminal (cyan) shown as spheres, B-C loop (pink), I helix (green), fluconazole (yellow spheres or yellow and blue sticks), heme (red sticks) and red arrows suggest the entry route of fluconazole into the enzymes via the B-C loop opening. (A) Overall structure of CYP51B1 and topology of the fluconazole-bound form of *Mtb* CYP51B1 (PDB: 1ea1). The large deviation in the I helix is evident. Fluconazole is depicted as yellow spheres above the heme for CYP51B1. (B) A similar representation of the structure of fluconazole-bound CYP121, with a straight I helix (PDB: 2ij7). Parts (C) and (D) show close-ups of the immediate heme environments in the P450s. (C) Direct coordination of the CYP51B1 heme iron (N-Fe) by fluconazole. (D) Interactions of Arg386 and the I helix residue Ser237 with the water ligand (blue) to the heme iron in CYP121, which leads to stabilization of the low-spin heme iron form of CYP121 (PDB: 2ij5) (Leys *et al.* 2003; McLean *et al.* 2006b). All images were drawn using PyMol™ software (DeLano Scientific, 2005) based on the pdb files stated.

Of particular interest would be the exploitation of CYP51B1 and mutant forms that mimic azole drug-resistance-conferring mutations in yeast (e.g. *Candida albicans*) CYP51. Analysis of such mutants could enable a more detailed understanding of the structural basis of azole drug-resistance, and also of how this could be avoided through intelligent drug design. Both antifungal and antitubercular drugs may confer adverse effects in humans during the course of treatment (Gibson and Skett 2001, Harrison 2010). Dosage is a matter of balancing the effectiveness (fungicidal/bactericidal activity) of the drugs on the pathogen during the duration of treatment without exceeding the harmful threshold in the host, hence, the vigorous clinical screening of new drugs before it can be considered safe for use during treatment (Zhang *et al.* 2006, Koul *et al.* 2011). The potency of azoles as antitubercular drugs means such work could be of even greater relevance with respect to rationalising azole resistance mechanisms and *de novo* drug design. Although the potency of azoles as systemic drugs has been established, the fact that this class of drugs have high affinity for other P450 proteins in humans (e.g. CYP3A4) and that they are also used widely in other medications means that individual screening of these drugs need to be stringently tested for drug-drug interactions when taken alongside other drugs (e.g. antifungal, antitubercular, AIDS/HIV drugs) and drug-protein interactions to rule out negative effects before it can be administered safely (Guengerich and Rendic 2010).

Since the completion of Mtb genome in 1998 by Cole *et al.* (1998), much effort has been involved in determining the real function of CYP51B1 in Mtb, but without confirmatory results. The nearest explanation to the CYP51B1 function in Mtb has been borrowed from the catalytic cycle of CYP51 of plants and yeast or fungi which involves the main CYP51-dependent pathway whereby CYP51 catalyses a three step oxidation of sterol substrates. For instance, lanosterol for yeast and obtusifoliol for plants, which inherently leads to the production of ergosterol and phytosterol (sitosterol), respectively (Lepesheva and Waterman 2007). Cholesterol is important for the infectivity of Mtb into macrophages. However, Mtb itself does not produce cholesterol intrinsically due to the absence of a *de novo* sterol metabolic pathway, but it uses cholesterol from the host's membrane, likely breaking it down as an energy source while engulfed in the host macrophage (Waterman and Lepesheva 2005). This appears to be the main reason which clouds the efforts to uncover the primary role of CYP51B1 in Mtb, i.e. there is no compelling evidence as yet for its role in host sterol demethylation, but instead a suspicion that it may perform such a role or else be involved in a pathway involving host cholesterol metabolism. A large cluster, or regulon, of genes in Mtb is known to be involved in the oxidation of host cholesterol as a carbon source for growth, and these genes include CYP125 and CYP142, both shown to

encode cholesterol 27-hydroxylase P450 enzymes that likely initiate a pathway of cholesterol degradation (Driscoll *et al.* 2010; McLean *et al.* 2009; Waterman and Lepesheva 2005). However, the specific role (if any) of CYP51B1 in this process is unclear, and CYP51B1 is not located in this regulon. However, CYP51B1 has been shown to catalyse oxidative demethylation of sterols, with highest activity towards the plant sterol obtusifoliol (Bellamine *et al.* 1999).

1.9 Background on Sterol Demethylase (CYP51)

CYP51 from Mtb, now designated CYP51B1, was suggested to be a progenitor for the entire CYP enzyme superfamily, but was also hypothesized to have arisen by lateral gene transfer from plants (Rezen *et al.* 2004). Eukaryotic CYP51s are integral membrane proteins tethered by a hydrophobic N-terminal anchor domain (McLean *et al.* 2006a). A multiple amino acid sequence alignment and the construction of a molecular phylogenetic tree revealed that CYP51 formed a distinctive evolutionary cluster independent of other P450 families, and thus is unlikely to have been a progenitor in the P450 superfamily. Figure 1.8 (A) taken from Yoshida *et al.* (2000), represents the most probable molecular phylogenetic tree of the CYP51 family with the closest relatives being CYP7A1, 7B1 and CYP8A1, 8B1 from humans which are cholesterol 7- α hydroxylase, dehydroepiandrosterone 7- α hydroxylase, prostacyclin synthase and sterol 12- α hydroxylase, respectively. The numbers at each node represent bootstrap values. In this tree, four eukaryotic kingdoms form a single cluster (animals, fungi, plants, slime mould). This suggests that CYP51 arose during the prokaryotic era even before the divergence of animals and fungi and has been distributed into major biological kingdoms concomitant with their diversification (Yoshida *et al.* 2000). A complementary multiple alignment analysis of CYP51s from the above mentioned kingdoms was made, as shown in Figure 1.8 (B). It revealed that CYP51B1 is closely related to CYP51s from the plant kingdom, the protozoan orthologues and the sole viral orthologue of unknown function (Lamb *et al.* 2009), instead to CYP51s from the animal kingdom, or from the fungi. This interesting fact paves the way for further research into CYP51B1 as a drug target using surrogate substrates from the plant and bacterial sterol metabolic pathway, especially since the precise function of CYP51B1 in Mtb is still unknown.

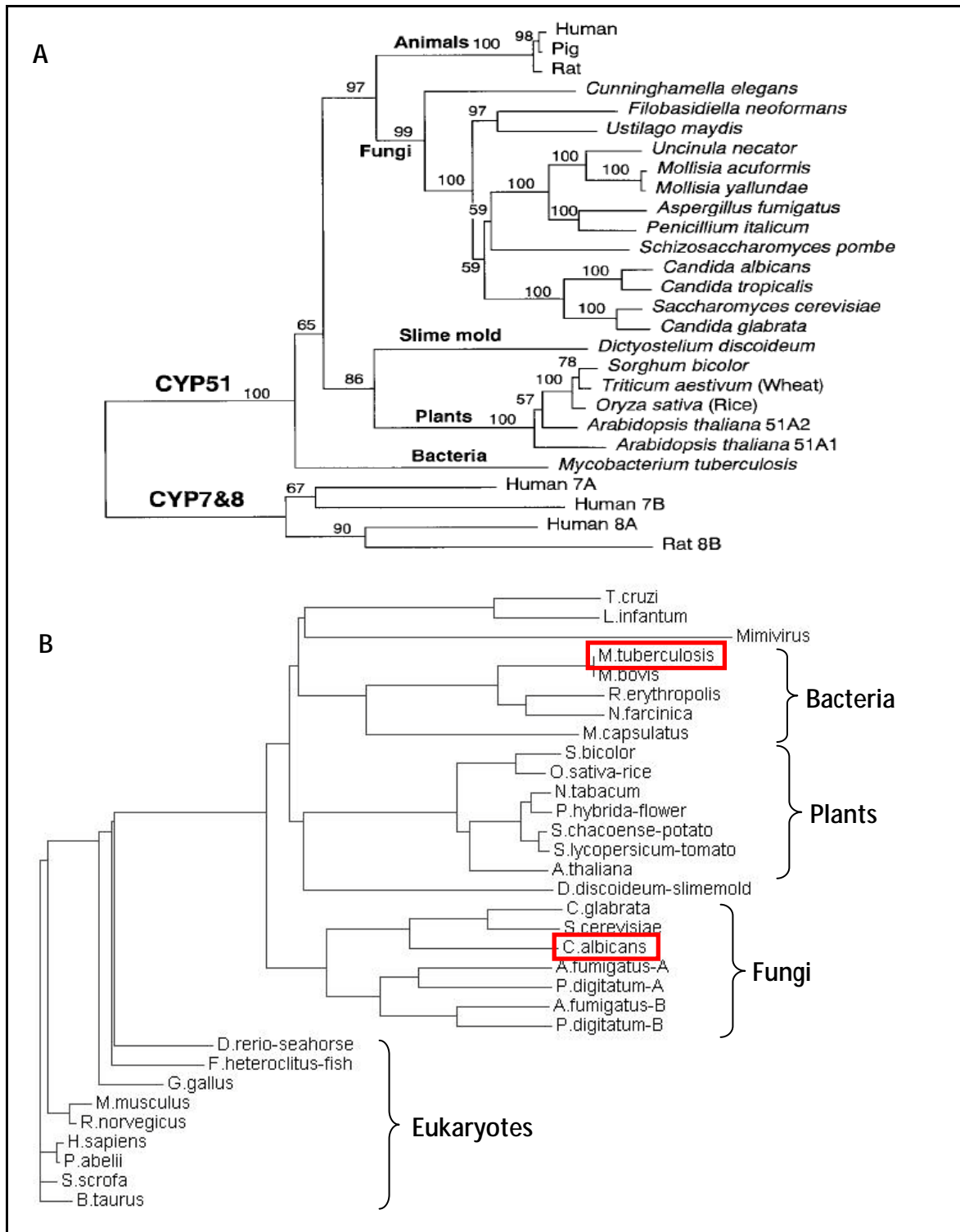


Figure 1.8: Phylogenetic comparison of CYP51 across families and phyla. Panel A describes the most probable molecular phylogenetic tree of the CYP51 family. The amino acid sequences of CYP7 and CYP8 families, which are the closest neighbours of the CYP51 family, are included as outlying groups to show the direct associations within the cytochrome P450 superfamily. The diagram was adapted from Yoshida *et al.* (2000). Panel B shows amino acid sequence multiple alignment analysis of CYP51 represented by the plant, fungi and animal kingdoms in comparison with CYP51B1 of *Mycobacterium tuberculosis*. The amino acid sequences of the respective CYP51 enzyme were aligned using the ClustalW2 programme via the EBI server (<http://www.ebi.ac.uk/Tools/clustalw2/index.html>). The phylogenetic tree was generated by comparing diverse CYP51s from different origins using the neighbour joining method. The only viral isoform is an outlier with longer C-terminal sequences and a relatively large molecular mass of 78 kDa. P450s tend to have molecular masses of 44 – 60 kDa (Nelson 2009).

Present conclusions are widely based on data from the end product of the whole sterol metabolic pathway in Mtb. CYP51B1 was, until recently, the only structurally solved sterol demethylase since 2001 (Podust *et al.* 2001a). However, CYP51 from humans (Strushkevich *et al.* 2010) and protozoa (Chen *et al.* 2010; Lepesheva *et al.* 2010b) have been successfully crystallised in their truncated forms without the N-terminal insoluble membrane anchor (which does not participate in catalysis), increasing the potential of drug targeting efforts especially those using azole antifungal drugs and their derivatives to address human infections e.g. candidiasis and trypanosomiasis (Chagas disease) on this particular enzyme as a drug target (Lepesheva *et al.* 2010a; Lepesheva *et al.* 2008; Zhang *et al.* 2010).

Sterol demethylase activity from the yeast *Saccharomyces cerevisiae* was first discovered in 1968 by Moore and Gaylor (Moore and Gaylor 1968) and was designated a gene name – *ERG11* in the 1970s (Trocha and Sprinson 1976). This led to the first characterisation and to the inhibition studies of 14- α demethylase activity on lanosterol in *S. cerevisiae*, by a fungicide buthioabate which conferred a characteristic type II Soret shift as identified by Aoyama and co-workers in 1983 (Aoyama *et al.* 1983). Subsequently, a plant CYP51 orthologue was discovered in sorghum grain (*Sorghum bicolor*) (Kahn *et al.* 1996) and studies on a mammalian CYP51 orthologue in rat liver was reported (Trzaskos *et al.* 1986). In 1998, at the same time as the publication of the Mtb genome, Aoyama and Yoshida identified a 14- α sterol demethylase-like protein in Mtb which showed 29-39% amino acid identity to known CYP51 orthologues in plants, mammals and fungi. They then went on to characterise the first novel soluble CYP51B1 heterogeneously expressed in *E. coli* binding it to an inhibitor ketoconazole, which happens to be a topical azole antifungal drug (Aoyama *et al.* 1998; Yoshida *et al.* 1997). Early catalytic studies on CYP51B1 by Bellamine and co-workers showed that it was able to turnover mammalian/yeast lanosterol (1%), 24, 25-dihydrolanosterol (20%) and plant obtusifoliol (98%) to the respective amounts of 8,14-diene product and liberating formate (formic acid) as the by-product. However, to date the *in vivo* role of CYP51B1 in Mtb remains a mystery since the bacterium lacks its own sterol biosynthetic pathway (Bellamine *et al.* 1999). The most likely explanation for the roles of CYP51B1 in Mtb is that it could function in host-cholesterol metabolism upon infectivity (or re-infection), in concert with the activities of CYP124, CYP125 and CYP142 of Mtb (Driscoll *et al.* 2010; Johnston *et al.* 2009; Johnston *et al.* 2010; McLean *et al.* 2007a; McLean *et al.* 2009). The above may hold true for Mtb as the functions of CYP51 homologues in prokaryotes are represented only by the bacterial sterol 14- α demethylase in *Methylococcus capsulatus* which is involved in cholesterol metabolism of its

intracellular membrane layers (Jackson *et al.* 2002). Interestingly, CYP51 from *Mycobacterium avium*, also an opportunistic pathogen in immunosuppressed patients, has a 79% amino acid sequence identity to CYP51B1 of *Mtb*, yet was reported to catalyse the 14- α demethylation of lanosterol but not of obtusifoliol (Pietila *et al.* 2006). Indeed, this proves that sequence similarity does not necessarily dictate the substrate specificity of CYP51 homologues, even from the same genus.

Six substrate recognition sites/sequences (SRS) in P450s were first postulated by Gotoh *et al.* (Gotoh 1992) and this was substantiated by the first evidences for substrate recognition and substrate distinction in the lanosterol backbone for yeasts, plants and mammalian CYP51, which were provided by Aoyama and co-workers from 1987-1992 (Aoyama and Yoshida 1991; Aoyama and Yoshida 1992; Aoyama *et al.* 1987; Aoyama *et al.* 1989a; Aoyama *et al.* 1989b; Aoyama *et al.* 1989c; Aoyama *et al.* 1991; Aoyama *et al.* 1992). The hydroxyl group at C3 and the double bond at C8 in the lanosterol backbone were important for substrate interactions with CYP51 (Aoyama *et al.* 1989b; Aoyama *et al.* 1989c) while different substrate preferences of yeast and mammalian CYP51 were identified (Aoyama and Yoshida 1991). The C3 hydroxyl and C14 methyl group are important for substrate recognition for both eukaryotic and prokaryotic CYP51 (Bellamine *et al.* 2001). The side chains at C25, C26 and C27 were crucial for heightened catalytic activity of CYP51 in yeast yet not essential for substrate recognition at the heme iron catalytic pocket (Aoyama *et al.* 1991). In addition to its crucial role in sterol biosynthesis in fungi, plants and mammals, CYP51 has also been reported to be involved in mammalian regulatory expression system as housekeeping genes and in the production of nuclear receptors in feedback regulatory control (Rozman *et al.* 1997; Stromstedt *et al.* 1996b). Besides hepatic cells, CYP51 is also present in mammalian germ cells and is involved as a key enzyme in the production of meiosis activating sterols in human spermatogenesis/oogenesis and estrogen biosynthesis (Rozman *et al.* 1999; Rozman *et al.* 1997; Rozman and Waterman 1998; Stromstedt *et al.* 1996a; Stromstedt *et al.* 1998), during pregnancy and lactation (He *et al.* 2007) and as a crucial enzyme in cholesterol regulatory control (Bartley *et al.* 2010; Debeljak *et al.* 2003). Irrespective of which kingdom it originates from, CYP51 shares the same three-step catalytic reaction as shown in Figure 1.9 (A) by demethylating the C-14 methyl group (Lepesheva and Waterman 2007).

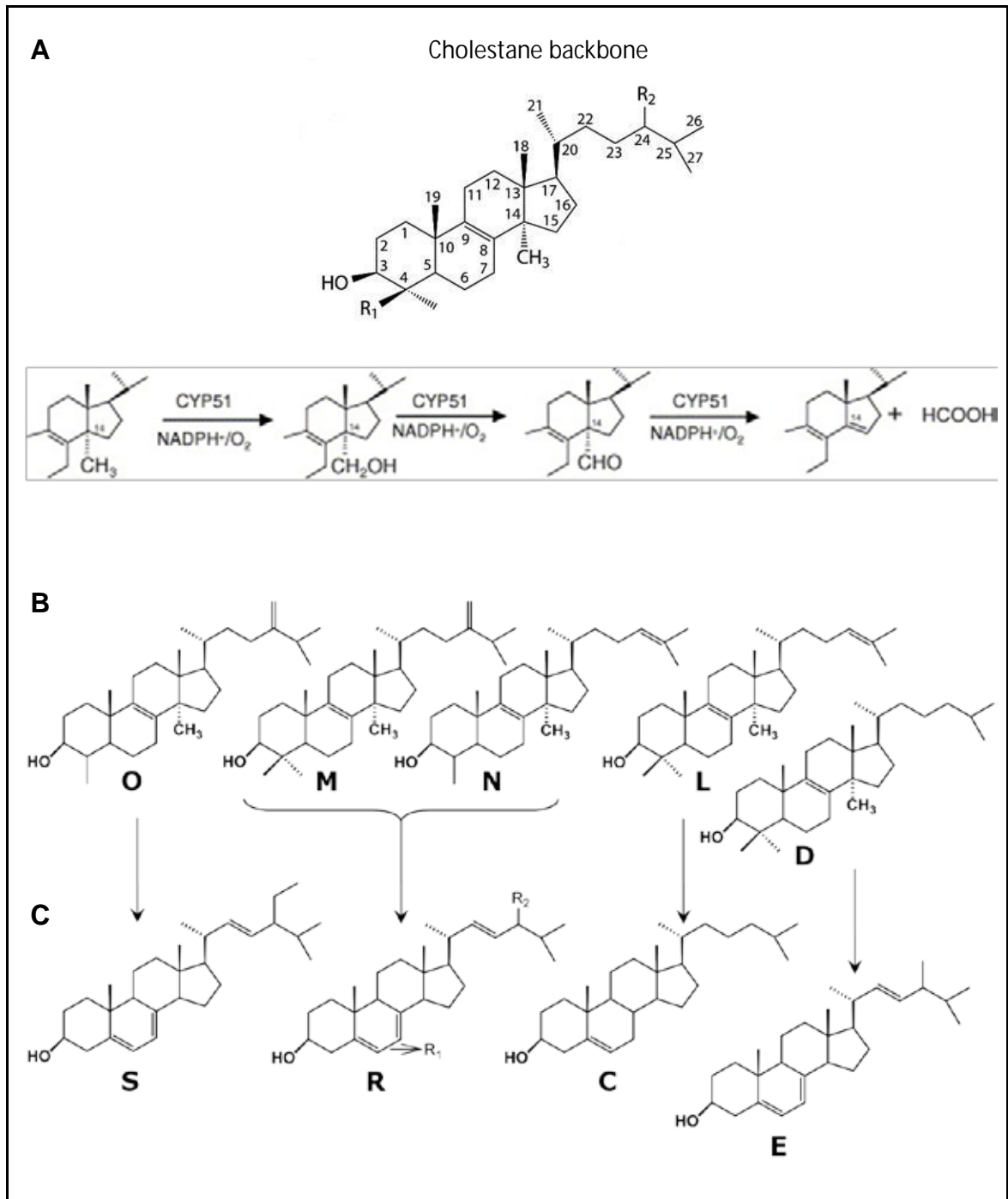


Figure 1.9: The CYP51 three-step reaction scheme. **Panel A)** The cholestane backbone with the respective C numbers and the CYP51 three-step catalysis. CYP51 catalyses a three-step reaction in plants, yeasts/fungi, humans/animals and protozoa sterol biogenesis by demethylating the C-14 methyl in a step-wise manner and producing first an alcohol derivative, then an aldehyde derivative, and finally a C-14 demethylated product from the cholestane ring with the release of formic acid as the other final product (Lepesheva *et al.* 2008; Waterman and Lepesheva 2005). **Panel B)** Substrates of CYP51 from plants – obtusifoliol (**O**), filamentous fungi – eburicol or 24-methylenedihydrolanosterol (**M**), trypanosomes – norlanosterol (**N**) and mammals/yeasts – lanosterol (**L**) or 24, 25-dihydrolanosterol (**D**) with their respective end products in **Panel C)** plants – sitosterol (**S**), filamentous fungi/trypanosomes – functional sterols with a double bond at C6/C7 or alkyl or alkylene groups at C24 (**R**), mammals – cholesterol (**C**), yeast – ergosterol (**E**) (Lepesheva and Waterman 2007).

In three step-wise reactions in sterol biogenesis according to the P450 catalytic cycle, using NADPH as the electron donor, molecular oxygen and its redox partners, a ferredoxin and a ferredoxin reductase or a flavoprotein and a flavoprotein reductase (depending on its origin) (McLean *et al.* 2005), CYP51 introduces a hydroxyl group to the C-14 methyl of the cholestane backbone to produce an alcohol derivative, followed by a second monooxygenase reaction to produce an aldehyde derivative, and finally the last monooxygenase reaction for the final demethylated C-14 and formic acid as the by-product (Aoyama and Yoshida 1992; Bellamine *et al.* 1999). Substrates and products of CYP51 vary from phylum to phylum uniquely due to its bulky catalytic crevice above the heme-iron which differs from other more substrate specialised P450s (Aoyama 2005; McLean *et al.* 2007a). This CYP51 substrate preference varies with crucial side group differences across the substrates and products, as can be seen in Figure 1.9 (B). Substrate of CYP51 from plants is obtusifoliol (**O**), filamentous fungi and some trypanosomes share eburicol or also known as 24-methylenedihydrolanosterol (**M**) as the substrate, and in general CYP51 from trypanosomes utilise norlanosterol (**N**) as their substrate and mammals/yeasts use lanosterol (**L**) or 24, 25-dihydrolanosterol (**D**) as a common substrate for sterol demethylation. Their respective CYP51 end products in are shown in Figure 1.8 (C) plants – sitosterol (**S**) or phytosterol, filamentous fungi/trypanosomes produce sterols with a double bond at C6/C7 or alkyl or alkylene groups at C24 (**R**) depending on the substrate, mammals – cholesterol (**C**) and yeast – ergosterol (**E**) (Lepesheva and Waterman 2007).

As increasing numbers of CYP51 isoforms are being structurally solved in their truncated (excluding the highly hydrophobic N-terminal membrane anchor which confers the insoluble characteristic to eukaryotic CYP51 isoforms) soluble forms, e.g. CYP51 from protozoa – *Trypanosoma cruzi*, *T. brucei*, *Leishmania infantum* (Lepesheva *et al.* 2010a; Lepesheva *et al.* 2010b), and CYP51 from humans (Strushkevich *et al.* 2010); researchers are beginning to realise that sequence similarity and functional relatedness which was typically used to classify a P450 protein into its family (>40% amino acid identity) and subfamily (>55% amino acid identity) may not be the only way to predict a P450's function, especially when CYP51B1 of Mtb, falling short (29-39% sequence identity to other CYP51 isoforms) of the >40% cut-off rule, was still retained in the same family due to its sterol demethylating activity (Yoshida *et al.* 1997). Substrate recognition sites (SRS) which are usually conserved across a P450 enzyme's secondary and tertiary structure may not overlap in its primary amino acid sequence with similar enzymes from different phyla (Lepesheva and Waterman 2011). This observation may initiate a different classification strategy based on secondary, tertiary and quaternary structures, so complementing the traditional

sequence/functional relatedness classification system, especially for the CYP51 homologues across phyla.

Structurally, there are six SRS regions on CYP51 where the majority of the conserved residues important for substrate recognition and binding are clustered (Podust *et al.* 2001b). Interestingly, these SRS regions are found only at the distal portion of the enzyme as shown in Figure 1.10 (A) away from the conserved cysteine axial ligand. CYP51 has a distinctively crooked I-helix, the longest helix (α I), almost broken in the middle, architecture extending across the molecule. This sets it apart from other P450 structures previously solved. In CYP51B1 this kink in the I-helix shifts depending upon the types of ligands coordinating to the heme, i.e. whether 4-phenylimidazole (smaller hence less interactions with substrate binding residues) or fluconazole (bulkier hence more interactions with the substrate binding residues on the I-helix) is coordinating to the heme iron (Podust *et al.* 2001a). SRS4 consist of amino acid residues at the C-terminal region of the I-helix (coloured green in Figure 1.10 A) which forms the ceiling above the heme iron and substrate cavity, with residues important for substrate binding (coloured red in Figure 1.10 B). Upon substrate binding, SRS1 forms the initial encounter with highly mobile, yet conserved, regions of the B-C loop, B'-helix and C-helix. SRS1 is also the region most prone to mutations in the CYP51 orthologue from clinical isolated of fluconazole-resistant *C. albicans*, as can be seen from the clustering of point mutations annotated in red across the molecule in Figure 1.10 (B). For example, the most commonly reported mutation at SRS1 is Y132H, corresponding to the F89 residue (Y145 in human CYP51) in CYP51B1 of *Mtb*. Studies done on this mutant showed decreased catalytic activity and modified spectral properties, which reflects structural perturbations affecting the heme region (Kudo *et al.* 2005). Essentially, both these SRS1 and SRS4 regions are considered the hallmark regions for CYP51 where its substrate binding (in red) architecture is the most conserved in other CYP51 structures, and has been extensively studied (Lepesheva *et al.* 2010a; Strushkevich *et al.* 2010). Indeed, this is how CYP51 maintains strict substrate selectivity from phylum to phylum with residue 78 suggestively the important discriminator of substrates in different CYP51 homologues (Podust *et al.* 2004). Yet in CYP51B1 of *Mtb* and CYP51 of *M. avium* the sharing of phenylalanine at position 78 does not translate into the same substrate for 14- α demethylase activity, since the latter enzyme prefers obtusifoliol over lanosterol, and the former enzyme prefers lanosterol (Bellamine *et al.* 1999; Pietila *et al.* 2006). In a related topic, CYP51B1 of *Mtb* coordinated directly to the heme iron for various azole drugs (both imidazoles and triazoles) demonstrating a clear-cut type II spectral shifts (Bellamine *et al.* 1999). However, for CYP51 of *M. avium*, only imidazole drugs (econazole

and ketoconazole) coordinated directly to the heme iron with prominent type II spectral shifts and the spectral shifts of triazoles (itraconazole, fluconazole and voriconazole) binding studies were relatively insignificant (Pietila *et al.* 2006). Ultimately, this would suggest that retention of residues considered important for substrate selectivity does not necessarily correlate with similar substrate turnover in all cases. Illustrated in Figure 1.10 (B), the substrate binding space can be portrayed as a funnel-shaped cavity with the B'-helix making up the wall just above the I-helix and the C-helix making up the wall just below the I-helix in-plane with the heme macrocycle, and the mobile B-C loop and F-G loop regions making up the funnel-like entry into the substrate cavity (Lepesheva *et al.* 2003; Podust *et al.* 2001a; Podust *et al.* 2001b). Studies on mutants at conserved residues at these sites have identified the importance of these substrate recognition and substrate binding residues for the formation of functional enzyme in Mtb and its human orthologue. Not only do mutants at these positions exhibit decreased protein expression but also aggregation and loss of its heme cofactor (Lepesheva *et al.* 2003; Sabri 2007). SRS2 and 3 are on the F and G helices, respectively while SRS5 and 6 ranges along the distal loop and the C-terminal end loop, respectively.

In this work, point mutants targeting SRS1 hinge regions where the initial substrate recognition occurs at the substrate cavity entry site, F89H and L100F mutations (corresponding to the Y132H and F145L mutants from its CYP51 orthologue from fluconazole-resistant *C. albicans*) on the B-C loop and G388S and R391K mutations (G464S and R467K) on the conserved cysteinyl loop (Figure 1.10 B) of CYP51B1, based on mutation site mapping of CYP51 from fluconazole-resistant *C. albicans*, have been structurally analysed and their azole-binding properties studied in Chapters 4 and 3 respectively.

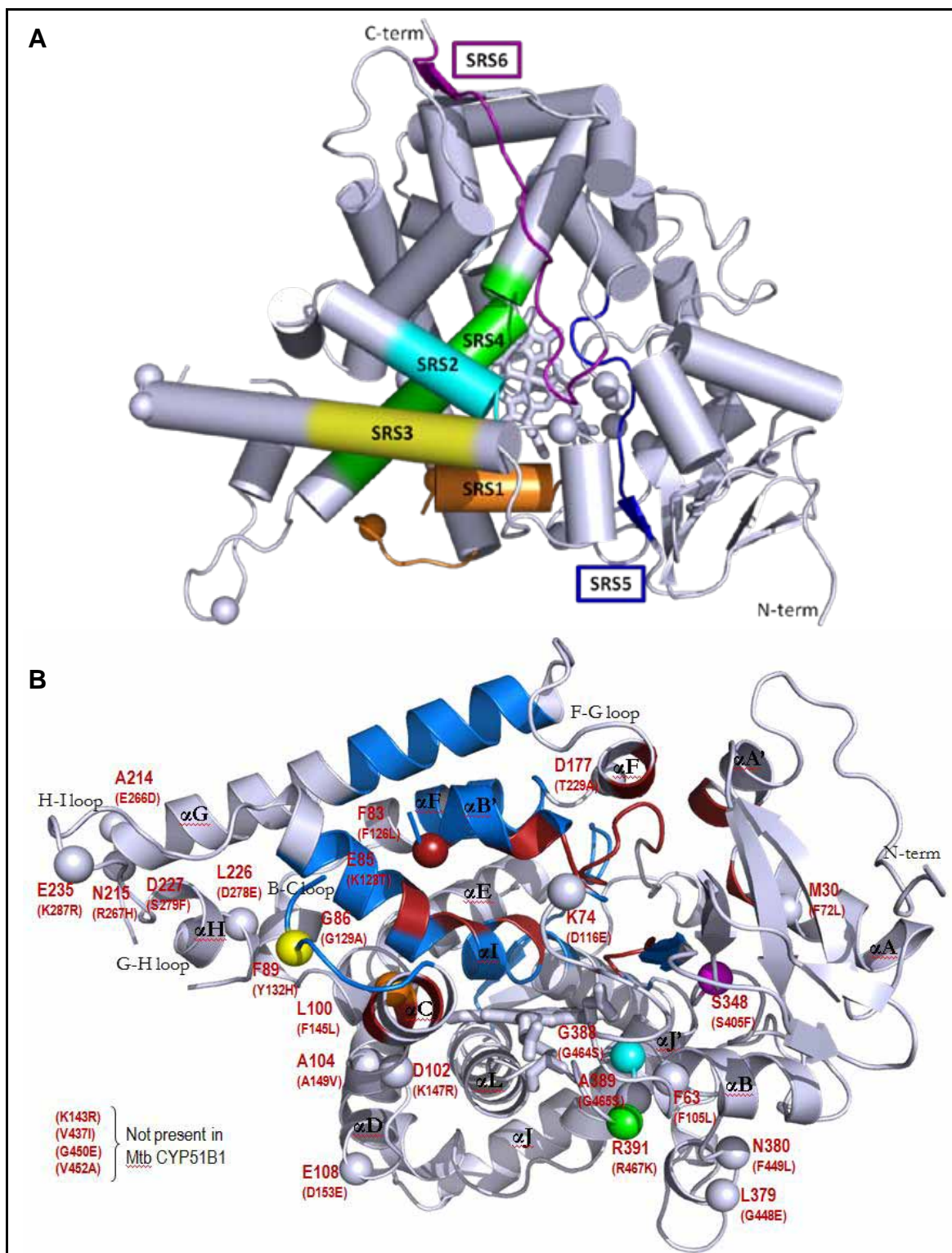


Figure 1.10: CYP51B1 substrate recognition sites (SRS), substrate binding sites (SBS) and mutations-prone residues by comparison with *C. albicans* CYP51. **A)** CYP51B1 is oriented 90° to the heme plane, looking from the top of the molecule. The SRS were as described by Gotoh on P450cam and Podust *et al.* on CYP51B1 (Gotoh 1992; Podust *et al.* 2001b). **B)** Mutation-prone residues were mapped from fluconazole-resistant *Candida albicans* CYP51 onto CYP51B1 of *Mycobacterium tuberculosis* (Podust *et al.* 2001b). The CYP51B1 molecule is oriented parallel to the heme plane where SRS are coloured in blue. The SBS are usually found within the SRS sites and are in red. All spheres represent the mutation-prone amino acids labelled in red with respective coordinates of Mtb CYP51B1 and of *C. albicans* CYP51 in parentheses. F83 (red) is the only mutation-prone residue to constitute both a substrate binding and recognition residue. Spheres coloured in yellow (F89H), orange (L100F), cyan (G388S), green (R391K) and purple (S348F) are point mutants studied in this thesis.

1.10 Evidence of Multiple CYP51 Systems

The presence of multiple copies of *CYP51* genes in various species across the phyla is ambiguous in relation to whether it occurs as a result of evolution from an ancestral progenitor or by means of lateral gene transfer (Rezen *et al.* 2004; Yoshida *et al.* 1997). As a result of this humans have three *CYP51* genes each on chromosome 3, 7 and 13 with the functional CYP51A1 enzyme on chromosome 7 (Rozman *et al.* 1996), *Arabidopsis thaliana* has two, with one functional CYP51A2 enzyme, *Aspergillus fumigatus* has two and both CYP51A and CYP51B are functional enzymes (Garcia-Effron *et al.* 2005; Mellado *et al.* 2005), rice has 10, *Aspergillus orizae* has three, tobacco has two, *Fusarium graminearum* has three and black oats have two. By the end of 2005, when three main *Aspergillus* spp. genome projects were completed, the feasible existence of two sterol demethylase homologues in filamentous fungi was reiterated by the presence of multiple *CYP51* genes (Jones 2007; Nierman *et al.* 2005). Prior to this, Mellado *et al.* (Mellado *et al.* 2001) successfully cloned and identified two 14- α sterol demethylase genes in *A. terreus*, *A. nidulans*, *A. flavus* and *A. fumigatus*, launching a new realm of CYP51 research for the ongoing quest to establish whether these genes encode functional CYP51 enzymes or are non-translated pseudogenes (Lepesheva and Waterman 2007). *A. fumigatus*, being an opportunistic pathogen in humans as aforementioned, gained popularity by having two functional sterol demethylases, CYP51A and CYP51B with 63% amino acid sequence identity, and which function in a complementary manner in its ergosterol biosynthesis. Gene knock-out experiments of either one did not affect growth. However, the removal of both the genes simultaneously inhibits growth (Garcia-Effron *et al.* 2005; Mellado *et al.* 2005). Interestingly CYP51B bound/coordinated more tightly to azole antibiotics ($0.2 \mu\text{M} < K_d < 4.0 \mu\text{M}$, while weaker binding was observed for CYP51A ($1.0 \mu\text{M} < K_d < 12.0 \mu\text{M}$), and both demonstrated type II difference spectra unique from each other (Warrilow *et al.* 2010b). Results of these studies will impact current azole drug design efforts for aspergillosis treatment and influence treatments with current azole antibiotics derivatives (Warrilow *et al.* 2010b). CYP51A has higher protein sequence similarity to CYP51 of *C. albicans* and CYP51B1 of *Mtb*, and its affinity towards azole drugs is comparable to CYP51 of *C. albicans* (Martel *et al.* 2010c; Warrilow *et al.* 2010a; Warrilow *et al.* 2010b). Interestingly, both these CYP51 homologues from *C. albicans* and *A. fumigatus* (CYP51A) share a similar azole drug (fluconazole for *C. albicans* and voriconazole for *A. fumigatus*) resistant mutation-prone residue, with mutations G464S and G448S, respectively. This mutation-prone residue corresponds to the highly conserved glycine residue in CYP51 across the phyla, and located at position 388 on CYP51B1, which was preliminarily characterised and reported in

a PhD thesis previously (Sabri 2007). A multiple sequence alignment of CYP51 isoforms which have been studied with regards to azole drug resistance and binding in Figure 1.11 pin-points the above mutations sites as illustrated in Figure 1.10 (B) and also other fluconazole-resistant mutation-prone residues studied in the following chapters.

<i>M. tuberculosis</i>	-----MSAVA	5
<i>M. avium</i>	-----MTTSTV	6
<i>C. albicans</i>	-----MAIVETVIDGINYFLSLSVTQQISILGVPFVYNLVWQYLYSLRKDR	47
<i>C. krusei</i>	-----MSVIKAIAADVQRYVLLAYSHFQTFSLQQTLLVISIPFLYSALWQLLYSFRKDR	55
<i>A. fumigatus-A</i>	-----MVPMLWLTAYMAVAVLTAILLNVVYQLFRLWRNTE	36
<i>A. fumigatus-B</i>	-----MGLIAFILDGICKHCSTQSTWVLVIGLLSILAVSVIINVLLQQLFKN-PHE	51
<i>P. digitatum</i>	-----MDLVPLVTGQIKCIAYTTGLVLASIVLNVIKQLVF--YNRKE	41
<i>C. neoformans</i>	MSAII PQVQQLLQVQAQFPFPWFAALPTSLKVAIAVVGIPALII GLNVFQQLCLPRKDL	60
<i>T. cruzi</i>	-----MFIEAIVLALTALILYSVYSVKSFNTTRPTD	31
<i>T. brucei</i>	-----MLLEVAIFLLTALALYSFYFVKSFNVTRPTD	31
<i>L. infantum</i>	-----MIGELLLLLAAGLALYGWYFCKSFNTTRPTD	31
<i>H. capsulatum</i>	-----MSWSTIGTFGLAFVAVALNLVYQLLFRFLNKR	35
<i>M. graminicola</i>	-----MGLLQEVLAQFDAQFGQTSLWKLVLGLFLAFSTLAILLNVLSQLLFRGKSSD	52
<i>B. graminis</i>	-----MGISESFMFPYLQPLLQLGFGIALASGIISLLLLLTFNLVNLKQLLFRFN-PNE	51
<i>H. sapiens</i>	MLLLGLLQAGGSVVGQAMEKVTGGNLLSMLLIACAFTLSLVYLIRLAAGHLVQLPAGVK	60
<i>M. tuberculosis</i>	LP RVSGGHDEHGHLEEFRTDPIGLMQRVRDECG-DVGTFLQLAGKQVLLSGSHANEEFFFR	64
<i>M. avium</i>	VP RVSGGEEHGHLEEFRTDPIGLMQRVRDECG-DVGWFLVDKHVILLSGAQANEEFFFR	65
<i>C. albicans</i>	APLVFYWIPWFGSAASYGQQPYEFFESCRCQKYG-DVFSFMLLGIIMTVYLGPKGHEFVFN	106
<i>C. krusei</i>	VP MVHYWIPWVGS AVVYGMQPYEFFENCRCQKHG-DVFSFLLLGKVMTVYLGPKGHEFVFN	114
<i>A. fumigatus-A</i>	PP MVFHWVYPLGSTISYGDIPYKFFACREKYG-DIFTFILLGQKTTVYLGQVQNEF ILN	95
<i>A. fumigatus-B</i>	PP VVFWHVPF IGSTISYGDIPYKFFDCRAKYG-DIFTFILLGKKTTVYLGTKGNDP ILN	110
<i>P. digitatum</i>	PP VVFWHVPF IGSTVAYGMDPYQFFASRAKYG-NIFTFILLGKKTTVYLGVEGNEF ILN	100
<i>C. neoformans</i>	PP VVHYWIPWFGSAAYYGDIPYKFLFECRDKYG-DLFTFILLGRRITVALGPKGNLISLG	119
<i>T. cruzi</i>	PP VYPVTVPLFGHIVQFGKNPLEFMQRCKRDLKSGVFTISIGGQRVTIVGDPHEHSRFFS	91
<i>T. brucei</i>	PP VYPVTVPLFGHIIQFGKSLGFMQECRQLKSGIFTINIVGKRVTVIVGDPHEHSRFFL	91
<i>L. infantum</i>	PP VVHGTTFPVGHIIQFGKDLGFMMLKAKKKG-GIFTMNICGNRITVVDVGHQSKFFT	90
<i>H. capsulatum</i>	PP LVFHWVPLFGSTIRYGTDPYKFFESCRCQKHG-DIFTFVLLGRPTTVYLGKIGNEF ILN	94
<i>M. graminicola</i>	PP LVFHWVPLFGSTITYGIDPYKFFESCRCQKHG-DVFTFILLGKKTTVYLGTKGNDP ILN	111
<i>B. graminis</i>	PP IVFHWIPIIGSTISYGMNIPYKFFHESQAKYG-NIFTFILLGKKTTVYLGROGNF ILN	110
<i>H. sapiens</i>	PP YIFSPIPFLGHAIAFGKSPIEFLENAYEKYG-PVFSFTMVGKTFYLLGSDAAALLFN	119
clustalw annotation	* * * * *	
<i>M. tuberculosis</i>	AGDDDDLQAKAYP-FMTPIFGEGVVDASPERRKE--MHNNAALRGEQMKGHAATIEDQV	121
<i>M. avium</i>	SADEDDLQAEAYP-FMTPIFGKGVVDASPERRKE--MHNSALRGEQMKGHASTIEGEV	122
<i>C. albicans</i>	AKLSDVSAEDDAYKHLTTPVFGKGVYDCPN SRLMEQKKAKFALTTDSFKRYVPKIREEI	166
<i>C. krusei</i>	AKLSDVSAEDDAYTHLTPVFGKGVYDCPN NWLMEQKKAKVALTKESFIRYVPLIKDEM	174
<i>A. fumigatus-A</i>	GKLRDVAEEVY SPLTTPVFGSDVVYDCPN SKLMEQKKIKYGLTQSALESHVPLIEKEV	155
<i>A. fumigatus-B</i>	GKLRDVAEEVY SPLTTPVFGRHVVYDCPN AKLMEQKKVVKYGLTSDALRSYVPLIDEV	170
<i>P. digitatum</i>	GKLRDVAEEIY GKLTPVFGSDVVYDCPN SKLMEQKKIKYGLSQEALSYVPLIADEI	160
<i>C. neoformans</i>	GKISQVSAEEAYTHLTPVFGKGVYDCPN EMLMQKKIKSGLTTESLQSYPPMITSEC	179
<i>T. cruzi</i>	PRNEILSPREVYT-IMTPVFGEGVAYAAPYPMRQQLNLAEELTI AKFQNFVPAIQHEV	150
<i>T. brucei</i>	PRNEVLSPREVYS-FMVVFGEGVAYAAPYPMRQQLNLAEELTI AKFQNFVPAIQHEV	150
<i>L. infantum</i>	PRNEILSPREVYS-FMVVFGEGVAYAAPYPMRQQLNLAEELTV AKFQNFAPSIQHEV	149
<i>H. capsulatum</i>	GKLRDVAEEVY GPLTTPVFGPDVVYDCPN SKLVEQKKIKYGLTQAALSHVPLIEKEV	154
<i>M. graminicola</i>	GKLRDVAEEIY SPLTTPVFGKDVVYDCPN SKLMEQKKVVKYGLTTSALQSYVPLIAAET	171
<i>B. graminis</i>	GKLRDVAEEIY TVLTPVFGTDVVYDCPN SKLMEQKKMKAAALTEAFRSYVPIIQNEV	170
<i>H. sapiens</i>	SKNEDLNAEDVY SRLTTPVFGKGVAYDVPNPVFLEQKKMLKSGLNIAHFQHSVSIIEKET	179
clustalw annotation	: * : * * * * : : : * : : * :	
<i>M. tuberculosis</i>	RRMIADWG-----EAGEIDLDFFAELTIYTSSACLIGKKFRDQLDGRFAKLYHELE	173
<i>M. avium</i>	KKMIADWG-----DEGEIELLDFFAELTIYTSTACLIGLKFREQLDH-RFAEYHYHLE	174
<i>C. albicans</i>	LNYFVTDESFKLEKETHGVANVMKTQPEITIFTASRSLFGDEMRRIFDR-SFAQLYSDDL	225
<i>C. krusei</i>	LKYFN-----ANFRGDSGKTDVLKSQSEMTLFTASRSLFGDALRNRLDA-SYAEYSDLL	228
<i>A. fumigatus-A</i>	LDYLRDSP---NFQSSGRVDISAAMAEITIFTAARALQGQEVRSKLTAEFAADLYHDL	211
<i>A. fumigatus-B</i>	ESFVKNS---PAFQGHKGVDFVCKTIAEITTYTASRSLQKQEVRSKFDSTFAELYHNDL	226
<i>P. digitatum</i>	SSYIKSSP---SFKGQSGTIDLVPAMAEITFTTAARTLQGEVRSKLTTEFAKLFPHDDL	216
<i>C. neoformans</i>	EDFFTKEVG-ISPQKPSATLDDLKAMSELIILTASRTLQKQEVRESLNG-QFAKYEDDL	237
<i>T. cruzi</i>	RKFMAENWK----EDEGVINLLED CGAMIINTACQCLFGEDLRKRLNARHFAQLLSKME	205
<i>T. brucei</i>	RKFMAENWD----KDEGEINLLED CSTMIINTACQCLFGEDLRKRLDARRFAQLLAKME	205
<i>L. infantum</i>	RKFMAENWN----KDEGEINLLED CSAMIINTACQCLFGEDLRKRLDARQFAQLLAKME	204
<i>H. capsulatum</i>	MDYLDSSP---NFLGTSGEVDVSAMAEITIFTAGSALQGEVRSKLTAEFAVLYHDL	210
<i>M. graminicola</i>	RQFFDRNNPHKFFASTSGTIDLPPALAEITTYTASRSLQKQEVREGFDS-SFADLYHDL	230
<i>B. graminis</i>	KSFIKCD---DFRKS KGIINIDAVMAEITTYTASHTLQKQEVDRFDS-SLAVLYHDL	226
<i>H. sapiens</i>	KEYFESWG-----ESGEKNVFEALSELIILTASHCHLHGKEIRSQLENE-KVAQLYADLD	231
clustalw annotation	. : : * : * * * * : * : *	

```

M. tuberculosis      RGTDPPLAYVDP---YLPIESFRRRDEARNGLVALVADIMNGRIANPPTDK-----SDR 223
M. avium             RGTDPDLCYVDP---YLPIESFRRRDEARVKLVALVQEIIMDQRLANPPKDK-----ADR 224
C. albicans         KGFTPINFVFP---NLPLPHYWRRDAQKKISATYMKIKSRRERGDIDP-----NRD 275
C. krusei           KGFTPLNFVFS---YLPLPNYWKRDAAHKNISNTYLDLINTKRAGGEIK-----NED 277
A. fumigatus-A      KGFTPINFMLP---WAPLPHNKRDAAHARMRSIYVDITQRRDLGE--KDSQKS-----261
A. fumigatus-B      MGFAPINFMLP---WAPLPHNKRDAAQRKLTETEMEIKARRQAGS-----KKDS-E 275
P. digitatum       LGFTPINFMLP---WAPLPQNRKRDAAHRRMREIYVDIIQARREAGEEANDNGRDKTKGT 273
C. neoformans      GGFTPLNFMFPP---NLPLPSYKRRDEAQKAMSDFYLKIMENRRKGES-----DHEH 285
T. cruzi           SSLIPAAVFPWLLRLPLPQSARCREARAELQKILGEIIVAREKEEASKD-----NNTS 259
T. brucei          SSLIPAAVFLPILLKLPLPQSARCHEARTELQKILSEII IAREKEEVNKD-----SSTS 259
L. infantum        SCLIPAAVFLPWLLKLPLPQSYRCRDARAELQDILSEII IAREKEEAQKD-----TNTS 258
H. capsulatum      KGFSPINFMLP---WAPLPHNKRDAAHTLMHAIYLDIEKRRRAARNANGSQTQ----262
M. graminicola     MGFTPINFMLP---WAPLPQNRDRDAAQKMSSETYMSIIQKRRESKT-----GEHE-E 279
B. graminis        MGFTPINFMLH---WAPLPHNRARDHAQRTVAKIYMEIINSRRTQKE-----TDSNL 276
H. sapiens         GGFSHAAWLLPG---WLPSPFRRRDRAHREIKDIFYKAIQKRQSQE-----KID 279
clustalw annotation      .      *      *      :      :      :

M. tuberculosis      DMLDLVLIAVKAETGTPRFSADEITGMFISMMFAGHHTSSGTASWTLEILEM--RHRDAYAA 281
M. avium             DMLDLVLSIKDEDGKPRFSADEITGMFISLMFAGHHTSSGTASWTLELIL--RHPDVYAE 282
C. albicans         LIDSLLIHSTYKDGVK--MTDQEIANLLIGILMGQHTSASTSAWFLLHLG--EKPHLQDV 332
C. krusei           LVDALLKNSVYKDGTR--MTDEELAHLMIGVLMGQHTSASTSAWFLLHLG--EKPLQEE 334
A. fumigatus-A      DMLWNLMNCTYKNGQ--VPDKEIAHMMILLLMAGQHSSSISAWIMLRLA--SQPKVLEE 318
A. fumigatus-B      DMVWNLMSCVYKNGT--VPDEEIAHMMIALLMAGQHSSSSTASWIVLRLA--TRPDIMEE 332
P. digitatum        DMISNLMRCVYRDGTP--IPDKEIAHLMILLLMAGQHSSSISCWILLRLA--SQPMTEK 330
C. neoformans      DMIENLQSCKYRNGVP--LSDRDIAHMIALLMAGQHTSASTSWTLLHLA--DRPDVVEA 342
T. cruzi           DLLGLLKAVYRDGTR--MSLHEVCGMIVAMFAGQHTSTITTSWSMLHLMHPNKKWLDK 318
T. brucei          DLLSGLLSAVYRDGTP--MSLHEVCGMIVAMFAGQHTSTITTSWSMLHLMHPNAVKHLEA 318
L. infantum        DLLAGLLGAVYRDGTR--MSQHEVCGMIVAMFAGQHTSTITTSWSLLHLMDPRNKRHLAQ 317
H. capsulatum      DMIENLMQCTYKNGQR--LPDKEIANIMISLLMAGQHSSSSTTSWIMLHLA--SEPAVVE 319
M. graminicola     DMIHNLMQCKYKDGNA--IPDKEIAHMMIALLMAGQHSSSATESWITLRLA--SRPDIQDE 336
B. graminis        DIMWQLMRSSYKDGTP--VPDKEIAHMMIALLMAGQHSSSSTTSWIMLWLA--ARPDITEE 333
H. sapiens         DILQTLLDATYKDRP--LTDEVAGMLIGLLLAGQHTSTTSAWMGFLA--RDKTLQKK 336
clustalw annotation      :      *      *      .      .      :      :      :      :      :      :      *      *

M. tuberculosis      VIDELDELYDGR-----SVSFHALRQIPQLENVLKETLRLHPLILMRVAKGEFEVO 335
M. avium             VLAELELYADGQ-----EVSFHALRSIPKLDNVVKETLRLHPLILMRVAKGEFEVE 336
C. albicans         IYQEVVLLKEKG--GDLNDLTYEDLQKLSVNNTIKETLRMHMPLHSIFRKVTNPLRIP 390
C. krusei           IYREIQSVLGEN---FERELTYDDLQKLDVNATIKETLRLHMPLHSIFRKVTRDLPVP 390
A. fumigatus-A      LYQEQLANLGPAGDGSLPLQYKDLDKLPFHQHVIRETLRIHSISIMRKVKSPLPVP 378
A. fumigatus-B      LYQEQIRVLGS-----DLPPLTYDNLQKLDLHAKVIKETLRLHAPIHSIRAVKNPMAVD 387
P. digitatum       LFAEQVNNLG---ADLPLLQYKDLDKPLHRNVIKETLRLHSISITLMRKVNPMVP 385
C. neoformans      LYQEQKQLGNPD--GTFRDYRYEDLKELPIMDSIIRETLRMHAPIHSIYRKVLSDIPVP 400
T. cruzi           LHKEIDEFPAQLN-----YDNVMDEMPFAERCVRESIRRDPLLMVMRMVKAEVKVG 370
T. brucei          LRKEIEEFPAQLN-----YDNVMDEMPFAERCARESIRRDPLLMLMRKVNPMVVG 370
L. infantum        LHQEIDEFPAQLN-----YDNVMEMPFAEQCARESIRRDPLLVMLRKVLKPVQVG 369
H. capsulatum      LYQEQLDNLPRTGPNGSLGPLQYGDLDRLPLHRNVIKETLRLHTSIHSLLRKVMNPMPVA 379
M. graminicola     LLQEQKDMLGVNA--DGSIKELTYANLSKLTLNQVVKETLRIHAPVHSILRKVSPMPIE 395
B. graminis        LYQEQLLGS-----ELPLKYEDLSKLSLHQNVLKEVLRLHAPIHSILRKVNPMPVP 388
H. sapiens         CYLEQKTVCGEN---LPPLTYDQLKDNLDRCIKETLRLRPPIMIMRMARTPQTVA 391
clustalw annotation      *      :      :      :      :      :      :      :      :      :      :      *      *

M. tuberculosis      G-----HRIHEGDLVASPAISNRIPEDFPDPHDFVPARYEQPRQ----- 375
M. avium             G-----FPIHEGDYVASPAISNRIPEDFPDPDAFKPDRYNKPEQ----- 376
C. albicans         E-----TNYIVPKGHYVLSPGYAHTSERYFDNPEDFDPTRWDTAAKAN---SVSFN 440
C. krusei           N-----TSYIVPKGHYVLISPYTMLSERYFNASEFQPHRWDEIKSIDG--GLSLP 440
A. fumigatus-A      G-----TPYMIPPGRVLLASPGVTALSDEHFPNAGCWDPHRWENQA-----419
A. fumigatus-B      G-----TSYVIPTSHNVLSSPGVTARSEHFPNPLEWNPHRWDEN-----I 428
P. digitatum       G-----TDFVIPPSHTLLSSPGVTARDERHFRDPLRWDPHRWGSR-----425
C. neoformans      PSLSAPSENGQYIPKGHYIMAPGVSQMDPRIWQDAKVWNPARWHDEKG----FAAAA 455
T. cruzi           S-----YVVPKGDIIACSPLLSHHDEEAFPNRLWDPER--DEKVDG-----410
T. brucei          S-----YVVPKGDIIACSPLLSHHDEEAFPPRRWDPER--DEKVEG-----410
L. infantum        K-----YVVPEGDIIACSPLLSHQDEEAFPNPREWNPERNMKLVDG-----410
H. capsulatum      G-----TPYVIPPSHVLSAPGVTALSDEYFNPTMWDPNRWETQE-----420
M. graminicola     G-----TAYVIPTHTLLAPGTTSRMDEHFPDCLHWEPHRWDESPSEKYKHLSPTT 447
B. graminis        G-----TSYVIPKTHSLLAPGWTSRDASYFNPLKWDPHRWDTG-----SGGV 432
H. sapiens         G-----YTIPPGHQVCVSPTVNQRLKDSWVERLDFNPDRYLQDNP-----431
clustalw annotation      .      :      :      :      :      :      :      :      :      :      :      *      *

M. tuberculosis      -----EDLLNRWTWIPFGAGRHRCVGAFAIMQIKAIFSVLLREYEFEM 419
M. avium             -----ADIVNRWTWIPFGAGRHRCVGAFAQMQIKAIFSVLLREYDFEM 420
C. albicans         SSDE----VDYGFGVSKGVSPYLPFGGRHRCIGEQFAYVQLGTILTFVNLRWTI 495
C. krusei           AEGENAKETVDYGFGISKGVASPYLPFGGRHRCIGEPFAYTQLGTLLVHYIQNFKWTA 500
A. fumigatus-A      TKEQENDKVDYGYGAVSKGTSSPYLPFGGRHRCIGEKFAYVNLGVILATIVRLHLRLFN 479
A. fumigatus-B      AASAEDDEKVDYGYGLVSKGTSPYLPFGGRHRCIGEQFAYLQLGTITAVLRLFRFRN 488
P. digitatum       VEAEDSSDTVDYRYGAVSKGTRSPYLPFGGRHRCIGEKFAYLNLGVIIATLLREPFFN 485
C. neoformans      MVQYTKAEQVDYGFGSVSKGTESPYQPFGAGRHRCVGEQFAYTQLSTIFTYVVR--NFTL 513
T. cruzi           -----AFIGFGAGVHKCIGQKFALLQVKTILATAFREYDFQL 447
T. brucei          -----AFIGFGAGVHKCIGQKFLLQVKTILATAFRSYDFQL 447
L. infantum        -----AFCGFGAGVHKCIGEKFLLQVKTVLATVLRDYDFEL 447
H. capsulatum      PKVDEKEDMVDYGGAISKGTSSPYLPFGAGRHRCIGEKFAYVNLTVIVAIMVRHLQFSN 480
M. graminicola     ALGSIAEEKEDDGYGLVSKGAASPYLPFGAGRHRCIGEQFAYVQLQTITATMVRDFKFYN 507
B. graminis        IGTDMEDEKFDYGYGLISTGAASPYLPFGAGRHRCIGEQFATVQLVTIMATMVRSFKFHN 492
H. sapiens         -----ASGEKFAYVPFGAGRHRCIGENFAYVQIKTIWSTMLRLYEFDL 474
clustalw annotation      .      :      *      *      *      *      *      *      :      :

```


<i>M. tuberculosis</i>	AQPP-ESYRNDHSMVVQLAQPAQACVRYRRRTGV-----	451
<i>M. avium</i>	AQPA-DSYRNDHSMVVQLARPAKVRVYRKRNA-----	451
<i>C. albicans</i>	DGYK--VPDPDYSSMVLPTPEAEI IWEKRETCMF---	528
<i>C. krusei</i>	K-----VPPIDYTSMTLPTQPAEIKWERRQKN-----	528
<i>A. fumigatus-A</i>	VDGKKGVPE TDYSSLFSGPMKPSIIGWEKRSKNTSK--	515
<i>A. fumigatus-B</i>	LPGVGIPD TDYSSLF SKPLGRSFVFEKRESATKA--	524
<i>P. digitatum</i>	PEGMEGVPD TDYSSLF SRPMQPATVRWEVRS-----	516
<i>C. neoformans</i>	KLAVPKFPETNYRTMIVQPNPLVTF TLRNAEVKQEV-	550
<i>T. cruzi</i>	LRD--EVPDPDYHTMVGPTLNQCLVKYTRKKLPS--	481
<i>T. brucei</i>	LRD--EVPDPDYHTMVGPTASQCRVKYIRKAAAA--	481
<i>L. infantum</i>	LG---PLPEPNYHTMVGPTASQCRVKYIKKKAAAA--	480
<i>H. capsulatum</i>	IGGKTGVPRTDYSSMFSEPMKPARINWKRRTAKSG---	515
<i>M. graminicola</i>	VDGSDNVVGT DYSSLF SRPLSPAVVKWERREEKEKN-	544
<i>B. graminis</i>	LDGRNSVAETDYSSMFSRPMAPATIAWEKRDKKDKTEC	530
<i>H. sapiens</i>	IDG--YFPTVNYT TMIHTPENPVIRYKRRSK-----	503
clustalw annotation	:: ::.	

Figure 1.11: Multiple sequence alignment of CYP51 isoforms identified as drug targets with their respective host organisms shown. The highlighted residues correspond to frequently reported mutation hot-spots isolated from clinical strains of *C. albicans* which are reported in this thesis. Other CYP51 isoforms in the alignment except for *M. avium* and *H. sapiens* have been reported in azole drug resistant strains of their respective organisms. CYP51 of *M. avium*, an opportunistic pathogen in immunosuppressed patients, has been reported to bind to azole drugs and the pathogen has shown sensitivity to imidazole drugs (Pietila *et al.* 2006). Alignments were generated using the BLOSUM matrix on CLUSTALW (Thompson *et al.* 1994). (*) means the column contains the same residues, (:) means highly conserved types of amino acid residues, while (.) means the residues in the column have some similar characteristics but differing side chain properties. The cysteine proximal ligand is highlighted in black.

1.11 Characterisation of CYP51B1

There are 25 atomic structures of CYP51 solved to date in the protein data bank (PDB). CYP51B1 of Mtb, whether ligand-bound or substrate-free, represents 12 of the solved structures in the PDB and it has been extensively characterised biochemically and structurally (Lepesheva and Waterman 2007; Lepesheva and Waterman 2011; McLean *et al.* 2007a). All CYP51 isoforms (inclusive of the sole viral and three protozoan CYP51s) reported till now were purified in the LS hexa-coordinated resting form with the major heme *b* feature reflected via the Soret band absolute spectrum at 417-419 nm and the corresponding α and β bands (Q bands) at ~572 nm and 535-536 nm, respectively, while the CO-Fe(II) adduct shifts and stabilises the Soret band to 446-447 nm for most CYP51 isoforms (Lamb *et al.* 2009; Lepesheva and Waterman 2007; McLean *et al.* 2006c). The earliest characterisation of CYP51B1 was performed by Aoyama *et al.* (Aoyama *et al.* 1998) by binding CO to dithionite-reduced ferrous heme, establishing its P450 heme thiolate instability to form the controversial P420 heme thiol species over a matter of six minutes (Aoyama *et al.* 1998). This conversion to the P420 form was widely thought to be an irreversible structurally denatured P450 form, as earlier mentioned (Hui Bon Hoa *et al.* 2002; Perera *et al.* 2003; Wells *et al.* 1992). However, this perception was refuted by demonstration of the reversibility of P450/P420 transition in Mtb CYP51 and CYP121 by McLean and co-workers, who attributed the transition to thiol and thiolate ligand

protonation and deprotonation (Dunford *et al.* 2007). The temporary CO-Fe(II)-thiolate adduct at 449 nm (P450) which progressively collapses to the CO-Fe(II)-thiol form at 422 nm (P420) can be stabilised by the introduction of a substrate analogue, estriol, to the system where it was shown to substantially stabilise the Fe(II)-thiolate form at 448 nm (McLean *et al.* 2006b; McLean *et al.* 2006c). Catalytically, CYP51B1 was shown to catalyse the 14- α demethylation of lanosterol, 24, 25-dihydrolanosterol and obtusifoliol in the presence of two different redox partner systems which help facilitate electron transfer from NADPH; these being the 3Fe-4S ferredoxin (Fdx – *Rv0763c*) of Mtb and its electron donor spinach ferredoxin reductase (Fnr) (since the Fdx electron donor was not known at that time, but could now possibly be the Mtb flavoprotein reductase A or FprA); and *E. coli*'s flavodoxin (Fld) and flavodoxin reductase (Fldr) (Bellamine *et al.* 1999). Mtb itself has several potential P450 redox partner systems, two of which have been characterised: Fdx (McLean *et al.* 2006c) and an adrenodoxin reductase homologue – FprA (McLean *et al.* 2003b), and 20 P450s which may all share these redox partners for their monooxygenase activity (McLean *et al.* 2007a).

1.12 Scope of Research

This project aims **(1)** to holistically describe the effects of introducing mutations into Mtb CYP51B1, corresponding to reoccurring fluconazole-resistant point-mutants situated at important structural regions of CYP51B1, have on its function and structure and **(2)** to understand the underlying mechanism of azole drug-resistance in CYP51 from *Candida albicans* by using the soluble CYP51B1 from Mtb as a template. Results of which may aid the understanding of mutations which may influence viability and infectivity of Mtb. The chapters were written in a manner to focus on rationalising the structure and function of the Mtb CYP51B1 mutants at important regions (substrate entry/exit channel) of this enzyme. This work is also done with a view to determining if the azole antifungal drugs may be potential antitubercular drugs targeting one or several of the 20 P450 enzymes in Mtb, hence the presentation of K_d values of azole drug binding to CYP51B1 (Tables 3.5 and 3.6).

This thesis starts off with Chapters 1 and 2 as the introduction and materials and methods sections leading on to the research work presented in Chapters 3, 4 and 5. Initial studies will focus on the CYP51B1 enzyme – the soluble sterol demethylase of Mtb, and on F89, L100, S348, G388 and R391 mutants of this P450, which mimic mutations found in azole resistant isolates of *C. albicans* CYP51. Little is known of how the *C. albicans* CYP51 mutations afford azole drug-resistance, and the membranous protein is not well

understood structurally. By contrast, the Mtb CYP51B1 is readily expressed, purified and structurally analysed without use of detergents or chaotropic agents to facilitate solubility. As such, it provides an excellent model system for analysis of the molecular basis of azole drug-resistance. CYP51B1 and relevant mutants were heterogeneously expressed in *E. coli*, protein production and purification by standard methods were done (e.g. by His-tag technology and/or ion exchange methods typically used in purification strategies for other P450 enzymes). CYP51B1 has already been shown to express well in *E. coli* (Sabri 2007). Purification of these enzymes is simplified by their red colour and by the fact that the bacterial P450s are soluble, cytosolic enzymes. Purified wild-type and mutant P450s were subjected to detailed characterisation by a variety of biophysical and kinetic methods. The formation and the kinetic collapse of the CYP51B1 P450 complex were followed when ferrous enzyme was bubbled with carbon monoxide (CO) gas which reports on the protonation of the cysteinate ligand to the heme iron that occurs in the ferrous form as shown in Figure 1.12.

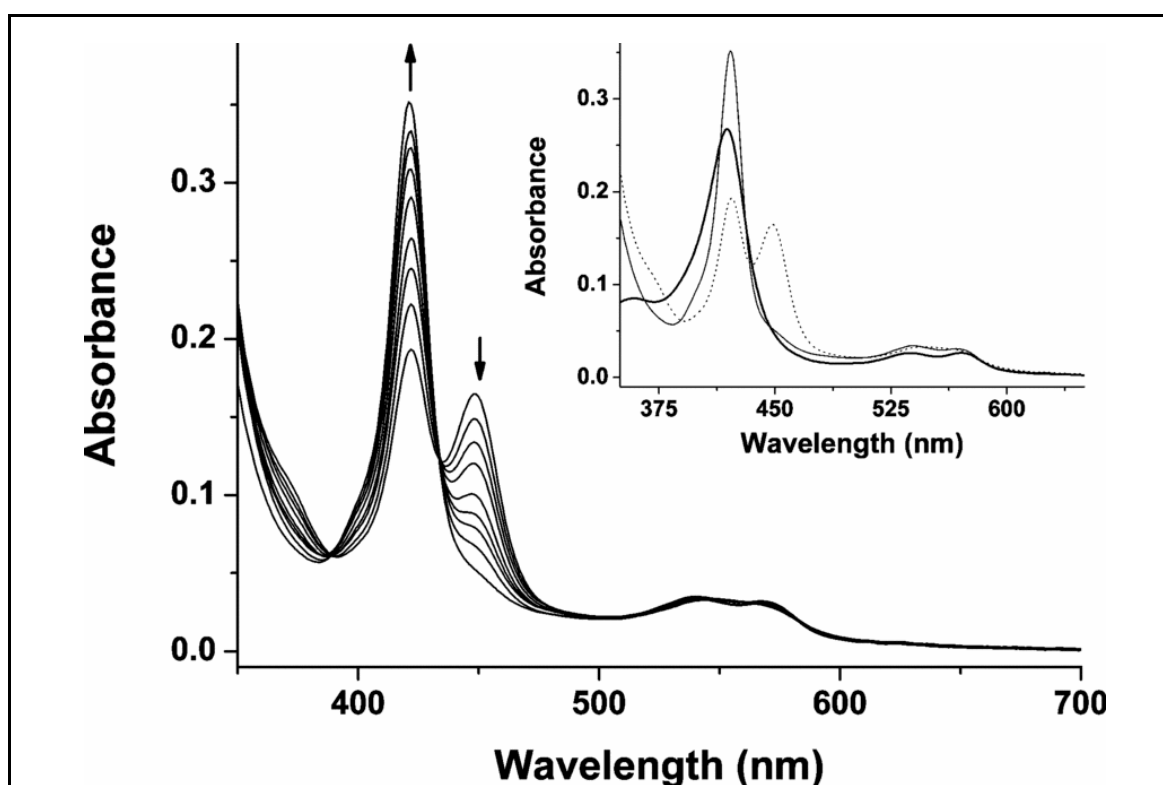


Figure 1.12: Example of Mtb CYP51B1 P450 complex collapse to P420 (McLean *et al.* 2006b). The formation of the P420 species following carbon monoxide bubbling is illustrated, due to the protonation of the cysteinate ligand to the heme iron and the formation of Fe^{2+} -CO adduct. Directions of absorbance change are shown by arrows. The inset shows spectra collected in a parallel experiment with the starting (ferric) enzyme indicated by a thick solid line; an early Fe^{2+} -CO spectrum is shown as a dotted line and with similar amounts of P450 and P420 species; and the final P420 form is indicated by a thin solid line.

The main spectrum shows the formation of an Fe(II)-CO adduct of Mtb CYP51B1 ($\sim 2 \mu\text{M}$) recorded immediately following bubbling of ferrous CYP51B1 with CO gas (spectrum with highest absorption at 450 nm) and subsequent spectra collected at regular intervals over the next 30 min, demonstrating the progressive collapse of the P450 form to the P420 species (spectrum with highest absorption at 420 nm). Also see Figure 1.5 for association to the P450 catalytic cycle. Arrows indicate directions of absorption change with time at these wavelengths. The inset shows spectra collected in a parallel experiment (again with $\sim 2 \mu\text{M}$ CYP51B1), with the starting (ferric) enzyme indicated by a thick solid line; an early Fe(II)-CO spectrum is shown as a dotted line and with similar amounts of P450 and P420 species, and the final P420 form is indicated by a thin solid line. The P420 species clearly has a substantially larger Soret molar absorption coefficient than does the ferric form (Dunford *et al.* 2007), where the Soret is the major heme absorption band. The same experiment was followed systematically with WT and mutants substituting dithionite with NADPH and redox partner enzymes found in Mtb, and with the addition of estriol which was shown to stabilise the P450 complex in previous work (McLean *et al.* 2006c). The reduction of CYP51B1 and mutants with dithionite were followed kinetically using stopped-flow analysis under anaerobic environments to study the Soret band trends in ferric to ferrous reduction and the conversion of thiolate to thiol species without external ligands involved. This step was replicated using Mtb redox partner proteins (ferredoxins and/or ferredoxin reductases) with the view to establish a functional class I redox partner system for substrate turnover reactions with CYP51B1 variants.

Aside from spectrophotometric characterisation and analysis of the P450/P420 equilibrium, the binding of WT and mutant CYP51B1 enzymes to a range of azole and other P450 inhibitor drugs was established by spectrophotometric titrations, as described previously (McLean *et al.* 2002a). The azoles coordinate to P450 heme iron and induce a well-defined spectral shift of the Soret band. This enabled simple optical titration studies to measure drug binding at equilibrium (i.e. to determine the K_d value) (Figure 1.13). The K_d values reflect the affinity of the drug to the P450 heme iron. By determining the K_d values of a range of azole drugs for the different Mtb CYP51B1 mutants, inferences may be made regarding drug binding to the drug-resistant forms of fungal CYP51. Furthermore, trends could be correlated with the positions of the mutations on the protein structure. Equilibrium binding (EB) K_d were previously determined with sporadic results in the Y132H and G464S mutants of CYP51 from *C. albicans* due to the use of detergents (Kelly *et al.* 1999a, b). This work was aimed to address the gap within the already available data and to avoid the use of chaotropic agents throughout.

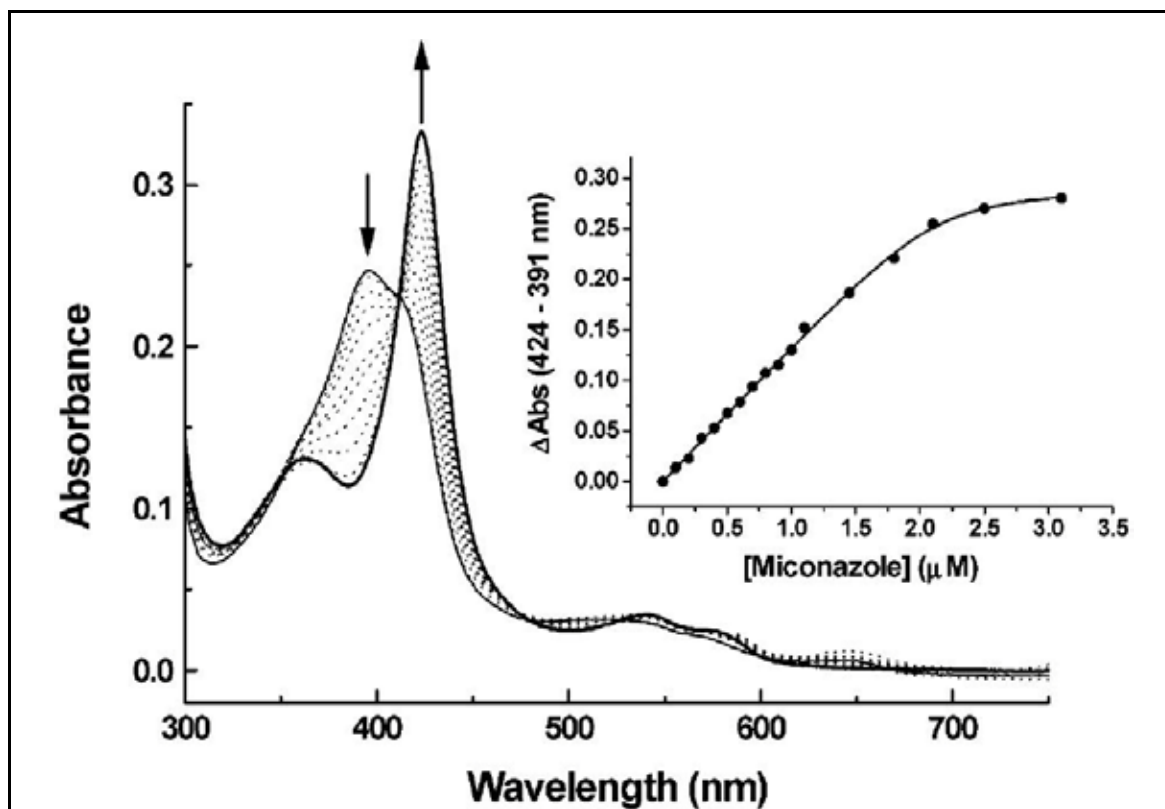


Figure 1.13: Example of spectral binding data for the interaction of an azole drug (miconazole) with a bacterial P450 (*Bacillus subtilis* P450 BioI). The main figure shows heme spectral changes induced on binding miconazole (arrows indicate direction of absorption changes as miconazole is added). The inset shows a tight binding curve for the drug, with a K_d value of $0.045 \mu\text{M}$ determined in this case (Lawson *et al.* 2004).

The K_d values determined in this way (EB) were correlated with K_d values independently determined using stopped-flow absorption methods by defining the k_{on} and k_{off} parameters ($K_d = k_{\text{off}}/k_{\text{on}}$). By this method, K_d values from equilibrium and transient kinetic studies were compared and substantial differences were observed suggesting the importance of structural rearrangements in the P450 following azole binding. Typically, substrates and substrate-like molecules bind close to the P450 heme and induce a large type I spectral shift as a consequence of their removing a water ligand from the heme iron (Munro *et al.* 2007a). This provides a simple assay by which substrate-like molecules can be identified. Reconstituted catalytic assays with type I substrates, as described by Bellamine *et al.* (1999) were utilised in this way and the turnover products were examined using HPLC and/or gas chromatography linked to mass spectrometry. Crystallisation trials were undertaken to obtain mutant CYP51B1 azole-bound and substrate-free crystals that diffracted x-rays well and could be used to determine the crystal structures of these new forms of the P450. Further work was then pursued to determine structures in presence of other CYP51B1-stabilising ligands and the P450-ligand mixtures were subjected to stability assays by difference scanning calorimetry to establish the extent of their protein-stabilising

properties before crystal trials were set up. The crystal structures of the mutants solved in the presence and absence of ligands by difference Fourier and molecular replacements methods helped to establish whether structural changes in the P450 occurred following azole entry into the CYP51B1 active site and whether the point mutations affected the overall structure of CYP51B1. The monomeric properties of CYP51B1 proteins were determined using light scattering (MALLS) analysis and their secondary structural compositions were verified using far-UV circular dichroism. Locations of some of these mutants were not only in the SRS regions, but also at the highly conserved cysteinyl loop. Therefore, EPR analyses were also conducted on all the mutants in ligand-free and azole-bound forms to check if there were any structural perturbations at the ferric-heme site which might affect the ability of these mutants to bind azoles or to bind azoles directly to the heme iron, or otherwise to bind azoles by indirectly coordinating to them, perhaps via an interstitial water molecule. These studies provided important data on the role of individual amino acids in conferring azole-resistance in CYP51 and to provide an idea of how these mutations at Mtb CYP51B1 hinge regions across the molecule affected overall structure.

The finding that *Aspergillus* spp. have two functional sterol demethylases, while humans have three genes and rice have ten genes encoding for CYP51s (including pseudogenes) triggered the prospect of dual or triple sterol demethylase genes (or pseudogenes) encoding more than one CYP51 in Mtb. In support of this idea, results from BLASTp identified CYP136 of presently unknown function as a probable sterol demethylase having >25% sequence identity to CYP51 from *Plesiocystis pacifica* (marine slime bacteria), lanosterol 14- α demethylase from *Rattus norvegicus* (rat) and *Mus musculus* (mouse) (McLean *et al.* 2006a). Another possible candidate is CYP123 which shares the same operon as CYP51B1 and is encoded by *Rv0766* gene next to *Rv0764c* encoding CYP51B1. The results of expression and characterisation of both *CYP123* and *CYP136* genes and proteins of Mtb form the basis of Chapter 5, as various molecular biology techniques and expression systems were employed for both *CYP123* and *CYP136* genes.

1.13 Objectives of Research

In conclusion, this PhD research consists of two major aims mentioned elaborately in paragraph 1 section 1.12 i.e. **(1)** to describe the effects of point mutations in Mtb CYP51B1 (corresponding to reoccurring fluconazole-resistant single mutations situated at important structural regions of CYP51B1 as mapped from the *Candida albicans*

ERG11 gene coding for CYP51ca) have on its function and structure and (2) to understand the underlying mechanism of azole drug-resistance in CYP51ca from *C. albicans* by using the soluble CYP51B1 from Mtb as a template. This thesis was also written to reflect four method-based objectives. The objective are firstly to clone, express, purify and characterise CYP51B1 and azole-resistant point mutants. Thereafter, optimisation of the production of the Mtb CYP51B1 P450 and its mutants by fermentation to facilitate large scale production with a view to detailed structural and mechanistic studies, and particularly with a view to analysing interactions with azole drugs using equilibrium binding and stopped-flow kinetic methods. Subsequently, the development of purification protocols to enable isolation of pure CYP51B1 proteins. Secondly, the systematic characterisation of each mutant with regards to P450/P420 conversions and CO and NO adduct formation and biophysical characterisation to determine the effects of the mutations towards the heme region. Thereafter, determination of the substrate specificity of CYP51B1 and mutants with the examination of their steady-state/transient kinetic profiles in order to understand their binding mechanisms and rate-limiting step(s) in their catalytic cycles and their interactions with azole drugs and other prospective inhibitors. Thirdly, the determination of K_d values for binding of these molecules. Subsequently, the determination of kinetic constants (k_{on} and k_{off} values, and hence K_d by independent measurement) to obtain evidence for structural rearrangements in CYP51B1 following azole binding and to help define roles of the mutated residues in affording azole-resistance. This leads to crystallisation trials with CYP51B1 and mutants, both in presence and absence of potent inhibitor molecules, and structural analysis by x-ray crystallography – leading to understanding of their structural properties and interactions with inhibitors, and thus providing the basis for *de novo* design of selective inhibitor molecules as novel antitubercular drugs. Finally, to clone, express, purify and characterise CYP123 and CYP136 (potential CYP51 homologues) from Mtb with the view to produce enough soluble holoenzyme to study its binding capabilities to CYP51B1 surrogate substrates and inhibitors and determination of their P450 assignment by biochemical characterisation through forming CO adducts to ferrous heme. This will serve as an initial platform for further study of their functions in Mtb, and to establish whether the idea of multiple sterol demethylases in Mtb is plausible.



Chapter 2 | General Materials and Methods

- 2.1 *Materials*
- 2.1.1 *E. coli strains and Plasmid Vectors*
- 2.1.2 *Growth and Strain Maintenance Media*
- 2.1.3 *Expression Media*
- 2.1.4 *Antibiotics and Other Reagents*
- 2.1.5 *Buffers for Purification and Assays*
- 2.2 *Methods*
- 2.2.1 *Agarose Gel Electrophoresis*
- 2.2.2 *Sodium-Dodecyl-Sulphate-Polyacrylamide Gel Electrophoresis (SDS-PAGE)*
- 2.2.3 *Protein Engineering and Primer Design*
- 2.2.4 *Expression Trials*
- 2.2.5 *Protein Purification*
- 2.2.6 *Protein Identification – MALDI-TOF and Western Blotting*
- 2.2.7 *Spectrophotometric P450 Characterisation*
- 2.2.8 *Kinetic Spectroscopic Analysis*
- 2.2.9 *Hemoprotein Estimation by Pyridine Hemochromogen Technique*
- 2.2.10 *Biophysical Analysis*
- 2.2.11 *Crystallogensis*
- 2.2.12 *Potentiometric Studies*
- 2.2.13 *Redox Cycling of CYP51B1*
- 2.2.14 *Stabilisation of the P450 Species by CO Trapping with Redox Partners*
- 2.2.15 *CYP51B1 Reconstitution of Catalysis*

2 GENERAL MATERIALS AND METHODS

2.1 Materials

2.1.1 *E. coli* Strains and Plasmid Vectors

Genes *Rv0764c*, *Rv0744c* and *Rv3059* from the *Mycobacterium tuberculosis* H37Rv genome project encoding CYP51B1, CYP123 and CYP136 respectively were obtained from Professor Stewart Cole at the Pasteur Institute, France, on a chromosomal DNA cosmid library. Genes for CYP51B1 and CYP123 from a pre-cloned pGEM-T easy vector (Promega) were provided by Dr. Kirsty McLean and Dr. Jim Belcher respectively with NdeI/HindIII restriction sites (CYP51B1 in pET20b) and NdeI/BamHI restriction sites (CYP123 in pET15b). Genes for CYP136 with NdeI/BamHI restriction sites and CYP123 with NdeI/HindIII restriction sites were excised as sticky-ended-gene fragments from pGEM-T easy vectors and cloned into respective secondary vectors for expression trials using the protocol from the Quick Ligation™ Kit (M2200S, NEB). Various high copy number plasmid vectors were employed for construct and protein expression trials (Novagen) (Figure 2.1 A-C). These constructs contain a T7 *lac* promoter which ensures tighter control of gene expression with IPTG – pET11a, pET15b (N-terminal His₆-tag), pET24b (C-terminal His₆-tag), pET28b (C-, N-terminals His₆-tag); T7 promoter – pET20b (C-terminal His₆-tag). To address insolubility issues, a novel high copy number cold shock expression plasmid system with a T7 *lac* operator, pCOLD™TF (Takara Bio Inc.) (Figure 2.1 D) was employed. It has an *E. coli* trigger factor as an N-terminal His₆-tagged soluble chaperone (48 kDa) that fuses to the target protein at the N-terminal and assists translational folding of the target protein.

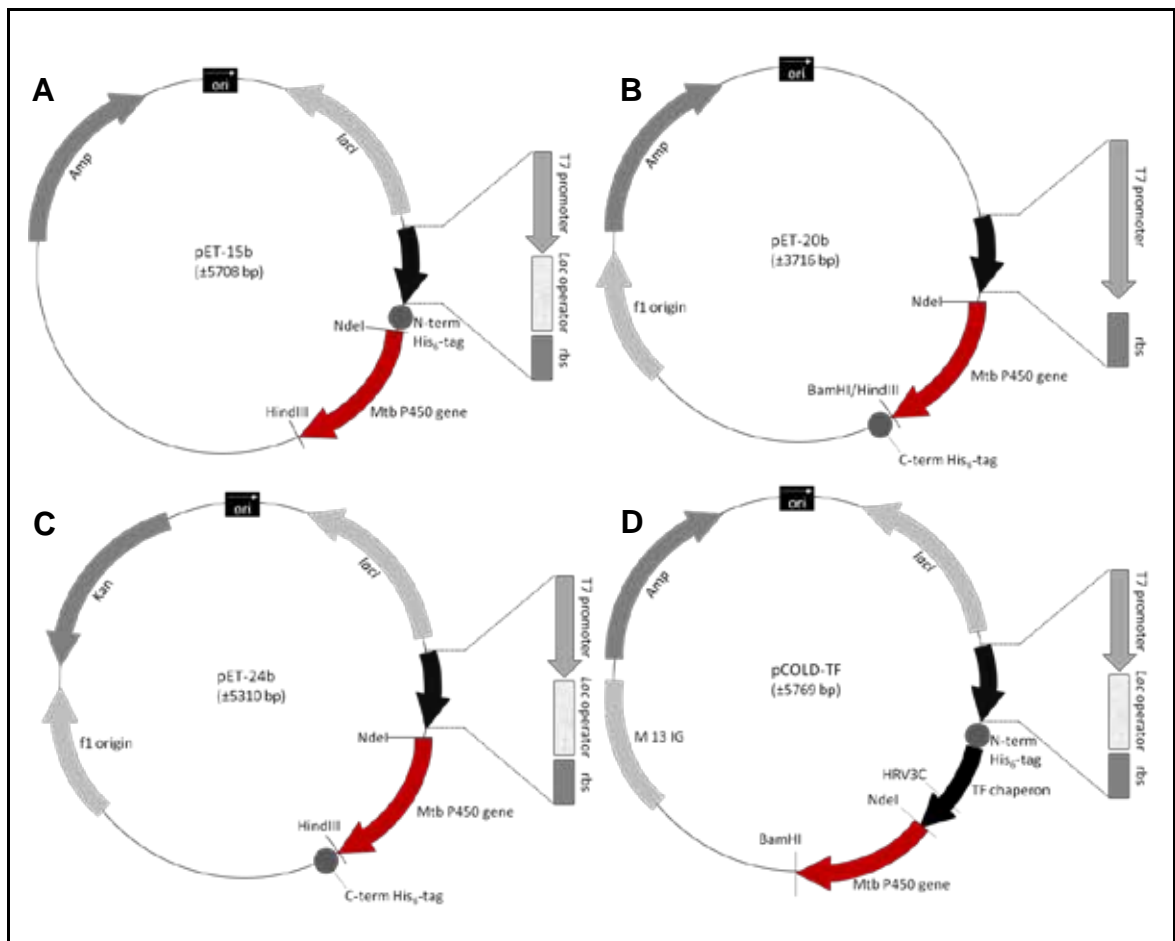


Figure 2.1: Plasmid maps of vectors used for the expression of CYP51B1 WT and mutants, CYP123 and CYP136. *Mycobacterium tuberculosis* (Mtb) P450 genes (red arrow) were excised from the pGEM-T easy (Promega) and inserted into the respective vectors above using NdeI/BamHI or NdeI/HindIII restriction sites. **A)** pET15b has an ampicillin (Amp) resistance gene and the T7 *lac* operon and an N-terminal His₆-tag. **B)** pET20b has the above without the T7 *lac* operon and an optional C-terminal His₆-tag depending on BamHI or HindIII insertions. **C)** pET24b has a C-terminal His₆-tag and kanamycin (Kan) resistance gene, and when induced switches on the T7 *lac* operon and the expression of genes downstream. **D)** This pCOLD™TF (Takara Bio Inc.) vector is a novel cold-shock expression system with an ampicillin resistance gene, T7 *lac* operon and a trigger factor chaperone which aids solubility and correct folding of target proteins downstream. It has an N-terminal His₆-tag and a HRV3C protease restriction site that enables cleavage of the chaperone post expression/purification.

Escherichia coli strain HMS 174 (DE3), a T7 RNA polymerase expression host (genotype: F⁻, *ompT*, *hsdR*(*r*_{K12}⁻*m*_{K12}⁺), Rif^R, (DE3)) from Novagen was used for protein expression of wild type and mutants of CYP51B1. The high copy number plasmid vector pET20b (Novagen) containing the gene of interest was transformed into the above expression host. pET20b incorporates the *E. coli* T7 promoter, enabling IPTG-dependent induction of the gene of interest downstream of the *lac* gene. Expression trials for *CYP123* (*Rv0766c*) and *CYP136* (*Rv3059*) utilised several expression hosts also with the DE3 lysogens as follows; *E. coli* strains as mentioned above and BL21 (DE3) – a B834 derivation, general expression host and T7 RNA polymerase lysogen host as for the others used (genotype: F⁻, *ompT*, *hsdS*_B(*r*_B⁻*m*_B⁻), *gal*, *dcm*, (DE3)); Origami B (DE3) – derivative of the Tuner™ (B strain) which enables strict gene expression control by varying IPTG concentration (genotype: F⁻, *ompT*, *hsdS*_B(*r*_B⁻*m*_B⁻), *gal*, *dcm*, *lacY1*, *ahpC*, (DE3), *gor522::Tn10*, *trxB*, Kan^R, Tet^R); Rosetta 2 (DE3) – derivative of BL21 (DE3) which provides tRNA genes for seven rare codons (AGG, AGA, AUA, CUA, CCC, GGA, CGG) infrequently found in the *E. coli* genome (genotype: F⁻, *ompT*, *hsdS*_B(*r*_B⁻*m*_B⁻), *gal*, *dcm*, (DE3), pRARE2, Cam^R). The maintenance of plasmid DNA stocks and the genes of interest for protein engineering methods were done using either *E. coli* strains XL-1 Blue (*recA1*, *endA1*, *gyr96*, *thi-1*, *hsdR17*, *supE44*, *relA1*, *lac* [F', *proAB*⁺, *lacI*^q, *lacZMΔ15::Tn10*, Tet^R]) [Stratagene, Amsterdam, The Netherlands] or NovaBlue (*endA1*, *hsdR17*(*r*_{K12}⁻*m*_{K12}⁺), *supE44*, *thi-1*, *recA1*, *gyrA96*, *relA1*, *lac* [F', *proAB*⁺, *lacI*^q, *lacZMΔ15::Tn10*, Tet^R]) [Novagen].

2.1.2 Growth and Strain Maintenance Media

Expression host strain, HMS 174 (DE3), and plasmid maintenance strains, XL-1 Blue and NovaBlue, were maintained on Luria Bertani (LB) agar plates at 4°C as short term stocks and at -80°C in glycerol as long term stocks. All media components were obtained from ForMedium™ (Norfolk, UK). LB medium was used as general growth and inoculum media and contained 10 g tryptone, 5 g yeast extract, and 10 g NaCl (per litre). Super optimal broth with catabolite repression (SOC) medium was used as a rich medium for growing transformed competent cells. This contained 20 g tryptone, 5 g yeast extract, 585 mg NaCl, and 187.5 mg KCl (per litre). Ten millilitres of pre-sterilised 1 M MgSO₄ and 20 mM glucose were added to the basal medium. Agar plate medium was prepared with LB agar with the same constituents as LB medium, and with the addition of 12.5 g/L bacteriological agar. Agar was allowed to cool to ~55°C following sterilization before

adding respective antibiotics at their working concentrations for plasmid selection according to Table 2.1. Cooled medium was then promptly poured into sterile Petri dishes.

2.1.3 Expression Media

Expression trials for target genes (*Rv0764c*, *Rv0766c*, and *Rv3059*) were carried out with LB, Yeast-Tryptone Broth (2xYT) and Terrific Broth (TB) media (ForMedium™). Expression of mutant and wild type (WT) forms of *CYP51B1* was carried out in 800 mL (total volume) pre-sterile TB broth in ~30 x 2 L shake flasks. TB medium consists of (per litre) 10 g tryptone, 24 g yeast extract, and 4 % (v/v) glycerol. After sterilization, 100 mL of sterile potassium phosphate buffer (0.17 M KH_2PO_4 , 0.72 M K_2HPO_4) were added to the media to make a total volume of 800 mL. Filter-sterilised ampicillin (0.8 mL) from a 50 mg/mL stock was added to each shake flask.

2.1.4 Antibiotics and Other Reagents

Table 2.1 below summarises the preparation of antibiotic and reagent stocks used in all experiments. All reagents were obtained from Sigma Aldrich (Poole, UK) and were of the highest grade available, unless otherwise stated. All antibiotics were purchased from Melford (Suffolk, UK). Aliquots of reagents and antibiotics were maintained at -20°C and were filter sterilised prior to use.

Table 2.1: Antibiotics and reagents used throughout experiments.

Antibiotics/ reagents	[Stock] (mg/mL)	Solvent	[Working] (µg/mL)
Ampicillin (sodium salt)	50	Deionised water	50
Carbenicillin (disodium salt)	50	Deionised water	50 (in broth) 100 (in agar)
Rifampicin	10	67 % methanol + 0.17 N NaOH	200
Chloramphenicol	34	Ethanol	34
Kanamycin	30	Deionised water	30
Tetracycline	5	Ethanol	12.5
IPTG	1 M	Deionised water	0.5 – 1.0 mM
5 – aminolevulinic acid hydrochloride (δ-ala)	0.45 M	Deionised water	0.18 mM

Chromatography resins were from the following suppliers: ion-exchange chromatography and hydrophobic interaction (GE Healthcare, Bucks, UK), ceramic hydroxyapatite (Bio-Rad, Hemel Hempstead, UK), and 2', 5' -ADP-Sepharose resin (GE Healthcare or Sigma). Azole antifungal drugs; fluconazole, voriconazole and clotrimazole (MP Biomedicals, London, UK) and econazole, ketoconazole and miconazole (ICN Biomedicals Inc., Hampshire, UK). 24, 25-dihydrolanosterol (8-lanosten-3 β -ol) was synthesized by Avanti Polar Lipids Inc. (Cat#179740).

2.1.5 Buffers for Protein Purification and Assays

Buffer systems for the preparation of gels, preparation of TB medium, and for use during cell lysis and in purification protocols, during enzyme kinetic assays, redox potential analysis and for other biophysical techniques are listed in Table 2.2 below.

Table 2.2: Composition of all buffers used in experiments.

Buffer name	Constituents
A	50 mM Tris base, 1 mM EDTA, pH 7.2 adjusted with HCl
B	25 mM KPi by adding 25 mM KH ₂ PO ₄ (dibasic) to 25 mM K ₂ HPO ₄ (monobasic) to reach pH 6.5
C	500 mM KPi by adding 500 mM KH ₂ PO ₄ (dibasic) to 500 mM K ₂ HPO ₄ (monobasic) to reach pH 6.5
D	100 mM KPi by adding 100 mM KH ₂ PO ₄ (dibasic) to 100 mM K ₂ HPO ₄ (monobasic) to reach pH 7.0+ 50 % (v/v) glycerol
E	10 mM Tris, 150 mM NaCl pH 7.5 in distilled water and adjusted with HCl
Assay	100 mM KPi by adding 100 mM KH ₂ PO ₄ (dibasic) to 100 mM K ₂ HPO ₄ (monobasic) to reach pH 7.5
Redox	100 mM KPi by adding 100 mM KH ₂ PO ₄ (dibasic) to 100 mM K ₂ HPO ₄ (monobasic) to reach pH 7.0 + 10 % (v/v) glycerol
TAE	40 mM Tris-acetate, 1 mM EDTA, pH 8.0 adjusted with HCl
HEPES	100 mM HEPES, pH 7.5 in distilled water and adjusted with HCl

2.2 Methods

2.2.1 Agarose Gel Electrophoresis

Horizontal agarose gels were prepared for the separation, rough quantification, and diagnostic restriction digest analysis of DNA fragments according to their sizes (number of base pairs). Agarose gels were prepared by dissolving 1.1% (w/v) agarose into 1 x TAE buffer followed by microwave heating until the agarose has dissolved, before adding 1.2 µg/mL ethidium bromide into the cooled solution. The mixture was promptly poured into a gel cast and allowed to solidify. DNA samples (12 µL) were prepared by mixing 2–4 µL DNA (according to concentration) with 3 µL 6 x loading dye, and adding sterile distilled water (11–13 µL) before dispensing into the gel wells. The pre-mixed loading dye contains 0.25% bromophenol blue, 0.25% xylene cyanol FF, 30% (v/v) glycerol in water and was stored at 4°C till needed. The gels were run with a wide or mini-sub cell GT cell (BioRad) at 80 V until appropriate DNA migration and separation of the loading dyes were observed. A 2–log DNA ladder between 0.1–10 kb (N3200S, NEB) was used in each run.

2.2.2 Sodium-Dodecyl-Sulfate-Polyacrylamide Gel Electrophoresis (SDS-PAGE)

The separation of protein according to molecular weight and for protein identification was done by SDS-PAGE for all protein expression and purification steps analysis. The system contains the stacking gel and the separating gel, which contain 5% and 12.5% polyacrylamide respectively. Constituents of both gels are given in Table 2.3 and gels were run in a Mini-Protean III vertical gel electrophoresis system (BioRad) at 180 V for 1 hr. Otherwise, 12% gels and 4–12% gradient (for higher molecular weight protein separation) precast horizontal polyacrylamide Gebagel gels (Generon Ltd., UK) were run at 160 V for 1 h. Protein molecular weight markers between 2–212 kDa (P7702S, NEB) were used in each run.

Table 2.3: Constituents of stacking and separating gels for 12.5% gel in SDS-PAGE.

Constituents	Stacking gel (mL) 5% in 4 mL	Separating gel (mL) 12.5% in 10 mL
Distilled water	2.675	3.15
Tris HCl	0.625 (1 M pH 6.8)	2.5 (1.5 M pH 8.8)
10% (w/v) SDS	0.05	0.1
30% (w/v) acrylamide	0.65	4.2
10% (w/v) ammonium persulfate (freshly prepared/stored at -20°C)	0.05	0.05
TEMED (polymerisation catalyst)	0.008	0.008

2.2.3 Protein Engineering and Primer Design

The sterol demethylase gene from *Mycobacterium tuberculosis* (*CYP51B1* or *Rv0764c*) was cloned from Mtb strain H37Rv cosmid genomic library (obtained from Professor Stewart Cole, Pasteur Institute, Paris) as described by McLean *et al.* (McLean *et al.* 2006b). Mutants of *CYP51B1* were mapped from *CYP51* variants of fluconazole resistant *Candida albicans* strains, and the mutant *CYP51Bs* were generated using the Stratagene QuikChange kit using the following oligonucleotide primers for corresponding point mutations: (new/removed restriction enzyme site(s) underlined, mutated nucleotides to change amino acid in bold): F89Hfor- GGC GAG GGC GTG GTG CAC GAC GCC AGC CCG GAA CGG (TaqI site removed, new ApaLI site), F89Hrev- CCG CTC CCG CAC CAC GTG CTG CGG TCG GGC CTT GCC; G388Sfor- CGG TGG ACG TGG ATT CCG TTC **TCC** GCC GGC CGG CAT CG (KasI site removed), G388Srev- GCC ACC TGC ACC TAA GGC AAG **AGG** CGG CCG GCC GTA GC; R391Kfor-CG TTC GGC GCC GGC **AAG** CAT CGT TGC GTG G (EagI site removed), R391Krev-GC AAG CCG CGG CCG **TTC** GTA GCA ACG CAC C; S348Ffor-CTG GTG GCG GCC **TTC** CCG GCG ATC TCC AAC CG (HpyAV site removed), S348Frev-GAC CAC CGC CGG AAG GGC CGC TAG AGG TTG GC; L100Ffor-CGG CGT AAA GAG ATG **TTC** CAC AAT GCC GCG CTA CGC G (HpyCH4V site removed), L100Frev-GCC GCA TTT CTC TAC **AAG** GTG TTA CGG CGC GAT GCG C. His₆-tagged primers (to introduce 6 histidines at the C-terminal of the mutant P450 in the pET20b plasmid) were amplified onto the WT and S348F mutant with the following primers: His₆-tagged forward- CCG GCG AAC GGG AGT-**TAA** GCT TGC GG, His₆-tagged reverse- GGC CGC TTG CCC TCA-**ATT** CGA ACG CC. PCR conditions were an initial denaturation step of 95°C (60 s), followed by 18 cycles of (a) denaturation at 95°C for 20 s, (b) annealing at

55°C for 30 s, and (c) polymerization at 72°C for 60 s. The PCR was completed with a polymerization step of 72°C for 10 min. PCRs were carried out in a Techne PHC-2 thermal cycler. PCR mixes contained ~10–25 ng of template *CYP51B1* WT DNA in pET20b (Novagen), 0.2 µM primers (10 pmol), 0.2 mM dNTPs, 1.5 mM MgCl₂, and 2 units of Pfu Ultra II, in a total volume of 50 µL. PCR products were incubated for an hour with DpnI at 37°C to digest methylated template DNA before transforming into XL1 Blue competent cells (Stratagene). Successful transformants were screened on LB agar with 12.5 µg/mL of tetracycline and 34 µg/mL of chloramphenicol. Stock mutant plasmid DNA was obtained from cultures of successful XL1 Blue transformants using the QIAprep® Spin Miniprep Kit (Qiagen) and stored at -20°C till further use. Mutant plasmid DNA sequences were determined either by MWG Eurofins plasmid DNA sequencing service or by Geneservice (Source BioScience LifeSciences). In each case the presence of the desired mutation and absence of secondary mutations was confirmed in the *CYP51B1* genes.

The *CYP123* and *CYP136* genes from Mtb were cloned from Mtb strain H37Rv cosmid genomic library (obtained from Professor Stewart Cole, Pasteur Institute, France) into pGEM-T vectors to introduce unique restriction enzyme sites before cloning into pET15b (Dr. Kirsty McLean and Dr. Jim Belcher, University of Manchester, pers. comm.). Consequently, both genes were re-excised from respective pGEM-T vectors and cloned into pET20b, pET24b and pET28b for *CYP123* and into pET11a, pET20b and pCOLD™TF for *CYP136*.

2.2.4 Expression Trials

Preliminary expression trials of *CYP123* and *CYP136* were carried out in 100 mL volumes in 250 mL shake flasks using various media, IPTG concentrations (0.1-1.0 mM), expression temperatures (15-26°C), with/ without addition of heme-precursor δ-aminolevulinic acid (0.18 mM δ-ala), using pET vectors or the pCOLD™TF cold shock expression system and different expression hosts (Novagen). Expression vectors for *CYP51B1* WT and mutants were as previously reported (McLean *et al.* 2006b). The *CYP51B1* genes were expressed in *E. coli* HMS174 (DE3) under control of a T7 RNA polymerase promoter in pET20b. Transformed cells were grown at 37°C overnight in LB medium plus antibiotic (300 mL) as inoculum for 30 L Terrific Broth (TB medium), with cells grown at 37°C for 3 hours then 26°C for 18 hours with IPTG (1 mM) induction at an OD₆₀₀ of 0.6–0.8. *CYP51B1* G388S and S348F mutants were expressed with the addition of 0.2 µM heme precursor δ-ala followed by 0.5 mM IPTG, while *CYP51B1* F89H, L100F

and R391K mutants were grown without the addition of δ -ala or IPTG. Cells were collected by centrifugation (5000g for 20 min at 4°C). Cell pellets were pooled, washed in 50 mM Tris-HCl and 1 mM EDTA (buffer A) and re-pelleted as previously described, weighed and stored at -20°C until further use.

2.2.5 Protein Purification

Frozen cell pellets were thawed and resuspended in a minimal volume of ice-cold buffer A containing protease inhibitors (phenylmethanesulfonyl fluoride [PMSF] and benzamidine hydrochloride, both at 1 mM), and cells were broken by a passage through a French press with one pass at 950 lb/in.², followed by sonication on ice (15 s bursts at 40% amplitude on a Bandelin Sonopuls instrument, with 1 minute cooling time between pulses) for an hour. Broken cells were centrifuged to pellet cell debris (60 000g for 20 min at 4°C), and the extract was dialysed into buffer A for a minimum of two hours and loaded directly onto a DEAE ion-exchange column which was equilibrated with buffer A (>3X column volume) prior to loading. After >2X column volume washes with buffer A, elution in a linear gradient with buffer A containing 500 mM KCl was carried out. Heme-containing fractions were pooled, dialyzed into buffer A, and purified on an equilibrated Q-Sepharose column followed by the same wash and gradient elution step used for the DEAE column. Partially purified heme-containing fractions were pooled, concentrated and dialysed into buffer B overnight with at least two buffer changes and loaded directly onto a hydroxyapatite (HA) column which was equilibrated with buffer B prior to use. At least 2X column volume washes with buffer B were carried out before elution in a linear gradient with buffer C was done to obtain semi-pure heme-containing fractions. Selected post HA column fractions were pooled, concentrated and buffer exchanged into buffer A by dialysing overnight with at least two buffer changes before loading onto an equilibrated hiPrep QXL or Resource Q column depending on concentration and volume of sample. Wash and elution steps were the same as for the DEAE and Q-Sepharose columns. Pure heme-containing fractions were pooled, concentrated and dialysed into buffer D before carrying out further experiments or stored in -80°C until further use. The C-terminal His₆-tagged CYP51B1 S348F was extracted from cells as above using buffer containing 50 mM potassium phosphate [KPi], pH 7.5, 0.1 mM NaCl, 10% (v/v) glycerol and 30 mM imidazole. This was then loaded onto a Ni-NTA affinity column (Novagen). The column was extensively washed before elution with the same buffer containing 70 mM imidazole. Fractions with the highest purity (by RZ [Reinheitszahl] value of A_{419}/A_{280}) were

concentrated by ultrafiltration (Centriprep 30 kDa cut off, Millipore) and applied to a G-25 Sephadex gel filtration column and eluted. Finally, all final fractions were analyzed for purity spectrophotometrically according to the RZ value and pooled. Purity of final protein preparations was confirmed by SDS-PAGE. Samples for crystallogenesis were concentrated to at least 2 mM before loading onto a S-200 Sephacryl gel filtration column and buffer exchange into buffer E.

2.2.6 Protein Identification – MALDI-TOF and Western Blotting

Expressed and purified enzymes were identified (whether in the soluble or insoluble fractions) by trypsin-digest and MALDI-TOF peptide identification, which was then matched against the mass values of a collection of peptides on the Mascot database. This identification technique was carried out by Dr. Chris Storey (MIB, University of Manchester) who was provided with the target protein separated by 12% polyacrylamide gel electrophoresis for trypsin digestion.

Protein with His-tags were isolated and identified by Western blot techniques according to the Invitrogen Western Blotting workflow. Sufficient amounts of protein (1.5–3.0 µg/mL) were loaded onto a 12% or 4–12% (for high molecular weight protein) SDS-PAGE gel with 10 µL SeeBlue®Plus2 prestained standard protein marker (LC5925, Invitrogen). Vertical gel electrophoresis was carried out at 180 V for 1 hr. Thereafter a Western transfer of proteins from gel onto a PVDF membrane was carried out in an XCell II™ Blot Module (EI9051, Invitrogen) at 10 V for 16 h/ overnight. The successfully-protein-transferred PVDF membrane was then processed according to the WesternBreeze® chemiluminescent immunodetection kit (WB7104, Invitrogen) and accompanying protocol. The PVDF membrane was subjected to a round of washing according to the following: 10 min, milliQ water; 30 min, blocking solution; 10 min milliQ water; 60 min, primary antibody (mouse) solution; 15 min, antibody wash solution; 30 min, secondary antibody (anti-mouse) solution; 15 min, antibody wash solution; 4 min, milliQ water; and 5 min, chemiluminescent substrate solution. The processed PVDF membrane was exposed to an X-ray film (X-OMAT AR, KODAK) for between 30 s to 6 min in a dark room. The PVDF membrane was subjected to a post-transfer analysis by 15 min staining with Ponceau S in 7% acetic acid and destaining in water or 7% acetic acid for 1 h.

2.2.7 Spectrophotometric P450 Characterisation

UV-visible and stopped-flow spectroscopic analyses of CYP51B1 WT and mutant P450s were carried out on a Cary 50 UV-vis. spectrophotometer (Varian) and on an Applied Photophysics SX18MV UV-visible stopped-flow instrument coupled to a monochromator UV-visible detector, respectively.

2.2.7.1 Analysis of the Thiolate to Thiol Conversion in WT and Mutant CYP51B1 Enzymes

To analyse stability of the Fe(II)-thiolate species during the reduction of Fe(III) heme to Fe(II) heme (in absence of CO) for WT and CYP51B1 mutants, stopped-flow spectroscopic analysis of enzymes mixed with reductant was performed. Experimental set up was as previously described under anaerobic conditions in a glove box with oxygen levels of <2 ppm at 25°C (McLean *et al.* 2006b). CYP51B1 proteins were prepared in anaerobic conditions with O₂-free 100 mM potassium phosphate buffer, pH 7.5 (Assay buffer) at a concentration of 9–10 μM (decreasing to 4.5–5 μM on mixing with an equal volume of reductant). Stopped-flow studies were done on an Applied Photophysics SX18MV UV-visible stopped-flow instrument coupled to a photodiode array UV-visible detector. Stock concentrations of sodium dithionite were prepared fresh in O₂-free assay buffer and P450s were pulsed-mixed with dithionite at a final concentration of 4.5–5.0 μM. Data were recorded over a 750–300 nm wavelength until such time as the spectral changes were complete. To determine if buffer pH affected thiolate to thiol conversion, studies were carried out for ligand-free CYP51B1 WT in the same assay buffer in the pH range 6.5–8.5, at 1.0 pH unit increments. CYP51B1 WT and mutants were reduced with 1 mM and 10 mM concentrations of sodium dithionite to monitor effects of reducing agent's concentration on the thiolate to thiol conversion. Rate constants were determined by fitting entire spectral changes observed using the global analysis ProKin software.

2.2.7.2 Analysis of the CYP51B1 Fe(II)-CO P450 to P420 Conversion in WT and Mutant CYP51B1 Enzymes

Conversion of the CYP51 Fe(II)-carbon monoxide (CO) complex from the thiolate-ligated form with a Soret band maximum close to 450 nm (P450) to the thiol-ligated form with a maximum near 420 nm (P420) was monitored spectrophotometrically.

Experiments were carried out as previously described under anaerobic conditions in a Belle technology glove box with O₂ levels of <2 ppm and at 25°C (McLean *et al.* 2006b). CYP51B1 WT and mutant proteins (final concentration 4–7 μM) were resuspended in 100 mM KPi buffer (pH 7.5) saturated with CO. UV-visible absorption spectra were recorded for the oxidized proteins on a Cary UV-50 Bio spectrophotometer at 23°C between 800–250 nm, and 10 μL of a freshly prepared 1 M sodium dithionite in the same buffer was added. The samples were mixed and spectra recorded immediately, and then recorded at 30 s intervals for up to 1 h to observe the P450-to-P420 collapse. Plots of the absorbance change at 448 nm or 420 nm against time were generated and data fitted to a single exponential function to derive rate constants for the process for each P450. These derived rates as obtained from data fitted to Equation 2.1 describe the transition from a water (distal ligand)-ferric-thiolate (proximal ligand) (418nm) species to a ferrous-thiolate species (essentially spectrally silent due to the rapid conversion to the CO-bound state), and on to CO-ferrous-thiolate (P450) and CO-ferrous-thiol (P420) forms.

$$y = y_o + \Delta A e^{k_{obs}x} \quad \text{Equation 2.1}$$

Where y_o = initial absorbance at the relevant wavelength; ΔA = the change in absorbance or amplitude; k_{obs} = rate of P450 collapse or P420 formation; x = time at which observed absorption y was made for the collapse or formation of the relevant species.

2.2.8 Kinetic Spectrophotometric Analysis

Equilibrium titrations and stopped-flow spectrophotometric analyses to determine K_d values for theazole drugs and for the substrate analogue estriol were carried out at 25°C with enzyme concentrations of 2–7 μM (equilibrium) and 4–6 μM (stopped-flow, post-mix concentration), respectively, in 100 mM KPi (pH 7.5). The final dimethylsulfoxide (DMSO) solvent concentration forazole drugs and estriol was maintained at <2% of the final volume of assay mixtures.

2.2.8.1 Equilibrium Titrations

Equilibrium titrations to determine K_d values were done by optical titration of six azole drugs; the imidazoles clotrimazole, econazole, miconazole, ketoconazole; the triazoles fluconazole and voriconazole; and the substrate analogue estriol. All experiments were carried out in 1 cm path length quartz cuvettes at 25°C over a 250-800 nm wavelength range. Procedures for the spectroscopic analysis using the optical titration method were carried out according to McLean *et al.* (McLean *et al.* 2006b) by diluting CYP51B1 WT and mutants in the assay buffer to between 1.4–6.0 μM in a 1 mL final volume. Titrations of each azole drug and estriol were done using concentrated aliquots of each ligand in DMSO solvent. Prior to this, a set of experiments were carried out, similar to the ligand titration method, to determine the maximum DMSO solvent tolerance of each CYP51B1 enzyme. Optical titrations were carried out using a micro-syringe (Hamilton) with the addition of 0.1–0.2 μL at each step. Difference spectra were generated from the initial scanning spectra by the subtraction of the spectrum of ligand-free P450 from the spectra collected following each addition of ligand. Wavelengths reflecting the minima and maxima in the difference spectra were identified and the overall absorption difference between the two points was determined for each difference spectrum. K_d values from equilibrium titrations were computed by fitting ligand-induced absorption change data versus the relevant ligand concentration using a quadratic function (Equation 2.2).

$$A_{obs} = (A_{max} / (2 * E_t)) * ((X + E_t + K_d) - \{[(X + E_t + K_d)^2 - (4 * X * E_t)]^{0.5}\}) \quad \text{Equation 2.2}$$

Where A_{obs} = observed absorbance change determined at ligand concentration X ; A_{max} = the maximal absorption change induced at saturating ligand concentration; E_t = enzyme concentration used; and K_d = dissociation constant for the ligand bound to the protein. All data analysis was done using MSoffice Excel (Microsoft) and unless otherwise stated, all fitting was done using Origin 8.0 or 8.1 software (OriginLab).

2.2.8.2 Stopped-Flow Kinetics

Stopped-flow kinetics approaches are necessary to determine the azole drug binding reaction rate with heme iron of the cytochrome P450 on a millisecond timescale. By using a monochromator detection unit and the photo-diode array detector with a stopped-flow instrument (Applied Photophysics SX18MV), the rates of reaction both at a single wavelength (that characterizes complex formation) and across a range of wavelengths (800–250 nm, to determine full spectral evolution of the complexes) were determined. All reagents, assay buffer solutions and the protein sample were filtered prior to analysis. A series of serial dilutions was made up for each azole drug between the concentrations of 10–500 μM (pre-mixed) using a stock concentration of 500 μM with a maximum of 20% DMSO in assay buffer. CYP51B1 WT, F89H and G388S proteins were diluted into 10 mL assay buffer within the range of 9–13 μM (pre-mixed). The experiment was carried out at 25°C with the assay buffer as described in Table 2.2. The observed reaction is the change in absorption at a particular wavelength against time (milliseconds/seconds/minutes) with a particular ligand concentration (Figure 2.2 B).

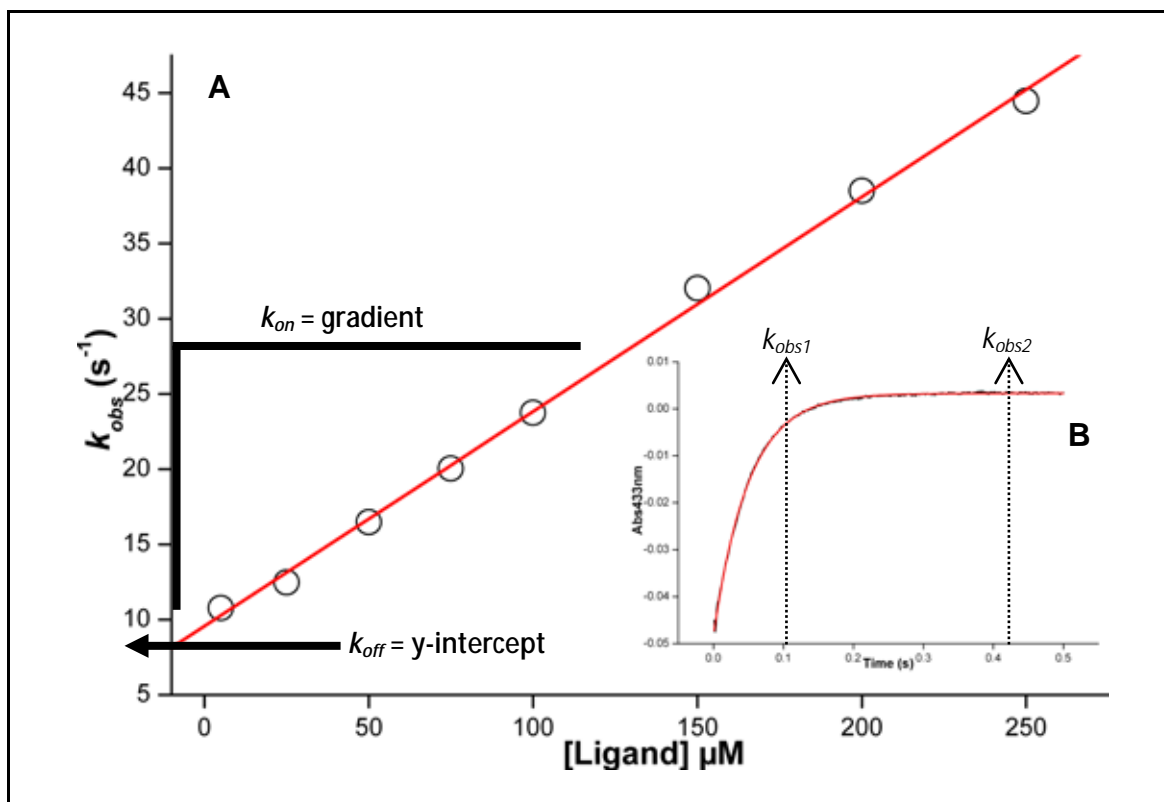


Figure 2.2: Derivation of second order rate constants from stopped-flow kinetics.

Illustration describes the derivation of rate of binding, k_{on} , and rate of de-binding, k_{off} from the gradient of the linear plot of individual rate constants (k_{obs}) and the y-intercept of this line, respectively. **B)** describes the initial observed reaction defined by the change in absorption at a particular wavelength against time in seconds for a reaction rate of CYP51B1 with a particular ligand concentration. **A)** is derived from multiple **B)** plots at different ligand concentrations with the linear fit shown through the various k_{obs} values plotted against their respective ligand concentrations. If in the case where the reaction extends over time in **B)**, data were fitted to a double exponential equation yielding a two rate reaction with k_{obs1} and k_{obs2} . Both these rates were plotted and compared and the best linear fittings obtained from observed rates were used to calculate k_{on} , k_{off} and the K_d .

Kinetic values from stopped-flow analyses were computed with ProKin software (Applied Photophysics) by monitoring global or single wavelength absorption changes. Reaction absorption transients were fitted using either single exponential (Equation 2.1) or double exponential (Equation 2.3) functions to generate apparent rate constants (k_{obs} values). The observed rates from each reaction with different ligand concentrations were noted and a linear graph plotted with observed reaction rates (k_{obs}) against different ligand concentrations. The second order rate constant (k_{on}) for ligand binding is given by the gradient/slope of the linear function (k_{obs} values versus relevant ligand concentrations); while the apparent de-binding rate constant (k_{off}) is derived from the y-axis intercept as illustrated in Figure 2.2 (A). The K_d was determined from the k_{off}/k_{on} ratio. Both K_d values from equilibrium titration and stopped-flow kinetics were compared.

$$y = y_o + \Delta A e^{k_{obs}x} \quad \text{Equation 2.1}$$

With reference to Figure 2.2 (B) and the binding of a ligand to a protein, y = observed absorption change y_o = initial absorbance at the wavelength of interest for the starting population; ΔA = the overall change of absorbance at the respective wavelength associated with the rate constant k_{obs} ; k_{obs} = observed rate of ligand binding; and x = time in seconds.

$$y = y_o + \Delta A_1 e^{k_{obs1}x} + \Delta A_2 e^{k_{obs2}x} \quad \text{Equation 2.3}$$

With reference to Figure 2.2 (B) and the binding of a ligand to a protein, the equation describes data fitting using a double exponential function. The terms are largely the same as those detailed for Equation 2.1, with the exception that ΔA_1 and ΔA_2 refer to absorbance changes in the first and second phases of the reaction that are associated with the respective rate constants k_{obs1} and k_{obs2} .

2.2.9 Hemoprotein Estimation by the Pyridine Hemochromogen Technique

Heme b concentration in CYP51B1 WT and mutants was estimated by the technique developed by Berry and Trumpower (Berry and Trumpower 1987). Solutions of 0.5 mL pure protein (5–6 μM and 10–12 μM) were prepared with the Assay buffer in 1 mL cuvettes (1 cm pathlength) and an initial UV-Vis scan was recorded. Using the same protein sample (10–12 μM), 0.5 mL of pyridine stock solution (40% (v/v) pyridine, 0.8 mM potassium ferricyanide, 200 mM sodium hydroxide) was added to a 1:1 ratio and mixed promptly. The oxidised spectrum was recorded within 1 min of mixing. The solution mix was reduced with 10 μL of a freshly prepared 1 M sodium dithionite in Assay buffer and spectra were recorded until no further changes to the Soret band and 500–600 nm regions were observed. The difference in absorbance at 557 nm between the oxidised and reduced spectra was divided by a difference extinction coefficient $\Delta\epsilon_{557} = 23.98 \text{ mM}^{-1}\text{cm}^{-1}$ to obtain the concentration value X according to the Beer-Lambert law. In order to obtain the heme b extinction coefficient for the oxidised enzyme, ϵ_{419} , absorbance at the Soret band (A419)

was divided by $2X$. Averages of three separate experiments above were calculated to obtain ϵ_{419} for CYP51B1 WT and mutants.

2.2.10 Biophysical Analysis

2.2.10.1 Circular Dichroism (CD) Spectroscopy

Circular dichroism spectra in the far UV region (180-260 nm) were recorded either on a Chirascan™ Applied Photophysics or a Jasco J-715 spectropolarimeter at 25 °C in 0.1 mm pathlength quartz cuvettes. Spectra in the visible region (300-600 nm) were recorded on a Jasco J-715 spectropolarimeter at 25 °C in 2 mm pathlength quartz cuvettes. Measurements were made in 100 mM potassium phosphate (pH 7.5) containing 0.1 and 1 mg/mL CYP51B1 for the far UV and visible regions, respectively. Spectra for protein-free buffer were also recorded and subtracted from the protein spectra. Data from four scans were averaged in each case.

2.2.10.2 Electron Paramagnetic Resonance (EPR) spectroscopy

The ferric forms of WT and mutant CYP51B1 proteins in their ligand-free andazole-bound complexes were analysed by EPR spectroscopy. Spectra were obtained using a Bruker E500/E580 ELEXSYS instrument operating at X-band. Signals generated were from a 0.25 mL, 0.20–0.25 mM sample protein concentration in 4 mm Suprasil Quartz EPR tubes (Wilma, Vineland, NJ) frozen in liquid nitrogen prior to analysis. Temperature control was effected using an Oxford Instruments ESR900 liquid helium cryostat in conjunction with a ITC503 temperature controller. EPR spectra were obtained at 10 K, 100 mW microwave power, and at a modulation frequency of 100 KHz and a modulation amplitude of 5-9 G. Protein samples were made in 100 mM potassium phosphate (pH 7.5) (Assay buffer). Ligand-bound spectra were recorded using near-saturating amounts ofazole ligands (4-phenylimidazole [4-PI], voriconazole, and clotrimazole), as determined by spectral analysis.

2.2.10.3 Differential Scanning Calorimetry (DSC)

Differential scanning calorimetry studies were done on a Microcal VP-DSC calorimeter. Protein samples (0.7 mL of a 1 mg/mL solution) and reference buffers (100 mM potassium phosphate, pH 7.5) were filtered and degassed. Reference buffer was loaded in both sample chambers to obtain baselines. Readings were carried out between 20 – 90°C and repeat scans were carried out until a consistent reading was obtained. Every ligand-free and ligand-bound sample was recorded and baseline adjusted against only buffer with and without ligands, respectively. Ligands were added into the enzyme at equilibrium concentrations prior to initiating analysis. The same volume of enzyme sample and reference sample were loaded for each measurement. Data obtained were fitted using DSC OriginLab software (Microcal) to assign melting temperatures or transition midpoints (T_m), and enthalpy or calorimetric heat change (ΔH) and van't Hoff heat change (ΔH_v) values for protein unfolding transitions. All the results obtained were baseline-subtracted and normalized by concentration to convert from ΔC_p (cal/deg) to C_p (cal/mole/deg). Resulting data were fitted according to Model 2 – Non 2-state with zero ΔC_p from Levenberg-Marquardt non-linear least-squares method of the OriginLab DSC software (Appendix G).

2.2.10.4 Multiangle Laser Light Scattering (MALLS)

Purified samples of CYP51B1 WT and mutants (0.5 mL of 4–6 μ M protein) were applied to a Superdex 200 gel filtration column (GE Healthcare) running at a flow rate of 0.71 mL/min in buffer E. Samples eluting from the column were passed through an in-line DAWN HELIOS-II laser photometer (laser wavelength 690 nm) and an Optilab rEX refractometer with a quasi-elastic light scattering (QELS) dynamic light scattering attachment (Wyatt) to measure the refractive index and the hydrodynamic radius values, respectively. Light scattering intensity and eluant refractive index (concentration) were analyzed using ASTRA v5.21 software to give a weight-averaged molecular mass (Mw). Absorbance of eluted samples was monitored at 280 nm via a Jasco UV spectrophotometer.

2.2.11 Crystallogenesis

Crystallisation trials were carried out for CYP51B1 WT, F89H, R391K and L100F with commercial screens from Qiagen (JCSG I, JCSG II, JCSG III and JCSG+) and using screens from Molecular Dimensions (Clear Strategy I and II, PACT Premier and Morpheus). Custom screens of 0-7% isopropanol and 8-42% polyethylene glycol 4000 (PEG4K) were also employed as described by Podust *et al.* (Podust *et al.* 2007; Podust *et al.* 2004). Azole drugs and α -ethyl-N-4-pyridinyl- benzeneacetamide (EPBA) (Ambinter, France) were prepared in DMSO and added within a range of 0.5 mM, 1 mM, and 2 mM final ligand concentrations into 0.1-0.2 mM pure protein up to 2% (v/v) DMSO concentration. All pure protein samples for crystallogenesis were passed through a S-200 Sephacryl gel filtration column and buffer exchanged into buffer E, concentrated (by ultrafiltration) and made up to 0.1-0.2 mM in 20 mM Tris-HCl, 0.5 mM EDTA, 250 mM NaCl (pH 7.5). Protein-enzyme mix was added 1:1 to mother liquor from screens using a Mosquito® Crystal (TTP Labtech) protein dispenser to form sitting drops. A microseeding protocol, as described by D'Arcy *et al.* (D'Arcy *et al.* 2007), was also employed for F89H mutant crystallogenesis. The microseed stock was prepared with crushed co-crystals of CYP51B1 R391K-EPBA and WT-EPBA resuspended in its respective mother liquors and vortexed to obtain a homogenous stock solution of 0.5 mL volume. Immediately before setting the screens, 192 μ L of 0.2 mM pure protein was added to 48 μ L microseed stock at a 4:1 ratio of protein to seed and mixed gently to make the microseed-protein enzyme mix. Screens for the microseed method were prepared by adding the microseed-protein enzyme mix 1:1 to mother liquor using a Crystal Phoenix® protein crystallography dispenser (Art Robbins Instruments). Screens for the microseed method were incubated at 21°C and the others at 20°C in shake-proof incubators.

Crystals and co-crystals which appeared within a week were harvested with PEG 200 as a cryoprotectant and immediately flash-frozen in liquid nitrogen and transported to the Diamond Synchrotron (Oxford, UK) for X-ray diffraction analysis. Diffraction data were collected by Dr. Colin Levy and Dr. Mark Dunstan (University of Manchester). Data collected were fitted using WinCoot (Emsley *et al.* 2010) and CCP4 programs by Professor David Leys (University of Manchester) and the molecular structures were solved by the molecular replacement method for ligand-free crystal data and by the difference Fourier method for ligand-bound co-crystal data. Diagrams and models in this thesis were made by PyMol™ DeLano Scientific (2005) molecular graphics software using CCP4 mesh files and PDB files.

2.2.12 Potentiometric Studies

Redox titrations were performed in a glove box under a nitrogen atmosphere, as described previously (Munro *et al.* 2001; Ost *et al.* 2001; Prince *et al.* 1978). Purified CYP51B1 enzymes were run through a gel filtration column (BioRad Econo-Pac 10DG desalting column) in an anaerobic glove box with redox buffer (Table 2.2). Eluted fractions were collected to a total of 4.99 mL. The final concentration of CYP51B1 in a total of 5 mL was between 4.1–9.8 μM . Mediators for the redox reactions were prepared as follows and added to top up to the total volume of 5 mL:

Table 2.4: Mediators used in redox potential determination.

Mediators	Concentration (mM)	Weight (mg)	Volume of buffer to add to dissolve (mL)	Volume to add into 5 mL reaction mix (μL)	Midpoint redox potentials (mV)
Benzyl viologen (BV)	2.5	5.32	5	2	-350
Methyl viologen (MV)	1.5	1.93	0.3	1	-440
Hydroxy naphthoquinone (HNQ)	7	6.1	7	5	-140
Phenazine methosulfate (PMS)	5	1.53	2	2	+80

Both HNQ and PMS are light sensitive and were freshly prepared. All mediators were added to the eluted and diluted CYP51B1 to an exact concentration as stated above (Table 2.4) to mediate electrochemical potential readings between the solution mix and the electrode from the range of -440 to 80 mV. A concentrated solution of sodium dithionite (~ 100 mM) was made with redox buffer and a series of 10-fold dilutions were made in aliquots for the reduction titration. A diluted solution (1–10 mM, progressively increasing as the potential reduces) of sodium dithionite (1–2 μL) was titrated into the solution mix and stirred gently until the reading reached equilibrium (4–6 min after every titration). The changes in electrochemical potential (mV) were measured with a Hanna pH 211 meter coupled to a platinum calomel electrode (Thermo Fisher) at 25°C. Changes in absorbance were typically recorded between 250 and 800 nm wavelengths with a Cary UV-50 Bio UV-visible scanning spectrophotometer. A correction factor of 244 mV was added to the electrochemical potential data to account for the difference between the calomel electrode and the standard hydrogen electrode (SHE). Change in absorbance versus electrochemical potential (versus SHE) was plotted (at one or more wavelengths of the heme spectrum) via Origin software and fitted to the single electron Nernst equation (Equation 2.4) with the

RTF (Universal gas constant* temperature of experiment*Faraday constant) of -59 mV to determine the midpoint potential for the P450 Fe(III)/Fe(II) couple in each case.

$$A = \frac{(A_{abs} + B_{abs} \cdot 10^{((E^o - E)/RTF)})}{(1 + 10^{((E^o - E)/RTF)})} \quad \text{Equation 2.4}$$

In Equation 2.4, A is the absorption observed at the potential E , A_{abs} is the absorbance of the oxidised hemoprotein; and B_{abs} is the absorbance of the reduced hemoprotein; E is the applied electrode potential corrected against SHE, and E^o is the midpoint redox potential for the heme iron Fe(III)/Fe(II) transition. RTF is the compounded value of the Universal gas constant, temperature of experiment and Faraday constant. In order to rule out any possible hysteresis phenomena, reoxidation was carried out with potassium ferricyanide dissolved in redox buffer. Readings were taken after every ~ 4 – 6 minutes or until the system was equilibrated, and it was ensured that the oxidative pathway overlapped spectrally with that of the reductive pathway in the same potential range.

2.2.13 Redox Cycling of CYP51B1

In order to mimic the CYP51B1 redox cycling with its electron transport partners and to understand the consequence of repeated redox cycling on the heme of this P450, a set of experiments were carried out in which reduction and reoxidation of WT and mutant CYP51B1 enzymes were done with sodium dithionite and potassium ferricyanide in turns. All experiments were carried out in an anaerobic environment at 21°C . All purified CYP51B1 enzymes were run through a gel filtration column (BioRad Econo-Pac 10DG desalting column) in an anaerobic glove box with degassed assay buffer (Table 2.2). Both reducing and oxidising agents (100 mg/mL sodium dithionite and 70 mg/mL potassium ferricyanide solutions) were prepared in degassed assay buffer. CYP51B1 and mutants were prepared in 1 mL, 3–6 μM working concentration in a 1 cm pathlength quartz cuvette. One microlitre of sodium dithionite solution was added into the enzyme solution and spectra were taken every 1.5 min x 40, 6 min x 40 cycles until the maximum equilibrated (reduced) ferrous-heme was observed. To reoxidise the ferrous P450-heme, 1–3 μL of potassium ferricyanide were added to the mixture and again spectra were taken until the reoxidised Soret band reached equilibrium. After each reduction and reoxidation step the pH of the

enzyme mixture was taken to ensure pH maintained between 6.5 and 7.5. At this point the enzyme was reduced again with 1–2 μL of sodium dithionite and the spectra were recorded until equilibrium was reached, and CO was then bubbled into the solution and a spectrum was recorded. The entire redox cycling experiment per enzyme took 48–60 hours. It was observed that throughout this time the enzymes remained stable at 21°C with less than 5% of the enzyme precipitating.

To understand the effect of redox cycling on CYP51B1 ferric-heme, concentrated enzymes (~ 150 – $250 \mu\text{M}$) were prepared and were redox cycled in similar fashion as above for EPR analysis. The concentrated reduced and reoxidised species were monitored by Nanodrop scan (Thermo Scientific) using as little as 1 μL of concentrated enzyme and reading absorption between 500 and 600 nm associated with the heme α and β bands. Samples were promptly transferred into EPR tubes and frozen in liquid nitrogen upon reoxidation with a saturated solution of potassium ferricyanide in degassed assay buffer, added at up to 10% of the total concentrated enzyme volume. Samples were prepared for EPR analysis according to the protocol in section 2.2.10.2.

2.2.14 Stabilisation of the P450 Species by CO Trapping with Redox Partners

The formation of the Fe (II)-CO adducts, (P450) species, in CYP51B1 is relatively unstable as it collapses to its more stable P420 thiol-coordinated form over a period of several minutes. The thiol/thiolate transition is reversible upon reoxidation, since the reoxidised form was shown to regain thiolate coordination of the heme iron (Aoyama *et al.* 1998; McLean *et al.* 2006a; McLean *et al.* 2006b). This experiment was aimed to demonstrate how redox from partners in Mtb can influence the formation and stabilization of the CYP51B1 thiolate-coordinated form in the presence of estriol and CO, and to ascertain the properties of azole-resistant mutants in this respect. All redox partner proteins were provided by Dr. Kirsty McLean (University of Manchester) (McLean *et al.* 2003; McLean *et al.* 2006b; McLean *et al.* 2006c) and prepared as in Table 2.5. Assay buffer and 1 mL sealed cuvettes (1 cm pathlength) were degassed and CO-flushed/saturated. Stock solutions of 20 mM NADPH (freshly prepared in CO-saturated Assay buffer) and 50 mM estriol (in DMSO) were prepared.

Table 2.5: *Mycobacterium tuberculosis* redox partner proteins and components for CO trapping experiment.

Redox partner proteins	Gene names	Extinction coefficient (mM ⁻¹ cm ⁻¹) (λ_{\max})	[Stock] (mM)	[Working] (μ M)
Ferredoxin 1 (Fd1)	<i>Rv0763c</i>	12.0 (412 nm)	0.627	16.20
Ferredoxin 2 (Fd2)	<i>Rv1786</i>	12.0 (412 nm)	1.700	16.20
Ferredoxin reductase (Fdr)	<i>Rv0688</i>	10.5 (454 nm)	0.938	3.24
Flavoprotein reductase A (FprA)	<i>Rv3106</i>	10.6 (454 nm)	1.392	3.24
P450 Sterol demethylase (CYP51B1 WT and mutants)	<i>Rv0764c</i>	134.0 (419 nm)	various	3.24

Reaction components	[Stock] (mM)	[Working] (μ M)
Estriol	50	200
NADPH	20	300

Components of the reaction were assembled and a UV-Vis spectrum recorded after each addition on a Cary 50 UV-vis. spectrophotometer (Varian). The P450, ferredoxins and reductases were combined according to a 1:5:1 concentration ratio. Each experiment was carried out involving controls achieved by omitting the redox partner enzymes one after the other. Corresponding experiments were also carried out with either none or all of the redox partner enzymes. The reaction was initiated by the addition of NADPH (constantly topped up when depleted as no regeneration system was used) when all components except estriol were in the mixture, and a cycle of 10 x 1.5 min scans was started. Estriol was added and another cycle of 80 x 1.5 min scans were recorded. The absorbance change for P450 species (448 nm) formation and its collapse to P420 species (421 nm) were plotted against time. The resulting data were fitted to a single exponential equation to obtain rates of P450 collapse and P420 formation for CYP51B1 WT and mutants. The experiment was done at 30°C.

2.2.15 CYP51B1 Reconstitution of Catalysis

Sterol demethylases catalyse the demethylation of the methyl group at C-14 of the sterol backbone. As CYP51B1's *in vivo* function is still unknown, a variety of sterols have been tried and reported as potential substrates, namely lanosterol, 24,25-dihydrolanosterol, and obtusifoliol which gave 1%, 20% and 98% product yield respectively (Bellamine *et al.* 1999). In order to test the catalytic properties of CYP51B1 and the corresponding fluconazole-resistant point mutants, lanosterol and 24, 25-dihydrolanosterol as the substrates of choice were chosen based on chemical availability. Materials and methods were adapted from various previously established catalysis experiments with CYP51B1 and human CYP51 (Bellamine *et al.* 1999; Strushkevich *et al.* 2010). CYP51B1 WT and the fluconazole point mutants were prepared and concentrated to 0.1-2.5 mM stock concentration. Components of the catalysis reaction mixture were prepared in stock concentration (Table 2.6) and all components were made up in 100 mM HEPES pH 7.5 unless otherwise stated. Solutions were combined on ice in Universal bottles. Mtb ferredoxin (Fdx) and Mtb flavoprotein reductase A (FprA) were expressed, purified and provided by Dr. Kirsty McLean (University of Manchester) (McLean *et al.* 2003; McLean *et al.* 2006b; McLean *et al.* 2006c) as redox partner proteins of CYP51B1 forming electron transfer complexes with the P450 itself. Reactions were initiated by adding NADPH (5 mM). A NADPH regeneration system was also incorporated in the reaction mixture. The reactions were carried out on two or three different timescales, at 23°C (1 h) and 37°C (10 min) with both shaking at 180 rpm and static on ice overnight (18 h). Product turnover for lanosterol was detected by GCMS as previously reported (Strushkevich *et al.* 2010). Product turnover for 24, 25-dihydrolanosterol was detected by prior optimised LCMS techniques (Dr. Kirsty McLean, pers. comm.).

Table 2.6: Components of CYP51B1 catalysis reaction mixture.

No.	Components	Stock concentration (mM)	Working concentration (mM)	Volume (μ L)
1.	CYP51B1	As stated above	0.004	Various
2.	Mtb Flavoprotein reductase A	0.763	0.02	78.6
3.	Mtb Ferredoxin	0.77	0.004	15.6
4.	Lanosterol (in EtOH and 50 mg/mL β -cyclodextrin)	10	0.2	60.0
5.	β -cyclodextrin	450 mg/mL	10 mg/mL	66.7
6.	Glucose-6-phosphate	10	0.2	60.0
7.	Glucose-6-phosphate dehydrogenase	100 U/mL	0.1 U/mL	3.0
8.	KCl	1000	250	750.0
9.	MgCl ₂	1000	25	75.0
10.	NADPH	100	5	150.0
11.	HEPES pH 7.5	100	100	Top up to
Total volume		-	-	3000



Chapter 3 | Biochemical Characterisation of CYP51B1 and Fluconazole-Resistant Mutants

- 3.1 *Mapping Fluconazole-Resistant Point Mutants from Candida albicans*
- 3.2 *Site-Directed Mutagenesis on CYP51B1*
- 3.3 *Expression and Purification of Mutants*
- 3.4 *The Effect of Drug Solvent DMSO Concentration on CYP51B1*

- 3.5 ***Understanding the Molecular Mechanisms and Mode of Action/ Physiological Roles of Mtb CYP51B1***
 - 3.5.1 *Quantification of Heme b in WT CYP51B1 and Mutants*
 - 3.5.2 *CYP51B1 Heme-Coordination by NO and CO*
 - 3.5.2.1 *NO-Ferric-Heme Coordination*
 - 3.5.2.2 *CO-Ferrous-Heme Coordination*
 - 3.5.3 *Formation of CO-Free Ferrous-Thiol Species*
 - 3.5.4 *Stabilisation of the P450 Form in the Presence of Estriol and Redox Partners*
 - 3.5.5 *Redox Potentials of CYP51B1 Ligand-Free Form*
 - 3.5.6 *Redox Cycling with Chemical Reducing and Oxidising Agents*

- 3.6 ***Understanding the Mechanisms of Azole-Resistance in CYP51ca Using CYP51B1 as a Template***
 - 3.6.1 *CYP51B1 UV-Visible Spectral Ligand Binding Properties*
 - 3.6.1.1 *Photo-Diode Array Analysis of Estriol and Fluconazole Binding*
 - 3.6.1.2 *Equilibrium Titration of Azole Drugs and Estriol*
 - 3.6.1.3 *Stopped-Flow Analysis of Azole Drugs*
 - 3.6.2 *Reconstitution of CYP51B1 Enzyme Catalysis with Lanosterol and Dihydrolanosterol*

- 3.7 *Summary and Critical Assessment*

3 BIOCHEMICAL CHARACTERISATION OF CYP51B1 AND FLUCONAZOLE-RESISTANT MUTANTS

3.1 Mapping Fluconazole-Resistant Point Mutations from *Candida albicans*

In order to address the two main objectives of this research, which are **(1)** to gain a better understanding of the molecular mechanisms underpinning **Mtb CYP51B1 (CYP51B1)** mode of action/physiological role (by observing the effects of point mutations on its function and structure at important structural regions of CYP51B1 as mapped from the fluconazole-resistant *Candida albicans* ERG11 gene coding for CYP51ca) and **(2)** to understand the mechanism of azole-resistance in *C. albicans* CYP51 (CYP51ca), multiple point mutations were engineered onto CYP51B1 from reoccurring mutation hot spots of apparently 'fluconazole-resistant' CYP51ca isolated from fluconazole-resistant *C. albicans* clinical strains. Upon screening of the azole antifungal drug target CYP51ca in resistant *C. albicans* clinical strains, certain regions showed higher incidences of mutations. These point mutations occurred at mutation hot-spot residues which are illustrated in CYP51B1 of Mtb in Figure 3.1 (A) upon sequence alignment with CYP51ca. At the same time, *Aspergillus fumigatus* resistance towards voriconazole was also reported and the same drug target CYP51A was analysed and showed a mutual mutation hot-spot at glycine 388 of CYP51B1 when the three sequences were aligned (Figure 3.1 B). In CYP51B1 of Mtb, the N-terminal hydrophobic amino acid sequences are absent indicating it to be a soluble sterol demethylase, while in both CYP51s of *C. albicans* and *A. fumigatus*, the presence of 50-60 N-terminal hydrophobic amino acid residues (Figure 3.1 B) confirm that these two homologues are membrane-bound, insoluble sterol demethylases. Irrespective of whether cytoplasmic or membrane-bound, these homologues share conserved sequences (magenta shaded), at important substrate recognition sites (SRS) scattered throughout the molecule. The azole drug-resistant recurring residues are situated close to these sites, if not directly in these regions.

In this chapter, these heme-containing P450 proteins of the soluble Mtb sterol demethylase enzyme, WT CYP51B1 and the "azole-resistant" isoforms (i.e. Mtb CYP51B1 carrying mutations to mimic those found in azole-resistant fungal CYP51s), F89H, L100F, S348F, G388S and R391K have been produced. Their biochemical properties were interrogated in depth in the first half of this chapter to address objective no. **(1)** followed by azole drug binding studies and the catalytic viability of these CYP51B1 enzyme variants to address objective no. **(2)**. Table 3.1 below summarises the location of point mutations from the product of the *ERG11* gene (*CYP51*) of clinical *C. albicans* fluconazole-resistant

strains, while the following figure (Figure 3.1 A) maps these mutation points onto the structure of CYP51B1 from Mtb. Note that L100F is a reverse mutant for CYP51ca of azole-resistant *C. albicans*.

Table 3.1: Recurring point mutations in the *ERG11* gene encoding for sterol demethylase of fluconazole-resistant *Candida albicans*.

<i>ERG11</i> amino acid position	<i>ERG11</i> mutation	Position in <i>M. tuberculosis</i> <i>Rv0764c</i> gene	<i>Rv0764c</i> mutation	Similar mutations in CYP51 from other organisms which cause/may cause azole-resistance	References
Y132	Y132H	F89	F89H	<i>Aspergillus flavus</i> , <i>Mycosphaerella fijiensis</i> , <i>Erysiphe graminis</i> , <i>Blumeria graminis</i> , <i>Puccinia triticina</i>	Delye <i>et al.</i> 1998, Sanglard <i>et al.</i> 1998, Favre <i>et al.</i> 1999, Kelly <i>et al.</i> 1999a, Marichal <i>et al.</i> 1999, Kakeya <i>et al.</i> 2000, Kudo <i>et al.</i> 2005, Xu <i>et al.</i> 2008, Canas-Gutierrez <i>et al.</i> 2009, Stammler <i>et al.</i> 2009, Kamai <i>et al.</i> 2004, Wang <i>et al.</i> 2009, Yan <i>et al.</i> 2009, Krishnan-Natesan <i>et al.</i> 2008
F145	F145L	L100	L100F	n.d.	Kudo <i>et al.</i> 2005, Xu <i>et al.</i> 2008
S405	S405F	S348	S348F	n.d.	Manavathu <i>et al.</i> 1999, Sanglard <i>et al.</i> 1998, Wang <i>et al.</i> 2009
G464	G464S	G388	G388S	<i>Aspergillus fumigatus</i> , <i>Aspergillus flavus</i> , <i>Cryptococcus neoformans</i>	Kelly <i>et al.</i> 1999b, Loffler <i>et al.</i> 1997, Manavathu <i>et al.</i> 1999, Sanglard <i>et al.</i> 1998, Takahata <i>et al.</i> 2005, Goldman <i>et al.</i> 2004, Martinez <i>et al.</i> 2002, Krishnan-Natesan <i>et al.</i> 2008, Wang <i>et al.</i> 2009
R467	R467K	R391	R391K	n.d.	Lamb <i>et al.</i> 2000, White 1997, Sanglard <i>et al.</i> 1998, Wang <i>et al.</i> 2009

Note: n.d. – not detected

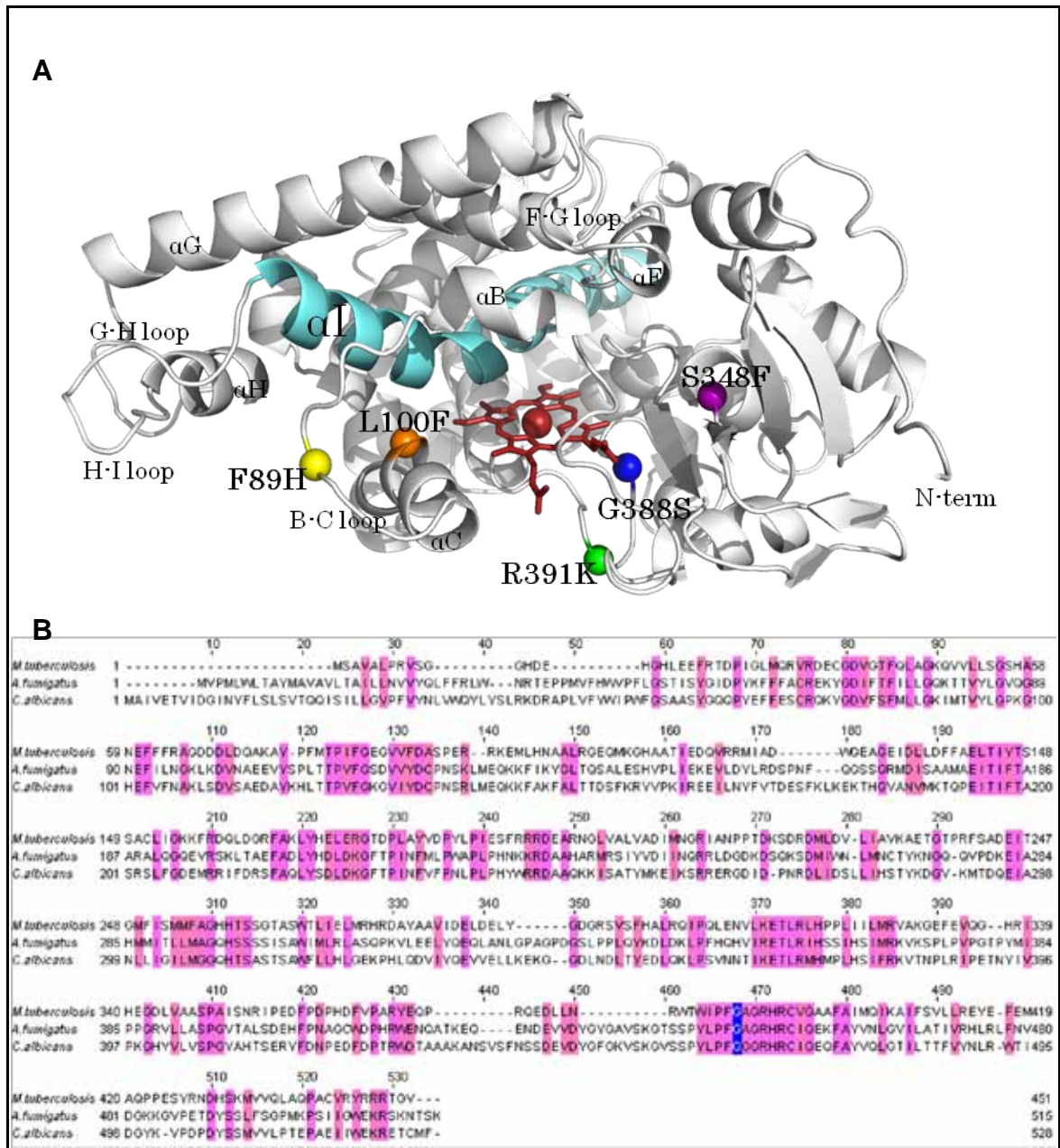


Figure 3.1: Fluconazole-resistant point mutations from *Candida albicans* CYP51. A) The location of mutations mapped from *C. albicans* CYP51 corresponding to the amino acid residues of CYP51B1 from *Mycobacterium tuberculosis*. Residues are located in the Mtb CYP51B1 B-C loop and C-helix (yellow-F89H and orange-L100F), I-helix (light blue), Fe-heme regions and the cysteinyl loop (green-R391K and dark blue-G388S), and the C-terminal helix and beta-sheets junction (magenta-S348F). B) Multiple sequence alignment (MSA) of CYP51B1 from Mtb, CYP51A1 from *C. albicans* and CYP51A from *Aspergillus fumigatus*. Magenta coloured residues denote sites of conserved amino acids; the blue highlighted glycine residue at G388 (Mtb), G464 (*C. albicans*) and G448 (*A. fumigatus*) positions was repeatedly found as the most-recurring fluconazole resistant mutation in the respective species of fungi. MSA was generated by ClustalW2 and drawn by Jalview software.

3.2 Site-Directed Mutagenesis on CYP51B1

All mutants of CYP51B1 were successfully made using the QuikChange site-directed mutagenesis kit from Stratagene and the resulting cloned pET20b plasmid constructs, transformed into *E. coli* XL1 Blue competent cells, were confirmed post-miniprep by DNA sequencing at MWG Eurofins using T7 forward and reverse primers provided by the sequencing company. Initially, successful cloning of the mutants was carried out by diagnostic restriction digestion against WT CYP51B1 pET20b plasmid DNA, using DNA restriction enzymes HpyCH4V (L100F), HpyAV (S348F) and EagI (R391K). The sequencing data in Figure 3.2 show the codons responsible for each mutant enzyme and confirmed the mutant pET20b clones from this site-directed mutation technique.

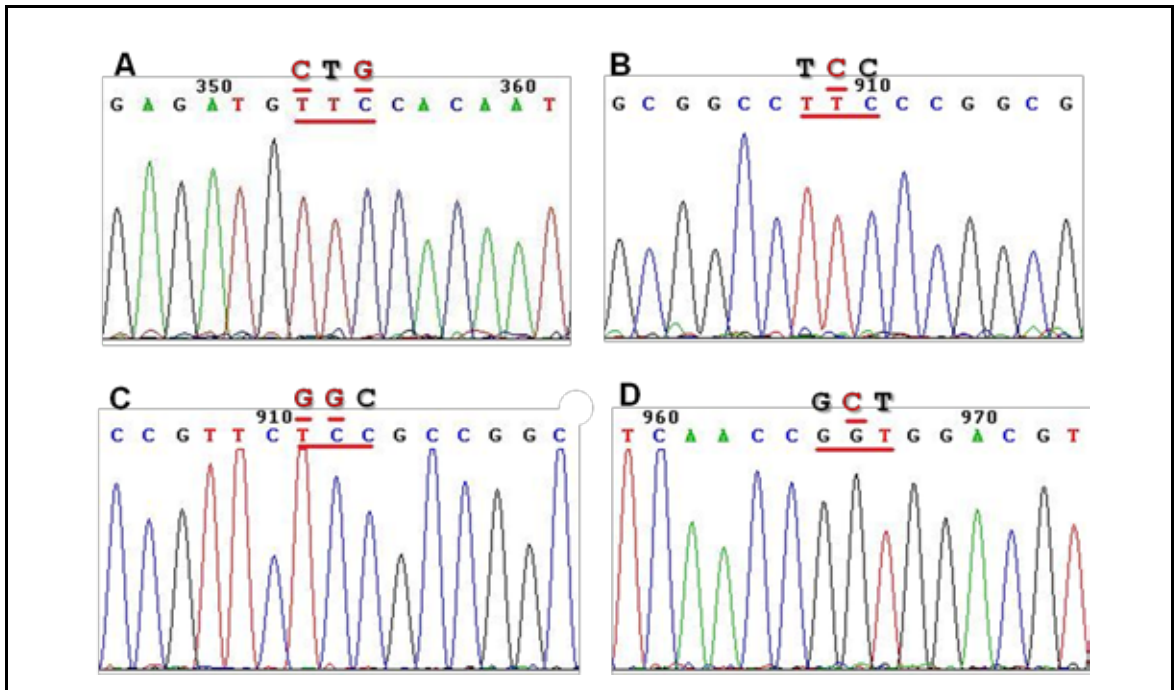


Figure 3.2: Sequencing results spectra for site-directed mutagenesis. Sequencing spectra were viewed with Chromas Lite software. Mutation-target codons are underlined in red. **A)** The L100F mutation introduces a phenylalanine by the substitution of C and G with T and C nucleotides, respectively, in the WT CTG codon coding for leucine. **B)** The S348F mutation introduced by substitution of C with T in WT TCC. **C)** The G388S mutation introduced by substitution of two Gs in WT GGC with T and C. **D)** The R391K mutation introduced by substitution of C in WT GCT with G to code for lysine.

3.3 Expression and Purification of Mutants

Plasmid DNA for mutant and WT CYP51B1 enzymes were transformed into the HMS174 (DE3) expression host and the respective isoforms were expressed and purified using a protocol of ion exchange, affinity and size exclusion chromatography (as described in section 2.2.5). Interestingly, although WT and mutant isoforms were grown and expressed in the same manner, the level of mutant enzyme expression varied considerably from one to another. For instance, the G388S and S348F mutants had to be expressed in the presence of the heme precursor δ -ala, otherwise almost negligible amounts of enzyme with its heme cofactor intact were detected by visually assessing the colour of the cell pellet after 20 h of expression at 23°C. Figure 3.3 shows the purification chromatogram of WT and G388S mutant enzymes using affinity Macro Prep Ceramic hydroxyapatite type 1 (HA) and the strong anion exchanger Resource-Q (RQ) columns on an AKTA purifier system.

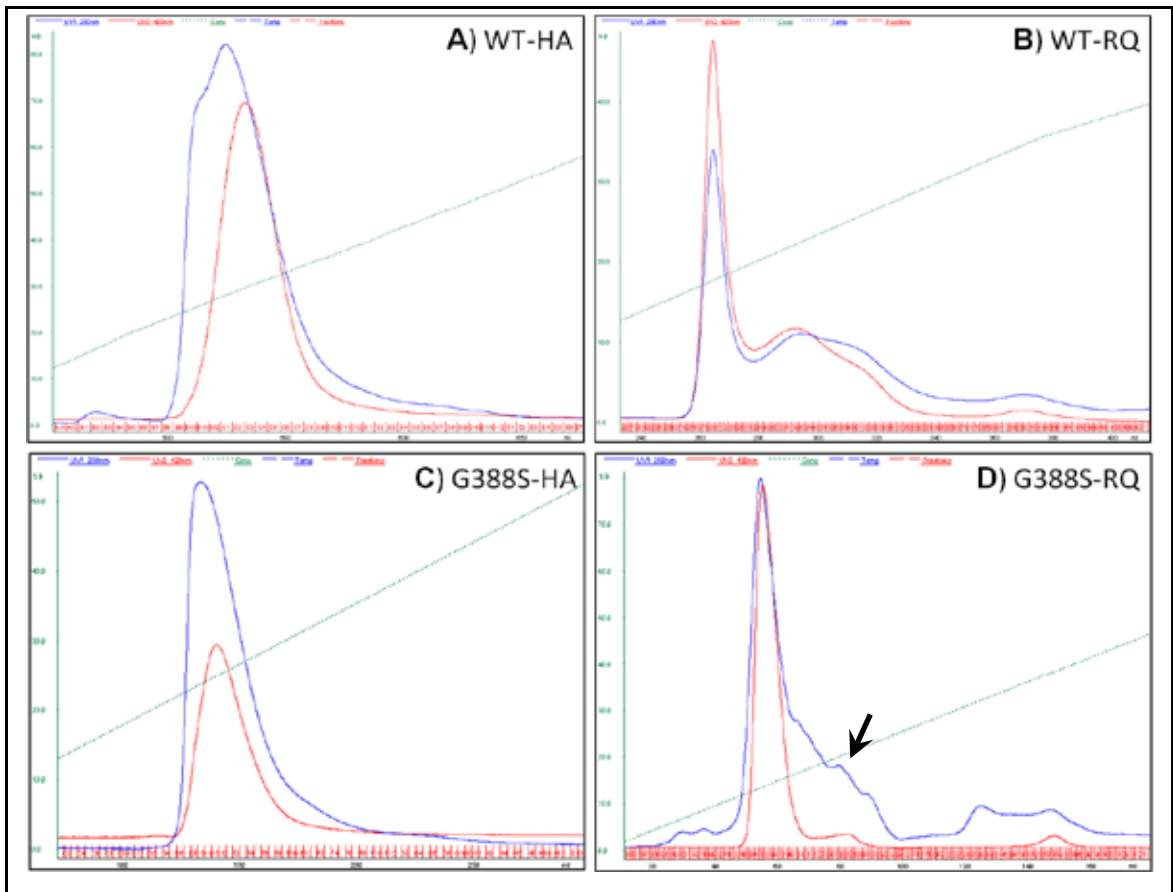


Figure 3.3: Purification chromatogram of CYP51B1 WT and G388S. Both isoforms were purified using an AKTA purifier system. Prior to ceramic-hydroxyapatite (HA) affinity purification, both proteins were partially purified on a DEAE-Sepharose weak anion exchanger column followed by a Q-Sepharose anion exchanger according to purification protocols in Chapter 2. Blue spectra represent 280 nm UV absorbance, red spectra represent 420 nm absorbance and green dotted lines represent percentage of high salt elution buffer in the system. **A)** WT elution chromatogram from 40 mL HA column at 25-30% 500 mM Kpi pH 6.5. **B)** WT elution chromatogram from 6 mL high loading Resource Q strong anion exchanger column at 15-20% 500 mM KCl, 25 mM Tris, 1 mM EDTA pH 7.2. **C)** G388S eluted in clean peak (red line) from the HA column at 20-25% 100 mM Kpi pH 6.5, comparable to WT. **D)** G388S eluted in a clean peak from Resource Q at 12-15% high salt buffer represented in a red line as the holoenzyme, while the broad blue line (arrow) following the sharp peak results from P450 apoprotein elution without its heme cofactor.

Comparing both protocols, WT and G388S showed similar purification and elution gradients on the HA column (the third step in the CYP51B1 purification protocol), with most of the enzymes eluting at 20-30% of high salt buffer, as shown by the red line for absorbance at 420 nm and the blue line for absorbance at 280 nm in Figure 3.3. However, purification of G388S on DEAE-Sepharose (weak anion exchanger) and Q-Sepharose (strong anion exchanger) columns, before the HA and RQ columns, showed the retention of heme on the column resin after elution, and even after 100% high salt buffer and NaOH were used to wash both columns. The loss of the G388S heme cofactor during purification reflected the effect this mutation had at such close proximity to the cysteine proximal ligand which, aided by other conserved amino acid residues in the vicinity, covalently anchors the heme iron of the macrocycle at the catalytic pocket. Conservation of this particular residue (G388) in CYP51 across phyla (and functionally similar P450 proteins) suggests that it is an essential residue, and the importance of the conserved glycine for catalysis/structural stability will be explored further on in this chapter. The loss of heme, reflecting its weak binding, during purification of the G388S mutant enzyme on the RQ column can be seen by the trail of a residual protein band (A280) in Figure 3.3 (D) with the parallel absence of the P450 band (A420) denoted by the black arrow. In comparison, the WT CYP51B1 purification on the RQ column shows that A280 and A420 bands elute together, consistent with the near-complete binding of heme in this enzyme. Thus, this column step can be used to separate holoenzyme and apoenzyme forms of CYP51B1, as evidenced for the G388S mutant.

Total P450 obtained after the purification process varied considerably for each CYP51B1 isoform. In contrast to the more weakly expressed G388S and S348F mutants, the expression of F89H, L100F and R391K mutants was at least double that of WT CYP51B1. From 25-30 L of culture, expression and non-tagged purification resulted in isolation of 200 mg of WT CYP51B1 from a typical preparation, compared to 330 mg from a typical preparation of F89H CYP51B1. Indeed, the true yield in the particular F89H preparation could have been ~550 mg were it not for loss of some protein due to selective retention of only fractions with highest heme content at the first purification step. In contrast to recovery of 470 mg of L100F from a typical preparation, just 6 mg of G388S was recovered in a particular preparation of this mutant CYP51B1. A typical preparation of the R391K mutant yielded 590 mg of protein. Apparently, changing arginine to lysine at position 391, although just three residues away from the strictly conserved 394 cysteine proximal ligand and three residues away from the most-mutation prone 388 position, does not confer problems in protein folding, heme incorporation and heterologous expression,

all of which were issues for the G388S mutant which was expressed as ~64% holoenzyme, demonstrated by comparing the Soret bands of both WT and G388S enzymes in Figure 3.4 (A). SDS-PAGE analysis showed all mutant enzymes and WT were relatively pure after at least four steps of purification. The Reinheitszahl (RZ) value from the ratio of A418/A280 reflects the purity of each enzyme and was a useful and convenient way to spectrally monitor hemoprotein purification before confirming its purity by the protein band(s) visible from SDS-PAGE analysis. This is shown by the Soret bands, RZ values and SDS-PAGE gels of WT and mutants in Figure 3.4.

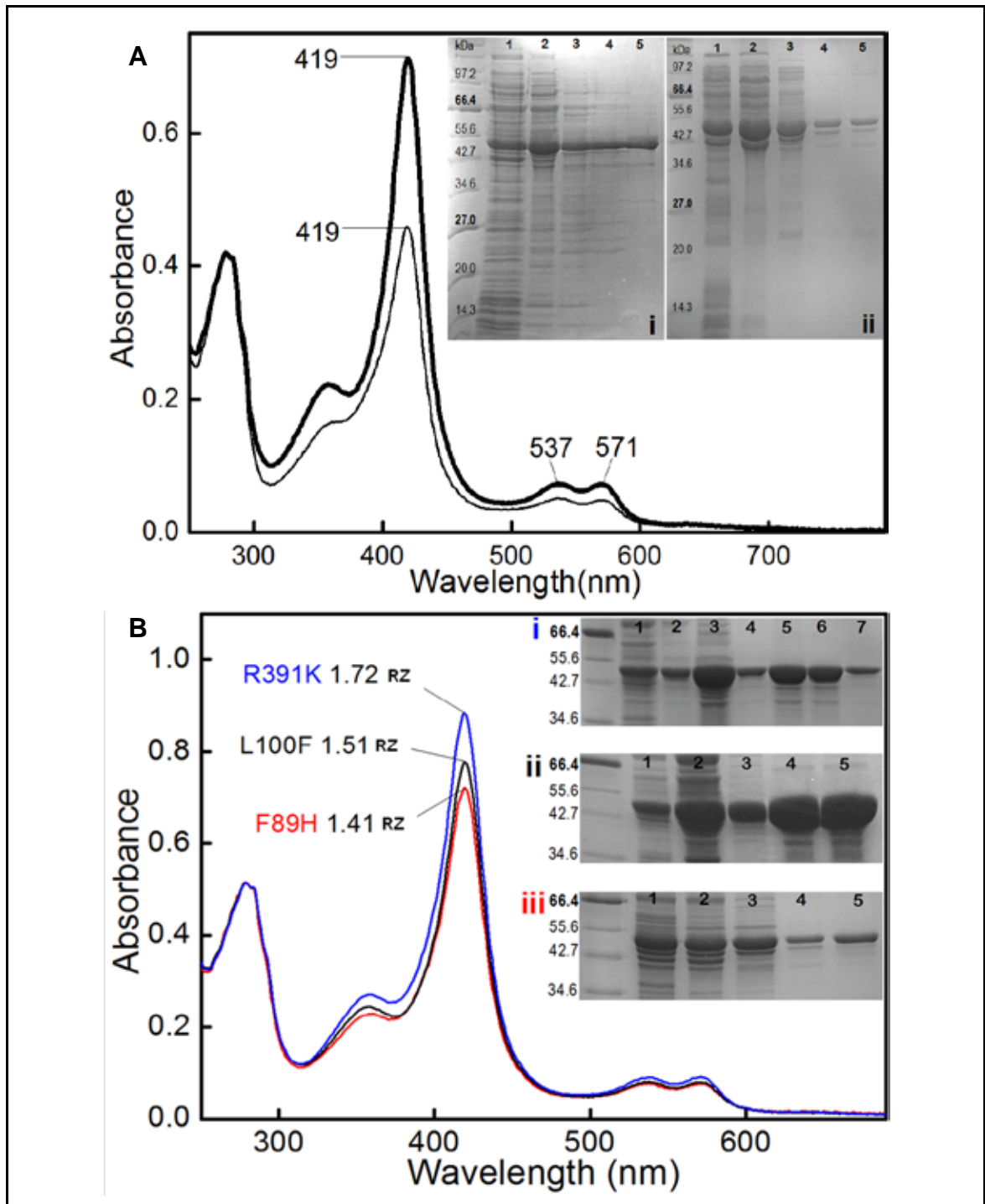


Figure 3.4: Expression of CYP51B1 WT and mutants. The Soret band of WT and G388S CYP51B1 enzymes are shown with their respective protein bands on 12% SDS-PAGE gels. **A)** WT (thick line) and G388S (thin line) shares the same Soret band and Q band wavelength maxima at 419 nm, 537 nm and 571 nm in their resting ferric-heme state. Intensity of the Soret band portrays the amount of P450 holoenzyme, while the 280 nm band portrays the total protein content. Using this ratio, WT has a 100% pure holoenzyme at 1.68 for the A419/A280 RZ value, while G388S has 64% pure holoenzyme with a 1.08 A419/A280 RZ value. SDS-PAGE gels **Ai** and **Aii** show the purity of WT and G388S, respectively, after every purification step, for the 50.8 kDa protein band. Lanes **1** – soluble cell lysate, **2** – post DEAE-Sepharose, **3** – post Q-Sepharose, **4** – post-ceramic hydroxyapatite, **5i** – post Resource Q and **5ii** – post hiprep QXL-Sepharose. **B)** Illustrates the Soret band spectra of R391K, L100F and F89H mutants with their respective SDS-PAGE gel insets **i**, **ii**, **iii** after every purification step.

Another mutant which had similar expression to G388S was the S348F mutant, which was expressed without a His-tag as inclusion bodies, and was not red in colour although δ -ala was added to aid heme cofactor production. In addition, the expression of a S348F His-tagged isoform in pET20b did not hugely improve its solubility, as shown by the immunoblot in Figure 3.5 (A) where the His-tagged signal came largely from the whole cell and insoluble fractions. The soluble fraction post-Ni-NTA affinity purification was transparent yellowish in colour when concentrated. This soluble S348F mutant enzyme had a Soret band at 409 nm and did not respond to the classical P450 CO-Fe(II) characterisation. It is believed that the soluble S348F mutant was expressed as soluble apoprotein corresponding to the overwhelming protein absorbance at 280 nm (Figure 3.5 C) and was catalytically dysfunctional. The small heme-like signal seen in Figure 3.5 (C) may result from a fraction of the S348F mutant with heme bound without cysteine-lation to the P450. Figure 3.5 (D) shows the structure of CYP51B1 and the position of the 348 phenylalanine mutant residue (red arrow) at the C-terminal domain of the enzyme. This mutation is situated at the junction of α -helical and β -sheet secondary structures which constitute the highly conserved cysteinyl loop residue region. The size of the purified S348F mutant at \sim 50.9 kDa on SDS-PAGE gels, Western-blot His-tagged analysis and MALDI protein identification confirmed that it was not expressed as a truncated version of the apoprotein without its C-terminal region (which would likely lead to heme loss) in either inclusion bodies or soluble forms. Substituting serine (a basic amino acid) with the bulkier aromatic phenylalanine (non-polar) at this position apparently was compatible with production of the S348F CYP51B1 enzyme, but resulted in failure to incorporate heme and in an insoluble, aggregated form of this enzyme.

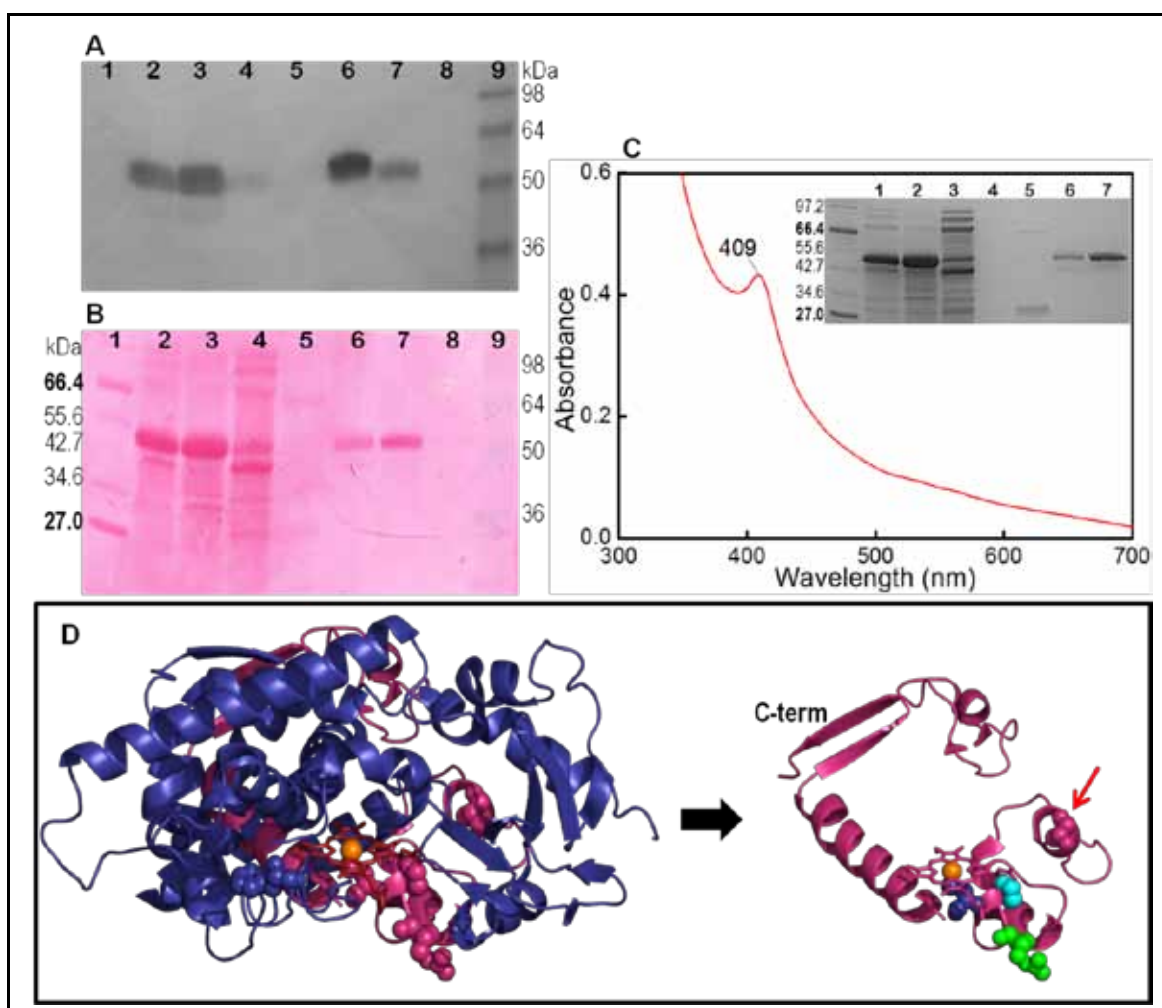


Figure 3.5: Immunoblot and Soret band spectrum for the S348F CYP51B1 mutant.

Panel **A** shows the immunoblot for His₆-tagged S348F CYP51B1 in Lanes 2, 3, 6 and 7 at different purification stages after 60 seconds exposure. Panel **B** illustrates the corresponding protein bands on the PVDF membrane post-Western Blot transfer after staining with Ponceau S in 7% acetic acid. Lane 1 – broad range molecular weight marker ladder, 2 – whole cell fraction, 3 – insoluble fraction, 4 – soluble fraction, 5 – after Ni-NTA elution with 40 mM imidazole, 6 – after elution with 50 mM imidazole, 7 – after elution with 70 mM imidazole, 8 – after elution with 80 mM imidazole and 9 – prestained SeeBlue® Plus2 protein ladder (Invitrogen). Panel **C** illustrates the apparent Soret band of the His₆-tagged S348F CYP51B1 mutant and the SDS-PAGE gel inset shows purification of S348F CYP51B1 by Ni-NTA chromatography. Lanes 1 – whole cells, 2 – insoluble fraction, 3 – soluble cell lysate, 4 – after Ni-NTA elution with 20 mM imidazole, 5 – after elution with 40 mM imidazole, 6 – after elution with 50 mM imidazole, 7 – after elution with 70 mM imidazole. Panel **D** illustrates the overall structure of CYP51B1 and the location of the 348 residue at the conserved C-terminal end of the enzyme (magenta) encompassing the cysteinyl loop, α L and β -sheet regions. The red arrow points to the S348 residue substituted with phenylalanine, which is located at the junction of the helix and sheet structures. The residues in coloured space-fill spheres in the right-hand structure of Panel **D** are C394 (dark blue) – the heme proximal ligand, C388 (cyan) and R391 (green).

3.4 The Effect of Drug Solvent DMSO Concentration on CYP51B1

Before beginning studies of ligand binding kinetics with CYP51B1 enzymes, the influence of solvent on WT and mutant CYP51B1 enzymes was assessed. In order to determine the maximum solvent concentration that is tolerated by CYP51B1 enzymes (and as a prelude to titration with azoles suspended in DMSO), a titration of DMSO solvent was carried out for each enzyme to determine the maximum percentage of DMSO tolerated before enzyme precipitation or heme loss. Figure 3.6 (A) shows that CYP51B1 WT started to precipitate out of solution when the DMSO concentration was more than 2% of the total solution. This result also correlated with that for the CYP51B1 G388S enzyme tolerance to DMSO concentration in solution (Figure 3.6 C). However, it was interesting to observe that CYP51B1 F89H was highly sensitive to increases of DMSO concentration. This was shown when F89H started precipitating out even at the beginning of the DMSO titration. These observations, however, may be correlated with the positions of the amino acid mutations in the CYP51B1 structure. Specifically, CYP51B1 F89H is a mutant enzyme with a histidine substitution at the B-C loop region on the molecule. The B-C loop region was well characterized to be the entry port of ligands into the catalytic site of CYP51B1 (Podust *et al.* 2001; Podust *et al.* 2007; Podust *et al.* 2004). The bulkier phenylalanine residue with an aromatic ring in the WT enzyme could result in a smaller opening or entry for ligands into the catalytic centre of the molecule, but with the azole-resistance-mimicking residue F89H substitution, the smaller histidine side chain may widen the entry port, suggesting a different B-C loop orientation and perhaps enabling easier access of DMSO to the heme site.

The different mutation location of CYP51B1 G388S, which is situated within the heme binding motif region near the catalytic site, away from both entry and exit ports of the enzyme structure, resulted in a similar solvent tolerance pattern to CYP51B1 WT (Figure 3.6 C). The perturbation of the heme cofactor of the enzyme (possibly causing heme loss) due to high DMSO content would definitely affect successful kinetic analysis of ligand binding with the highly water-insoluble azole drugs, and with the substrate analogue estriol. Both of these hydrophobic ligands have to be dissolved in a certain concentration of DMSO before any optical or stopped-flow analysis can be carried out. Keeping this in mind, in the following titration experiments where DMSO was added, it was ensured that less than 2% DMSO final volume was added to CYP51B1 enzyme solutions, and in unavoidable cases (where larger amounts were needed), appropriate corrections were made to the optical baseline to facilitate studies of ligand binding. Essentially, no Type I or Type II Soret shifts were observed on DMSO addition to the three enzymes, suggesting that

(other than precipitating the enzyme out of solution and other effects including heme dissociation and enzyme dilution, hereafter referred to as heme degradation), DMSO has no relevant substrate- or inhibitor-like binding effects on the iron of the heme catalytic centre. Other non-polar solvents, e.g. ethanol, have also been tried, but due to their lower boiling point, volatility and limited azole-solubility properties, DMSO was the solvent of choice in this study.

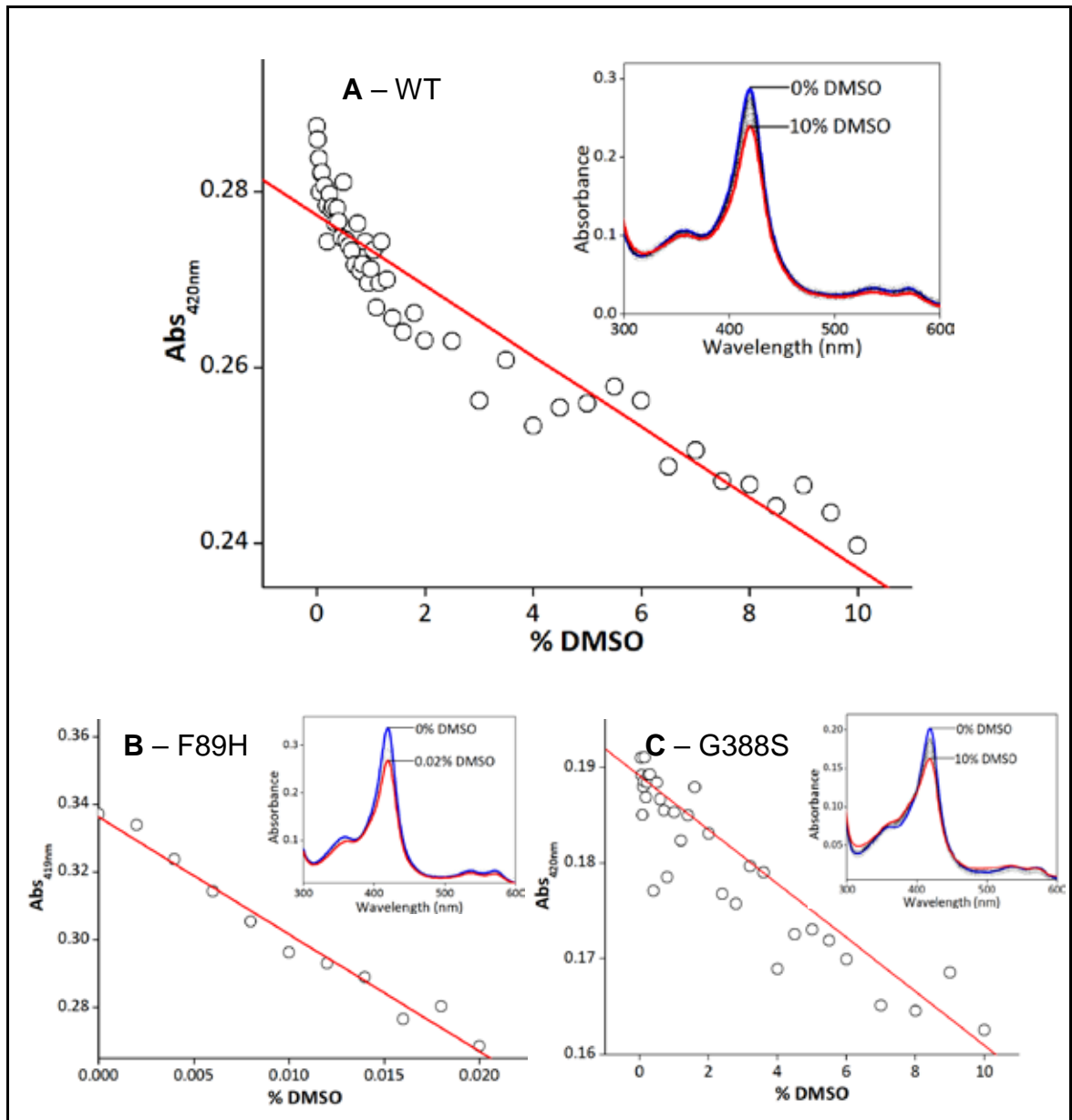


Figure 3.6: Heme perturbation profile of CYP51B1 titrated with DMSO. A) CYP51B1 WT has modest DMSO tolerance to a maximum 2% DMSO before the enzyme starts to precipitate to a significant extent such that optical studies are made difficult, B) CYP51B1 F89H has the least tolerance, with progressive enzyme degradation with as little as 0.005% DMSO, C) CYP51B1 G388S has similar DMSO tolerance to WT, with progressive loss of heme signal after ~4% DMSO. The blue line in each graph inset is the starting spectrum before DMSO titration and the red line is the end spectrum after titration at the respective DMSO concentrations.

3.5 Understanding the Molecular Mechanisms and Mode of Action/Physiological Roles of Mtb CYP51B1

3.5.1 Quantification of Heme *b* in WT CYP51B1 and Mutants

Previous work on heme quantification has been done on WT CYP51B1 and it was found to have an extinction coefficient at 419 nm of $134 \text{ mM}^{-1} \text{ cm}^{-1}$ at the oxidised Soret peak (McLean *et al.* 2006c). Using this method (i.e. using characteristic absorption spectrum differences between oxidized and reduced forms of the hemochrome formed by replacing the axial Cys/water ligands of the heme with pyridine), the resting ferric enzyme was firstly oxidised by a pyridine-ferricyanide solution and then reduced with dithionite to obtain the reduced ferrous enzyme, as illustrated in Figure 3.7 for the R391K mutant enzyme. The heme content of each CYP51B1 mutant, except for G388S, was systematically determined using this method, and each displayed similar spectral trends for the pyridine complex. The heme extinction coefficient of the CYP51B1 isoforms were calculated at the Soret band at 419 nm, ϵ_{419} . Interestingly, WT had an ϵ_{419} of $96.1 \pm 2.0 \text{ mM}^{-1} \text{ cm}^{-1}$, and an average of five experiments were inconsistent with previously published work (McLean *et al.* 2006c). Almost similar ϵ_{419} values were observed for the mutants with $92.9 \pm 1.0 \text{ mM}^{-1} \text{ cm}^{-1}$ for F89H, $93.8 \pm 1.0 \text{ mM}^{-1} \text{ cm}^{-1}$ for L100F and $90.7 \pm 2.0 \text{ mM}^{-1} \text{ cm}^{-1}$ for R391K. At least two experiments were done in each case to obtain these values. The difference in WT ϵ_{419} from previously published values using this method might call into question the reliability and convenience of this technique in quantifying heme *b* content in hemoproteins. Ideally, this method should be complemented with other techniques, e.g. employing reverse phase HPLC or radioactive heme labelling assays to determine heme quantity (Sinclair *et al.* 2001). Alternatively, an EPR analysis using copper (II) as the metal standard compared to P450 ferric-heme EPR spectra could be used. This would be done by spectral integration and calculating the area within the integrated spectrum to obtain the ferric heme concentration. In this case, a rough estimation of heme *b* content was done to determine if the mutations influenced heme content/absorption coefficient in the hemoproteins. Essentially, the results obtained for WT and mutants were consistent with the RZ ratio (A_{420}/A_{280}) of pure holoenzymes (Figure 3.4). Heme *b* concentrations in the mutants studied here were subsequently quantified using the established extinction coefficient, $\epsilon_{419} = 134 \text{ mM}^{-1} \text{ cm}^{-1}$ for WT CYP51B1, reported by Mclean *et al.* in a comprehensive CYP51B1 biophysical characterisation study, and to provide consistency with previous data (McLean *et al.* 2006c).

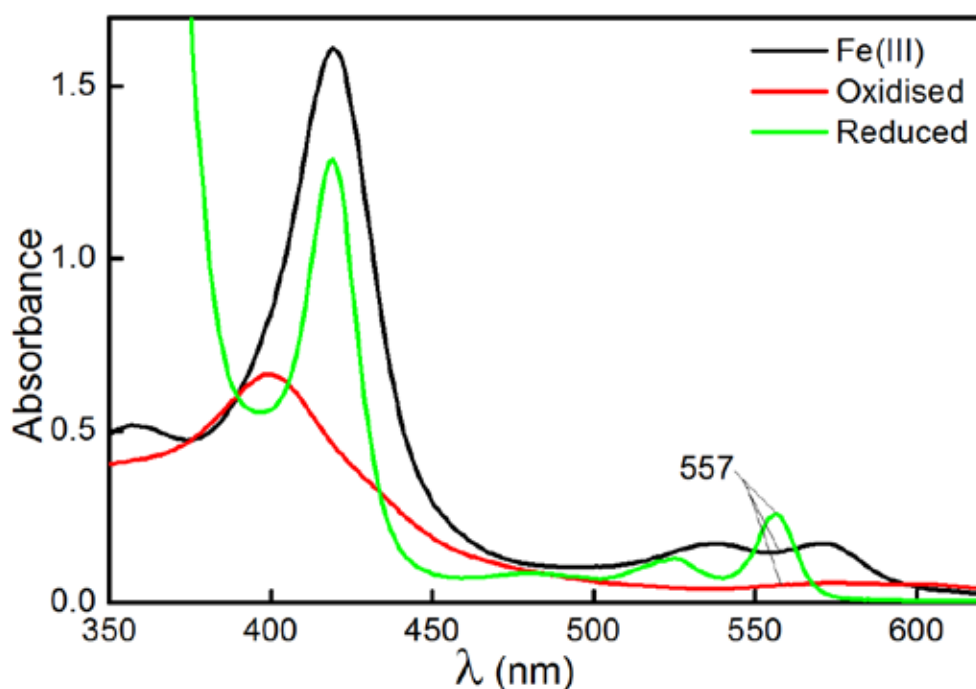


Figure 3.7: Heme *b* quantification by the pyridine hemochromogen technique. The Resting ferric heme enzyme (black spectrum, R391K CYP51B1) was oxidised by the same volume of the pyridine-ferricyanide-hydroxide solution (red spectrum, see section 2.2.9 for solution composition) and was then reduced with a few grains of sodium dithionite (green spectrum) until no changes were observed at the Q-band region (557 nm). Using the established extinction coefficient for the 557 nm heme signature of $23.98 \text{ mM}^{-1} \text{ cm}^{-1}$, the heme *b* content and extinction coefficient at 419 nm was calculated according to the Beer-Lambert law, which was $90.7 \pm 2.0 \text{ mM}^{-1} \text{ cm}^{-1}$ for R391K CYP51B1.

3.5.2 CYP51B1 Heme-Coordination by NO and CO

Carbon monoxide (CO) and nitric oxide (NO) binding provides two signature characterization methods to confirm whether a protein is a cytochrome P450. In particular, the Fe(II)-CO complex gives a hallmark absorption close to 450 nm (hence P450) that is indicative of the proximal coordination of the heme iron by a cysteine thiolate. As observed previously, CYP51B1 is unstable in this form, and there is a ‘collapse’ to a P420 form (Soret at close to 420 nm) that originates from protonation of the thiolate. The NO complex also gives a quite diagnostic Soret shift for P450s to ~ 435 nm in the ferric form of the hemoprotein, and with substantial changes in intensity of the Q-band features between 500-600 nm (McLean *et al.* 2006a; McLean *et al.* 2006c).

3.5.2.1 NO-Ferric-Heme Coordination of CYP51B1

Nitric oxide is a well known, tight binding diatomic ligand for P450s, often used to characterize these enzymes, and frequently alongside other molecules such as cyanide (CN⁻)

and CO. NO is also recognised as an important intracellular signalling molecule (Ouellet *et al.* 2009). In humans, there exists a NO-dependent Mtb inhibitory system governed by CD4+ T cells (Cooper 2009), and NO is also released by Mtb infected macrophages as an initial barrier to TB infection. NO targets P450s, other hemoproteins and iron-sulphur cluster proteins, inhibiting them (and other enzymes) and rendering Mtb infection latent (Long *et al.* 1999). At the same time, nitrate, a product of metabolised NO by nitrite reductase activity in the host and the pathogen, aids Mtb's survival in its dormant state during O₂ depletion (Sohaskey 2008). Quantitative studies of NO as an inhibitory ligand of heme iron in Mtb P450s (CYP51B1, CYP125, CYP130 and CYP142) have been carried out on both the ferric and ferrous forms, with CYP130 and CYP51B1 exhibiting essentially irreversible inhibition when their ferrous-NO complexes failed to dissociate in the presence of O₂, while CYP125 and CYP142 were more resilient and demonstrated reversible NO dissociation to regenerate their ferric-heme states (Ouellet *et al.* 2009). In view of these data and as a means of initial characterisation, CYP51B1 azole-resistant mutants were bubbled with NO in their ferric enzyme forms to monitor spectral changes at the Soret band and Q-bands when their nitrosyl complexes formed, and later dissociated back to the water-bound hexa-coordinate low spin ferric-heme resting state as shown in Figure 3.8. WT and mutant ferric-heme nitrosyl complexes were characterized by Soret, α and β bands located at 433-435 nm, 572-574 nm and 541 nm, respectively, which were comparable to values reported by Ouellet *et al.* (2009) for the WT CYP51B1 ferric-NO complex in anaerobic conditions. All enzymes demonstrated a type II Soret shift upon binding to NO, which (for WT, L100F and R391K) collapsed back (indicated by red arrows) to the original LS ferric-heme state over 30 min upon dissociation of NO and its depletion by reaction with oxygen. However, over-bubbling with NO gas in an aerobic environment resulted in acidification of the enzyme mixture by the formation of excess nitrous acid, and also resulted in long-lived ferric-NO complexes for the F89H and G388S mutants (Figure 3.8 **B, D**). It was likely that the persistent ferric-NO complex in both F89H and G388S was a consequence of higher concentrations of NO, and this should eventually collapse in air over a longer incubation time.

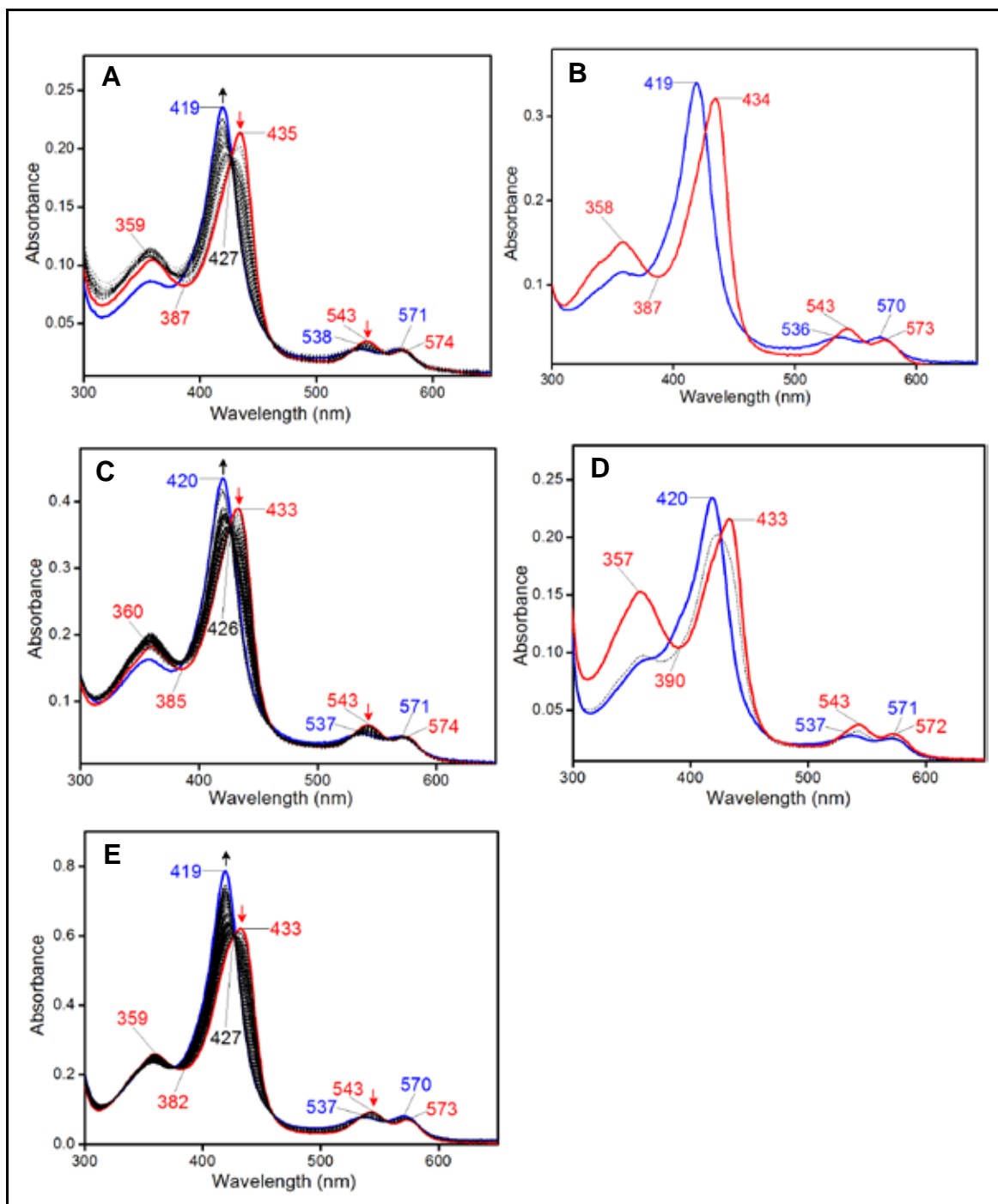


Figure 3.8: Spectral characterisation of CYP51B1 ferric-heme nitrosyl complexes.

The graphs reveal that the oxidized CYP51B1 mutant enzymes (1.7–5.9 μM) have features similar to WT (1.7 μM), with Soret maxima at 418–420 nm and an isosbestic point at 426–427 nm in all cases upon binding to NO. Spectra are consistent with cysteinate as the proximal ligand in all cases. The mutants and WT enzymes form NO complexes with the Soret band shifted to **A**) 435 nm (WT), **B**) 435 nm (F89H), **C**) 434 nm (G388S), **D**) 433 nm (L100F) and **E**) 433 nm (R391K), and are reversible to form ferric-heme resting enzyme over 30 minutes under aerobic conditions as shown by the dotted lines. For F89H (**B**) and G388S (**D**) mutants, the reversible dissociation of NO to form ferric-heme species was not observed over the same time scale following excessive bubbling with NO gas, which also resulted in production of nitrous acid. All reactions were done at 23 °C in 100 mM Kpi buffer, pH 7.5. In **A**, **C** and **E**, spectra for the NO complex are shown in red, and those for the reoxidized enzyme in blue. Intermediate spectra are shown as black dotted lines. In **B** and **D**, the starting (oxidized) spectrum is in blue, and the NO complex formed on addition of excess NO gas is in red. In each spectrum, maxima and minima are indicated in colour code.

3.5.2.2 CO-Ferrous-Heme Coordination of CYP51B1

The ferrous-CO (Fe(II)-CO) adduct was formed when the reduced CYP51B1 was bubbled with CO, as shown in Figure 3.9 in an anaerobic atmosphere. After reduction with a reducing agent, in this case sodium dithionite, the formation and then the kinetic collapse of the CYP51B1 P450 complex (when bubbled with CO gas) can be followed, and the later formation of P420 reports on the protonation of the cysteinate ligand to the heme iron that occurs in the ferrous form (McLean *et al.* 2006c). The formation of an Fe(II)-CO adduct of Mtb CYP51B1 was recorded immediately following bubbling of ferrous CYP51B1 with CO gas (spectrum with highest absorption at ~450 nm) and subsequent spectra were collected at regular intervals over the next 20-40 min, demonstrating the progressive collapse of the P450 form to the P420 species (spectrum with highest absorption at 420 nm). In Figure 3.9, arrows indicate directions of absorption change with time at these wavelengths. The P420 species (red spectra) clearly has a substantially larger Soret molar absorption coefficient than does the ferric form (blue spectra), where the Soret is the major heme absorption band. Mutants situated on the SRS 1 'hinge' region, the B-C loop (F89H) and α C (L100F), demonstrated slower thiolate protonation compared to WT. The rate constant for WT P450-to-P420 collapse was $0.31 \pm 0.02 \text{ min}^{-1}$, while those for F89H and L100F were $0.17 \pm 0.01 \text{ min}^{-1}$ and $0.26 \pm 0.03 \text{ min}^{-1}$, respectively. The rate constants for WT and L100F CYP51B1 enzymes are consistent with the one reported for WT CYP51B1 at 0.246 min^{-1} at pH 7.0 (McLean *et al.* 2006c). Inherently, a distinguishing characteristic of CYP51B1 lies in its formation of an unstable ferrous-thiolate (P450 species) in the presence of CO, which more readily collapses to its P420 form by comparison with other Mtb P450s (McLean *et al.* 2007). Figure 3.9 demonstrates the transient formation and then collapse of the unstable P450 species (449 nm) to the stable alternate P420 ferrous-thiol species (422 nm) in the absolute spectra in the panels on the left, with the corresponding difference spectra on the right, collected over 30 min. WT, F89H and L100F enzymes exhibited an isosbestic point at 434 nm throughout the transition. Interestingly, one would expect the mutant rates of thiolate protonation to be comparable to WT, as these mutations are not situated anywhere near the cysteine proximal ligand which could directly affect proton transfer. Even faster rates of thiolate protonation might have been predicted by the introduction of these mutations at the substrate entry hinge region, where the entry channel to the enzyme active might be expected to widen, as previously discussed for the F89H mutant with its increased sensitivity to DMSO solvent compared to WT CYP51B1, or for the G388S mutant. Evidently, these F89H and L100F mutations, even though they are distant from the heme motif region, have a significant impact on this important

protonation reaction which can control the catalytic competence of the enzyme. This suggests that dynamic regions of CYP51B1 can directly influence important biochemical processes which happen buried elsewhere within the molecule, and that interactions between these separate regions of the protein can have a 'domino effect' throughout the molecule, apparently influencing rates of heme thiolate protonation. This 'chain reaction' is discussed further, and complemented by data for solved mutant CYP51B1 crystal structures, in the next chapter.

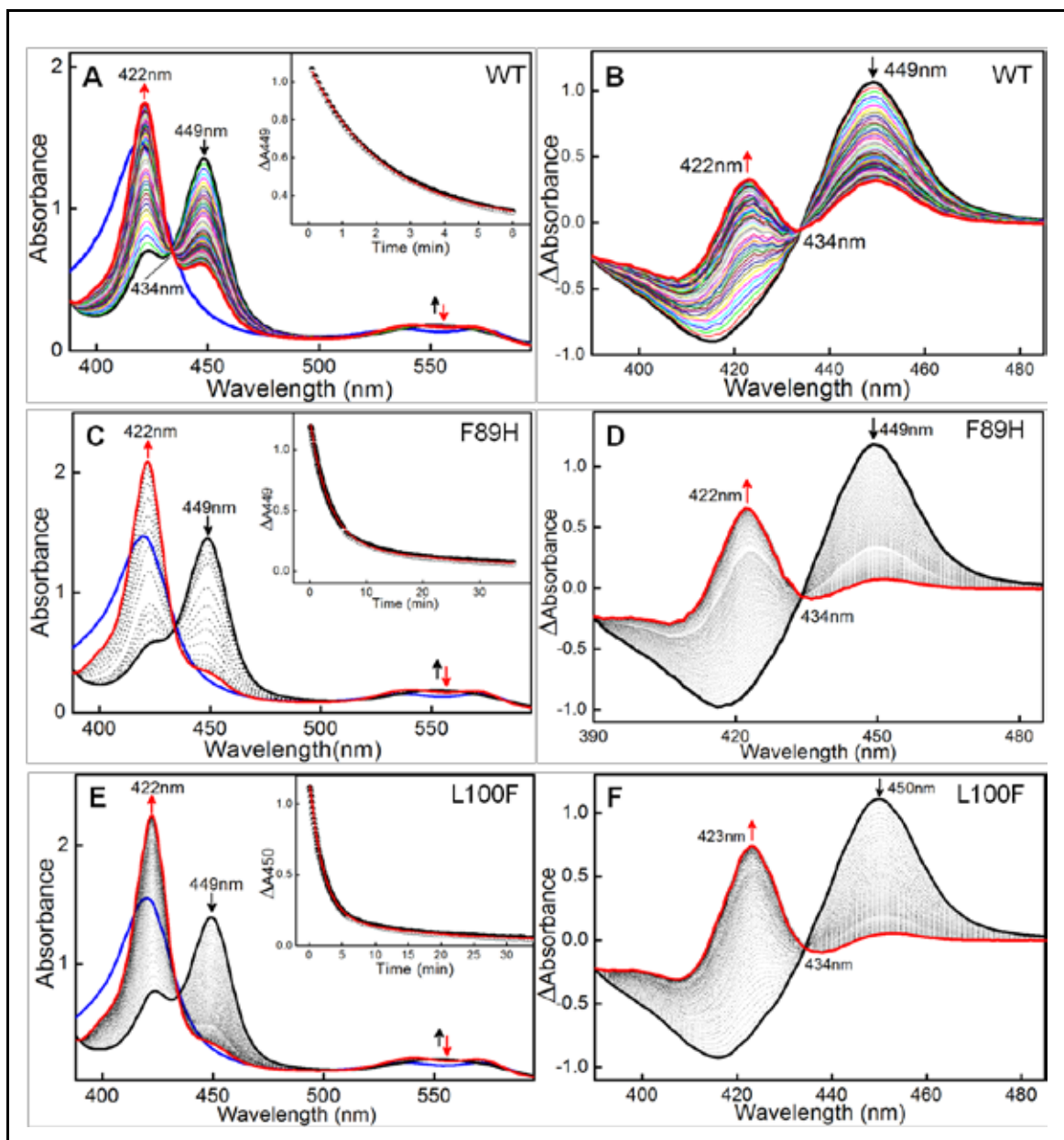


Figure 3.9: Spectral properties of Fe(II)-CO adduct complexes for CYP51B1 enzymes with B-C loop mutations. Graphs show accumulation, then collapse, of the Fe(II)-CO complex in the cases of WT, F89H and L100F enzymes (11-12 μM of CYP51B1). This is due to heme thiolate protonation that occurs readily in the ferrous enzyme. The shift is from the P450 species towards the P420 species. The blue lines represent the spectra for the thiolate ferric-heme forms, which upon reduction and CO coordination, form CO-ferrous thiolate adducts at ~ 450 nm (P450 form, black lines) which then collapse (illustrated by dotted black lines) to the stable CO-ferrous thiol adducts at ~ 420 nm (P420 form, red lines). **A)** WT P450-P420 formation with coloured lines representing the transition between the two species. The inset shows a plot of P450 collapse (ΔA_{449} nm data), derived from the difference spectra (**B**). Spectra in **C** and **E** are the P450-P420 transition absolute spectra for the F89H and L100F CYP51B1 mutants, respectively, with their related difference spectra in panels **D** and **F**. Both these mutants demonstrated slower thiolate protonation compared to WT ($0.31 \pm 0.02 \text{ min}^{-1}$) with $0.17 \pm 0.01 \text{ min}^{-1}$ for F89H (data fitted using a single exponential function) and $0.26 \pm 0.03 \text{ min}^{-1}$ (single exponential fit) for L100F CYP51B1. Fits are indicated in red in the insets in panels **A**, **C** and **E**. Peak absorption (and difference absorption) features and directions of absorbance change occurring over time are indicated with arrows.

The mutants at the cysteinyl loop region, G388S and R391K, both demonstrated Fe(II)-CO adduct formation and the collapse of their P450 species to the stable P420 species over several minutes. This is shown in Figure 3.10, with the arrows showing the direction of the P450 species (447 nm – G388S and 449 nm – R391K) collapse, with the concomitant increase in the P420 species (421 nm – G388S and 422 nm – R391K). Most interesting, however, was that both these mutants demonstrated faster thiolate protonation than WT CYP51B1 or the SRS1 hinge mutants, with G388S at $0.88 \pm 0.01 \text{ min}^{-1}$ and R391K at $0.54 \pm 0.02 \text{ min}^{-1}$ (derived from single exponential fits to the data). The accessibility of the cysteinate axial ligand to protonation is possibly enhanced in both these cysteinyl loop CYP51B1 mutants, which are only 6 (S388) and 3 (K391) residues away from the C394 proximal ligand. Figure 3.10 (E) demonstrates how the apparent rates of thiolate protonation were derived by fitting ΔA_{450} data from the difference spectra to either a single exponential equation (blue line) or a double exponential equation (red line) in the case of the WT CYP51B1. The rate constants reported are from single exponential fits, since data for the thiolate to thiol transition event underlying the P450/P420 switch fit best to a single exponential function for data collected over the first ~8 min of the reactions. In the case of R391K CYP51B1, over prolonged data collection times (>8 min) the ΔA_{450} data were fitted better using a double exponential function. This may suggest that a slow molecular rearrangement reaction occurs for this enzyme (and possibly also for other CYP51B1s), and that this also influences the P450 collapse. Possibly, this is related to conformational equilibria in the enzyme(s) and the kinetics of switches between conformational states.

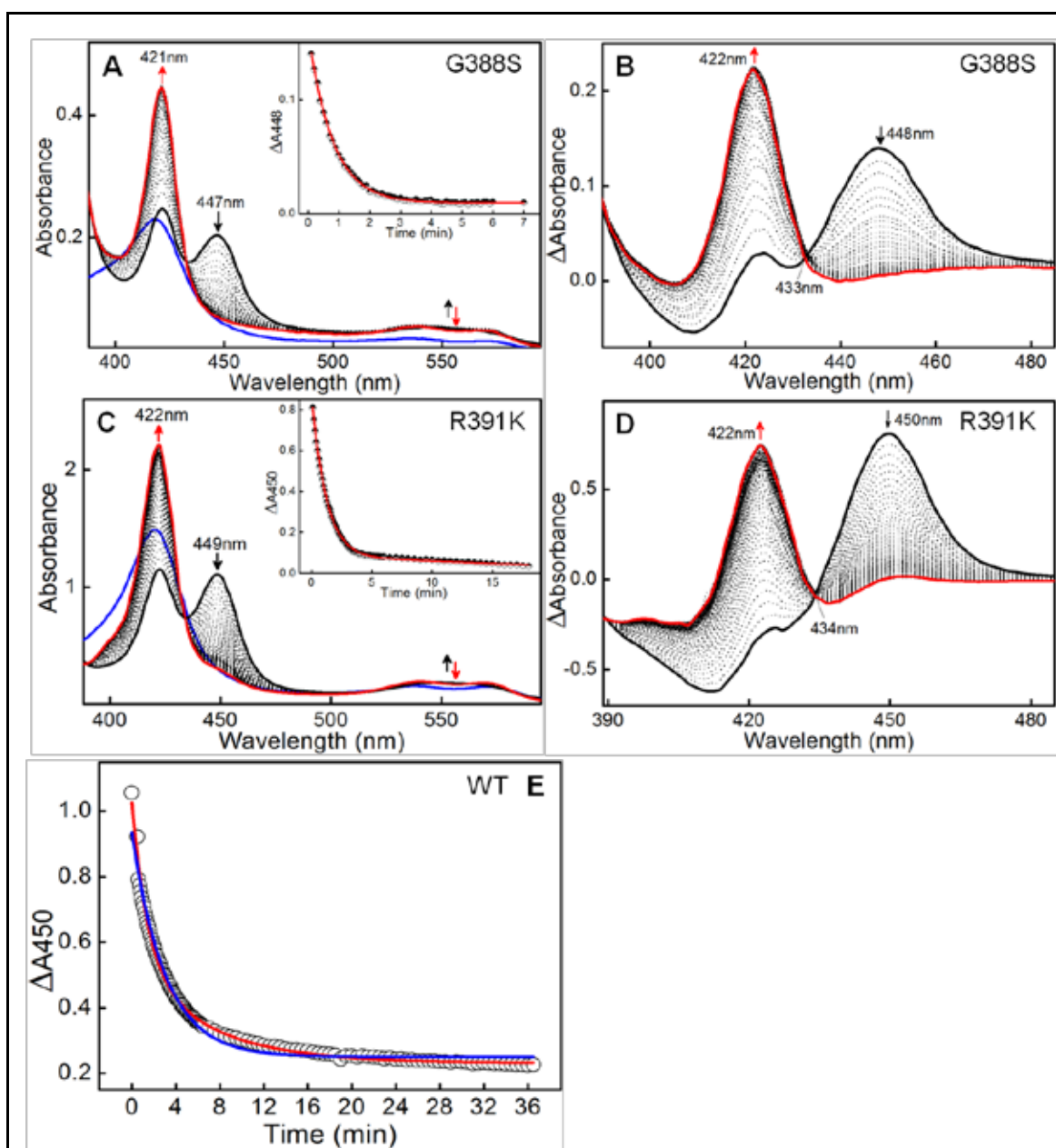


Figure 3.10: Fe(II)-CO adduct complexes and their conversions in CYP51B1 cysteinyl loop mutants. A) The Fe(II)-CO complex is less stable in the G388S CYP51B1 than in the WT enzyme, where the mutation is located in the immediate vicinity of the heme cofactor. Heme is more weakly bound in this mutant, with purified G388S P450 containing ~64% holoenzyme. Thiolate in the G388S Fe(II)-CO adduct was protonated more rapidly than in WT CYP51B1 and the other mutants, with a rate constant (k) of $0.88 \pm 0.01 \text{ min}^{-1}$ (panel A inset). In panel (C), the R391K mutant also demonstrated a relatively fast rate of P450 species collapse (data fitted better using double exponential (DE) function in Inset C). From single exponential (SE) fitting the rate for R391K P450 collapse was $k = 0.54 \pm 0.02 \text{ min}^{-1}$. B and D illustrate the P420 formation at the expense of P450 collapse for the G388S and R391K mutants, respectively, with a clear isosbestic point at 433-434 nm describing the clean and near-complete transition of one species to the other. Panel E shows the fitting data of the ΔA_{450} data for the WT CYP51B1, either using a single exponential equation (blue line) or a double exponential equation (red line) over a time period of ~36 min. These data plots show that the fitting was superior using the DE function over the longer time period ($k_1 = 0.482 \pm 0.030 \text{ min}^{-1}$, $k_2 = 0.101 \pm 0.008 \text{ min}^{-1}$ compared to SE $k = 0.310 \pm 0.020 \text{ min}^{-1}$).

3.5.3 Formation of CO-Free Ferrous-Thiol Species of CYP51B1

In the absence of added CO, none of the CYP51B1 enzymes (WT, or those with mutations at the B-C loop region (F89H and L100F) and the heme motif region (G388S and R391K)), form any notable amount of the Fe(II)-CO complex, but instead can be reduced to the ferrous CO-free state (Fe(II)), which can react with dioxygen (O₂) and then disproportionate into Fe(III) and superoxide. However, under anaerobic conditions the Fe(II) form is stabilized and this enables the study of its properties. Previous work has shown that the Fe(II) form of WT CYP51B1 undergoes first a blue shift of the Soret band (to ~414 nm), followed by a red shift (to ~425 nm), indicative of formation of a cysteine thiolate-bound form which collapses into a thiol-bound state, as also seen for the CO complex (McLean *et al.* 2006c). To measure the P450/P420-type transitions for CO-free CYP51B1 enzymes, a dithionite-reduced stopped-flow kinetic (millisecond timescale) experiment was performed using a photodiode array (PDA) apparatus, and the transition rates derived by fitting the absorbance change data using global kinetic software. WT and mutant CYP51B1 enzymes were prepared in an oxygen-free atmosphere and the chemical reductant sodium dithionite was freshly prepared at 10 and 1.0 mM concentrations in degassed assay buffer. Upon reduction of each enzyme, 1600 spectra were recorded over 2100 seconds using different pH ranges for WT CYP51B1 and different dithionite concentrations. The rate constants for the ferric-heme thiolate (**A**) to ferrous-heme thiolate (**B**) transition, and for the **B** to ferrous-heme thiol (**C**) transition, were calculated by global spectral analysis and are presented in Table 3.2 below.

Table 3.2: Rate constants for CYP51B1 ferrous thiolate to thiol conversion upon reduction with dithionite.

pH	CYP51B1	Fe(III) to Fe(II) thiolate (s ⁻¹) A → B	Fe(II) thiolate to Fe(II) thiol (s ⁻¹) B → C
6.5	WT	0.431 ± 0.001	0.00502 ± 0.00001
7.5	WT	0.153 ± 0.0008	0.00105 ± 0.00001
8.5	WT	0.055 ± 0.0001	0.00587 ± 0.00002
7.5	WT	0.0521 ± 0.0001	0.00104 ± 0.00002
	F89H	0.0673 ± 0.0002	0.00104 ± 0.00001
	L100F	0.0534 ± 0.0003	0.00039 ± 0.00001
	G388S	0.241 ± 0.0005	0.00978 ± 0.00002
	R391K	0.0453 ± 0.0001	0.00044 ± 0.00001
	R391K	0.118 ± 0.0004	0.00068 ± 0.00001

Note: All enzymes were reduced with 0.5 mM dithionite except for those in bold black text which were reduced with 5 mM dithionite.

The rate constants for the **A** to **B** reduction for WT CYP51B1 decreased as the pH increased. **A** to **B** reduction was also proportional to the concentration of dithionite, $S_2O_4^{2-}$, which exist in equilibrium with its reducing SO_2^- anion monomer (Hintz and Peterson 1980), i.e. slower ferric reduction to ferrous (0.0521 s^{-1}) with 0.5 mM dithionite compared to faster (0.153 s^{-1}) reduction with 5 mM dithionite. Differences were observed in the apparent rate constants for protonation of the WT P450 thiolate species **B** to form the stable but catalytically inactive P420 thiol species **C**. The apparent rate constants for heme thiolate protonation at pH 6.5 (0.00502 s^{-1}) and 8.5 (0.00587 s^{-1}) were ~ 5 fold greater than that observed at a more physiologically relevant pH 7.5 (0.00105 s^{-1}). The intracellular pH of Mtb is maintained close to 7.0 (Zhang *et al.* 1999).

The rate constant for protonation of the cysteinate proximal ligand in WT CYP51B1 was also not influenced significantly by the concentration of the dithionite anion monomer, as demonstrated by the comparable WT P450 to P420 conversion rate constants of 0.00105 s^{-1} and 0.00104 s^{-1} at pH 7.5 for 5 mM and 0.5 mM dithionite, respectively. These slower rate constants reflecting ferrous-cysteinate protonation were comparable to those determined in similar studies previously done on WT CYP51B1 with NADPH (and redox partners) as the electron donor, at $\sim 0.0013\text{ s}^{-1}$ in the absence of CO (Dunford *et al.* 2007). It is understood that the active form of the enzyme, ready to undergo catalysis upon substrate binding and displacement of its weak 6th distal water ligand, exists in the penta-coordinated HS ferrous-cysteinate ligated form at step (ii) of the P450 catalytic cycle (Figure 1.5 A). In aerobic environments this ferrous-penta-coordinated HS species will complex with dioxygen to form ferrous-dioxygen or ferric-superoxide complexes (in equilibrium, step iii), the last stable intermediates in the P450 cycle (Conner *et al.* 2011). In the set of experiments performed here, the oxy complex could not form, as they were carried out in an anaerobic atmosphere. The slow cysteinate protonation of CYP51B1, demonstrated here, should result in inactivation of the enzyme as a sterol demethylase. However, previous studies have shown that the binding of a substrate analogue (estriol) substantially decreases the rate of heme thiolate protonation, and also that thiol deprotonation occurs on reoxidation of the enzyme (i.e. that inactivation is reversible) (McLean *et al.* 2006c). The overall lower **B** to **C** rate constants compared to **A** to **B** rate constants also provide an extended window for catalysis if atmospheric oxygen were available to a substrate bound, ferrous CYP51B1 enzyme, since electron transfer and catalysis would be expected to occur more rapidly than the reversible catalytic inactivation to the P420 form by ferrous-cysteinate protonation (McLean *et al.* 2006c). Intracellularly, this would suggest that the cysteinate protonation phenomenon might only happen in the

absence of substrates for catalysis, and in situations in which electrons can be delivered to the substrate-free enzyme from pyridine nucleotide coenzyme(s) (NAD[P]H) via redox partner enzymes.

Azole-resistant mutants were also subjected to the same reduction experiments at pH 7.5. While rate constants determined still reflected (i) the reduction of ferric to ferrous enzyme and (ii) thiolate protonation from the ferrous-thiolate to the ferrous-thiol species, spectral changes accompanying these events in the L100F mutant were subtly different from WT and the other mutants, as shown in Figure 3.11 (D). In fluconazole-resistant *C. albicans* the L100 residue differs from the others studied here because it is naturally mutated from a phenylalanine to a leucine to afford resistance. In the CYP51B1 enzyme studied here, a leucine is already present in the WT sequence, and the reciprocal mutation was made (L100F) to provide comparison with the WT CYP51B1 (which already has the “fluconazole resistant” sequence by comparison with the *C. albicans* enzyme). Thus, this “reverse” mutation with respect to the *C. albicans* CYP51 was made to explore the influence that a mutation in this position would have in CYP51B1 in terms of its effects on its biochemical interactions with inhibitor ligands, and specifically the azole drugs which are explored in detail further on in this chapter.

The global fitting for the absorption change data for CYP51B1 L100F (see panel D in Figure 3.11) shows the intermediate species (red spectrum) as one with a Soret peak at 421 nm, and split alpha/beta band features. These features suggest that this intermediate form (reflecting the transition of A to B in L100F) has both ferrous heme thiolate and ferrous heme thiol character. This is different from the WT and G388S mutant (panel B and C), where the intermediate form has its Soret peak at 414/412 nm, and appears mainly thiolate in character. This could, for instance, suggest that a considerable proportion of the L100F ferric heme iron is already in the thiol form. The relatively slow rate constant for the B to C transition thus could reflect the residual ferrous thiolate portion of the enzyme converting to ferrous thiol. The apparent rate constant for F89H CYP51B1 heme iron reduction was comparable to that for WT CYP51B1, and the slightly faster F89H reduction of ferric-cysteinate to ferrous-cysteinate at 0.0673 s^{-1} , compared to WT at 0.0521 s^{-1} , perhaps reflects that this mutation at the B-C loop hinge region facilitated the entry and diffusion of the reducing agent towards the F89H ferric-heme centre.

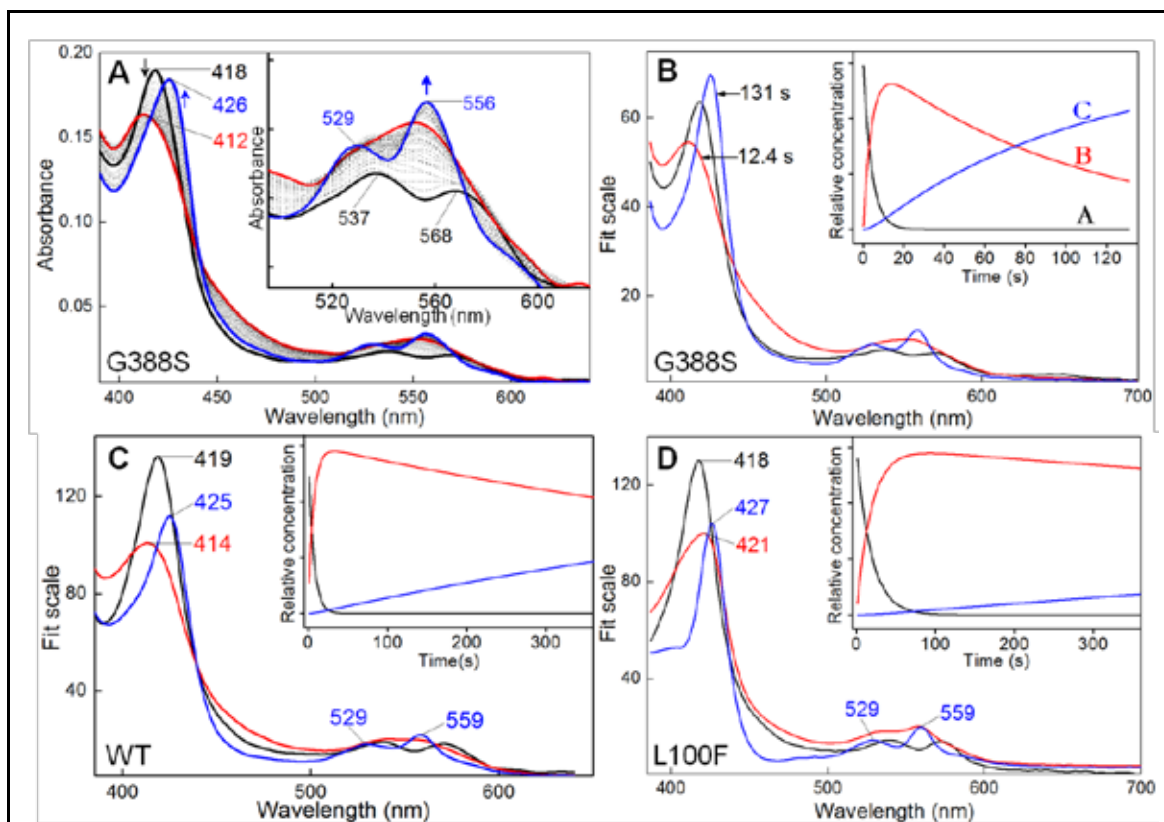


Figure 3.11: Formation of Fe(II)-thiolate and Fe(II)-thiol species in CYP51B1 enzymes. Black lines represent the resting Fe(III)-heme, red lines are the intermediate Fe(II)-thiolate species following dithionite reduction, and blue lines are the final Fe(II)-thiol species. The dotted black lines illustrate progress of formation for the different species in the case of the G388S mutant in Panel A. Panel A demonstrates the reduction of Fe(III) heme iron in G388S CYP51B1 (2.0 μM) with dithionite, where the Soret band at 418 nm decreases in intensity in forming the intermediate Fe(II)-thiolate species (maximum at 412 nm) before the protonation of cysteinates to form the Fe(II) heme-thiol form at 426 nm in the final stage of the reaction. Panel A inset is a magnified spectral region encompassing the Q-bands, and showing the changes upon heme iron reduction. Panel B shows the global fitting of species formed for the CYP51B1 G388S mutant upon reduction with dithionite (hence the term “fit scale” at the y-axis for the above global fit graphs in panel B, C and D), with spectra shown at 12.4 s (heme Fe(II)-thiolate) and 131 s (heme Fe(II)-thiol). Insets in panels B, C and D show progression curves illustrating the formation and collapse of species A, B and C for the respective CYP51B1 isoforms. The main figure in panel C illustrates species A (black), B (red) and blue (C) for WT CYP51B1 (2.9 μM), and that in panel D shows the same species for CYP51B1 L100F (2.9 μM). The nature of the intermediate (ferrous-thiolate) form is clearly different in the L100F CYP51B1 mutant compared to the WT and G388S mutants. Parallel studies of the F89H (2.9 μM) and R391K (2.9 μM) CYP51B1 mutants showed similar spectral trends to WT CYP51B1 on heme iron reduction, perhaps reflecting a proportion of ferric heme thiol form in only the L100F mutant. The rate constant for the heme Fe(II)-thiolate to heme Fe(II)-thiol conversion is much faster in the case of the G388S CYP51B1 mutant than for the WT CYP51B1 and the other mutants.

CYP51B1 mutants in the heme motif region, upon reduction with 5 mM sodium dithionite, (and especially G388S) showed faster ferric-thiolate to ferrous-thiolate reduction and thiolate protonation. Figure 3.10 (A) demonstrates the G388S resting Fe(III)-thiolate (black spectrum) progressively collapsing (dotted black spectra) to its Fe(II)-thiolate form at 0.241 s^{-1} (from data recorded at 412 nm and tabulated data in Table 3.2) and then slowly converting to its ferrous-thiol form at 0.00978 s^{-1} (426 nm) over 130 s. These events occurred in approximately half the time taken for WT CYP51B1, with rate constants of 0.153 s^{-1} (A to B) and 0.00105 s^{-1} (B to C) (see Table 3.2). Conversely, R391K had a slower reduction rate than G388S and WT CYP51B1 at 0.118 s^{-1} , and also a substantially slower thiolate protonation rate at only 0.00068 s^{-1} , 8 times slower than that for the G388S ferrous-thiolate protonation rate constant (please see Table 3.2). The rate constant for R391K CYP51B1 thiolate protonation is comparable to that for L100F, but with spectral trends more similar to that for WT CYP51B1 (i.e. with a more clearly defined ferrous-thiolate species formed before the collapse to the ferrous-thiol form).

The results for the collapse rate constant of R391K may initially seem contradictory, since there was a faster P450 species collapse rate (protonation of ferrous-thiolate) when bound to CO; the rate constant in this case being higher than that for WT and comparable to that for G388S CYP51B1. However, the presence of a ligand (CO in this case) to the R391K ferrous heme might stabilise the R391K mutant cysteinyl loop structure. It is possible that interactions between the lysine (3 residues away from C394) and/or other residues in close proximity to the heme macrocycle and the cysteinate-proximal ligand stabilise the thiolate coordination for this mutant in its Fe(II)CO form. The importance of a strong 6th distal ligand to the stability of this mutant have also been shown in the next chapter, where ferric R391K CYP51B1 bound to 4PI and EPBA (both type II inhibitors) readily leads to formation of co-crystals. By comparison, crystals of CYP51B1 mutants at the SRS 1 hinge region proved more difficult to obtain, even in ligand-bound forms.

3.5.4 Stabilisation of the P450 Form in the Presence of Estriol and Redox Partners

Studies of the ferrous-CO adduct in WT CYP51B1, which forms a transient Soret band at $\sim 448\text{ nm}$ before collapsing back to the ferrous-CO thiol form at $\sim 421\text{ nm}$, have been extensively studied by Mclean *et al.* (2006b; 2006c) Studies were done using a Class I redox partner system comprising the ferredoxin (Fd1, *Rv0763d*) situated next to the

CYP51B1 gene and flavoprotein reductase A (FprA), and showed that the thiolate-bound P450 form can be stabilised in the presence of estriol (a lanosterol substrate analogue). Dunford *et al.* (Dunford *et al.* 2007) demonstrated that while kinetics of binding of CO to Mtb CYP121 were biphasic (perhaps reflecting access of CO to the heme iron from both an internal protein CO-binding site and the external solution), CO binding to ferrous CYP51B1 was monophasic. In both these studies, the CYP51B1 ferrous CO-bound or CO-free thiolate species were unstable and were readily protonated to form the P420 species in processes influenced by pH (Dunford *et al.* 2007; McLean *et al.* 2006c). Earlier in this chapter, I reported that CYP51B1 WT and the azole-resistant mutants formed ferrous-CO adducts at ~448 nm which were unstable and which readily collapsed to the P420 form over a matter of minutes. In addition, these P420 formations (reflecting heme thiolate protonation) differed according to location of the mutants in the enzyme. Here, considering previous work done on CYP51B1 in this field, similar experiments were done to those by Mclean *et al.* (McLean *et al.* 2006c), in order to attempt to stabilise the CYP51B1 P450 form using estriol with the redox partner proteins, FprA and Fd1 (instead of the chemical reducing agent, sodium dithionite). In addition, two more redox partner enzymes from Mtb were introduced: the ferredoxin reductase (Fdr) situated next to the CYP51B1 operon in Mtb and a second Mtb ferredoxin 2 (Fd2, *Rv1786* – located adjacent to the P450 *CYP143*) in order to assess their electron transfer capabilities from NADPH to CYP51B1. Table 3.3 summarises the P450 ferrous-thiolate formation in the presence of CO and estriol in WT CYP51B1, coupled to various combinations of the four different redox partner enzymes from Mtb.

Table 3.3: Summary of P450 species formation in WT CYP51B1 with various Mtb redox partners and coenzymes.

Rate of P450 formation (min ⁻¹)	Formation of P450 (√ or X)	FprA <i>Rv3106</i>	Fdr <i>Rv0688</i>	Fd1 <i>Rv0763</i>	Fd2 <i>Rv1786</i>
a) n.d.	X	√*	X	√	X
b) n.d.	X	√*	X	X	√
c) 0.020 ± 0.001 (A)	√	√*	√	√	√
d) 0.024 ± 0.001 (B)	√	√*	√	X	√
e) 0.056 ± 0.004 (C)	√	√*	√	X	X
f) 0.019 ± 0.001 (D)	√	√*	√	√	X
g) 0.024 ± 0.001 (E)	√	X	√	X	X
h) 0.082 ± 0.009 (F)	√	√	X	X	X

note: n.d. = not detected. Basal reaction mixture consisted of 0.2 mM NADPH, CO-saturated, pH 7.5 100 mM phosphate buffer, 0.2 mM estriol and 3.24 μM WT CYP51B1 in anaerobic environment. The concentration ratio of CYP450:reductase:ferredoxin used was 1:1:5. The √ signage signifies functional redox partners while X signage denotes that respective redox partners were not included in the reaction mixture and the √* signage signifies inactive FprA (FprA*) which was used in the first batch of experiments and did not support an electron transport process.

From Table 3.3, the presence of Fdr in the reaction was the determining element for the formation of ferrous-thiolate species. Control experiments constituting i) WT CYP51B1 minus redox partner enzymes but with NADPH, CO and estriol did not result in either P420 or P450 formation, and ii) WT with NADPH alone also did not result in any spectral shifts. However, other reactions: iii) WT with NADPH, CO, estriol, FprA and Fd1, iv) WT with NADPH, CO, estriol, FprA and Fd2 and v) WT with NADPH, CO, FprA, Fdr, Fd2 without estriol all gave rise to formation of Fe(II)CO adducts. The non-formation of P450 species with the FprA* and Fd1 combination (Table 3.3 a) was inconsistent with published data by Mclean *et al.*, where formation and stabilisation of the P450 species in WT CYP51B1 was detected (McLean *et al.* 2006c). In view of this inconsistency, this initial result was attributed to an inactive FprA* preparation with respect to electron transfer to the P450(s). In view of previous work (McLean *et al.* 2006c), a second preparation of FprA was used and this time found to be functional in supporting electron transfer to CYP51B1 in absence of other redox proteins (Table 3.3 h).

SDS-PAGE analysis of the initial inactive FprA* did not indicate proteolysis had occurred, hence its inactivity in electron transfer may have been related to flavin loss or loss of activity caused by freezing/thawing. Likely as a consequence of this, the FprA* and Fd2 combination (Table 3.3 b) also gave negative P450 formation. The formation of P450 species using the Mtb Fdr and Fd1 combination agreed with results published by Zanno *et al.* (2005) with CO and NADH in terms of lanosterol turnover catalysis (but without estriol present in this case), although individually the proteins did not support CYP51B1's

catalysis of lanosterol demethylation. Interestingly, NADH was reported as a better electron donor compared to NADPH, yielding faster P450 formation (reaction completed in less than 5 min), with the minimum NADH and NADPH concentrations being 0.1 mM and 1.0 mM, respectively, for effective electron transfer during lanosterol catalysis by CYP51B1 with Fdr and Fd1. However, no further improvements were observed when these coenzymes were used above 1 mM in reconstitution of CYP51B1 lanosterol catalysis (Zanno *et al.* 2005). Indeed, the concentration and choice of electron donors are also important determining factors for the effective electron transfer process in the CYP51B1 system. The first occurrences of P450 species formation in WT CYP51B1, and in all positive cases from Table 3.3, were detected after ~8 min on average, except for cases where the reductases were used individually (Table 3.3 g,h and Figure 3.12 E,F) where the P450 formation was detected after 30 min (Fdr) and 25 min (FprA).

Rate constants presented in Table 3.3 were determined spectrally by following the formation of the ferrous-thiolate species in WT CYP51B1, as illustrated by the gradual spectral shift from the resting ferric-thiolate species and formation of the CO complex at 450 nm in Figure 3.12. The collective influence of estriol and electron transfer partners (Mtb reductases and ferredoxins) in maintaining the P450 form of CYP51B1 is clear from the data presented in Figure 3.12 B. A native-like electron transfer system (compared to dithionite) thus also appears to be important in stabilizing thiolate ligation in this enzyme.

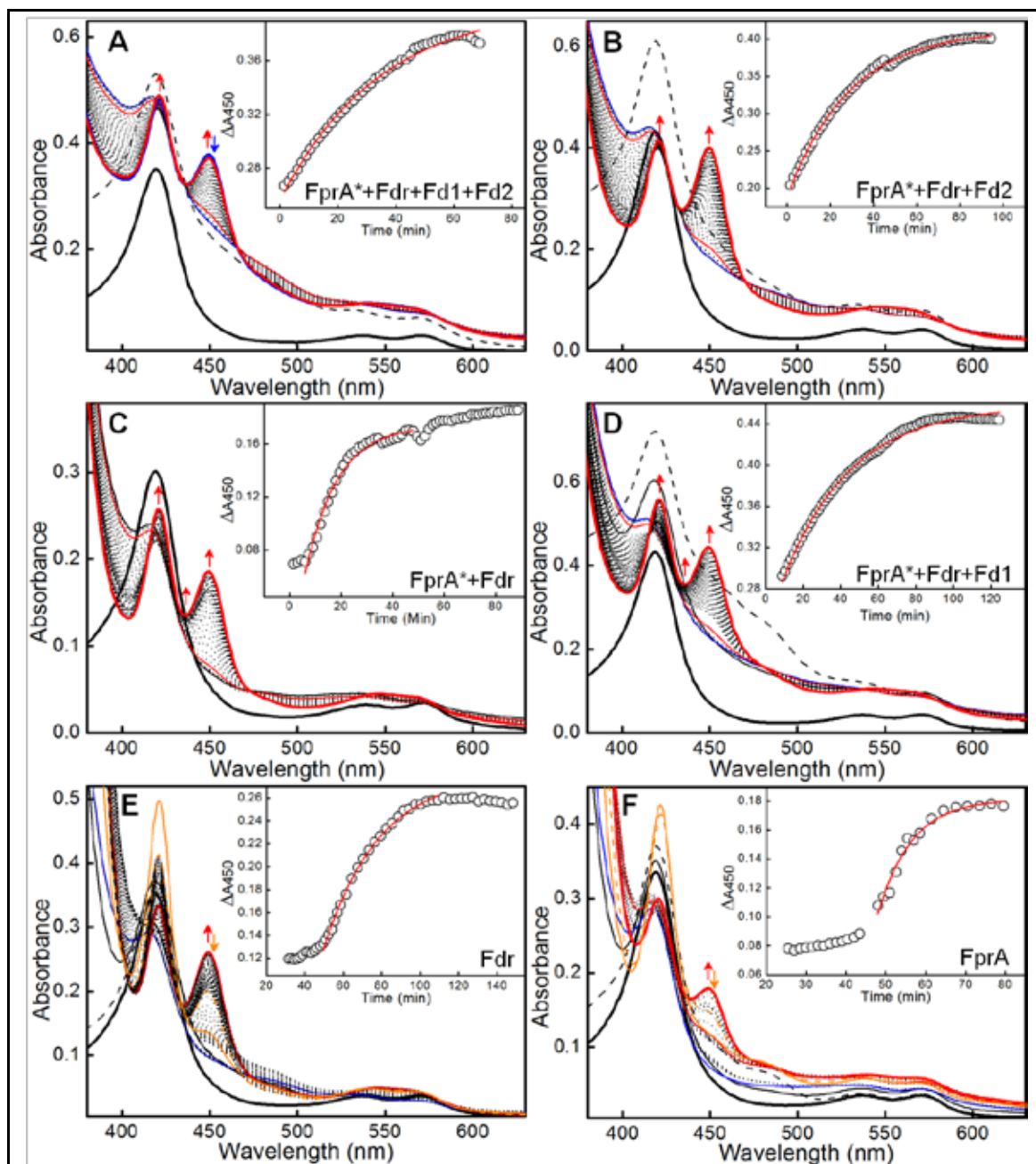


Figure 3.12: P450 species formation in CYP51B1 WT with various Mtb redox partners. The thick solid black line is the Fe(III)-enzyme before the addition of redox partners (dashed black spectra) and the addition of NADPH (thin solid black spectra in panels D-F) and estriol (thin solid blue spectra), followed by the first P450 Fe(II)-thiolate species formation (thin red spectra) gradually changing (progressively shown by black dotted spectra) until the P450 species was maximally stabilised at ~ 450 nm (thick red spectra). However, in **A**, with the presence of FprA* (inactive FprA), Fdr, Fd1 and Fd2 redox partners, the P450 species collapsed (blue arrow) over 2 h while the P420 species continued to form (red arrow in A-D), and this happened to a lesser extent in **B** with the presence of FprA*, Fdr and Fd2, which was used in the following experiments with the mutant CYP51B1 enzymes. Interestingly, formation and stabilisation of this P450 species also occurred when only the reductases, FprA* and Fdr, were added in **C**, and this was also the case in **D** with the addition of both FprA* and Fdr and Fd1. Both Fdr (**E**) and FprA (**F**) individually were shown to support electron transport process from NADPH by P450 formation (red arrow) of which $\sim 80\%$ (**E**) and $\sim 98\%$ (**F**) decayed (orange arrow) to the P420 form overnight (~ 18 h) (solid orange spectra) while $\sim 50\%$ of the P450 species decayed over 7 h (**E,F**) (dashed orange spectra). Insets show the data for P450 formation fitted using a single exponential (**Equation 2.1**) to derive the rates as shown in **Table 3.3**. No formation of either P420 or P450 species occurred when either NADPH alone without (i) the redox partners present or (ii) without

CO and estriol present were included in the system. Similarly, no formation of P450 species occurred when Fdr was omitted from the experiment.

Without Fd2 or Fd1, the formation of a P450 species still occurred, consistent with the ability of Fdr and FprA to reduce CYP51B1 in isolation (Figure 3.12 C, E, F). It would be interesting to prove whether these reductases alone (either together or individually) can also support CYP51B1 demethylation activity towards either lanosterol or 24,25-dihydrolanosterol, results of which are still pending analysis via LCMS (Paul Williams, LCMS/GCMS experimental officer, Manchester Interdisciplinary Biocentre, pers. comm.).

In all experiments, CYP51B1 WT ferric enzyme (thick solid black spectra) in presence of CO was mixed with redox partner enzymes (dashed black line), followed by the addition of estriol (thin solid blue spectra) and bubbling with more CO gas, before the reaction was initiated with the addition of NADPH (thin solid black spectra). Absorbance change data at A450 for the system containing both reductases and ferredoxins (Figure 3.12 A,B,D) were fitted with a single exponential function while the system containing only reductases (Figure 3.12 C,E,F) were fitted with a sigmoidal function. Comparisons between the reductases indicated that neither alone had the same P450 stabilizing effect as observed in the presence of the Fd1/Fd2 ferredoxins. However, experiments using Fdr resulted in ~65% P450 formation over 140 min, followed by a slow collapse to the P420 form over 7 h (~50%) and 18 h (~80%) (Figure 3.12 E) with a P450 formation rate constant of **0.024 min⁻¹**. In the case of FprA, a much lower amount of P450 was formed (~30% at 90 min) albeit ~4 fold faster (**0.082 min⁻¹**) than the other combination, and again decayed to P420 over 7 h (~50%) and 18 h (~98%). The FprA reductase system supported P450 formation faster in isolation than when both (FprA and Fdr) were present in the system together (**0.056 min⁻¹**). With these rate constants differences and the sigmoidal-shaped curve in the systems with reductases only (in addition to an initial lag-phase) these suggested a few possibilities including allosteric interactions between these co-enzyme proteins and CYP51B1 (the heme domain) i.e. (i) a competitive binding between the two FAD domains onto the heme domain of CYP51B1 surface recognition sites in order to facilitate electron transfer (Figure 3.12 C), (ii) inefficient electron transfer from NADPH via the FAD-reductases due to improper coupling to the heme domain of CYP51B1 (Figure 3.12 E,F), (iii) a slow complexing of the reductase with CYP51B1 and/or (iv) a slower reduction of the FAD in the reductases before the electrons were transferred relatively rapidly (inferred from the lag-phase to the exponential-phase) to the heme domain.

Flavin adenine dinucleotide (FAD)-containing flavoprotein/ferredoxin reductases (FprA and Fdr) alone were demonstrated to enhance the rate of P450 formation (Table 3.3) suggesting that the first electron transfer process to CYP51B1 can take place with these FAD-associated flavoproteins and without the presence of the partner iron-sulfur cluster ferredoxins. Preceding discussions relating to FprA* likely indicate that Fdr alone may be responsible for the CYP51B1 reduction. The absence of the 3Fe4S-ferredoxins “shortens” the electron transport chain from NADPH via FAD-associated reductase(s) to CYP51B1, as illustrated by the electron transfer scheme in Figure 3.13, likely explaining the difference in rate constants for the reductase combinations in the above experiments (Table 3.3).

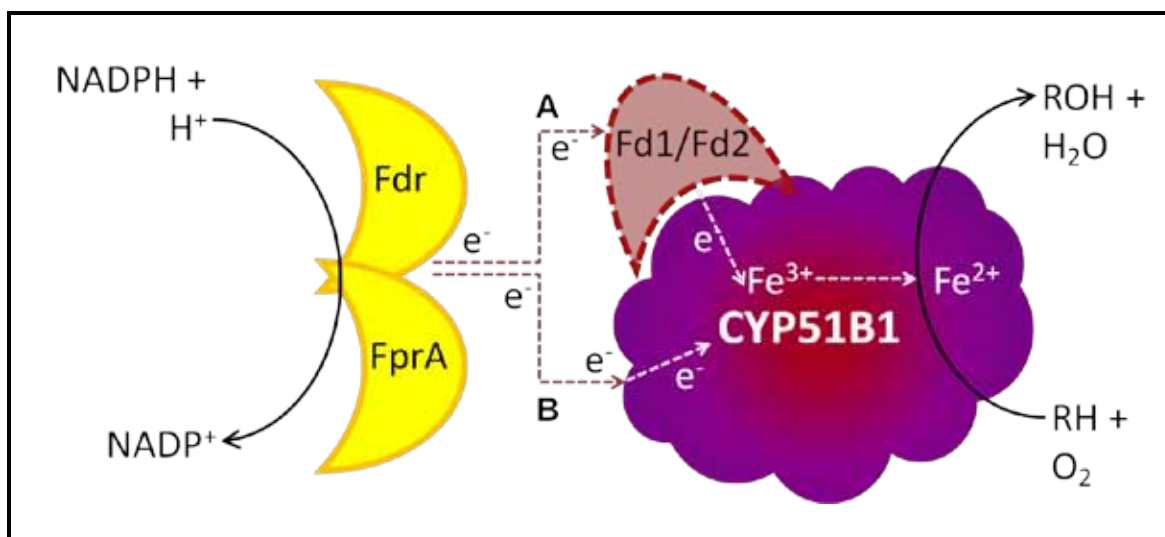


Figure 3.13: Electron transfer scheme between Mtb redox partner enzymes and CYP51B1. The electron donor NADPH is oxidised by Mtb FAD-containing flavoprotein reductases, flavoprotein reductase A (FprA) (*Rv3106*) and ferredoxin reductase (Fdr) (*Rv0688*) and the electrons can be passed through the FAD cofactor and onto the CYP51B1 heme via two pathways; **A**) via Mtb 3Fe4S-ferredoxin partner enzymes, Fd1 (*Rv0763*) or Fd2 (*Rv1786*) or **B**) bypassing the ferredoxins and directly reducing ferric-heme P450 to ferrous-heme. The oxidation of sterol substrate has been shown to occur when both ferredoxin reductase/ferredoxin are used, but it is not clear whether a productive monooxygenase reaction can occur in absence of a ferredoxin partner.

It is pertinent to note that these CYP51B1/redox partner combinations proposed in the above scheme (Figure 3.13) have yet to be empirically proven with substrate turnover experiments. By measuring sterol substrate turnover via LCMS with the above Mtb redox partner combinations (and with different proven substrates of CYP51B1, e.g. lanosterol, obtusifoliol or 24,25-dihydrolanosterol), an optimal partner set supporting catalytic function may be established. Defining appropriate partner proteins would be beneficial with respect to rationalizing CYP51B1's proposed participation in Mtb-host

macrophage infection (Gatfield and Pieters 2000) in concert with other Mtb P450 enzymes already established (or possibly) as essential for bacterial viability, virulence or host cholesterol metabolism (CYP121, CYP124, CYP125, CYP128, CYP130, CYP142 and CYP144) (Driscoll *et al.* 2011; McLean *et al.* 2010; McLean *et al.* 2007).

In view of the Fd2's apparent stabilising effect on formation of the ferrous-thiolate P450 Fe(II)CO species and the availability of this redox partner enzyme, a mixture of Fdr and Fd2 was employed for electron transfer and P450 stabilisation studies in the azole-resistant mutants. Table 3.4 exhibits the rate constants for P450 formation for WT, F89H, L100F and R391K, while the rate constant for the G388S mutant was for P420 formation. Although the P450 form was stabilized in WT CYP51B1 and mutant enzymes (F89H, L100F and R391K) by the ferredoxins, the P450 form did, however, partially collapse to the P420 form over several hours (Figure 3.14). This conversion was sufficiently slow that it occurred over a similar timescale to the reoxidation of the Fe(II)CO back to Fe(III).

Table 3.4: Rate constants for P450 species formation of CYP51B1 mutants with Mtb Fdr and Fd2 redox partners.

CYP51B1	Rates of formation (min ⁻¹)
WT	0.0241 ± 0.0004
F89H	0.0206 ± 0.0006
L100F	0.0352 ± 0.0012
*G388S	0.0176 ± 0.0004
R391K	0.0265 ± 0.0006

Note: * Rate constant for G388S is for P420 species formation. Conditions were as described in section 2.2.14.

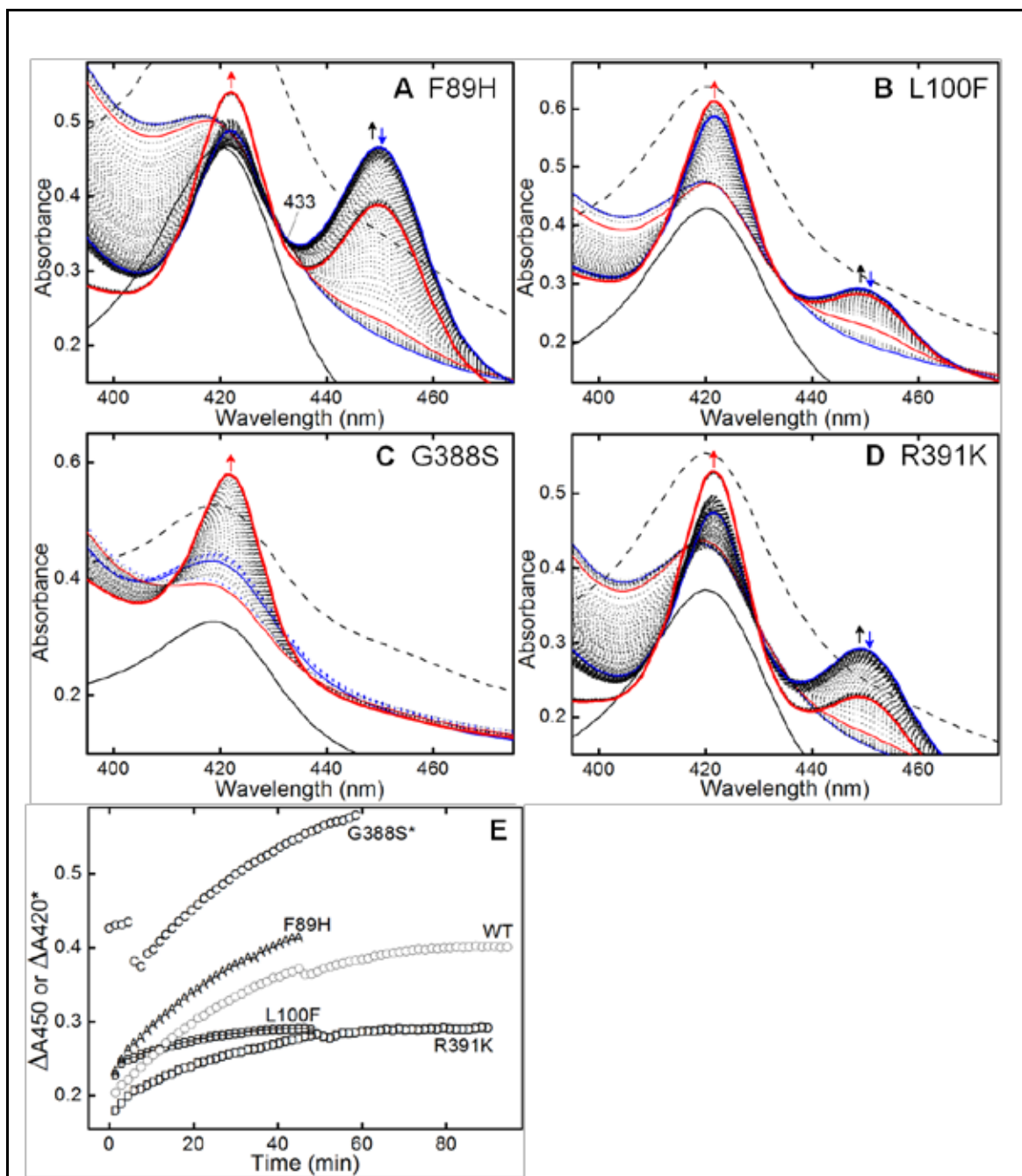


Figure 3.14: P450 species formation and stabilisation in CYP51B1 mutants with Fdr, and Fd2. In panels A-D, the solid black line is for the Fe(III)-enzyme in each case, and before the addition of redox partners (dashed black line) and the addition of NADPH and estriol (thin blue line). The thin red line indicates the first P450 Fe(II)-thiolate species formation observed, and (progressively shown by black dotted lines and black arrows) this leads to the maximal P450 species stabilised at ~448 nm (thick red line) in all but one case. The exception is for G388S (panel C), where only the P420 species is formed. Over periods of 2 h or more, the P450 species collapsed (blue arrow) while P420 species continued to form (red arrow). This was the general case for F89H (A), L100F (B) and R391K (D), but not for G388S (C) which demonstrated only P420 Fe(II)-thiol species formation. Progression curves for the formation of the P450 species (*apart from G388S which is for P420 formation) are illustrated as changes in ΔA_{450} versus time in panel E, with L100F CYP51B1 showing the least conversion to P450. The data for the G388S mutant show the ΔA_{420} versus time, since essentially no P450 was formed in this enzyme. In all the above cases (other than G388S) an apparent single P450/P420 isosbestic point was maintained at 433 nm.

The instability of the G388S P450 Fe(II)CO species may be consistent with the underlying property of this mutation in destabilising the binding (leaching of the heme cofactor during purification) of the heme, which in WT CYP51B1 is more firmly anchored at the catalytic site. The direct reduction of the ferric-thiolate G388S to the ferrous-thiol CO-bound species was a slower process (0.018 min^{-1}) in the presence of lanosterol-substrate analogue (estriol) and Mtb redox partners (Table 3.4), as opposed to 0.880 min^{-1} for ferrous-CO adduct reduction with sodium dithionite (Figure 3.10 A). The fact that G388S has a more positive heme iron redox potential (-102 mV) compared to WT CYP51B1 (-283 mV) would boost its electronic affinity, and may expedite the electron flow from reduced redox partners to its heme-iron, impressing the fact that the slower P420 formation for this mutant (compared to dithionite reduction) is probably due to inefficient interactions and electron transfer reaction with the redox partner enzymes. This information can be extrapolated to predict G388S mutant catalytic properties with its substrate *in vivo* or *in vitro*. Since the G388S CYP51B1 is unstable in the active ferrous-thiolate (Fe(II)-S⁻) form (when bound to substrate and primed for catalysis), its more rapid conversion to the protonated ferrous-thiol form would render this mutant inactive in substrate oxidation, unless second electron transfer occurs faster than heme thiolate protonation. One might expect this “fluconazole-resistant” mutant to participate in substrate turnover more effectively than the WT CYP51B1 while in the presence of fluconazole inhibitor (assuming that the Mtb mutant enzyme faithfully reproduces the properties of the *C. albicans* mutant. This might be reflected in a higher affinity towards estriol compared to fluconazole (or at least weaker affinity for the latter). The K_d values from equilibrium binding experiments showed relatively tight binding of this ferric-heme mutant enzyme to fluconazole ($13 \mu\text{M}$) compared to estriol ($78 \mu\text{M}$) while ferric-heme WT CYP51B1 showed the same binding affinities to both fluconazole ($21 \mu\text{M}$) and to estriol ($21 \mu\text{M}$). These profound results will be discussed later in this chapter.

From the table above, L100F showed the highest rate constant for P450 species formation, while the F89H and R391K CYP51B1 mutants' rate constants were quite similar, and close to those for the WT enzyme, which confirms that the combination of redox partner enzymes does facilitate electron transfer from NADPH to the heme-iron of these mutants, and with a similar rate to the WT CYP51B1. The first clear P450 spectral species formation for this combination of redox partner enzymes (FprA, Fdr and Fd2) was seen at 7.5 min for WT and at 15 min, 6 min and 13 min for F89H, L100F and R391K mutants, respectively. Spectral data for the formation and stabilisation of the P450 species by estriol is shown in Figure 3.14. Resting ferric enzymes (solid black spectra) were mixed

with the redox partners simultaneously (dashed black spectra) followed by addition of estriol and CO bubbling, and initiation of the reaction by NADPH addition (thin blue spectra). The gradual progress of formation of the Fe(II)CO complex was followed (thin dotted spectra) with the first P450 spectrum observed shown as thin red lines, and the progressive P450 build up indicated by a black arrow. The maximally formed P450 species in each case are shown as thick blue spectra, and its gradual collapse denoted by blue arrows with the concurrent P420 species formation indicated by red arrows. The reactions were terminated after ~8 h in each case. Substrate-analogue-assisted P450 species stabilisation was observed for WT with the different redox partners (Figure 3.12). However, for the mutant CYP51B1 enzymes (shown in Figure 3.14), partial P450 stabilisation was observed for F89H and R391K mutants, and a somewhat slower formation of the P450 species was observed for the L100F mutant, albeit with stabilisation of the P450/P420 equilibrium. In the above cases, the isosbestic points remained stable at 433 nm, denoting the clear transition between the two species (P450 and P420). Substrate-assisted ferrous-thiolate stabilisation has been previously observed by the binding of native substrate epothilone D to dithionite-reduced P450 EpoK from a myxobacterium *Sorangium cellulosum* (an enzyme important for anticancer agent production [epothilones A and B] by epoxidation of its substrate). This enzyme showed recovery at relatively low temperatures (~15°C) of the ferrous-thiol P420 form to the catalytically active ferrous-thiolate P450 form (Ogura *et al.* 2004). In this study, estriol (a lanosterol analogue with greater solubility) was observed to stabilise the ferrous-thiolate P450 form in WT CYP51B1, and to a certain extent in the azole-resistant mutants at 30°C.

Related work done by Mclean *et al.* (2006c) on WT CYP51B1 showed that estriol enhanced the P450 species formation (70/30 P450/P420 species ratio ~3.5 min after introduction of CO to a dithionite-reduced sample), but did not prevent its eventual collapse to P420. McLean *et al.* (2006c) also showed that the CYP51B1 P420 species was reversible upon complete reoxidation, and that the enzyme was able to undergo another cycle of reduction to P450 and the subsequent collapse to P420. A similar phenomenon of P450 species stabilisation was observed in Mtb CYP142 by cholest-4-en-3-one, a native substrate, where a 80/20 P450/P420 ratio was achieved, and complete P420 formation seen in absence of substrate (Driscoll *et al.* 2010). These findings lead to the conclusion that, upon finding the native substrate for CYP51B1, it too will innately stabilise the active P450 ferrous-thiolate species and likely prevent enzyme inactivation.

3.5.5 Redox Potentials of WT and Mutant CYP51B1 Ligand-Free Forms

The redox potential or mid-point potential for any substance is a measure of its affinity towards electrons and its oxidising potential. At pH 7.0, the reducing agent, sodium dithionite, has a redox potential of -660 mV while the oxidising agent, potassium ferricyanide, has a redox potential of 436-450 mV, both against the standard hydrogen electrode (Mayhew 1978). The measurement of a CYP51B1 mutant enzyme's heme iron redox potential is important to ascertain its heme-iron affinity towards electrons which, during catalysis, will be provided by NADPH and delivered via redox partners that have been previously examined (section 3.5.4). A more positive redox potential would favour electron transfer from the redox partner to the ferric-heme in a P450 and vice versa. With respect to redox partner interactions, the importance of a positively charged region surrounding the proximal face of the P450 heme is well established, and several basic residues were identified in the structure of rabbit CYP2C5 (the first mammalian P450 crystal structure) that could form electrostatic interactions with an acidic surface on the CPR partner (Wang *et al.* 1997; Williams *et al.* 2000). In the case of P450nor (CYP55A1), however, the redox partner has been dispensed with in favour of direct interaction with NADH, which binds within the active site cavity (Oshima *et al.* 2004). In P450nor (-307 mV) there is a distinct lack of positive charge on the heme distal surface, as might be expected (Munro *et al.* 2007).

Figure 3.15 depicts potentiometric titrations of CYP51B1 WT, G388S and R391K enzymes and Nernst plots that enable the determination of the redox potentials for their heme iron Fe(III)/Fe(II) couple. Reduction with the artificial reductant dithionite, rather than by NADPH via redox partner enzyme flavoprotein/ferredoxin reductases (FprA/Fdr) and ferredoxins, produced a characteristic absorption band at 423 nm in WT CYP51B1 consistent with the ferrous-thiol species. Subtly different spectral shifts were observed for mutants at the cysteinyl loop region, G388S and R391K, with formation of the ferrous-thiolate (402 nm – G388S and 399 nm – R391K) and ferrous-thiol (427 and 422 nm, respectively) forms, and resultant differences in spectral shape and wavelength maxima. In previous stopped-flow analysis with dithionite as reductant (section 3.5.3, Figure 3.11 C), a similar 425 nm peak was observed in WT CYP51B1 over a timescale of several seconds with a preceding peak at 414 nm indicative of ferrous-thiolate formation. In the potentiometric procedure, the enzyme-reductant mixture was left to equilibrate over 4-6 minutes at each dithionite titration point before readings were taken, allowing the thiol/thiolate system to come to equilibrium for ferrous enzyme at each applied potential.

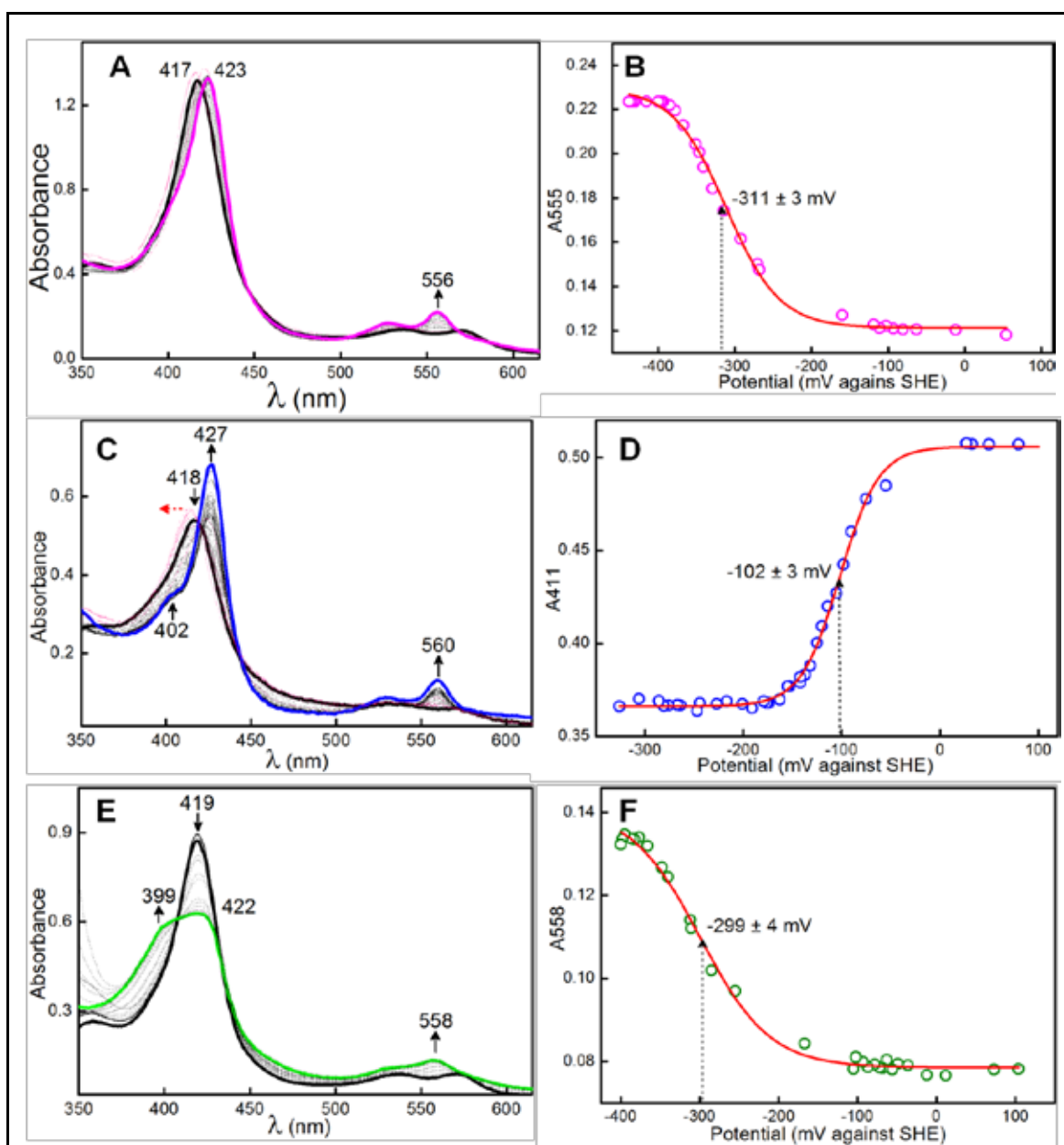


Figure 3.15: Redox potentials of ligand-free WT CYP51B1 and cysteinyl loop mutant enzymes. A-B) Spectral redox titration of WT CYP51B1 (9.30 μM) and its accompanying absorption versus potential plot, with a redox potential of -311 ± 3 mV determined by fitting the data using the Nernst function (Equation 2.4) in panel (B). The spectra accompanying the reduction of the WT heme iron show a Soret band shift (A) from 417 nm (black spectrum) to 423 nm (purple spectrum). Intermediate spectra are shown as dotted black spectra. This titration shows a near-complete formation of the thiol-coordinated species, consistent with previous studies (McLean *et al.* 2006c). Repeated redox titrations of the WT enzyme showed similar spectral conversions, although sometimes with a small proportion of thiolate-coordinated ferrous enzyme retained at ~ 401 nm. Reoxidation with potassium ferricyanide followed a similar reduction path as shown by dotted red spectra. C-D) show the comparable spectral and fitting data for the G388S CYP51B1 (4.13 μM), with heme iron redox potential of -102 ± 3 mV (D), and (C) showing the changes in absorption upon reduction with sodium dithionite and reoxidation with potassium ferricyanide (dotted red spectra) for the G388S mutant, as shown by the red arrow, followed almost similar pathways. SHE = standard hydrogen electrode. The solid black spectrum shows the initial resting state of the enzyme with a 418 nm Soret peak. After progressive reduction, denoted by dotted black spectra, the Soret maximum finally reaches 427 nm, with notable increases in spectral intensity at 560 nm in the Q-band region (solid blue spectrum). E-F) A different type of Soret band shift upon reduction for another mutant in the cysteinyl loop region is demonstrated by R391K (6.57 μM), with a $\sim 50\%$ mixture of Fe(II)-thiolate and -thiol forms observed as Soret maxima at

~399 and ~422 nm, respectively (green spectrum). For this mutant (which binds heme much better than does G388S) the resulting mid-point heme iron potential (-299 ± 4 mV) did not differ substantially from that for the WT CYP51B1.

Essentially, the approaches applied in section 3.5.3 measure the rate of reduction of CYP51B1, while the potentiometric (spectroelectrochemical) procedures measure equilibrium reduction of the heme iron with varying amounts of dithionite. Both these methods complement one another: the kinetic procedures capture the reaction rates associated with the P450 (ferrous thiolate) collapse to the P420 (ferrous thiol) form, while the potentiometric analysis provides equilibrium data that report on the differing electron affinity for WT and mutant CYP51B1 heme iron. Although complementary, the latter procedure involved including mediators in the system and may be liable to subtle changes in pH or ionic strength at different sodium dithionite titrations. During multiple potentiometric assays of WT CYP51B1 (on three separate occasions) variations were observed which were reflected by formation of small amounts of the ferrous-thiolate-coordinated form as well as near-complete ferrous-thiol-coordinate form (data not shown) may be attributable to the above factors.

In order to ensure that there was no hysteresis behaviour in the potentiometric titrations (a phenomenon which may be observed in iron-heme proteins due to the existence of iron in two states i.e. Fe(II) and Fe(III) coupled with the electronic (electron flow) affinity during reduction and reoxidation processes using either chemical or physiological redox agents (McLean *et al.* 2006c)), reduced enzymes were subsequently reoxidised using potassium ferricyanide. This showed that the process was fully reversible in each case, and that the P420 form was not a permanently denatured version of the protein. Furthermore, the reoxidation spectra followed the same absorbance versus potential pattern as observed for the reductive path, ruling out any hysteresis phenomena.

Interestingly, the G388S mutant displayed a very positive heme iron redox potential of -102 ± 3 mV, revealing a higher electron affinity and thus a higher propensity to attract electrons from NADPH (via the redox partners) in a ligand-free state due to an increased driving force of about 209 ± 3 mV by comparison to WT CYP51B1. This behaviour of the G388S mutant may be attributed to the location of the mutation within the heme-binding region of the P450, where all catalytic redox reactions take place and in the environment in which inhibitors and substrates bind, as shown in Figure 3.16. The influence of a polar serine residue, by virtue of the G388S mutation near the heme site, clearly results in an increase in heme iron redox potential, possibly as a direct consequence of structural perturbations in the highly conserved glycine-rich cysteinyl loop surrounding

the totally conserved cysteinate proximal ligand (C394 in Mtb, C470 in *C. albicans* and C454 in *A. fumigatus* CYP51 enzymes). The ~90% conversion to the P420 species, as shown by the Soret shift from 418 nm to predominantly 427 nm (Figure 3.15 C) demonstrates the destabilisation of the cysteine thiolate to protonation in the equilibrium redox titrations, consistent with data from the stopped-flow dithionite reduction analysis (section 3.5.3). A major difference of CYP51B1 from various other P450s is shown by its ready conversion to the ferrous-thiol species (with absorption maximum at ~430 nm) during reduction, while other P450s, e.g. Mtb CYP121 remained predominantly in the ferrous-thiolate form (~410 nm) in their reduced state (McLean *et al.* 2006b). This instability of the catalytically active P450 species to heme thiolate protonation was decreased on the binding of estriol, consistent with structural rearrangements that prime the enzyme for substrate turnover. However, the G388S mutant (that introduces a hydroxyl containing aliphatic chain close to the cysteinate) accelerated the P450 to P420 conversion by ~9-fold (WT = 0.00105 min⁻¹, G388S = 0.00978 min⁻¹) compared to WT CYP51B1 (Table 3.2).

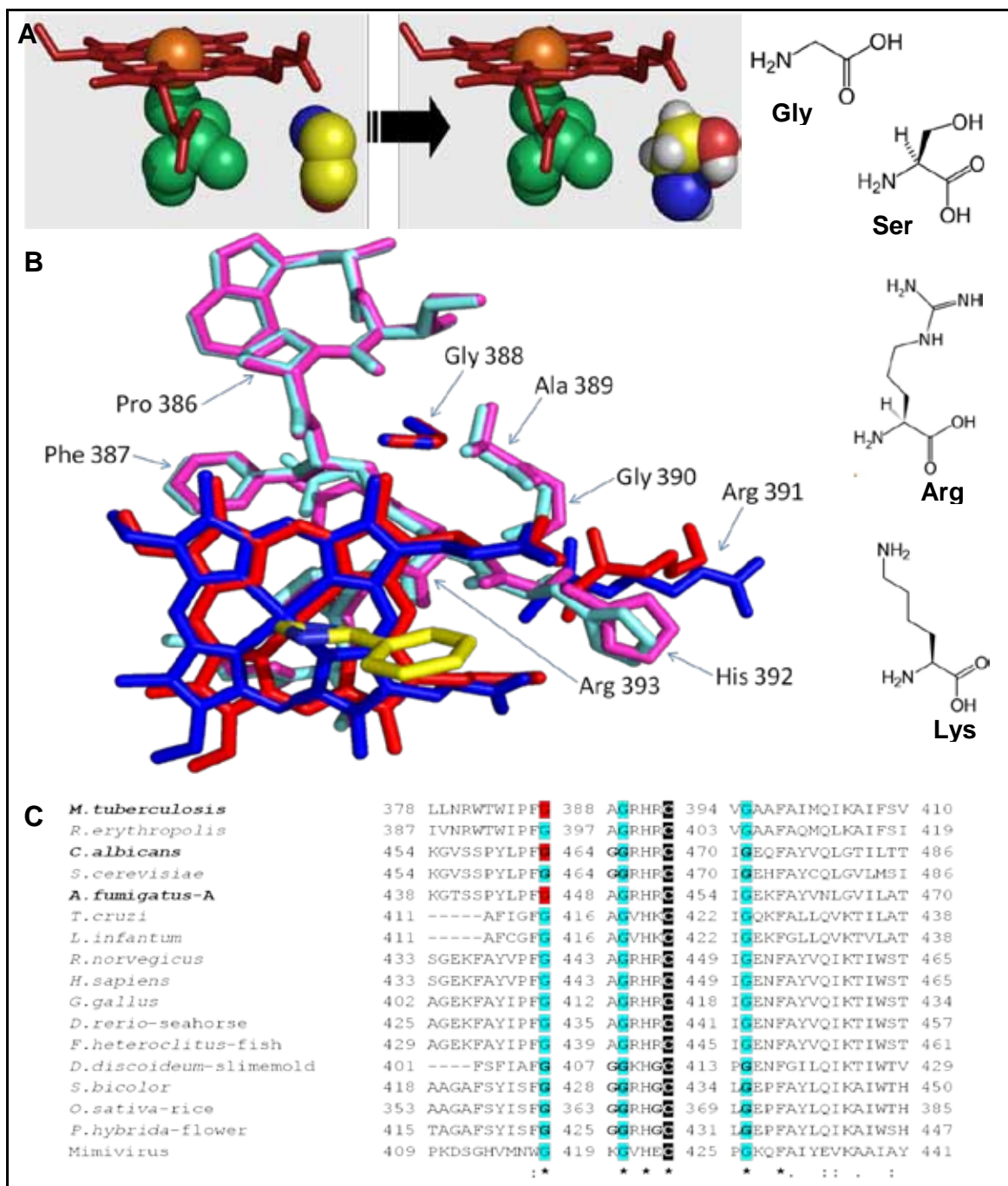


Figure 3.16: Residues at the β -bulge of the cysteinyl loop *trans* to the substrate binding site. (A) shows the substitution of glycine to serine at position 388, six residues away from the heme proximal Cys (green) ligand at position 394. Spheres representing Gly and Ser are colour coded - NH₂ (blue), C backbone (yellow), COOH and OH ends (red) and H (white). The model in (B) looks down towards the ligand free (pdb: 1h5z – WT CYP51 2.05 Å: cyan residues and dark blue heme porphyrin ring) and 4PI-bound (R391K-4PI mutant – 1.70 Å: yellow and blue 4PI, magenta residues and red heme porphyrin ring) heme of CYP51B1 and the cysteinyl loop residues close to the C394 proximal heme ligand. Structures are backbone aligned and superimposed. The network of residues at these positions (labelled) are highly conserved across CYP51 enzymes from different kingdoms, likely pointing towards retention of structure around the thiolate ligand that helps regulate the redox properties of the heme centre. (C) exhibits a multiple sequence alignment of CYP51 enzymes in the heme motif region, with the cysteinate proximal ligand highlighted in black and the highly conserved Gly residues highlighted in cyan. Gly-rich heme sites are especially prominent in CYP51 enzymes of yeasts, slime mould and plants. Gly residues highlighted in red in the *C. albicans* and *A. fumigatus* CYP51 enzymes are prone to azole-resistance conferring mutations to a Ser residue.

Assuming that the properties observed for the Mtb CYP51B1 G388S mutant are also observed for the *C. albicans* CYP51, some suggestions could be made for how this fungal mutation might affect the enzyme. (i) Assuming that, like WT CYP51B1 bound to estriol, the redox potential of fungal CYP51 G388S bound to a substrate (lanosterol or 24, 25-dihydrolanosterol) is also further increased, this could translate into a faster reduction by redox partner enzymes, and enhanced rates of 14 α -demethylation of substrate. (ii) If, due to increased heme iron potential, electron flow to the heme iron occurs even in the absence of a sterol substrate, then a non-productive reduction of molecular oxygen will occur via one of the three shunt pathways in the P450 catalytic cycle (Figure 1.5 A) and reducing equivalents will be wasted in formation of superoxide, peroxide or water. It is not immediately obvious how such thermodynamic/kinetic effects could impact on fluconazole affinity, but they might help overcome azole effects by more rapid product formation in non-azole inhibited enzymes. What remains unknown is whether the fungal G388S mutants have a lower affinity for fluconazole (the antifungal drug to which the mutant confers resistance in *C. albicans*) or voriconazole (in *A. fumigatus*), or whether structural changes in the mutants otherwise affect their relative affinities for substrate and azole(s). These phenomena are studied further on in this chapter for the Mtb CYP51B1 in interactions with azoles and its substrate.

For the R391K mutant, the ligand-free heme iron redox potential (-299 ± 4 mV) was comparable to the WT ligand-free potential. The R391K mutant's spectral properties showed differences from that of the G388S mutant. However, the R391K mutant was found to exist in an approximately 50/50 ferrous-thiolate (399 nm – P450 species) and ferrous-thiol (422 nm – P420 species) equilibrium in its reduced form, as demonstrated in Figure 3.15 (E), while the WT exhibited an ~30/70 P450 (401 nm) to P420 (425 nm) species equilibrium. For the R391K mutant, there is a slower rate constant for the P450/P420 transition (0.00044 s⁻¹) compared to WT CYP51 (0.00104 s⁻¹) (Table 3.2). The introduction of Lys at position 391 abolishes an important guanidinium arginine side chain, which is a semi-conserved residue in the CYP51 family, with the exception of CYP51 enzymes in protozoa (Val), slime mould (Lys) and mimivirus (Val), as illustrated by the multiple sequence alignment in Figure 3.16 (C). The conserved Arg at position 391 in Mtb CYP51B1 (position 467 in *C. albicans* CYP51), is adjacent to the second strictly conserved Gly residue (the middle Gly residue highlighted in the cyan column in Figure 3.16 C) and just 3 residues away from the totally conserved cysteinate proximal ligand. Lysine is also a basic amino acid, but structurally different from the more complex guanidinium group found in arginine. This structural change could potentially inhibit proton transfer to the

cysteine thiolate, hence explaining the slower protonation of the ferrous-thiolate species observed for this mutant and consistent with spectral trends from redox potential experiments and stopped-flow reduction by dithionite. The guanidinium side chain of Arg could thus have two roles at the cysteinyl loop of WT CYP51B1, i.e. (i) in forming H-bonds with adjacent amino acid side chains and (ii) in establishing an efficient proton transfer system during thiolate-thiol transitions of the reduced enzyme. The cysteinyl loop structural detail shown in Figure 3.16 (B) shows that the Arg 391 guanidinium side chain (for the WT ligand-free structure at 2.05 Å) faces outwards away from other nearby amino acids, while data from higher resolution (1.4-1.5 Å) structurally solved WT and F89H crystals from this work revealed that electron density for the Arg 391 side chain was missing, suggesting mobility of this residue. This raises some questions on the role of the guanidinium side chain in both stabilising the cysteinyl loop by H-bonds and/or in facilitating proton transfer to the thiolate side chain of Cys 394. This is further discussed in the next chapter, along with further data on solved CYP51B1 crystal structures.

Redox potentiometry analyses were also done for mutants generated in the flexible regions on the surface of the enzyme. The F89H and L100F enzymes were titrated using stocks of ~10-30 mM sodium dithionite (made up in 0.1 M KPi pH 7.5). The pH of the enzyme mixture did not vary from ~pH 7.5 during the titration. From Figure 3.17 (A, C), it can be seen that there is apparent formation of larger amounts of the ferrous-thiolate form (at ~401 nm) at earlier stages in the redox titration than are observed for the fully reduced F89H and L100F CYP51B1 enzymes. On completion of the redox titrations, these ferrous thiolate species have decreased somewhat in favour of the ferrous-thiol forms. Regardless of the kinetics of the thiol/thiolate conversions in the ferrous enzymes, both retain a small proportion of ferrous thiolate enzyme at the end of the titrations. It was found that L100F mutant had a slightly more positive redox potential to WT CYP51B1 (-239 ± 4 mV and -283 ± 3 mV, respectively), while the F89H mutant (Figure 3.17 A, B) had a more negative potential of -350 ± 4 mV. This similar redox potential of L100F to WT might have been predicted, since the mutation is situated away from the heme binding region and may not therefore impact on the environment of the heme catalytic centre. The more negative redox potential of F89H was not predicted. However, compared to previous work done by McLean *et al.* (2006c) on WT CYP51B1, the F89H potential is close to the potential reported for WT (-375 mV in the ligand-free form). Upon estradiol binding, which displaces the axial water ligand and shifts the spin state from LS to HS to yield a penta-coordinated form, the WT heme-iron redox potential increased to -225 mV, which is similar to that reported here for the L100F ligand-free mutant. This elevated potential

evidently creates a positive driving force in the electron transport chain from NADPH (-320 mV) via its redox partner enzymes, FprA (-230 mV for the 2-electron reduced FAD hydroquinone) (Fischer *et al.* 2002; McLean *et al.* 2003) and Fd1 (-31 mV) to the estriol-bound CYP51B1 (-225 mV) (McLean *et al.* 2006c), which reflects steps (ii) and (iv) of the P450 catalytic cycle (Figure 1.5 A). Spectrally, both these mutants showed similar trends to that of WT CYP51B1, with the formation of a ferrous-thiolate species at 401 nm, and the progressive conversion to the ferrous-thiol form at 422 nm (partial thiol form) and 426 nm for the F89H and L100F CYP51B1 enzymes, respectively. In the Q-band region, there was also the development of major band and a minor band at ~560 and ~535 nm, respectively, upon reduction of all mutants and the WT CYP51B1, reflecting considerable amounts of the ferrous-thiol form of the heme.

Reoxidation experiments were carried out for the reduced mutant and WT CYP51B1 with potassium ferricyanide. Reoxidised spectra were consistent with reduced spectra at the same applied potentials, thus, ruling out hysteretic behaviour. However, for the L100F mutant in Figure 3.17 (E), reoxidation of the reduced form by titration with potassium ferricyanide (using small volumes of an ~10-50 mM stock solution) demonstrated the formation (arrow) of a mixed species with Soret maxima at 396 nm and 414 nm, and the concomitant collapse of the strong Q-band feature at 559 nm also signalled the reformation of a ferric heme enzyme. Interestingly, the blue shift of the major Soret band feature to 414 nm was distinct from that of the starting form, although its positioning was likely influenced by the apparent simultaneous formation of a proportion of a HS penta-coordinated band at 396 nm. To explain this atypical reoxidised Soret band shift, further experiments were carried out on WT and mutant CYP51B1 enzymes, using a redox cycling assay.

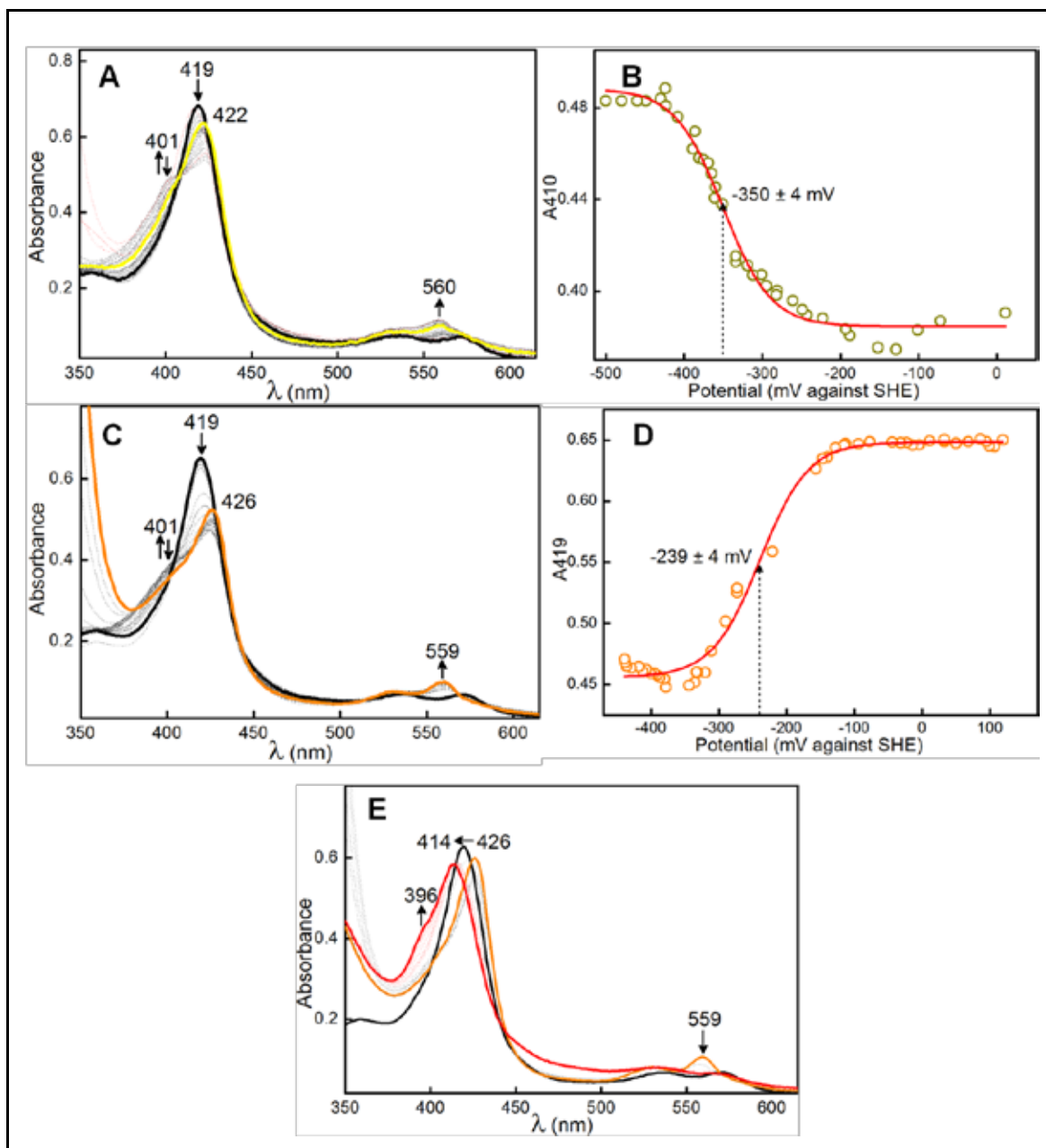


Figure 3.17: Redox potentials of ligand-free CYP51B1 B-C loop mutant enzymes. **A-B)** CYP51B1 F89H with a heme iron redox potential of -350 ± 4 mV (**B**) and the Soret band shift (**A**) from 419 nm (thick black spectrum) to 422 nm (yellow spectrum) accompanying heme iron reduction. The dotted black spectra in **A** reflect the shift of the reduced Soret peak from ~ 430 nm back to its ~ 420 nm species upon progressive reoxidation. This reoxidation step (dotted red spectra) was carried out to rule out the occurrence of hysteresis in the titration, and data analysis indicated that spectral changes were completely reversible and occurred at the same redox potentials in both directions. **C-D)** L100F CYP51B1 redox titration with sodium dithionite showing a gradual Soret red shift (oxidized enzyme in thick black spectrum, reduced enzyme in orange spectrum) with the same trend as F89H (**C**), and with a heme iron redox potential of -239 ± 4 mV (**D**). Both F89H and L100F demonstrate the formation of ferrous-thiolate form (401 nm) which collapses during reduction into a ferrous-thiol species at 422 nm for F89H (partial conversion to the thiol form) and 426 nm for L100F, comparable to WT CYP51B1's complete conversion to ferrous-thiol at 423 nm. **E)** Upon reoxidation with potassium ferricyanide, a gradual shift of the Soret band towards a shorter wavelength (426 to 414 nm) occurred, apparently with a concomitant formation of a HS component at 396 nm (red spectrum) for L100F. Dotted black spectra in **E** are intermediate spectra in the reoxidation process.

3.5.6 Redox Cycling with Chemical Reducing and Oxidising Agents

Following redox potential determination and the observation of a HS ferric species formation in L100F CYP51B1 at 396 nm upon reoxidation with ferricyanide, a diagnostic redox cycling experiment was carried out on all the mutant and WT CYP51B1 enzymes. Although spectra recorded in oxidative sections of redox titrations were generally highly similar to those recorded at the same potential in the reduction direction, the mixed formation of HS and LS species and the resulting Soret band peak position (414 nm) in the fully reoxidised L100F mutant suggested that some alterations to heme ligands might have occurred following successive reduction and oxidation of the L100F heme iron. To investigate this phenomenon further, 0.1-0.2 mg/mL of sodium dithionite was added into a solution of the enzyme, and the conversion of Fe(III) to Fe(II) heme iron was recorded until the maximum Fe(II)-thiol species was formed at 426 nm. This Fe(II)-thiol species was observed in WT and mutants, with no substantial differences in the nature and position of the reduced Soret band peak. Subsequently, 0.2 mg/mL (final concentration) of potassium ferricyanide was added to reoxidise the enzymes, with all experiments done in an anaerobic atmosphere. The enzymes were left to reoxidise at 21°C overnight and the formation of a HS species was observed to a significant extent in L100F CYP51B1 (Soret at 394 nm) and to a lesser extent in G388S CYP51B1 (at 396 nm). WT, F89H and R391K CYP51B1 enzymes did not demonstrate any notable amount of a ferric HS species at ~390 nm upon reoxidation. In addition, the reoxidised LS Soret band did not return perfectly to its native ~418-419 nm Fe(III)-resting state maximum, but instead to a shorter wavelength at 412 nm (WT), 413 nm (F89H and R391K) and 411 nm (L100F) in these experiments.

Figure 3.18 demonstrates the formation of Fe(II)-thiol (solid red line) upon reduction, collapse to Fe(III) HS or LS forms (thick blue line) upon reoxidation and once more the gradual formation of Fe(II)-thiol upon reduction (dotted red lines) for WT, L100F and G388S enzymes. When the enzymes were reduced for the second time with dithionite, a minor transient species at 463-464 nm was observed to form in all except G388S, which collapsed within 30 min into the reduction. These experiments were done in a semi-aerobic environment and there were no apparent pH changes from pH 7.5 (assay pH) prior to reduction by dithionite. The 460 nm species is not commonly recognised in reduction or CO binding experiments in P450s but due to the duration of the experiment and the presence of residual dithionite from the first reduction cycle in the enzyme mixture, it is possible that there is some formation of transient sulfur-ligated heme iron by species arising from the breakdown of dithionite. A similar suggestion was previously made for sulfur ligands binding to thiolate coordinated P450cam (Sono and Dawson 1982).

An ~460 nm species has also been observed by formation of carbene adducts from the breakdown of CO and chloroform with mammalian P450s. Some mutants of human CYP2A6 and nitric oxide synthase have also demonstrated transient Soret band splitting at ~370 and ~460 nm, which was putatively attributed to hyperporphyrin formation and bis-thiolate ligation (Gorren *et al.* 1997; Nolan 1986; Sakurai *et al.* 1990). To assess whether the CYP51B1 enzymes still retained their P450 characteristics, CO gas was bubbled into the second-round-reduced enzymes and the formation of P420 was observed (thin blue line) in WT (417 & 404 nm), F89H (417 & 405 nm), L100F (417 & 405 nm), G388S (418 nm) and R391K (417 & 405 nm) enzymes. Upon addition of estriol to reduced L100F, the same spectrum as CO-Fe(II)-bound was observed (Figure 3.18 **D**).

The entire redox cycling experiment was relatively slow and took 48 hours to complete. It was most logical to identify what caused the apparent HS formation upon reoxidation, particularly since this was not attributed to extreme pH changes (as the pH of the enzyme mixture was stable throughout the experiment). EPR analyses were therefore carried out for all reoxidised enzymes (except in the case of G388S, as no substantial HS species was detected) in order to examine the ligation states of the ferric-heme, and this is discussed in the next chapter.

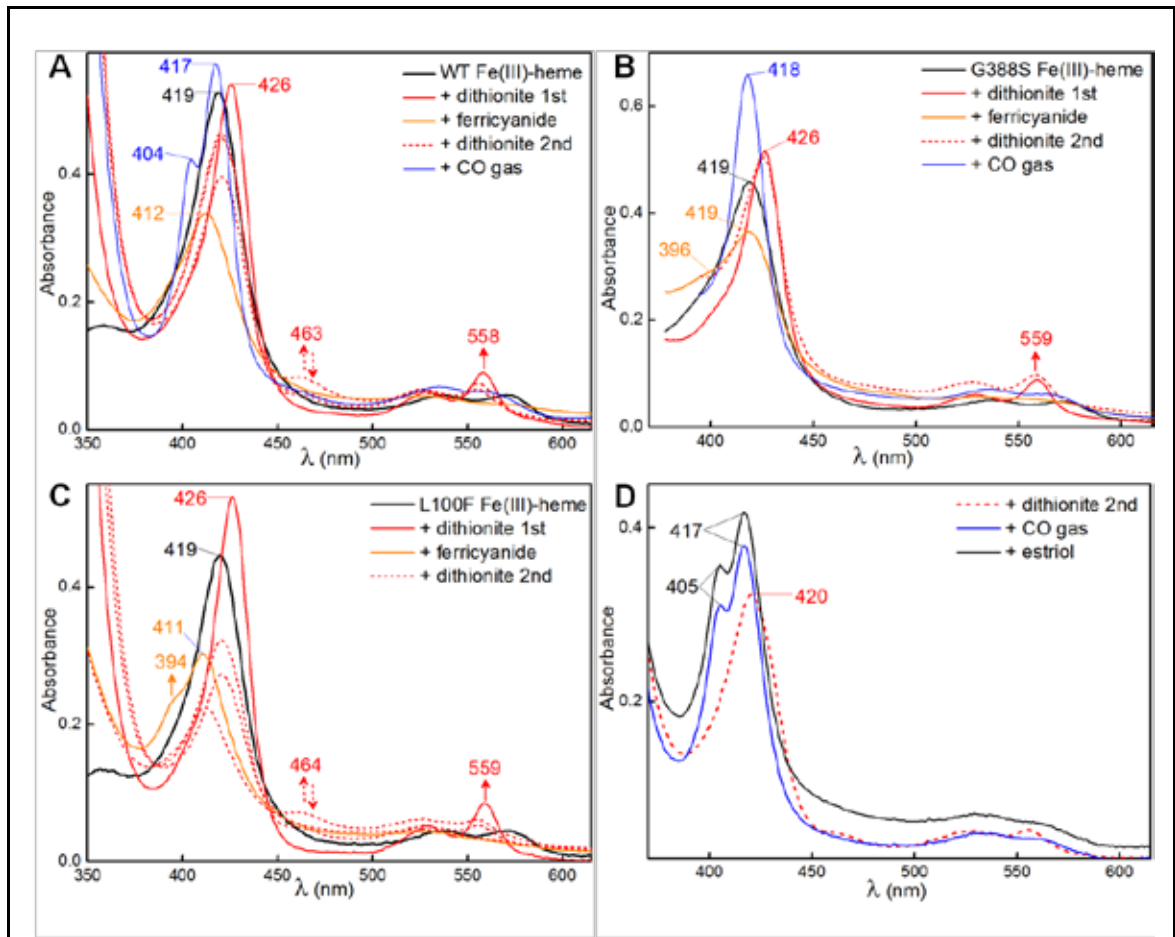


Figure 3.18: Redox-cycled CYP51B1 WT and mutants. A) F89H and R391K CYP51B1 mutants showed the same types of Soret band changes to WT CYP51B1 during the redox cycling experiment, with formation of a minor (transient) 463-464 nm species which gradually disappeared after 30 min in all enzymes, apart from G388S, where it was not observed (B). In B), G388S demonstrated clean conversions from Fe(III) to Fe(II)-thiol species and upon reoxidation showed a hint of a likely HS species at 396 nm, which was comparable to the 394 nm species in the L100F mutant (C). This HS species at ~390 nm was not observed in WT, F89H and R391K CYP51B1 enzymes. D) After the second round of reduction with dithionite, CO gas was bubbled into all enzymes, and in L100F the reduced Soret band at 420 nm shifted to a mixture of 405 and 415 nm species at ~40% to ~60% content (based on spectral intensity), respectively. Both estriol (black spectrum) and CO (blue spectrum) binding to ferrous-heme of L100F also showed the same Soret shifts trends.

3.6 Understanding the Mechanisms of Azole-Resistance in CYP51ca Using CYP51B1 as a Template

3.6.1 CYP51B1 UV-Visible Spectral Ligand Binding Properties

3.6.1.1 Photo-Diode Array Analysis of Estriol and Fluconazole Binding to CYP51B1

Parallel Photo-Diode Array (PDA) stopped-flow absorption spectroscopy studies were carried out on CYP51B1 WT and F89H mutant enzymes (post-mix concentrations at 4-5 μM) for their interactions with estriol and fluconazole, and across the 250–700 nm wavelength range to achieve full spectral acquisition describing the ligand binding events and to determine the wavelength with highest intensity spectral change, for subsequent single wavelength stopped-flow analysis. Control experiments were carried out with the solvent DMSO and assay buffer alone mixed with CYP51B1, to ensure that there were no non-specific interactions which may have resulted in spectral changes throughout the wavelength range. Essentially, the spectral observations for binding events with assay buffer and DMSO did not show any changes to the overall spectrum. Binding events over millisecond timescales with different concentrations of estriol and fluconazole were then carried out. Estriol, at 50-500 μM (post-mix concentrations, henceforth all concentrations used in stopped-flow analysis refer to post-mixing concentrations), was mixed in the stopped-flow instrument with WT CYP51B1 with analysis between 0.25-1.0 s timescales following the mixing event, and with a total of 100 spectra, and either 2.56 ms (estriol) or 5.12 ms (fluconazole) gaps between each spectrum collected.

As estriol concentration was increased in the stopped-flow mixing experiments, higher proportions of high-spin (HS) heme iron were seen to develop in the enzymes. For instance, at 100 μM estriol (concentration in the mixing chamber) negligible amount of HS heme was detected in both WT and F89H, while at 250 μM estriol clear development of HS species were observed at ~ 390 nm, and at 500 μM estriol substantial HS species development was detected at ~ 391 nm, clearly signifying type I estriol binding. Higher concentrations of estriol were not tested as the solubility of estriol is limited in DMSO (estriol is even less soluble in ethanol), and it was important to avoid estriol precipitation in the stopped-flow apparatus instrument. Precipitation of estriol could be observed by a shift in the spectral baseline at 700 nm (and turbidity at lower wavelength). Finally, 500 μM of estriol was stopped-flow mixed with both WT and F89H CYP51B1 enzymes over a 250 ms timescale with 2.56 ms between spectra, as shown in Figure 3.19. From previous studies, estriol was shown to bind to WT CYP51B1 and to induce a type I Soret band shift, with an

equilibrium K_d of $21.7 \pm 0.8 \mu\text{M}$. In contrast, the binding of the clinically relevant fluconazole inhibitor induces a type II shift and binds tighter ($K_d 3.57 \pm 0.25 \mu\text{M}$) (McLean *et al.* 2006c).

The K_d is an equilibrium binding constant, and can be described by the $k_{\text{off}}/k_{\text{on}}$ ratio (Figure 2.2). Thus, if a K_d value is low (tight binding), this means that the ligand binding rate (k_{on}) is faster relative to the ligand de-binding rate (k_{off}) than would be the case for a ligand displaying a higher K_d value. To define the K_d , stopped-flow binding experiments were done with estriol and with fluconazole at several different ligand concentrations, and apparent rate constants (k_{obs}) were determined at each concentration. A plot of k_{obs} versus [ligand] in each case then generated a straight line dependence, and a second order rate constant (k_{on}) for the ligand in units of $\text{s}^{-1} \text{M}^{-1}$. The y-axis intercept of the line gave the apparent k_{off} in units of s^{-1} , enabling the determination of the K_d . An illustration of this was shown in Figure 2.2.

For the binding of estriol, there is a rapid formation of HS penta-coordinate ferric-heme (with a signature Soret shift towards $\sim 390 \text{ nm}$) was observed from spectra collected during stopped-flow mixing at various estriol concentrations. The rapid binding of estriol was demonstrated by the very fast drop (solid black spectra to dotted black spectra) in the Soret band (Figure 3.19 A, B) and a concomitant blue shift in both WT and F89H mutant Soret spectra. The absence of any obvious gradual HS spectral change from the LS resting state (i.e. a series of spectra clearly defining the progression from the starting species to the final estriol complex) indicate that much of the estriol binding to the P450 occurs during the dead-time of the stopped-flow instrument, and that the rates observed are of the order of several hundred events per second at an estriol concentration of $500 \mu\text{M}$.

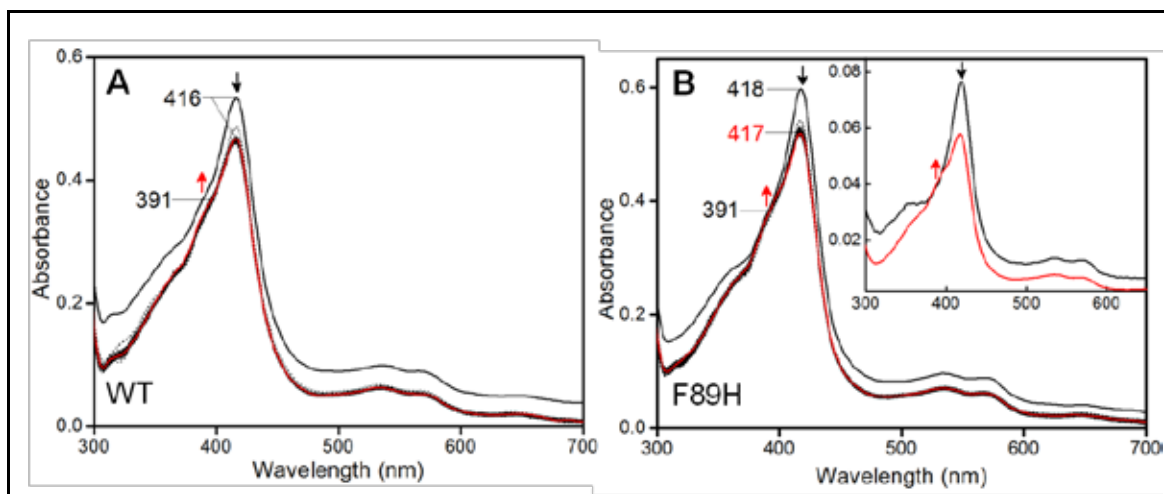


Figure 3.19: Estriol binding to WT and F89H CYP51B1 analysed by stopped-flow PDA analysis. Panels A and B show data collected from stopped-flow PDA analysis of CYP51B1 WT ($k_{\text{obs}} = 350.3 \pm 1.5 \text{ s}^{-1}$) and F89H ($k_{\text{obs}} = 258.8 \pm 1.8 \text{ s}^{-1}$) binding to estriol (500 μM) respectively. The rate constants cited are derived from fitting spectral changes to a simple A \rightarrow B model. The black line in both graphs denotes the initial spectrum for the ligand-free CYP51B1 enzymes. Dotted spectra were generated over a 250 ms timescale with multiple scanning and with each scan at 2.56 ms intervals (i.e. a total of 100 spectra). The binding of estriol induced type I spectral shifts for both enzymes, with increased HS absorbance at $\sim 391 \text{ nm}$ relative to the LS feature at $\sim 418 \text{ nm}$ (which decreases in intensity). Protein concentrations were A 4.10 μM WT and B 4.40 μM F89H in the mixture. Spectra shown were generated from Pro-Kineticist software version 1.06 (Applied Photophysics Ltd), following data export into OriginLab. The inset in panel B shows the start (black) and end (red) spectra from the global fitting process following mixing of WT CYP51B1 and F89H mutant enzymes with estriol.

The spectral data in Figure 3.19 were fitted using a global analysis ProKin software generating fitting spectra for WT and F89H (both having similar spectral trends), and giving the best fit for start and end spectra as illustrated in the Figure 3.13 (B) inset for the F89H mutant. Black arrows show the direction of LS Soret absorption change (decrease) at $\sim 416\text{-}418 \text{ nm}$, and red arrows show HS Soret formation at $\sim 391 \text{ nm}$. From this global fitting, estriol binding rates at 500 μM estriol (k_{obs}) were determined as $350.3 \pm 1.5 \text{ s}^{-1}$ for WT and $258.8 \pm 1.8 \text{ s}^{-1}$ for F89H CYP51B1, indicating very fast binding reactions. There was also a baseline shift (as seen at 700 nm) on estriol mixing, possibly due to the mixing with a hydrophobic substrate.

The next step was to analyse azole drug inhibitor binding kinetics to the CYP51B1 ferric-heme. Interestingly, not all azole inhibitors which bind to CYP51B1 produce a type II spectral shift, as demonstrated by 2-phenylimidazole (2PI) which, upon binding to CYP51B1, resulted in a HS type I Soret band shift towards 395 nm (McLean *et al.* 2006c). This uncharacteristic binding shift induced by 2PI was caused by the displacement of the 6th axial water ligand, but without direct coordination of the imidazole nitrogen to the heme-iron, producing the HS ferric-heme spectral signature (McLean *et al.*

2006c). This 2PI-bound spectral signature was very similar to the Soret band shift from equilibrium titration of estriol (a substrate analogue), which is displayed further on in this chapter. The clinically important antifungal drug fluconazole, as with various other commercially available azole-antifungal drugs, however, does cause a red shift of the Soret band, as demonstrated in Figure 3.20 for the binding of fluconazole to both WT and F89H CYP51B1 enzymes. Employing the same methods as used for estriol stopped-flow binding analysis, fluconazole (100 μM) was rapidly mixed with WT and F89H CYP51B1 (4-5 μM) and data collected over a 2 s and a 1 s timeframe, respectively. 80 spectra were collected for both mixing experiments, with a 25.5 ms gap between spectra for WT CYP51B1 and a 12.5 ms gap between spectra for F89H CYP51B1. Fluconazole, being more soluble than estriol in DMSO, did not show any noticeable precipitation problems during the experiment. Essentially, no baseline shift was observed during data collection. The type II Soret band shift (black arrows) from 418 nm to \sim 420 nm, and trough formation at 375 nm (F89H) and 376 nm (WT) demonstrated fluconazole inhibitor binding to the CYP51B1 ferric heme, reinforcing the LS form in both cases. Changes in the Q-band region (from 535 and 570 nm to 540-541 and 572 nm, respectively) are also a signature of type II inhibitor binding to CYP51B1. Data obtained were globally fitted to derive the fluconazole binding rate constants, k_{obs} , at this drug concentration, which were $24.45 \pm 0.32 \text{ s}^{-1}$ for WT and $16.67 \pm 0.13 \text{ s}^{-1}$ for F89H CYP51B1.

These fluconazole inhibitor binding rate constants were an order of magnitude slower than those for estriol binding (albeit at a 5-fold lower ligand concentration). It is possible that a faster rate constant for the binding of estriol reflects the substrate-like nature of estriol, i.e. that the structure of CYP51B1 enables more efficient access of this molecule than it does for the non-physiological inhibitor fluconazole. It would be interesting to perform competitive binding experiments with both fluconazole and estriol (or a true substrate, i.e. lanosterol or obtusifolol) to analyse spectral changes and their kinetics, but given the solubility issues for estriol this was not considered experimentally feasible.

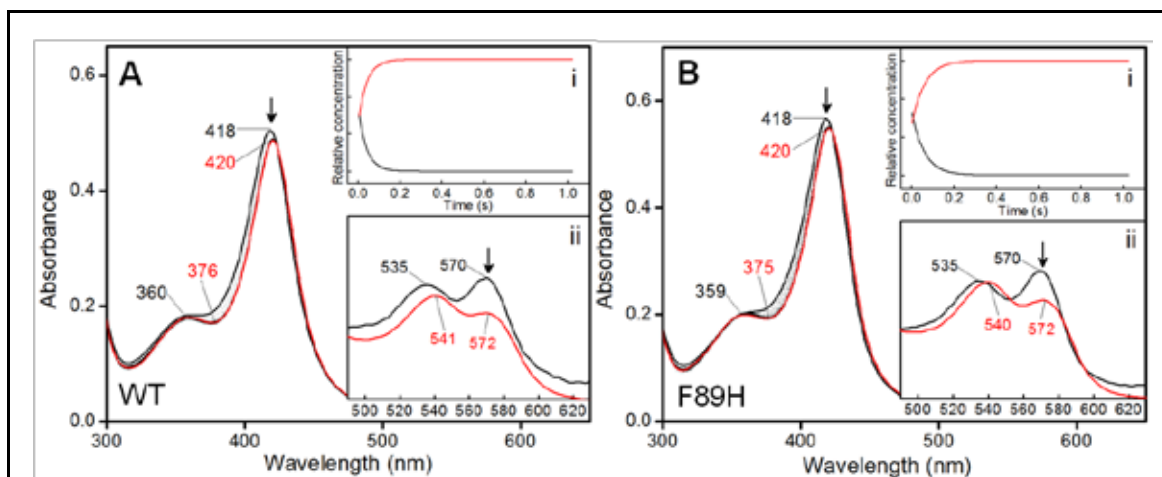


Figure 3.20: Fluconazole binding to CYP51B1 enzymes using stopped-flow global analysis. Panels **A** and **B** show CYP51B1 WT ($24.45 \pm 0.32 \text{ s}^{-1}$) and F89H ($16.67 \pm 0.13 \text{ s}^{-1}$) binding to fluconazole ($100 \mu\text{M}$) respectively. The solid black line in both graphs denotes initial spectra for the ligand-free CYP51B1 enzymes. The dotted spectra in both main graphs were generated with multiple scanning over **A** a 2.0 s timeframe with each scan at a 25.5 ms gap (total 80 spectra) and **B** a 1.0 s timeframe with scans at 12.5 ms gaps (total 80 spectra). Both experiments demonstrated type II optical shifts indicating direct ferric heme binding by an azole nitrogen group from fluconazole. Protein concentrations were **A** $4.10 \mu\text{M}$ and **B** $4.40 \mu\text{M}$. Spectra were generated from Pro-Kineticist software version 1.06 (Applied Photophysics Ltd.), with further data analysis using OriginLab. Arrows in both graphs illustrate the direction of type II Soret band shift from 418 nm to 420 nm and the development of a spectral trough at 375-376 nm. Insets (i) show the progression of formation of the final fluconazole bound complex (red line) on mixing ligand-free enzymes with the drug (time course of 1 second shown). The black lines show the corresponding data for the progress of depletion of the ligand-free heme forms. Insets (ii) are magnified spectra in the 500 – 620 nm regions, illustrating the effect of fluconazole coordination to ferric heme on the P450 Q-band absorptions.

3.6.1.2 Equilibrium Titration of Azole Drugs and Estriol

Binding of azole drugs results in a Soret shift from $\sim 418 \text{ nm}$ (for low spin P450 heme) to longer wavelengths, typically $\sim 424\text{-}425 \text{ nm}$, i.e. a red shift, often referred to as a P450 type II inhibitor binding shift. For azole-type drugs this Soret shift is typically of the order of $\sim 5\text{-}8 \text{ nm}$ (often dependent on the extent of heme iron coordination at ligand saturation), although selected studies of binding of particular P450s with certain triazoles caused a smaller shift of $2\text{-}4 \text{ nm}$ (Jackson *et al.* 2003; Pietila *et al.* 2006). Different modes of azole binding have been reported in various P450s (e.g. direct heme iron coordination, indirect coordination via the 6th ligand water or substrate-like binding without heme iron coordination). These can usually be detected spectrally, but alternate methods including alternative spectroscopic characterization or crystal structure determination have also been used to prove the nature of certain types of interactions. CYP101A1 binds to 2PI at the heme pocket while retaining the LS distal water ligand on its heme iron (Poulos and Howard 1987), while Mtb CYP51B1 interacts with 2PI with the ligand binding in the vicinity of the heme iron, displacing the distal water ligand and thus conferring a HS

spectral shift typical of a substrate complex (McLean *et al.* 2006c), and Mtb CYP121 binds indirectly to fluconazole at the heme iron, with the distal water molecule remaining in place. This mode likely explains the less extensive type II Soret shift observed for fluconazole binding to CYP121 (Seward *et al.* 2006). Mtb CYP130 (which is crystallized as a dimer) shows binding titrations with econazole that are typical of cooperative interactions between two or more molecules of the ligand, or between monomers in a CYP130 dimer (Ouellet *et al.* 2008). In addition, the structure of human CYP3A4 showed two ketoconazole molecules bound at the active site of this P450 (which has a large active site cavity), and binding studies also indicated cooperativity in ketoconazole binding (Ekroos and Sjogren 2006). There are clearly diverse types of interactions between azoles and P450s, but the majority of CYP51B1's interactions with clinically relevant azole drugs are via direct coordination of the nitrogen atom from the imidazole or triazole moiety to the heme iron, resulting in a LS hexa-coordinated ferric-thiolate species, and observed spectrally through a red shift of the Soret band. Figure 3.21 illustrates how estriol (left panel) and fluconazole (right panel) effected spectral perturbations on the Soret band of WT CYP51B1 (with their corresponding difference spectra also shown) and which classify the spectral shifts as type I (substrate-like) for estriol and type II (inhibitor-like) for fluconazole.

Substrate-bound (type I) optical changes were observed when estriol was titrated against the WT and mutant CYP51B1 enzymes. In such situations, there is a displacement of the water molecule from the resting heme iron, resulting in a Soret peak shift to ~390 nm, as shown in Figure 3.21 (A). Estriol was titrated at 0.9 μM concentration/titration point into WT CYP51B1 until a near-saturation state (130 μM estriol) was reached, at which point this sterol substrate mimic began to come out of solution, as observed by the increasing turbidity of the solution. Estriol is simpler in structure than cholesterol (or the CYP51 substrate lanosterol). It contains the principal sterol rings, but misses the long hydrocarbon side chain. This simpler structure, and the presence of a hydroxyl group instead of the hydrophobic side chain, makes estriol a little more soluble and more compatible with binding to CYP51B1 in aqueous solution, and thus easier to work with as a substrate mimic with which to determine K_d values for a substrate-like molecule.

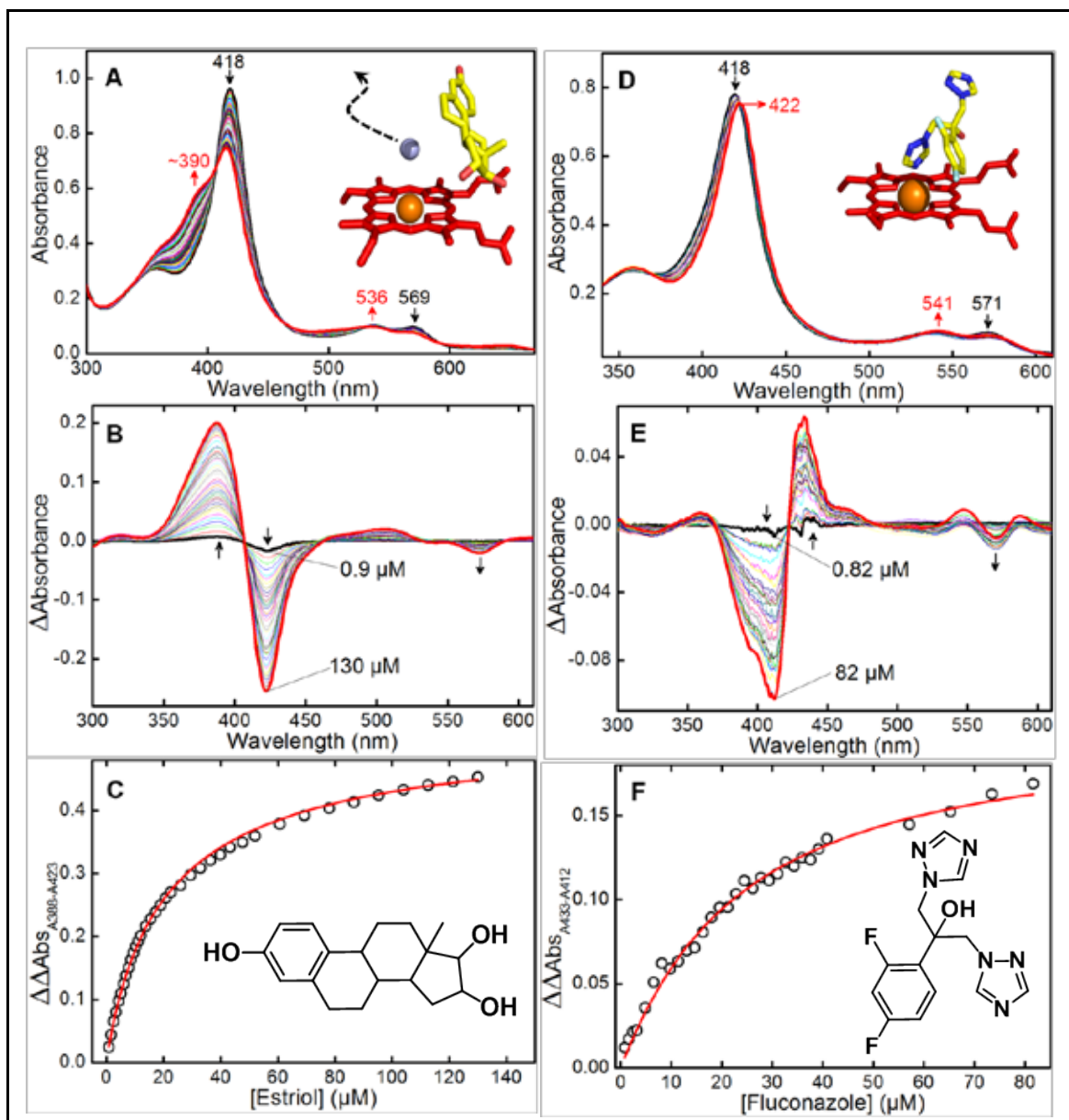


Figure 3.21: Spectral changes in CYP51B1 displaying type I and type II Soret band shifts. Panel on the left (A-C) demonstrates type I Soret band shifts upon titration of the substrate analogue estriol, which binds close to heme iron and induces the displacement of the sixth distal ligand water (inset A). Absolute spectra are shown in (A), with various microlitre volumes of estriol dissolved in DMSO titrated to give each spectrum shown. The related difference spectra, confirming a type I shift, were generated (B), demonstrating the progressive spectral shift (arrows) as the titration progresses to completion. Ligand concentrations used in the first and last difference spectrum shown are given. Panel C shows a plot of the absorbance difference between peak and trough in each difference spectrum, with data fitted to the quadratic function (Equation 2.2) to obtain the dissociation constant, K_d , which was $20.55 \pm 1.65 \mu\text{M}$ for estriol binding to WT CYP51B1. The panels on the right (D-F) demonstrate the type II Soret band shift upon titration with microlitre volumes of fluconazole inhibitor (dissolved in DMSO). In this case the ligand coordinates directly to the heme iron (inset D). A set of difference spectra (E) was generated, again confirming a typical type II spectral shift (arrows). Ligand concentrations used in the first and last difference spectrum shown are again given. Panel F shows a plot of the absorbance difference between peak and trough in each difference spectrum, with data fitted to the quadratic function (Equation 2.2) to obtain a K_d of $20.49 \pm 1.34 \mu\text{M}$ for fluconazole binding to WT CYP51B1.

Optical titrations with other azoles (performed in similar fashion to those described above) enabled determination of K_d values for a range of imidazoles and triazoles binding to CYP51B1 enzymes. Considerable differences were noted for the azole K_d values between WT and the mutant CYP51B1 enzymes, as tabulated in Table 3.5. For mutants at the SRS 1 region alone (F89H and L100F), there were some considerable variations in K_d values for the binding to azole drugs and estriol compared to the wild-type CYP51B1, suggesting significant changes to the active site structure and/or ligand access/exit routes in the mutants.

Both these mutations are situated at crucial semi-conservative regions of the B-C loop, $\alpha B'$ and αC and the nearby αD , as shown in the MSA in Figure 1.11. Since the L100F mutant is a manifestation of **WT CYP51A1 of *C. albicans*** (will be termed **CYP51A1** or simply CYP51ca henceforth), the weaker binding of azole drugs to this mutant enzyme could be a major reason for the difference between azole drug affinities between CYP51A1 and CYP51B1 isozymes. The K_d values were also different between the two mutants at the cysteinyl loop region, i.e. G388S and R391K. The latter generally binds tighter to estriol and azole drugs (except for econazole and miconazole) than does the heme-depleted G388S mutant.

Two recurring azole-resistance mutation hot-spots in CYP51A1 occur at positions F145 and D153 (which correspond to L100 and E108 in CYP51B1 of Mtb) and are mutated to L145 and E153 in azole-resistant strains, as illustrated in Figure 1.10 (B) (Podust *et al.* 2001). Thus, these *C. albicans* mutations appear to install residues already found in WT CYP51B1 in the comparable positions. This would mean that WT CYP51B1 has similar residues at these positions to a potential “double azole-resistant” mutant of CYP51A1, while the L100F mutant of CYP51B1 (generated in this study) could model an “azole-susceptible” (WT) form of CYP51A1. It was found that the CYP51B1 L100F mutant bound azoles more tightly compared to WT and the other mutants, which could be considered consistent with it being a model of a CYP51A1 azole-susceptible isoform. Table 3.5 summarizes the K_d values for CYP51B1 mutants from equilibrium binding studies with six azole drugs and with estriol. Structures for the various drugs and the estriol substrate analogue used in this experiment are shown in Figure 3.22. Across the board, fluconazole binds more weakly to WT and CYP51B1 mutants in comparison to the five other azoles, ketoconazole, voriconazole, clotrimazole, miconazole and econazole, as represented by higher K_d values for fluconazole binding. Enzyme concentrations used in these experiments varied, but since the quadratic equation (Equation 2.2) takes into account the concentration of enzymes used in these experiments (unlike the standard hyperbolic binding equation),

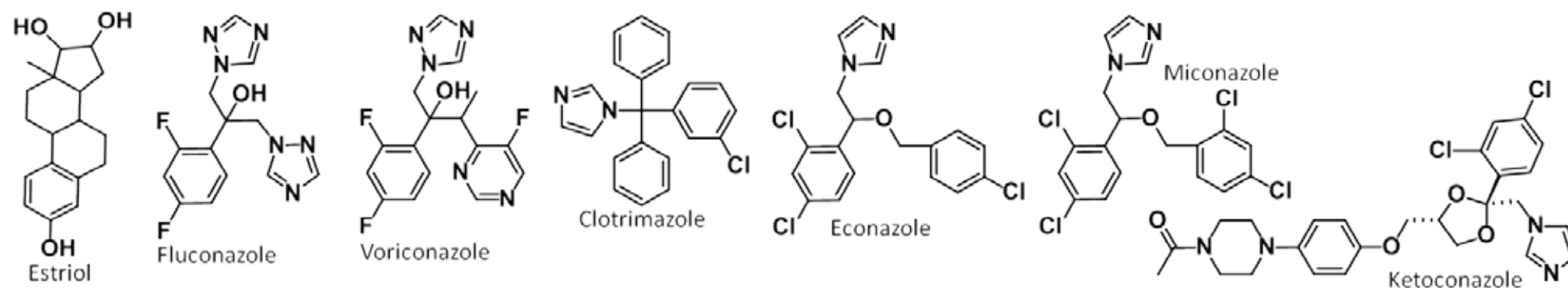
the differences between the enzyme concentrations over the various experiments with WT and mutant CYP51B1 enzymes are accounted for, and should not impact on accurate determination of K_d values. WT ($20.55 \pm 1.65 \mu\text{M}$) and F89H ($22.41 \pm 1.32 \mu\text{M}$) had similar K_d values for estriol binding, while R391K exhibited a slightly higher K_d value ($29.19 \pm 0.77 \mu\text{M}$). Interestingly, the L100F-estriol K_d was double that of WT and F89H ($41.22 \pm 0.72 \mu\text{M}$) showing that the azole-resistance mutations at the SRS 1 region (i.e. F89H and WT – by comparison to CYP51A1 sequence in this region) produced tighter binding for this substrate analogue, suggesting that improved substrate recognition/affinity (and, possibly, flexibility of the B-C loop region) may have occurred by the substitution of His at position F89 (Y132) and, by extension, the presence of Leu at L100 (F145) and Glu at E108 (D153) of the F89H mutant enzyme (which may thus be considered a putative fluconazole-resistant “triple mutant” enzyme derivative of CYP51A1). Thus, WT CYP51B1 may already, by default, have a “fluconazole-resistant” substitution with Glu at E108 (D153), despite the fact that both Glu (E) and Asp (D) share similar properties, making it comparable to an existing fluconazole point-resistant mutant of CYP51A1. These described fluconazole-resistant mutations in the F89H mutant enzyme are all located at an important substrate entry channel of CYP51B1, allowing ligand entry via the B-C-loop region, but not necessarily influencing azole coordination with the heme iron.

Conversely, the G388S mutant at the cysteinyl loop showed weaker binding ($78.75 \pm 7.44 \mu\text{M}$) to estriol compared to the L100F and R391K CYP51B1 enzyme (the latter a mutant only 3 residues away), possibly as a consequence of the changes in its heme environment that is also seen to give rise to instability in heme binding. The Gly residue is highly conserved at this position in the CYP51 family of enzymes.

Table 3.5: Dissociation constants of CYP51B1 WT and mutants from equilibrium binding analysis at pH 7.5.

Ligand	WT K_d (μM)	[WT] (μM)	F89H K_d (μM)	[F89H] (μM)	L100F K_d (μM)	[L100F] (μM)	G388S K_d (μM)	[G388S] (μM)	R391K K_d (μM)	[R391K] (μM)
Estriol	20.55 \pm 1.65	4.49	22.41 \pm 1.32	8.27	41.22 \pm 0.72	5.8	78.75 \pm 7.44	5.84	29.19 \pm 0.77	6.05
Fluconazole	20.49 \pm 1.34	5.89	10.20 \pm 0.20	3.40	4.59 \pm 0.35	6.35	13.24 \pm 0.34	1.40	8.19 \pm 0.28	6.09
Voriconazole	2.10 \pm 0.16	5.96	1.59 \pm 0.05	2.20	0.31 \pm 0.02	5.70	3.87 \pm 0.12	1.70	0.94 \pm 0.05	6.01
Clotrimazole	0.18 \pm 0.03	4.57	0.13 \pm 0.01	2.30	0.05 \pm 0.01	5.82	0.94 \pm 0.02	1.60	0.065 \pm 0.005	6.17
Econazole	0.67 \pm 0.08	4.54	0.58 \pm 0.04	2.60	0.23 \pm 0.03	5.40	0.24 \pm 0.02	1.60	0.49 \pm 0.04	6.09
Miconazole	1.25 \pm 0.16	5.54	0.36 \pm 0.04	2.10	0.11 \pm 0.01	5.71	0.58 \pm 0.05	1.40	1.03 \pm 0.04	6.09
Ketoconazole	4.55 \pm 0.27	5.71	1.10 \pm 0.07	2.30	0.64 \pm 0.03	6.40	9.77 \pm 0.74	1.50	3.28 \pm 0.07	6.16
4-phenylimidazole	390.9 \pm 23.2	5.35	n/a	n/a	n/a	n/a	n/a	n/a	545.04 \pm 9.78	5.87
EPBA	1.31 \pm 0.12	5.35	n/a	n/a	n/a	n/a	n/a	n/a	1.17 \pm 0.05	5.05

Note: The concentrations (μM) of enzymes used in the various experiments are indicated as '[WT]' *etc.* Colour coded shades are assigned to each isoform and will be employed throughout this thesis where possible. To be noted is that the L100F CYP51B1 mutant is comparable to the WT *C. albicans* CYP51 (azole-susceptible) enzyme, while WT and the remaining mutants mimic the azole-resistant forms.

**Figure 3.22: Structures of selected azole drugs and the substrate analogue estriol used in CYP51B1 ligand binding studies.**

Note the differences between imidazole type drugs (2 nitrogens in azole ring) and the triazoles (fluconazole and voriconazole, with three nitrogens in the heme coordinating azole ring).

It might have been predicted that in the “azole-resistant” mutants of CYP51B1, these azole drugs would bind less tightly (larger K_d values) compared to estriol. However, it should be remembered that estriol is not a true substrate for these enzymes. In addition, it is not clear (for the *C. albicans* CYP51A1 enzyme) what is the exact extent of diminution of affinity for fluconazole (or other azoles) in the various mutants, or indeed how the K_d values for estriol or lanosterol vary. The resistance of the *C. albicans* CYP51A1 mutants towards the azole drugs may seem questionable, because the relevant Mtb CYP51B1 mutants actually bound tighter to azole drugs (except for the small 4PI molecule and for fluconazole with WT, whose K_d was comparable to that for estriol for WT CYP51B1). However, detailed analysis of the true affinity for fluconazole and several other azoles is absent for the CYP51A1 mutants. The finding that various azole drugs bind tightly to WT and mutant CYP51B1 enzymes, however, does point to their potential usefulness as potent inhibitors of CYP51 mechanism either *in vitro* or *in vivo*. It is possible that these *in vitro* experiments do not necessarily mirror the intracellular environment (where other proteins may also have affinity for the azoles), thus possibly making the K_d values determined here slightly misleading with respect to comparative intracellular values. Also, it should be borne in mind that estriol is not a true substrate for CYP51B1, and thus that relative affinities of mutants versus WT CYP51B1 for this molecule may not correspond directly to those for the known sterol substrates (e.g. lanosterol, dihydrolanosterol or obtusifolliol). Structural comparisons of estriol with the preferred obtusifolliol substrate are shown in Figure 1.9 and Figure 3.28, and these may have substantial effects on the binding of these substrate molecules that are compounded by mutations in key regions of CYP51B1. Further variations from *in vivo* conditions relate to use of DMSO solvent in these *in vitro* experiments, and another factor could be temperature.

However, these equilibrium binding experiments and the K_d values derived from these studies serve as a tool to decipher the azole drugs' affinity for heme iron in WT and mutant CYP51B1 enzymes, and are useful to guide further stopped-flow kinetic assays with these azole drugs by identifying wavelengths (of maximal change) at which K_d values can be determined through transient kinetic experiments. Comparisons between azole K_d values from equilibrium binding and stopped-flow experiments are discussed later in this chapter.

Importantly, all the azole drugs elicited a type II Soret band shift in WT and mutant CYP51B1 enzymes, while estriol elicited a type I Soret band shift. Type I spectral shifts upon binding estriol varied only slightly among the mutants, as depicted in Figure 3.23 (A, B). While the extent of accumulation of HS penta-coordinated ferric-heme at 394 nm was most pronounced in L100F CYP51B1 on estriol binding, the difference spectra for

all mutants and WT clearly demonstrated type I binding behaviour in all cases (Figure 3.23 C-F). In studies of estriol binding by stopped-flow PDA, 500 μM estriol was the final concentration used. However, in equilibrium binding studies, 130 μM (WT Figure 3.21 A) and 139 μM (F89H Figure 3.23 A) estriol was the final concentrations used, which resulted in near-maximal spin-state conversion. Stopped-flow studies did not appear to show the same extent of heme HS formation (at ~ 390 nm) as in equilibrium binding studies for CYP51B1 enzymes, even though higher concentrations of estriol were used than in the equilibrium binding experiments. This may be a consequence of the limited solubility of estriol in aqueous solution, and possibly due to influence of differing final concentrations of DMSO solvent ($\sim 50\%$ of total volume in stopped-flow mixing chamber).

However, regardless of issues of solubility of estriol and possible influences of the use of DMSO and its affect on CYP51B1 heme stability, the following conclusions can be drawn from the stopped-flow and equilibrium binding studies with estriol: (i) estriol is bound by CYP51B1 WT and mutants in a substrate-like manner, eliciting a type I spectral shift, (ii) the mutations created to mimic azole resistance conferring mutations in CYP51A1 had no substantial effect on these enzymes binding estriol in a substrate-like manner, and (iii) estriol binding is rapid in WT and mutant CYP51B1 enzymes.

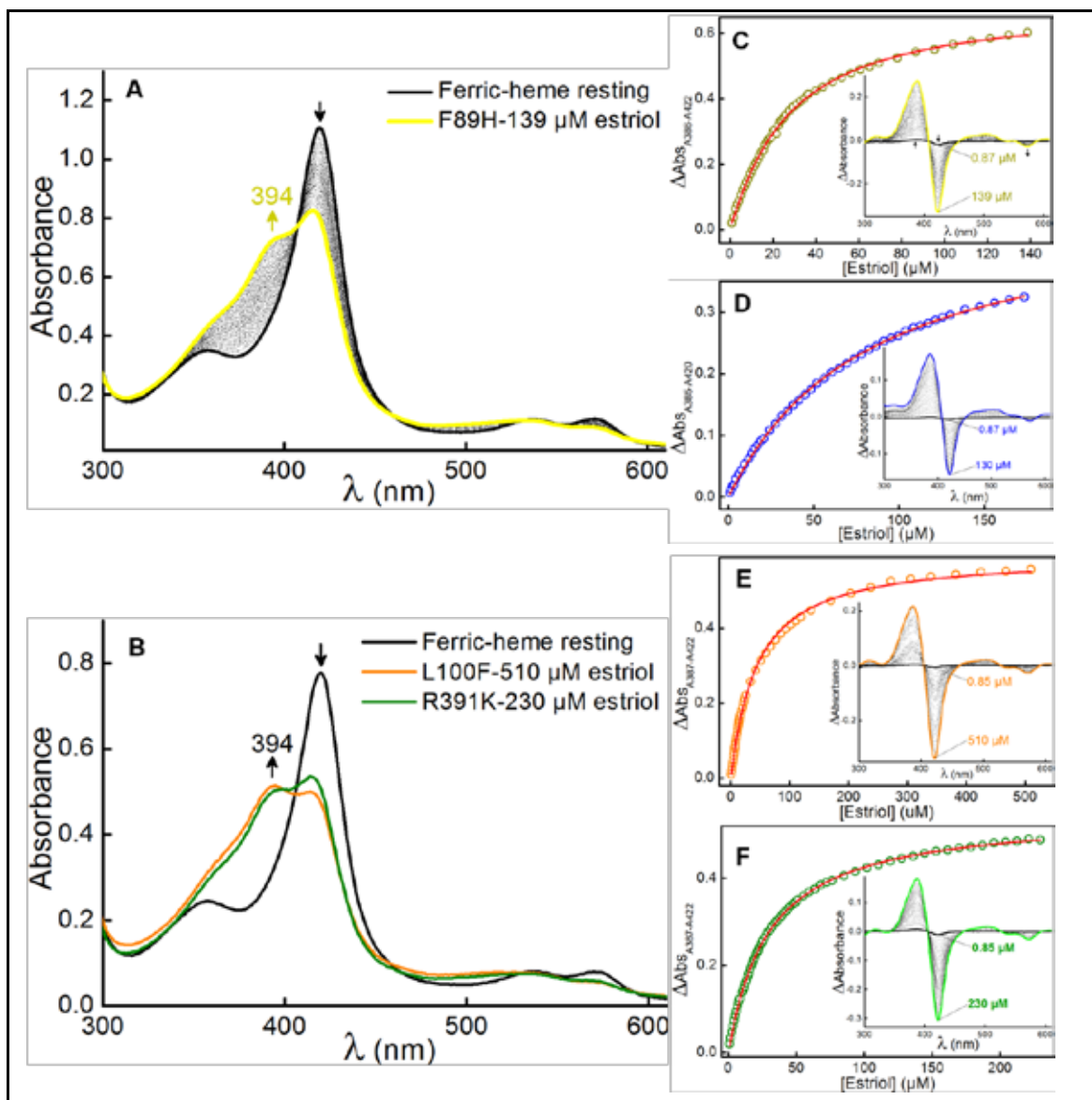


Figure 3.23: Optical titrations of CYP51B1 enzymes with the substrate-like analogue estriol. A) A F89H CYP51B1 estriol equilibrium binding curve showing a type I Soret band shift from the starting species (solid black spectrum, 8.2 μM enzyme) through intermediate points (dotted black spectra), until final, the near-saturated titration spectrum at 139 μM estriol (yellow spectrum). B) The L100F (orange spectrum) and R391K (green spectrum) final spectra at the end of an estriol titration show the high spin penta-coordinated ferric heme species signal at 394 nm. The black spectrum shows the starting (ligand-free) spectrum in the case of the L100F mutant (5.8 μM enzyme). Panels on the right illustrate F89H (C), G388S (D), L100F (E) and R391K (F) equilibrium binding curves with estriol, fitted (red line) to the quadratic function (Equation 2.2) to obtain K_d values for estriol. The respective initial (solid black spectra) and final (coloured spectra) estriol titration spectra are shown in insets (C-F) as difference spectra (with the respective estriol concentrations noted), with intermediate difference spectra shown as dotted black spectra).

While performing optical titrations with azole drugs on WT and mutant CYP51B1 enzymes, it was considered that mutations below the heme macrocycle at the cysteinyl loop region might be more “sensitive” to ligand binding (e.g. in terms of heme stability), noting their proximity to the cysteinate ligand on the other side of the heme to the coordinating site for inhibitors. While WT and other mutants showed typical type II spectral shifts of the Soret band (to ~422 nm, with a small loss in Soret intensity) (Figure 3.21 D), the G388S mutant demonstrated a distinctive type II Soret band shift upon ligating to fluconazole ($K_d = 13.24 \pm 0.34 \mu\text{M}$). This occurred without the slight drop in Soret peak intensity (as illustrated by an arrow in Figure 3.24 A), but with a typical peak maximum shift from 418 nm to 422 nm. This small drop of Soret intensity was also not observed for G388S CYP51B1 on binding voriconazole ($K_d = 3.87 \pm 0.12 \mu\text{M}$), also a triazole drug. A slightly larger shift of the Soret band with a drop in its intensity was seen when clotrimazole ($K_d = 0.94 \pm 0.02 \mu\text{M}$), and other imidazole-type drugs, were titrated to G388S, with the Soret band shifting from 418 nm to 426 nm. For G388S, this mutation is within the heme binding motif region, and thus not at a substrate entry port for the protein. Thus, effects on azole affinity are difficult to predict from first principles. It was observed that the tested imidazole drugs bound more tightly to ferric heme compared to the triazoles. Among the imidazoles, ketoconazole bound weakest to WT and mutant CYP51B1 enzymes. Ketoconazole, with an extended hydrophobic structure, is a bulky azole. Due possibly to a wider opening at the B-C-loop region in the F89H mutant, the entry of larger and bulkier molecules into the active site may be facilitated, and thus affinity of ketoconazole may be improved. This could explain the tighter binding of ketoconazole to F89H than to WT CYP51B1. The larger Soret shift (~419 nm to 425 nm) upon azole drug binding occurred only for imidazole type drugs, and was observed in Soret band absolute spectra for CYP51B1 WT and mutants bound to clotrimazole, econazole, miconazole and ketoconazole. The triazole type drugs, fluconazole and voriconazole, demonstrated a smaller Soret shift from ~419 nm to 422 nm, consistent with previously reported studies on Mtb CYP51B1 and CYP51 enzymes from *M. smegmatis* and *M. avium* (Jackson *et al.* 2003; McLean *et al.* 2006c; Pietila *et al.* 2006). This might suggest that the presence of a third nitrogen atom in the triazole ring might destabilise these triazole drugs’ coordination to CYP51B1 ferric heme. However, other explanations include incomplete coordination (i.e. different binding modes for bound triazoles) and coordination occurring via the 6th water ligand – as was seen for CYP121 with fluconazole (McLean *et al.* 2002; Seward *et al.* 2006).

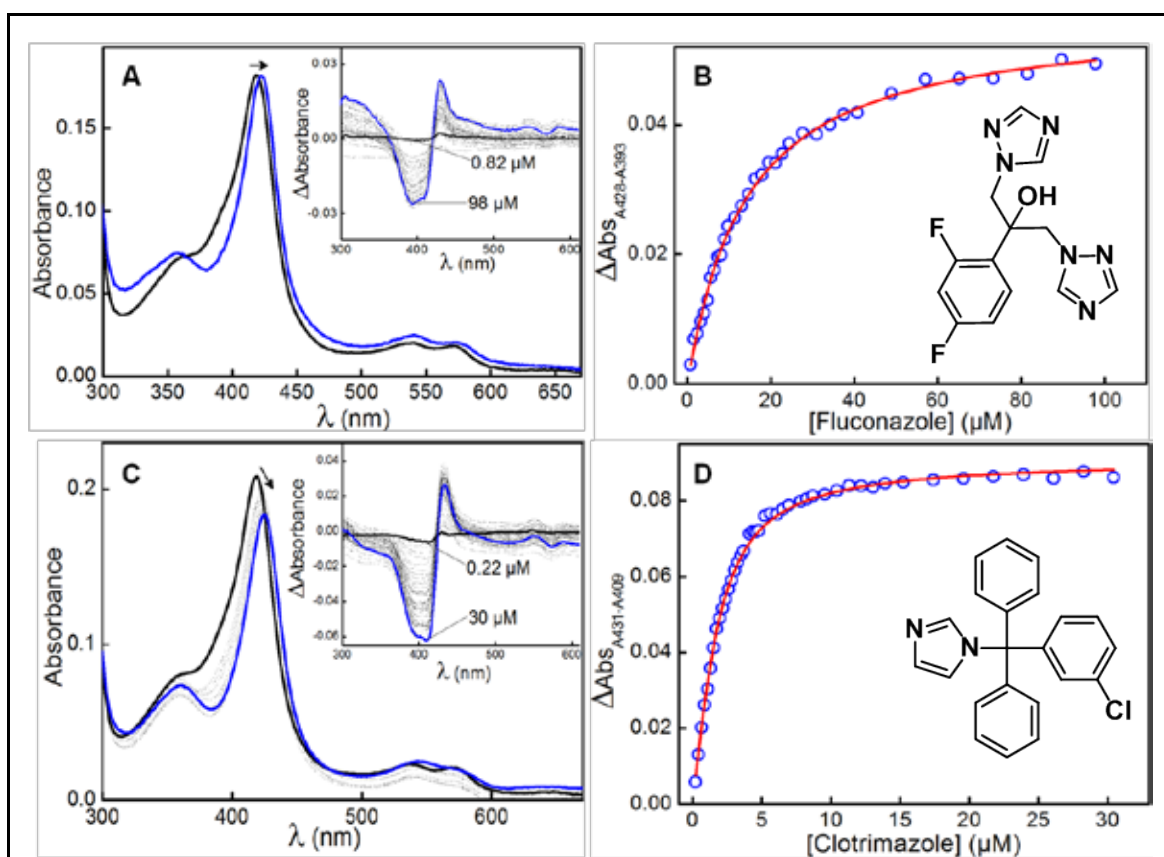


Figure 3.24: Optical titrations of the G388S CYP51B1 mutant with azole inhibitors.

A) Optical titration of G388S (1.4 μM) with fluconazole (a triazole) yielding a K_d of 13.24 ± 0.34 μM , and illustrating a type II Soret shift from 418 nm to 422 nm. The graph inset in **A** shows the optical difference spectra from different stages in the titration, with the first titration spectrum collected at 0.82 μM fluconazole (solid black line) and the final spectrum collected at 98 μM (blue line). **B)** The equilibrium binding plot was generated by subtracting A393 from A428 in each case, then plotting these values against the relevant ligand concentration to obtain a hyperbolic dependence. The chemical structure of fluconazole is also shown. **C)** Typical type II spectral changes (Soret shift from 418 nm to 425 nm) due to the binding of the azole inhibitor clotrimazole (an imidazole) to G388S CYP51B1 (1.6 μM) are shown. The black spectrum is for the ligand-free form, dotted black spectra are for intermediate points in the titration, and the blue spectrum is for the near-saturated ligand-bound form of the P450. **D)** The equilibrium binding plot for clotrimazole was generated by subtracting A393 from A428 in each case, and data points were plotted against relevant ligand concentrations and fitted to quadratic function, Equation 2.2, to give a K_d of 0.94 ± 0.02 μM . The structure of clotrimazole is shown as an inset in **D**.

In the case of the R391K mutant, when compared to WT and the two other stable mutants F89H and L100F, a similar red shift of the Soret band (when titrated with fluconazole and other azole drugs) was observed. However, in contrast to the previous G388S-fluconazole results, the decrease in the Soret peak intensity (on ligand saturation) was more pronounced (and consistent) when the same concentration of drugs and solvents were used for this mutant. This can be seen in Figure 3.26, where the R391K CYP51B1 titrations with fluconazole and miconazole are compared to L100F CYP51B1 using similar amounts of drugs and solvent concentrations. This could suggest that the introduced K391 residue (3 residues away from the proximal ligand) might destabilise the heme ligation somewhat in the azole complex, or else this residue might otherwise influence the heme absorption coefficient for the complex.

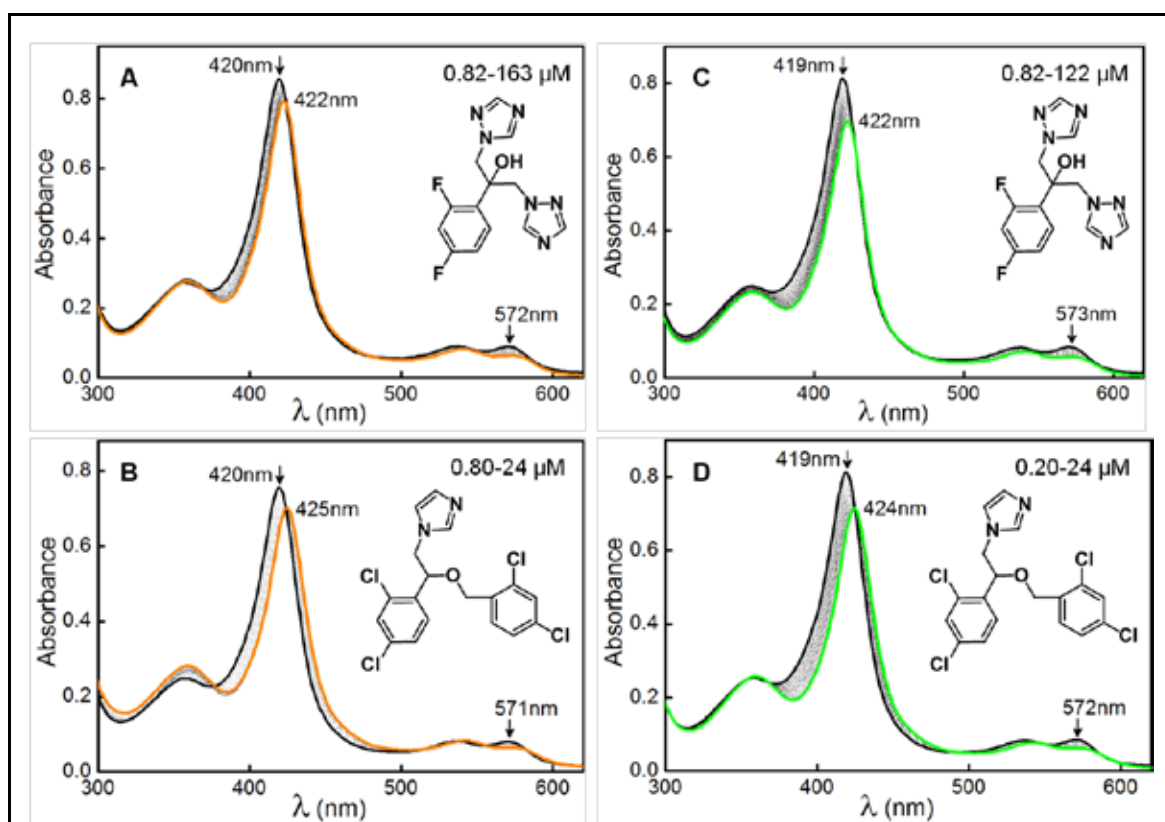


Figure 3.25: Optical titrations of L100F and R391K CYP51B1 mutants with azole inhibitors. Panels on the left show optical titrations of the L100F (6.35 μM , solid black line) mutant enzyme with fluconazole (inset **A**) at 0.82 μM initial concentration and at each titration point (dotted black line spectra) until near-saturation at 163 μM total fluconazole concentration (orange line). A type II Soret shift from 420 nm to 422 nm was observed. Panel **B**) shows L100F (5.71 μM) titrated with miconazole (inset **B**) at an initial concentration of 0.80 μM until near-saturation at 24 μM (orange line), where the Soret band shifted from 420 nm to 425 nm. Panels on the right (**C** and **D**) are optical titrations with the aforementioned azole drugs with the R391K (6.09 μM for both **C** and **D**), and with CYP51B1 mutant demonstrating similar Soret band shifts for the triazole (**C**) and imidazole (**D**) drugs. **C**) Fluconazole was titrated at an initial concentration of 0.82 μM until near-saturation at 122 μM , while miconazole (**D**) was titrated initially at 0.20 μM until near saturation at 24 μM . The ligand-free enzymes are shown as solid black line spectra, intermediate concentrations of azoles are represented by dotted black lines, and the near-saturated spectra are shown as green spectra in both cases. All azole drugs were dissolved in DMSO.

3.6.1.3 Stopped-Flow Analysis of Azole Drugs

Analysis of reaction processes by stopped-flow methods enables analysis of CYP51B1 reaction rates down to the millisecond timescale (typically up to $\sim 700\text{ s}^{-1}$). The positive points from use of this method are that it enables a rapid mixing of CYP51B1 enzymes with the relevant azole inhibitors at different concentrations, in order to determine directly the kinetic components of the K_d , which are k_{on} and k_{off} values from the second order dependence of k_{obs} versus [azole], as described in the Methods chapter. However, as previously shown, this method has its limitations in that reactions on a very fast time scale might fall into the dead-time (i.e. the time for the mixing event) and be immeasurable, e.g. for the apparently very fast binding of estriol to WT and F89H enzymes analysed using PDA stopped-flow analysis (section 3.6.1.1).

Therefore, stopped-flow assays using the PDA monochromator detector unit were not done for estriol binding, as it was considered that reactions might be completed too quickly for analysis of complete spectral changes. Instead, analysis of the binding of azole drugs to CYP51B1 enzymes was done by stopped-flow mixing, using single wavelength data to report on the formation of the azole complexes. This approach enables capture of more data points at the selected wavelength than would be the case for PDA studies, and thus facilitates a more thorough analysis of absorbance changes over a short timescale. Following stopped-flow experiments, data fitting for individual reaction transients (ΔAbs versus time) was done using both single (SE) or double exponential (DE) functions. Thereafter, the various k_{obs} values obtained from these fitting procedures were plotted against the relevant azole drug concentrations, as shown in Figure 3.26 for fluconazole and econazole with the L100F mutant. Linear correlations were obtained for k_{obs} values derived from fitting to the SE function (**C**) and to the first rate (k_{obs1}) from the DE function (**A**), but there was no apparent dependence of k_{obs2} on fluconazole concentration (**B**). Some differences were noted in the K_d values computed (i.e. SE K_d was higher than DE K_d derived from data using the k_{obs1} fit), although deviations were to be expected once attempts were made to fit progress curves to a multiphasic process.

Since k_{obs} values obtained from SE fits provided better k_{obs} versus [azole] fits to the linear function, all k_{obs} values for subsequent experiments were derived from fitting to the SE function, in order to maintain uniformity of results. The fact that the slower rate constants (k_{obs2}) obtained from fits to the biphasic expression did not show any clear dependence on [azole] also suggested that these may be related to a different phenomenon,

e.g. protein structural changes in adaptation to the ligand binding that also influence the absorption change.

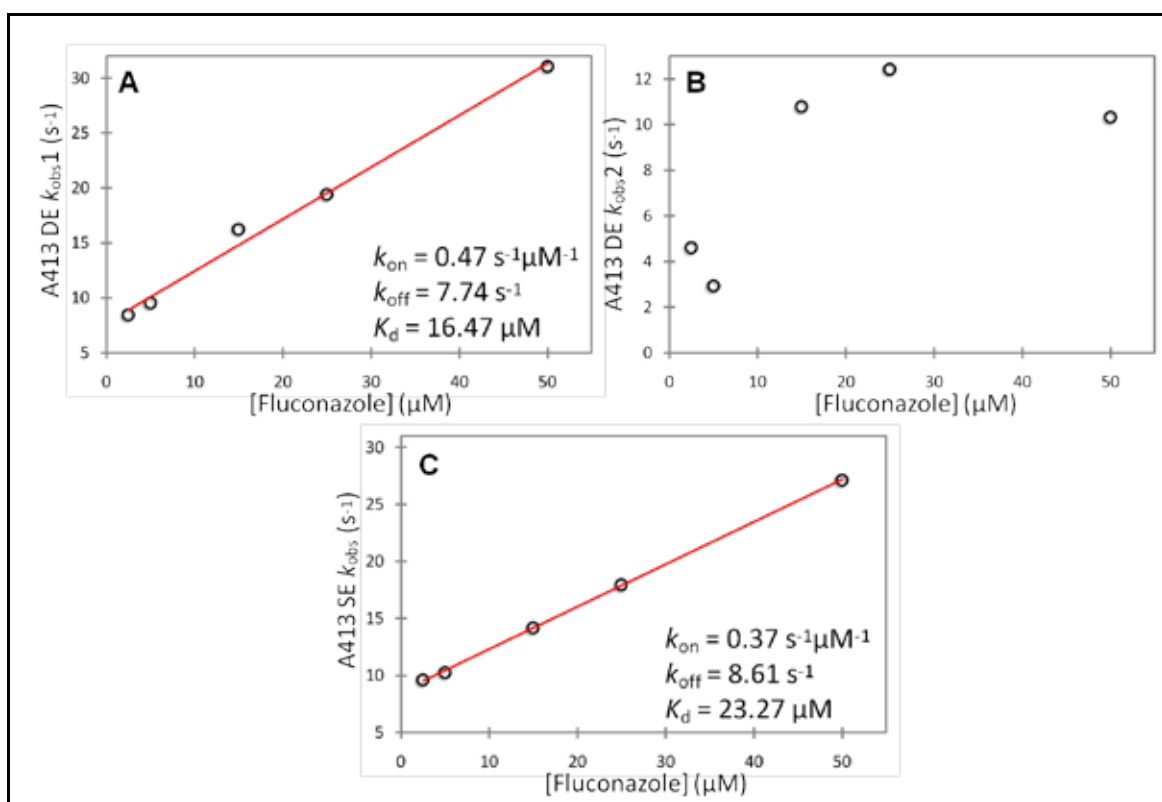


Figure 3.26: Plots of apparent azole drug-CYP51B1 binding rates (k_{obs}) versus azole concentration. Data were collected using single wavelength stopped-flow absorption spectroscopy (as change of absorbance at 413 nm against time in milliseconds) for the binding of fluconazole to the CYP51B1 L100F mutant. The reaction transients were thereafter fitted using either a single exponential (Equation 2.1) or a double exponential equation (Equation 2.3) to obtain the observed binding rate constants (k_{obs} or k_{obs1}/k_{obs2} , respectively). The above plots of k_{obs} values versus fluconazole concentrations illustrate how the values derived from double exponential fits (using the first rate constant, DE k_{obs1}) (A), and derived from single exponential fits (SE k_{obs}) (C) fit to a linear equation, in order to calculate the k_{on} and k_{off} values from the slope of the fit line and the y-axis intercept, respectively. These fittings processes produced slightly differing K_d values, with $16.47 \mu M$ from a DE k_{obs1} fit and $23.27 \mu M$ from a SE k_{obs} fit. However, the k_{obs2} values from double exponential second rates, DE k_{obs2} (B), showed a lack of any clear dependence of observed rate versus ligand concentration. Since linear fitting of SE k_{obs} versus [azole] data was notably superior to that for DE k_{obs1} versus [azole] data in all cases, all reaction transient data reported subsequently were from fits to a single exponential equation (Equation 2.1).

Hence, the transient kinetics of azole binding were systematically investigated for WT, F89H and G388S CYP51B1 enzymes with a range of different azole drugs: fluconazole, voriconazole, clotrimazole, econazole, miconazole and ketoconazole. The L100F and R391K enzymes were analysed with fluconazole. Ketoconazole however, due to its bulky hydrophobic side chain, had solubility issues and the resulting data were affected by turbidity (and did not fit well to either a SE or a DE function), and so further work with

this azole was aborted. Figure 3.27 (B, C) depicts fluconazole binding reaction progress curves for F89H CYP51B1 at low (5 μM) and high (250 μM) ligand concentrations, with reaction transient data fitted (red line) to a SE equation to derive the k_{obs} values. Multiple k_{obs} values at different concentrations were plotted against fluconazole concentration in Figure 3.27 (A), and the second order kinetic rate constant was calculated from a linear fit. Figure 3.27 (E, F) depicts econazole binding to G388S at 5 μM and 20 μM ligand concentration, again with transients fitted to a SE equation (red line), and the resulting k_{obs} values at various other miconazole concentrations were again plotted and fitted to a linear function in Figure 3.27 (D) to obtain the second rate constant for miconazole binding. At the lower end of the drug concentrations scale (i.e. where ligand concentration was less than P450 concentration), signal intensity was lower. However, all reaction transients could be fitted accurately. In these studies, it was important to maintain drug solubility using solvent concentrations that were compatible with enzyme stability, and the data plots shown (indicating a good linear dependence of k_{obs} on ligand concentration) indicate that was achieved successfully.

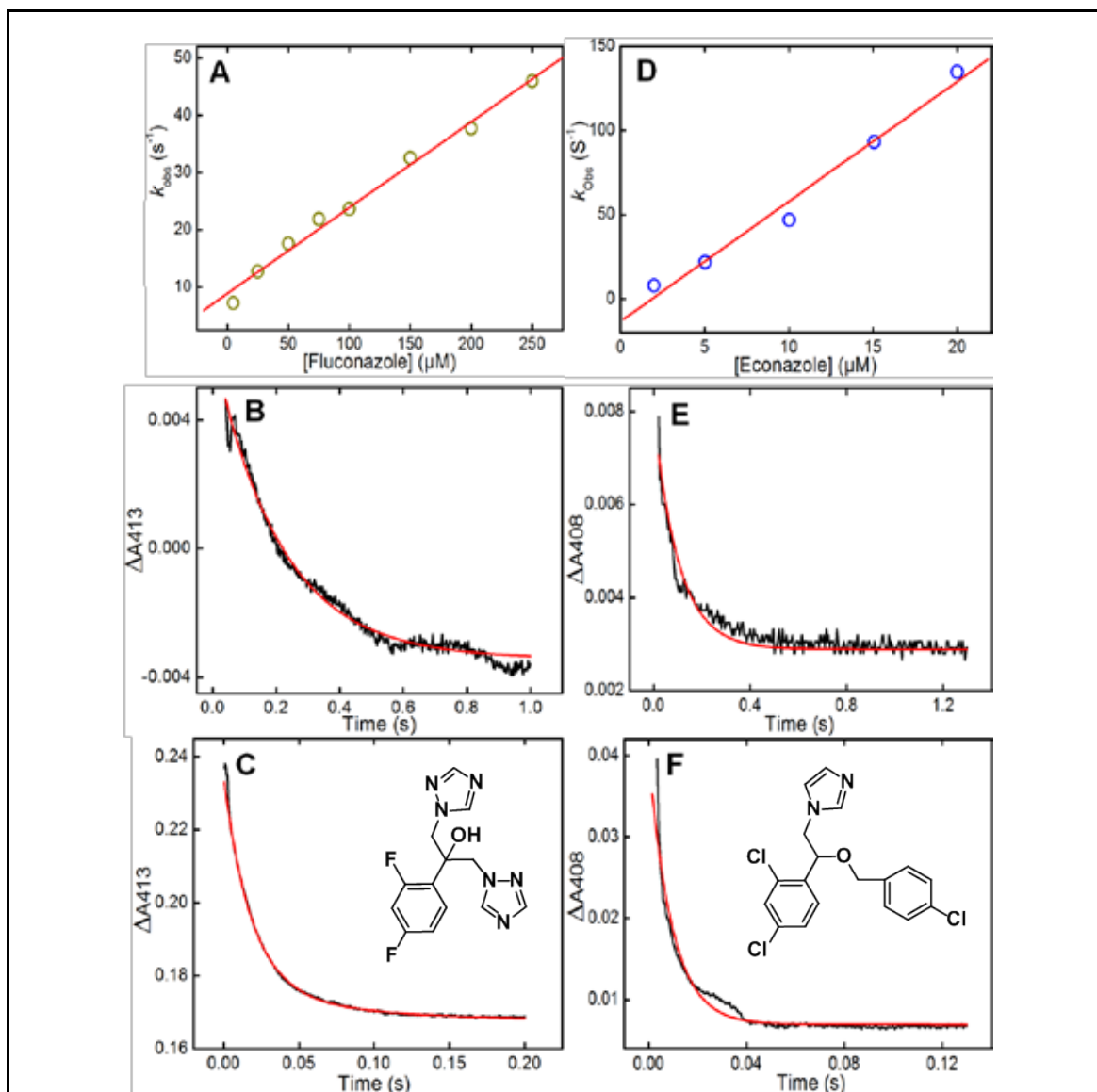


Figure 3.27: Apparent CYP51B1 enzyme with azole drug binding reaction rates observed from stopped-flow binding studies. Panel A shows a plot of the k_{obs} values for F89H CYP51B1 (4.6 μM) binding to fluconazole at different concentrations of the drug. The data are fitted to a linear function. Panel D shows a similar data set for G388S CYP51B1 (4.2 μM) binding to econazole. Panels B and E show reaction transients (black lines) reporting absorbance changes at 413 nm for F89H and 408 nm for G388S (choice of wavelength obtained from maximal absorbance changes observed in azole equilibrium binding difference spectra). These are shown over a 1 s timescale for the binding of 5 μM fluconazole to F89H CYP51B1 (B), and over a 1.3 s timescale for 5 μM econazole binding to G388S CYP51B1 (E). Panels C and F demonstrate the reaction transients observed with 250 μM fluconazole over 0.2 s, and with 20 μM econazole over 0.12 s upon ligand binding to F89H and G388S CYP51B1 enzymes, respectively. Reaction transients were fitted using a single exponential function (red line), Equation 2.1, to obtain observed rate constants (k_{obs}) at the respective wavelengths. The above graphs represent similar trends that were observed for all the azole drugs employed in similar experiments done for CYP51B1 WT and all mutant enzymes. The binding constants (K_d values) derived from k_{off}/k_{on} ratios for fluconazole binding are 68.68 μM (WT), 66.36 μM (F89H), 23.27 μM (L100F), 60.78 μM (G388S) and 36.96 μM (R391K). Insets show the chemical structures of fluconazole (C) and econazole (F).

Table 3.6 displays the rate constants derived from azole-binding stopped-flow analyses, which were then used to calculate the “kinetic” K_d values. These kinetic K_d values should be comparable to K_d values obtained from equilibrium binding methods. The ligand k_{on} and k_{off} values reflect the ligand binding (second order) and dissociation (first order) rate constants with the enzyme, and the K_d values are computed by dividing the k_{off} value by the k_{on} value in each case.

Table 3.6: Summary of K_d values obtained through stopped-flow analysis of azole drug with CYP51B1 WT and mutants.

CYP51B 1	Ligand	k_{on} ($s^{-1} \mu M^{-1}$)	k_{on} error	k_{off} (s^{-1})	k_{off} error	K_d (μM)	K_d error	premix [mutant] (μM)
WT	Fluconazole	0.19	0.01	12.67	0.85	66.68	0.09	9.1
	Voriconazole	0.56	0.03	12.44	5.63	22.21	0.46	9.1
	Clotrimazole	0.52	0.02	1.51	0.50	2.90	0.33	8.8
	Econazole	2.33	0.17	19.68	3.03	8.45	0.17	9.1
	Miconazole	3.28	0.25	92.20	6.89	28.11	0.11	8.3
F89H	Fluconazole	0.14	0.003	9.57	0.39	68.36	0.05	9.0
	Voriconazole	0.42	0.03	10.24	3.86	24.38	0.38	9.0
	Clotrimazole	0.39	0.02	2.48	0.52	6.36	0.22	12.8
	Econazole	5.72	0.35	6.39	7.79	1.12	1.22	12.8
	Miconazole	2.32	0.15	63.39	9.89	27.32	0.17	10.8
L100F	Fluconazole	0.37	0.01	8.61	0.39	23.27	0.05	10.1
G388S	Fluconazole	0.09	0.001	5.47	0.09	60.78	0.02	9.7
	Voriconazole	0.83	0.15	27.05	9.80	32.59	0.41	10.3
	Clotrimazole	0.31	0.03	12.01	0.52	38.74	0.10	8.3
	Econazole	6.23	0.49	1.61	5.99	0.26	3.73	8.3
	Miconazole	3.08	0.20	34.46	5.07	11.19	0.16	8.0
R391K	Fluconazole	0.28	0.01	10.35	0.85	36.96	0.09	9.2

Comparatively, consistently lower K_d values were obtained from equilibrium binding (EB) studies of fluconazole binding (**20.49 μM (WT)**, **10.20 μM (F89H)**, **4.59 μM (L100F)**, **13.24 μM (G388S)** and **8.19 μM (R391K)**) than those K_d values determined from stopped-flow methods. L100F exhibited tighter binding to fluconazole than WT CYP51B1 and other mutants, as shown by both equilibrium K_d and kinetic (SF) K_d values. This would seem to be consistent with the hypothesis that this “reverse” mutation indeed confers azole drug susceptibility, as reflected in the apparent opposite effect seen for a fluconazole resistant F145L *C. albicans* CYP51A1 mutant enzyme. On the whole, the SF K_d value are higher than the K_d values from EB methods. Since the EB K_d values likely accurately reflect

affinity for these drugs, an interesting question is raised as to the origin of the difference between the K_d values from SF and EB methods. One possibility is that the structural changes in the enzyme occur on ligand binding and over a time scale of e.g. hundreds of milliseconds, and that these result in a 'locking-in' of the azole drugs. These could possibly occur by structural rearrangements of the P450 to 'trap' the ligand in the active site, possibly involving changes in structure of the B/C and F/G loop regions that are known to be critical for substrate/inhibitor entry and exit in the P450s. This type of structural change could explain why higher affinity for the ligand is determined at equilibrium, whereas the inferred K_d from measurements on a stopped-flow timescale could be affected by an overestimated k_{off} rate projected from k_{on} data prior to the structural reorganization being completed.

To describe this model in an alternative way, there may exist a rapid and reversible reaction which can be described by the following scheme:



Where E = ligand-free enzyme, I = inhibitor or ligand, EI = enzyme-ligand complex, E^*I = a transient intermediate enzyme-ligand complex.

Equation 3.1 proposes the manner in which CYP51B1 WT and mutants may behave during SF and EB experiments and how differences in the K_d values may be obtained. $E + I$ is the initial state before CYP51B1 was mixed with the ligand (azole drugs/estriol), E^*I is a rapid transient state observed during the SF reaction, when absorption measurement changes used to determine K_d values were obtained over a millisecond timescale, and EI is the final CYP51B1-ligand complex when the system achieves equilibrium, and is the same state as that from which the K_d values are obtained via EB in optical titrations with azoles/estriol. It should be noted that the E^*I state would still require formal coordination of the heme iron by the azole drugs (since optical changes of this type are observed on the stopped-flow time scale).

Tryptophan fluorescence experiments were carried out according to prescribed protocols (Mugnol *et al.* 2008) with ligand-free and fluconazole-bound WT and F89H enzymes, but no signal changes were observed between the two different enzyme forms,

possibly due to the locations of Trp residues in the molecules (2 at the conserved cysteinyl loop region near the C-terminal proximal to the heme, i.e. W382 and W384, 1 at the N-terminal helical region, i.e. W128, and 1 at the static C-terminal end of the I-helix, i.e. W267) and their relative lack of environmental change between the ligand-free and azole-bound forms. As a consequence of this result, attempts were not made to probe CYP51B1 structural rearrangements and their kinetics by stopped-flow fluorescence. The possibility of Cys-labelling with a fluorophore was also considered as a route to probing CYP51B1 structural changes, but the location of the 4 cysteine residues in the protein were considered inappropriate. One of these cysteines is the proximal ligand to the heme iron (C394), one buried at the N-terminal end (C151) and two are at the different terminals of the enzyme polypeptide chain, i.e. C37 and C442 (and this might not provide useful information on structural rearrangement), and one is buried in the molecule and would likely be inaccessible to fluorophore labelling.

3.6.2 Reconstitution of CYP51B1 Enzyme Catalysis with Lanosterol and Dihydrolanosterol

As described above, the various CYP51B1 mutants were characterised using structural and spectroscopic methods, their electron transport systems were reconstituted and azole drug binding affinity was determined using both transient kinetic and equilibrium binding methods. However, their ability to catalyse 14α -demethylase reactions on sterol substrates remained to be defined, and such data are required to establish whether these mutations impair catalytic function or not. Turnover studies for WT and all mutants with lanosterol and dihydrolanosterol were carried out according to methods previously established by Bellamine *et al.* (1999), with minor modifications as described in Chapter 2. CYP51B1's native substrate is still uncertain, and the study of Bellamine *et al.* (1999) indicated that its ability to catalyse 14α -methyl group demethylation of lanosterol and 24,25-dihydrolanosterol is limited to 1% and 20% turnover, respectively, following extended incubation with the substrate and a redox partner system. In contrast, CYP51B1's preference for obtusifoliol (the substrate for plant sterol demethylases) was demonstrated by a 98% turnover to its demethylated products in the same system. Figure 3.28 shows the differences between these three substrates in comparison to estriol, the substrate analogue used in equilibrium and stopped-flow binding studies in this thesis, and the three stages of substrate oxidation that lead to the final demethylated products. Turnover products were first analysed using the GCMS technique, and these experiments were done in the laboratory of Prof. Irina Pikuleva (at CASE Western Reserve University, Cleveland, USA)

by Dr. Kirsty McLean from our group. No 14α -demethylated products above the detection threshold were obtained for all enzymes in reaction with lanosterol, perhaps reflecting the poor solubility and/or reactivity of the enzymes with this substrate and/or interactions with its redox partners. In these experiments FprA and Fd1 were used as the redox partners. While Fd1 has quite a positive potential, experiments reported earlier in this chapter and from published work by McLean *et al.* (2006c) do indicate that this system is viable in electron transport to CYP51B1 enzymes.

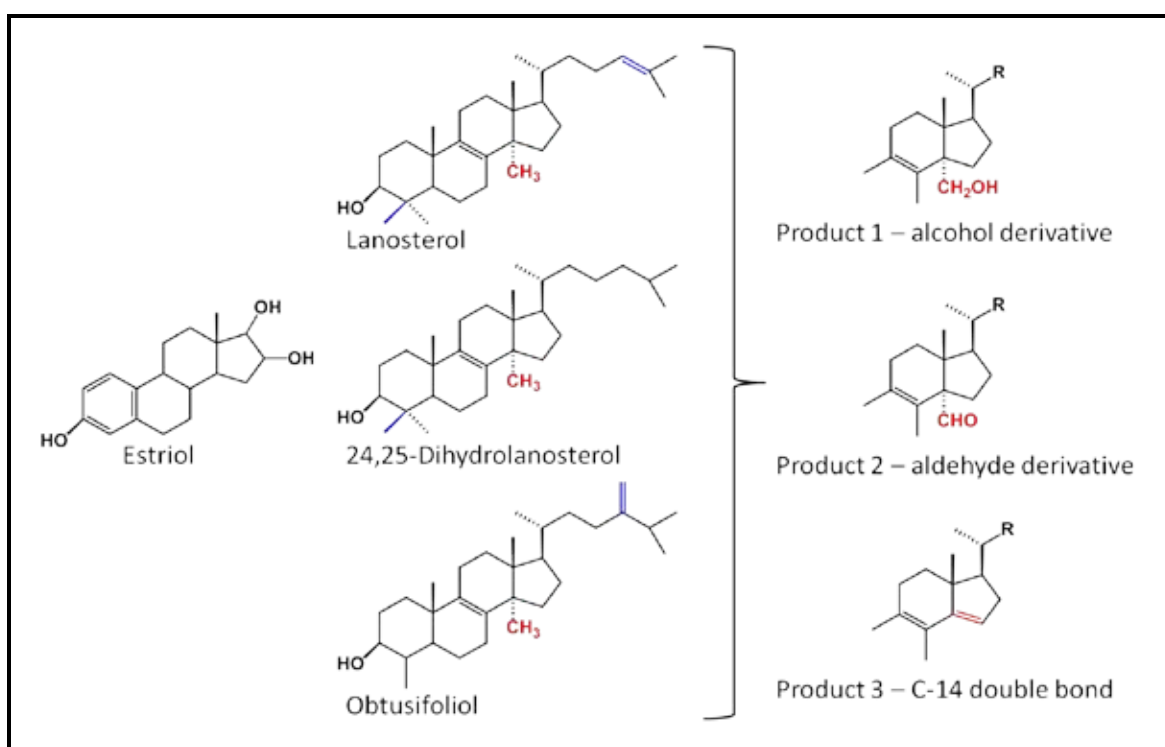


Figure 3.28: Structures of substrates and products of CYP51B1 catalysis, and comparison with the substrate analogue estriol. Bonds and side chains unique for each substrate are coloured in blue. The C-14 methyl group is highlighted in red, and is the site for the triple oxidation reaction catalysed by CYP51B1. Products generated at each catalytic step are presented in the panel on the right. The absence of the 2 hydroxyl groups found on the estriol 5-membered ring and the presence of hydrophobic side chains at C-17 in the three known substrates of CYP51B1 makes these molecules highly insoluble.

Obtusifoliol is not commercially available, but was reported by Bellamine *et al.* (1999) to undergo 98% conversion to demethylated product with CYP51B1. In further attempts to establish the catalytic capacity of the WT and mutant CYP51B1 enzymes generated in this study, further experiments were performed using redox partner enzymes from *E. coli* (flavodoxin) and spinach (ferredoxin reductase) as previously published (Bellamine *et al.* 1999) and also using Mtb Fdr and Fd1 or Fd2 ferredoxin partners (Zanno

et al. 2005). Initial results using WT CYP51B1 and lanosterol and the turnover products detected by LCMS showed positive results with substantial amounts of C-14 demethylated lanosterol. As the lanosterol stock used (Sigma-Aldrich) was apparently contaminated by dihydrolanosterol (as revealed by HPLC analysis), it seemed that the turnover products from WT CYP51B1 C-14 demethylase activity by were from both lanosterol and the apparent dihydrolanosterol contaminant in near-equal amounts. This contrasts with previous work, where dihydrolanosterol was reported to be demethylated to a 20-fold greater extent than lanosterol (Bellamine *et al.* 1999). However, my results demonstrated that catalytic turnover of dihydrolanosterol (the apparent contaminant) by WT CYP51B1 was definitely >50% over a similar incubation time to that used by Bellamine *et al.* (1999), more than twice the extent of turnover reported previously. In addition, lanosterol was extensively demethylated, in contrast to the 1% turnover reported by Bellamine *et al.* (1999). In order to confirm these data and to test the mutant enzymes catalytic activity, further sets of experiments were carried out with a cleaner and higher quality 24,25-dihydrolanosterol stock and results are awaiting analysis (Paul Williams, LCMS/GCMS experimental officer, Manchester Interdisciplinary Biocentre, pers. comm.).

3.7 Summary and Critical Assessment

This chapter, for the first time, presents quantitative biochemical characterisation of CYP51B1 enzymes containing mutations mapped from fluconazole-resistant variants of the membranous CYP51A1 (or CYP51ca) from *C. albicans*, thus addressing the **second objective** of this study which is to understand the mechanisms of azole-resistance in CYP51ca using CYP51B1 as a template. Although CYP51B1 (from *Mtb*) and CYP51A1 (from *C. albicans*) share only 26% amino acid sequence identity, they have both been shown to catalyse 14 α -demethylase reactions on sterol substrates (Bellamine *et al.* 1999). The prospect of elucidating mechanisms of azole drug-resistance in CYP51B1 mutant enzymes (using spectroscopic, kinetics and crystallographic methods) are much greater for the soluble CYP51B1 enzymes by comparison to using detergent-solubilised CYP51A1, and given the difficulties in expression and isolation of high quality CYP51A1 proteins. Previous studies of CYP51A1 have used detergents and chaotropic agents, e.g. the recent report from Warrilow *et al.* (2010a; 2010b) and the later report from Kelly *et al.* (1999a, b) on CYP51A1 of *C. albicans* and *A. fumigatus* binding to azole drugs, and such studies have not been able to provide serious quantitative or structural data on mutant enzymes and their interactions with azoles. Results in this chapter and the next chapter have addressed

the above issues by using the soluble CYP51B1 as the best template of choice. The fact that CYP51ca and CYP51B1 are not 100% identical in the amino acid sequence demonstrates the diversity of this enzyme (Figure 1.11) while multiple sequence alignment showed essential conserved sites (Figure 3.1 B) between these two homologues which are the SRS and SBS regions (blue and red shaded regions, respectively in Figure 1.10 B) on this enzyme.

The choice of mutants presented in this chapter was based on their frequency in azole-resistant clinical cases in CYP51A1 and on their location in the CYP51B1 structure. These strategically located mutations in CYP51B1 enabled me to address the **first objective** of this research together with crystal structure results of CYP51B1 variants from the next chapter which is to understand the molecular mechanisms and mode of action/physiological roles of Mtb CYP51B1 complementing previous work which have been done on WT CYP51B1 by McLean *et al.* (2006). However, outsourced ongoing analyses on various substrates (lanosterol and dihydrolanosterol) turnover studies with different combinations of redox partners (Fd1/Fd2 and Fdr/FprA) and WT CYP51B1 and the mutants are underway to fulfil both main objectives of this research.

Y132H (F89H in CYP51B1) and G464S (G388S) are two mutants with the highest frequency found in clinical fluconazole-resistant *C. albicans* strains. Both F89H (Y132H in CYP51A1) and L100F (a reverse mutant, restoring a CYP51A1 WT residue in CYP51B1) are located at SRS 1 flexible hinge regions, while G388S (G464S) and R391K (R467K) are at the highly conserved β -bulge of the cysteinyl loop. The S348F (S405F) mutant is situated at the conserved C-terminal region between an N-terminal helix and beta sheets. The S348F mutation resulted in a misfolded and inactive CYP51B1 enzyme. All the mutants (except for G388S and S348F) showed full heme incorporation and expression levels comparable of that of WT CYP51B1, as judged by the amount of their heterologous expression in the absence of added δ -ala heme precursor, and by their comparable RZ values for pure enzyme and their heme *b* content relative to WT CYP51B1. The G388S mutant, however, was expressed as a soluble protein at ~ 30 x lower levels than WT CYP51B1 and, with the addition of δ -ala, could be purified with ~ 64 % heme-bound holoenzyme present. Spectrophotometric characterisation showed that all mutants (F89H, L100F, G388S and R391K) retained their P450 nature by binding CO in the ferrous-heme state, and through formation of a ferrous-CO complex with maxima at ~ 450 nm, which decayed to the P420 form over time.

Mutants in the cysteinyl loop region displayed interesting, yet contrasting, behaviours during kinetic and equilibrium reduction studies with dithionite. G388S CYP51B1 demonstrated fast reduction of ferric heme to ferrous-heme and a 9-fold faster protonation of the cysteinate proximal ligand compared to WT CYP51B1. This was consistent with the dominant ferrous-thiol species observed during redox potentiometry experiments, and with the relatively fast collapse (0.88 min^{-1}) of the P450 ferrous-CO adduct to the P420 thiol form. G388S CYP51B1 exhibited a very positive redox potential (-102 mV) in the substrate-free form, even higher than that reported for WT CYP51B1 in complex with estriol, and thus reflecting a higher electron affinity than the estriol-bound WT enzyme. Its inability to form a P450 ferrous-CO species with redox partners and estriol is its distinguishing property. In WT CYP51B1, the P450 species was stabilised (i.e. an equilibrium between P450 and P420 forms was obtained) with redox partners (FprA, Fdr and Fd2) providing the electrons in the presence of estriol, while in the other mutants this P450 species was stabilised to a certain extent in the presence of estriol. Indeed, the effect of mutating the extensively conserved Gly residue mutation at the Gly-rich cysteinyl loop (by incorporation of the hydroxyl side chain-containing Ser residue in G388S) not only destabilised the binding of the heme cofactor, but also enhanced the rate of the catalytically active P450 species formation on reduction with dithionite (and of the collapse of the ferrous-CO P450 form to P420) and, more relevantly, no P450 formation was detected when the G388S mutant was reduced by an enzyme-based system (NADPH, FprA and/or Fdr, Fd1 and/or Fd2), likely as a consequence of relatively fast rate of heme thiolate protonation with respect to heme reduction using this non-optimised electron transport system. In view of the unusual behaviour of the G388S mutant, there might seem to be two possible catalytic outcomes for this mutant (once CYP51B1's physiological substrate is confirmed and an efficient redox partner system established). These two routes might be (1) a productive and relatively fast 14α -demethylation reaction on a *bona fide* substrate (avoiding heme thiolate protonation through efficient turnover) and (2) a non-productive route with decay of iron-oxo intermediates via one of the three shunt pathways (forming superoxide, peroxide or water) and the abortive release of any bound substrate. Given the presence of some thiolate bound heme in the G388S mutant, it might be expected that this mutant would be functional in catalysis. However, its altered heme iron potential would likely compromise its ability to reduce and activate dioxygen, and thus further impact on its catalytic competence. In the next chapter, the biophysical characteristics of G388S CYP51B1, the properties of its heme centre in ligand-free and -bound forms and its hydrodynamic properties are explored, complementing results in this chapter.

While, for G388S CYP51B1, the rate constants for both its ferric-to-ferrous heme iron reduction and heme thiolate protonation were increased by the mutation, in R391K, the thiolate protonation rate was decreased by 2-fold as compared to WT CYP51B1. This might suggest that the Arg391 residue is involved in proton transfer to the heme thiolate to facilitate P420 formation, and that its replacement by a lysine affects structure in this region and makes for less efficient thiolate protonation (which is possibly a beneficial outcome for the enzyme). Thus, the R391K CYP51B1 exhibited slower heme thiolate protonation, providing an extended duration of the catalytically active ferrous-thiolate form for substrate monooxygenation. Whilst the G388S mutant's heme cofactor was apparently weakly bound to the protein (i.e. full heme incorporation was not achieved, and "leakage" of heme was observed during purification) and was not further apparently stabilised (or destabilised) by azole drug binding, the R391K mutant showed good heme incorporation, but upon binding to a strong ligand (e.g. azoles), the stability of heme may have been perturbed, as discussed previously and illustrated by the fall in Soret band heme intensity for the azole complex seen in Figure 3.25. An alternative explanation might be that the extinction coefficient at 419 nm is lower for the azole complexes for this mutant in comparison to WT CYP51B1 and other mutants discussed in section 3.5.1. The G388S and R391K mutations may thus have profound impacts on enzymatic activity in both these cysteinyl loop mutant P450s, and these mutants have not been examined before in CYP51A1.

In contrast, the Y132H (F89H) and F145L (WT-like) mutants of CYP51A1 (CYP51B1) have been expressed and studies of fluconazole binding and catalysis have been previously reported by Kudo *et al.* (2005) in CYP51A1 of *C. albicans* and by Bellamine *et al.* (2004) in CYP51B1 of *Mtb*, and in human CYP51. Both studies found that the F89H mutant of CYP51B1 abolished 24,25-dihydrolanosterol demethylation and its binding at the catalytic pocket, but had essentially no effect on fluconazole binding as concluded from an absent type II spectral change derived from the difference spectra upon optical titration of fluconazole to this mutant enzyme (Bellamine *et al.* 2004; Kudo *et al.* 2005). However, these same mutants in CYP51A1 (Y132H) and human CYP51 (Y145H) did not confer any deleterious effect on substrate metabolism, but exhibited tighter fluconazole binding in the case of Y132H CYP51A1, and negligible effects in the latter case (Bellamine *et al.* 1999). Both these studies concluded that the F145L CYP51A1 mutation was responsible for fluconazole resistance in the fluconazole-resistant *C. albicans* isolates (Bellamine *et al.* 1999; Kudo *et al.* 2005). In this work, the L100F "reverse mutant" of CYP51B1 (a "model" for WT CYP51A1) and WT CYP51B1 (modelling the F145L fluconazole-resistant mutant of CYP51A1) biochemical characterisation data were somewhat consistent with the data for

molecules have not arrived at their final conformationally adapted states following azole drug binding. Several P450s are known to undergo conformational changes (particularly involving mobile loop regions involved in ligand entry/exit), and to crystallise in different conformational states for ligand-free and substrate/inhibitor-bound forms (e.g CYP3A4, CYP121 and CYP126). The weaker azole K_d values determined by SF methods might thus result from data that report on azole-heme ligation that occurs prior to completion of CYP51B1 structural adaptations to accommodate the inhibitors. If, for instance, these adaptations favour active site closure and a diminished “escape” rate for the azole, then the apparent k_{off} from stopped-flow studies may be inflated, leading to a K_d value elevated in comparison to the EB measurements. Such a phenomenon might be explored further by further rapid kinetic studies aimed at monitoring protein structural changes on azole binding.

Efforts to substantially confirm these suggestions were thus made by Trp fluorescence analysis, but failed to yield convincing data to support the model due to limited changes in fluorescence between ligand-free and fluconazole-bound forms of CYP51B1. Due to time constraints of this PhD project, further studies in this area were curtailed. Further spectroscopic techniques, which will be discussed in the following chapter, were aimed at addressing the effects of these CYP51B1 mutations on the heme and its vicinity, and especially its axial ligation state. In particular, it was considered that heme environment and axial ligation could be affected by the cysteinyl loop mutations at close proximity to the heme’s absolutely conserved C394 proximal ligand residue. Crystal structures of WT CYP51B1 and mutants at the B-C loop region were also determined (and will be discussed in the following chapter), and these structural data also advance the understanding of the mechanisms of ligand binding to CYP51B1 and conformational changes that accompany azole interactions.

*Chapter 4 | Biophysical and Structural
Characterisation of CYP51B1 and Fluconazole-
Resistant Mutants*

- 4.1 Available Crystal Structures of
CYP51B1*
- 4.2 Circular Dichroism (CD) Comparative
Analysis*
- 4.3 Dynamic Light Scattering Analysis*
- 4.4 Differential Scanning Calorimetry
(DSC) of Ligand-Free and Bound
Forms*
- 4.5 Analysis of Ferric-Heme Coordination
by Electron Paramagnetic Resonance
(EPR)*
 - 4.5.1 EPR of CYP51B1 Ligand-Free
and Bound Forms*
 - 4.5.2 EPR of CYP51B1 Post-Redox
Cycling of the Enzyme*
- 4.6 CYP51B1 Crystallisation*
- 4.7 CYP51B1 Crystal Structure Features
in Ligand-Bound Forms*
- 4.8 Summary and Critical Assessment*

4 BIOPHYSICAL AND STRUCTURAL CHARACTERISATION OF CYP51B1 AND FLUCONAZOLE-RESISTANT MUTANTS

4.1 Available Crystal Structures of CYP51B1

At the time of thesis submission, there are 25 structures of CYP51 available in the PDB, and 50% of these are structures of Mtb sterol 14- α demethylases (with and without ligands), half of which were solved in the last 5 years. This relatively high number of solved crystal structures of CYP51B1 from Mtb is attributed to its soluble nature, compared to the more recently solved N-terminal truncated isoforms from eukaryotes, where membrane anchor removal ultimately facilitated their successful crystallization. To date, CYP51B1 is the only structurally solved bacterial form of this ancient enzyme family that is found in all eukaryotes (Aoyama *et al.* 1996). While the role of one particular CYP51 bacterial isoform (a CYP51 fused to a ferredoxin) from *Methylococcus capsulatus* (MCCCYP51FX) is known (Jackson *et al.* 2002), the roles of the other six bacterial isoforms in Mtb, *M. smegmatis*, *M. avium*, *Rhodococcus erythropolis*, *Nocardia farcinica* and *Streptomyces coelicolor* remains undefined (Aoyama 2005; Jackson *et al.* 2003; Lamb *et al.* 2002; Pietila *et al.* 2006). In contrast, eukaryotic CYP51 has been shown to play an important role in sterol biosynthesis, and the reaction intermediates of CYP51 catalysis, i.e. 14 α -carboxyalcohol and 14 α -carboxyaldehyde, are important feedback regulatory transducers. In mammals, production of the 14 α -carboxyaldehyde derivative acts as a suppressor of HMG-CoA reductase translation (an important enzyme in the mevalonate pathway preceding sterol precursors synthesis) hence down-regulating cholesterol production (Acimovic *et al.* 2008). In *Trypanosoma* spp. this aldehyde intermediate acts as a switch to hijack the mammalian host's sterol precursors and to manifest Chagas disease by switching from endogenous sterol production to the energetically more favourable consumption of exogenous sterol precursors in the host's blood (Lepesheva *et al.* 2010). Despite the diverse physiological roles of CYP51 and its various reaction intermediates, CYP51 shares similar architecture to other structurally solved P450 proteins (Lepesheva and Waterman 2007; Lepesheva and Waterman 2011). However, some distinctions in CYP51 structure between species has been highlighted recently, especially in the SRS1 and SRS4 regions that correspond to the B-C loop and α I helical regions, respectively (Podust *et al.* 2001a). Figure 4.1 shows these two regions, which help to classify specific CYP51 enzymes in different phyla. In CYP51B1, an upward kink is prominent in the I helix (α I), while in human and protozoan isoforms a slight downward bend of the α I is observed in both the ligand-free (white) and azole-bound (blue) structures shown. This distinctive conformation of the CYP51B1 α I

places the B-C loop in a relatively open conformation, positioned parallel to the heme plane (Figure 4.1 topmost right panel). However, in human and protozoan isoforms the corresponding B-C loop is in a closed conformation restricting access/exit into/from the heme pocket. However, the altered conformation of αI appears to induce another channel perpendicular to the heme plane (between F-G loops and αA) to be in the open conformation. In the case of the ligand-bound form with ketoconazole (in human CYP51), the ligand is observed sticking out from this crevice. In CYP51B1, this 2nd channel is closed. However, it has been proposed by Podust and co-workers that while the 2nd channel closes (F-G loop- αA) and the 1st channel (B-C loop) opens prior to/during substrate binding, a subsequent, concerted structural rearrangement occurs during catalysis that causes the 1st channel to close and the 2nd channel to open, allowing product exit from CYP51B1 (Podust *et al.* 2001a). The arc-shaped αG in human CYP51 (middle panel) and its overall compact, yet bulky, architecture also differentiates it from *T. brucei*'s CYP51 that is slimmer and flatter (bottom panel). These relatively small structural differences and those SRS-conserved residues which are phylum-specific ultimately underlie the distinctive substrate/ligand binding properties of the various CYP51 isoforms characterized to date. Previously, it was recognised that CYP51-specific sequence signatures lie predominantly in the B-C loop and in the αI , where particular residues can indicate substrate preference (Lepesheva and Waterman 2007; McLean *et al.* 2007). These regions on CYP51B1 were identified by Podust *et al.* (2001) as the six substrate recognition sites (SRS) and Lepesheva *et al.* (2003) went on to identify phenylalanine at position 78 of CYP51B1 Mtb, which corresponds to a leucine at position 121 of CYP51A1 from *C. albicans*, situated at the B-C loop region ($\alpha B'$) as a substrate determining residue; where Mtb CYP51B1 and CYP51s from plants were shown to prefer substrates with mono-methylated C4 (obtusifoliol), while CYP51s from fungal and animal strains prefer a mono-methylated C4 substrate (lanosterol and 24,25-dihydrolanosterol) (Lepesheva and Waterman 2007; Bellamine *et al.* 1999). Also, the αI region has been extensively studied in site directed mutagenesis approaches by Lepesheva and co-workers, in order to understand the roles of conserved SRS4 residues in substrate binding and in catalytic function (Lepesheva *et al.* 2003). In this chapter, the "azole-resistant" mutants at both the B-C loop and the highly conserved heme motif regions have been biophysically and structurally characterised by spectroscopic techniques and by crystallogensis/structural elucidation to complement results in chapter 3, and in order to understand their influence on interactions with azole drugs and the effects that these point mutations have on the overall CYP51B1 structure.

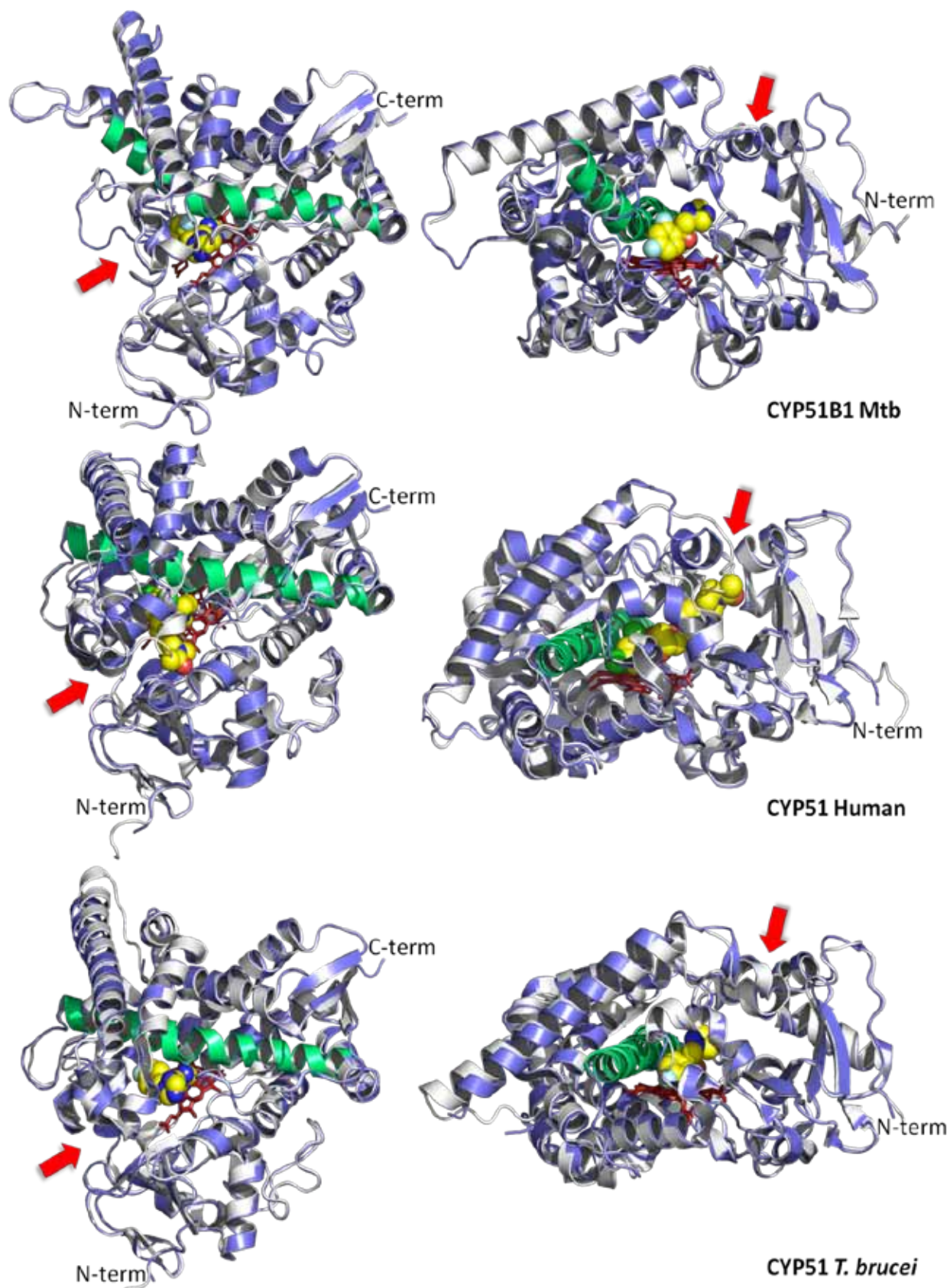


Figure 4.1: CYP51 from Mtb, human and *Trypanosoma brucei*. CYP51 structures of ligand-free (white) and azole-bound (blue) forms from these three species were C-alpha aligned and superimposed. Structure elements highlighted are the I-helix (α I) (green), heme (red sticks) and azole inhibitors (yellow and blue spheres). The red arrows point to the proposed entry/exit channels of the drugs into the heme binding site. **Top** panel represents CYP51B1 of Mtb in ligand-free (pdb: 1h5z 2.05 Å) and fluconazole-bound (pdb: 1ea1 2.21 Å) states, with root-mean-square distance (rmsd) values of 0.242 Å. **Middle** panel represents CYP51 of *Homo sapiens* in ligand-free (pdb: 3juv 3.12 Å) and ketoconazole-bound (pdb: 3ld6 2.80 Å) states with rmsd values of 0.624 Å. **Bottom** panel represents CYP51 of *T. brucei* in ligand-free (pdb: 3g1q 1.89 Å) and fluconazole-bound (pdb: 2wv2 2.70 Å) states with rmsd values of 0.445 Å. The panel on the left looks down into the enzyme through the F-G loop- α A crevice (entry/exit channel 1, SRS1) while the panel on the right looks into the enzyme via the B-C loop- α C access channel, which is open in CYP51B1.

4.2 Circular Dichroism (CD) Comparative Analysis

In order to confirm the secondary structural integrity of mutants, far UV CD spectra were carried out on enzymes using similar concentrations (0.1 mg/mL) in a 0.1 mm quartz cuvette. Although Figure 4.2 (A) shows some variations in the CD trough intensity at 224 nm (suggesting different protein concentrations) efforts were taken to ensure that the same amounts of protein were used in each experiment. However, the analyses were done using two different CD machines at different times in the research project. Despite some differences in CD spectral intensity, all the mutants and WT CYP51B1 showed similar features, with a trough at 224 nm. The differing intensities at 224 nm do provide some issues in establishing the alpha-helical content of the CYP51B1, since the ellipticity signal at this part of the spectrum is important in estimating α -helical content of a protein. However, similar CD spectral shapes for most of these enzymes are consistent with their conserved conformational states. All of the CYP51B1 enzymes showed alpha-helix rich CD signatures, estimating ~50% helical content, except for G388S CYP51B1 which showed a deeper trough at 224 nm and a flatter (less defined) peak at the 195 nm range. Taking into account the manner in which the hemoprotein concentrations were calculated (based on their heme *b* concentration) and the fact that the G388S CYP51B1 enzyme is a mixture of both apoprotein and holoenzyme, it can be appreciated that the CD spectrum describes both these conformations in equilibrium. Other measurements indicated that ~64% of G388S is the holoenzyme and the rest is apoprotein. The more intense G388S CD spectrum may reflect the fact that protein quantification by heme content leads to underestimation of total protein concentration. The different shape of its far UV CD spectrum may also indicate that the apoprotein component adopts a different folded state, and since previous work also indicated that this mutant loses heme progressively in

solution, it is likely also the case that the proportion of apoprotein is ultimately greater than 36%.

Figure 4.2 (B) shows WT (thick solid line) and R391K CYP51B1 (dotted line) in comparison to CYP121 (thin blue line), at protein concentrations of 0.93, 0.74 and 1.0 mg/mL, respectively. Similar far UV and visible CD studies have been done previously on WT CYP51B1, providing data consistent with my own WT CYP51B1 CD spectra in the far UV region, but demonstrated a negative (rather than positive) CD signal at 420 nm near the Soret band maximum (Lepesheva *et al.* 2001). The R391K mutation, located 3 residues away from the Cys axial ligand to the heme, did not dramatically change the structural arrangement of adjacent residues at the conserved cysteinyl loop proximal to the heme cofactor (see Figure 4.12 of section 4.7 on the crystal structure of the R391K mutant). The near-UV visible spectra for WT and R391K CYP51B1 are highly similar, again suggesting a similar heme environment in these proteins. A shoulder at 391 nm for WT and R391K CYP51B1, which is missing from CYP121, suggests strongly that there is a HS heme iron component in the CYP51B1 enzymes, while CYP121 is predominantly LS. These observations were consistent with the UV-Vis absorbance spectra of the heme Soret band for these three enzymes.

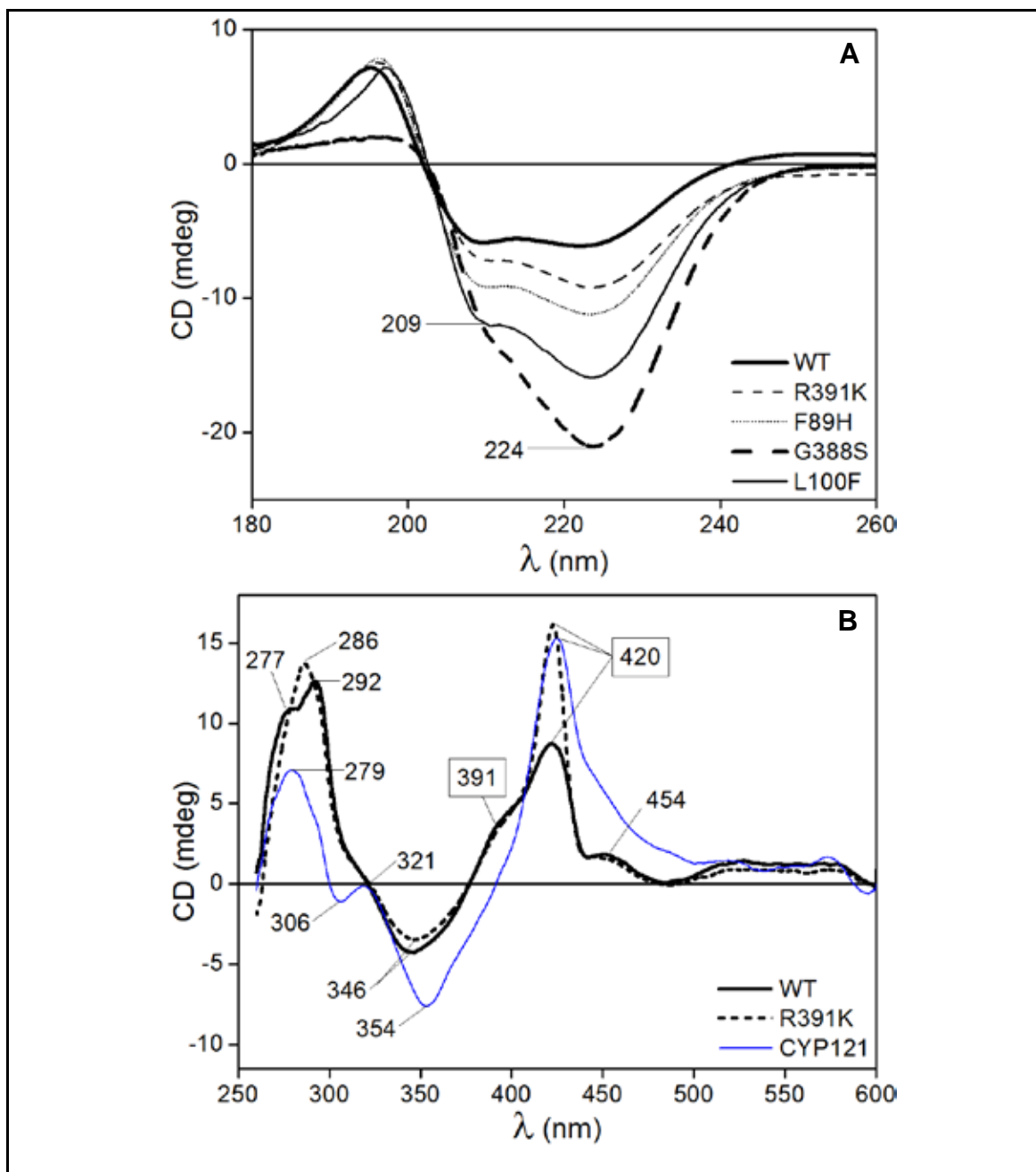


Figure 4.2: Far UV and near UV-visible circular dichroism spectra of CYP51B1 WT and mutants. A) Far UV CD spectra comparing mutants against WT CYP51B1. All spectra display α -helical rich secondary structures, with G388S having a sharper trough at 224 nm, possibly due to its ~64% holoenzyme and ~34% apoprotein mixture, and altered structural features for the apoprotein component. B) Visible CD spectra of WT (0.93 mg/mL, thick solid line) and R391K mutant CYP51B1 (0.74 mg/mL, dotted line) showing a positive heme peak at 420 nm (positive Cotton effect) and a minor high spin species at 391 nm. By comparison, CYP121 (1.0 mg/mL) (thin blue line) shows a similar heme peak at 420 nm but was predominantly low spin without any high spin signature, consistent with its UV-vis absorbance spectrum (not shown). Far UV and near UV-Visible CD analysis were carried out in 0.1 mm and 10 mm pathlength cuvettes, respectively. Wavelengths of various peaks, trough minima and shoulders are indicated.

4.3 Dynamic Light Scattering Analysis

Pure enzyme samples were passed through a size exclusion chromatography (SEC) column as described in the Methods section (Chapter 2), before being analysed using MALLS (Multi-Angle Laser Light Scattering) coupled to a QELS detector and another SEC column. MALLS-QELS differs from normal light scattering analysis by being able to report accurately on the average molecular weights of proteins (Mw), their radius of gyration (Rg) and molecular conformation from hydrodynamic radius (Hd) values. It can also provide a preliminary analysis of protein stability and homogeneity (Li *et al.* 2009). The effects of the point mutations at mobile regions and at conserved heme proximal loops in CYP51B1 were analysed in ligand-free forms and in P450 complexes with clotrimazole using MALLS. This technique was initially used to determine the homogeneity (i.e. presence of aggregates or oligomeric states) of pure protein samples before they were subjected to crystallography. Most Mtb P450 proteins are monomeric (including WT CYP51B1, CYP121, CYP125 and CYP144) in their crystal structures, consistent with other hydrodynamic studies (Driscoll *et al.* 2011). However, this is not always the case. Hydrodynamic analysis of CYP130 in complex with econazole indicated a monomeric state in solution. However, the crystal structures indicated a dimeric state (Ouellet *et al.* 2008). The different conclusions reached from hydrodynamic and crystal structure studies are likely due to inter- and intra-molecular interactions between ligand-protein and protein-protein molecules, allowing CYP130 to dimerise in the crystal state, but for such interactions to be undetectable in the solution state. A dimeric state was also observed for the recently solved Mtb CYP126 crystal structures (David Leys, University of Manchester, pers. comm.). Dimerisation is also observed for a particular P450 protein which is fused to its redox partner: *Bacillus megaterium* flavocytochrome CYP102A1 (P450 BM3, and presumably for its homologues in other bacteria). The heme (P450) domain is a monomer, but when fused to its reductase partner (a cytochrome P450 reductase, or CPR) the flavocytochrome dimerises to facilitate highly efficient electron transfer between the monomers to drive fatty acid hydroxylation (Neeli *et al.* 2005). It is expected that the Mtb P450 proteins are monomeric, and interact with monomeric ferredoxin reductase and ferredoxin proteins in a typical NADPH-driven class I redox system (Munro *et al.* 2007a; Munro *et al.* 2009). In this case, WT CYP51B1 and the F89H, L100F and R391K mutant enzymes were all found to be globular monomeric proteins with average molecular weights of 49.85 kDa, 51.49 kDa, 51.57 kDa and 54.46 kDa in their ligand-free forms, respectively. When bound to clotrimazole, the monomeric state was retained for WT, F89H and R391K enzymes, with average molecular weights of 50.82 kDa, 54.31 kDa and 55.60 kDa,

respectively (Figure 4.3 **B-E**). These proteins demonstrated singular light scattering peaks (red spectra) concurrent with refractive index peaks (blue spectra) and protein peaks at 280 nm (black spectra). The only exception is for the G388S mutant (Figure 4.3 **A**) which resulted in five fractions and peaks, with fractions 3 (34% and Mw 99.6 kDa) and 5 (47% and Mw 50.35 kDa) making up the majority of species, while peaks 1, 2 and 4 were the minor species with lesser extents of light scattering but relatively higher average Mw. These multiple peaks for G388S CYP51B1 revealed different oligomerisation states in its mixture of holoenzyme and apoprotein forms. This is likely explained by the different folded states for the holoprotein and apoprotein components of the G388S protein mixture, with interactions between these states giving rise to oligomeric forms not observed for the WT enzyme. The 99.6 kDa species is potentially a dimer formed between either holoprotein/apoprotein or apoprotein/apoprotein molecules. The largest peak 5 is likely that of the semi-stable holoenzyme, with a Mw of 50.35 kDa, close to the predicted WT CYP51B1 Mw of 50.9 kDa.

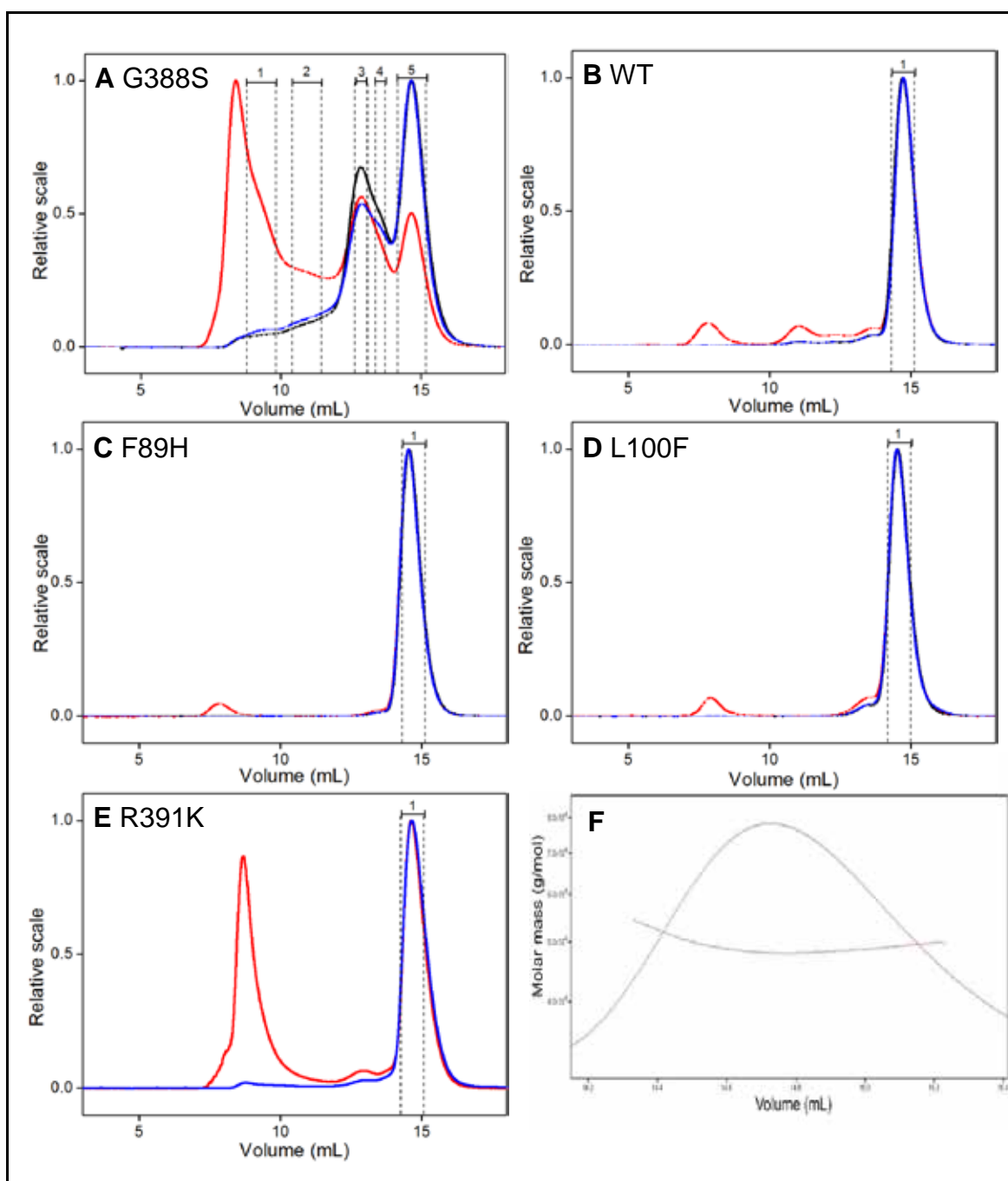


Figure 4.3: Multi-angle laser light scattering spectra of CYP51B1 WT and mutants.

The red line represents light scattering data, the black line represents protein absorption at 280 nm and the blue line represents the refractive index of the protein. **A)** MALLS for the G388S mutant showing five fractions with fractions 3 (34% and average molecular weight, Mw 99.6 kDa) and 5 (47% and Mw 50.35 kDa) making up the majority of species, while peaks 1, 2 and 4 are the minor species with a lesser extent of light scattering, but relatively higher average molecular weights. **B)** WT, **C)** F89H, **D)** L100F and **E)** R391K MALLS spectra show a single peak each, with average molecular weights of 49.85 kDa, 51.49 kDa, 51.57 kDa and 54.46 kDa, respectively. **F)** The average molecular weight (horizontal dots) spanning across the only peak eluted for WT CYP51B1. The data obtained were similar for the F89H, R391K and L100F mutants. Polydispersity indexes are 1.00 for all main peaks, which reflect protein stability, except for G388S CYP51B1. The hydrodynamic studies showed that all the CYP51B1 proteins were predominantly globular and monomeric.

4.4 Differential Scanning Calorimetry (DSC) of Ligand-Free and Bound Forms

Further stability assays were carried out for the azole-resistant mutants, using calorimetric analysis to analyse the thermal stability of these enzymes and the effect of ligand binding on stabilising the CYP51B1 structure. These studies were done initially in light of multiple failed crystallogenesis trials for CYP51B1 in the ligand-free form, where samples consistently precipitated rather than forming crystals. DSC measures enthalpy changes (ΔH) for unfolding events caused by heat-induced protein denaturation. The transition midpoint, T_m , is the temperature where 50% of the protein is in its native conformation and the other 50% is denatured. The higher the T_m , the more stable the molecule. During the same experiment, DSC also measures the change in heat capacity (ΔC_p) during thermal denaturation. Heat capacity changes associated with protein unfolding are primarily due to changes in hydration of side chains that were buried in the native state, but become solvent exposed in the denatured state (Gill *et al.* 2010). Control experiments were done for WT CYP51B1 with buffer, and with DMSO before ligands were added. It seemed unlikely that there would be large variations in the T_m of mutant enzymes from that of WT CYP51B1, particularly since CD analysis showed that all the mutants were folded and had similar secondary structural content. This prediction held true for all but the G388S CYP51B1 mutant, which showed interesting protein unfolding transitions widely differing from those for WT CYP51B1 and as demonstrated in Figure 4.4. A general two stage unfolding event with T_m values of $\sim 49^\circ\text{C}$ and $\sim 51^\circ\text{C}$ (which were slightly increased upon ligand binding) was observed for WT, F89H, L100F and R391K CYP51B1 enzymes, and this possibly relates to the consecutive unfolding of the two major structural domains in the P450 (i.e. the helix-rich alpha domain and the sheet-rich beta domain) that occur before irreversible aggregation occurs at higher temperatures. In G388S CYP51B1, however, the mixture of apoprotein and holoenzyme was evident by the multiple T_m values for the enzyme at 41.5, 45.6, 54.1 and 58.3 $^\circ\text{C}$. The major unfolding event was at 54.1 $^\circ\text{C}$, possibly reflecting one of the transitions for the major holoprotein species. Aggregation of different forms of the enzyme (potentially both folded and unfolded states) at higher temperatures was consistent with precipitation (observed by increasing turbidity) of the enzyme solution at these temperatures.

The binding of inhibitors increased the CYP51B1 T_m values for both transitions (by $\sim 2\text{-}4.5^\circ\text{C}$ for fluconazole and EPBA), as seen in Table 4.1. Inhibitors thus enhanced the stability of enzymes, most effectively for the L100F CYP51B1 mutant bound to fluconazole. Therefore, from these results, crystallogenesis trials for WT CYP51B1 and the mutant enzymes (except for G388S) were carried out for their complexes with EPBA, 4PI

and fluconazole. The fact that both 4PI and EPBA are more soluble in aqueous buffer than is fluconazole made it easier to work with the latter two ligands in crystallogensis studies, particularly since DMSO (the solvent for fluconazole and other azole drugs) was shown to have a minor destabilizing effect (decrease in the T_m values) in WT CYP51B1 (Table 4.1).

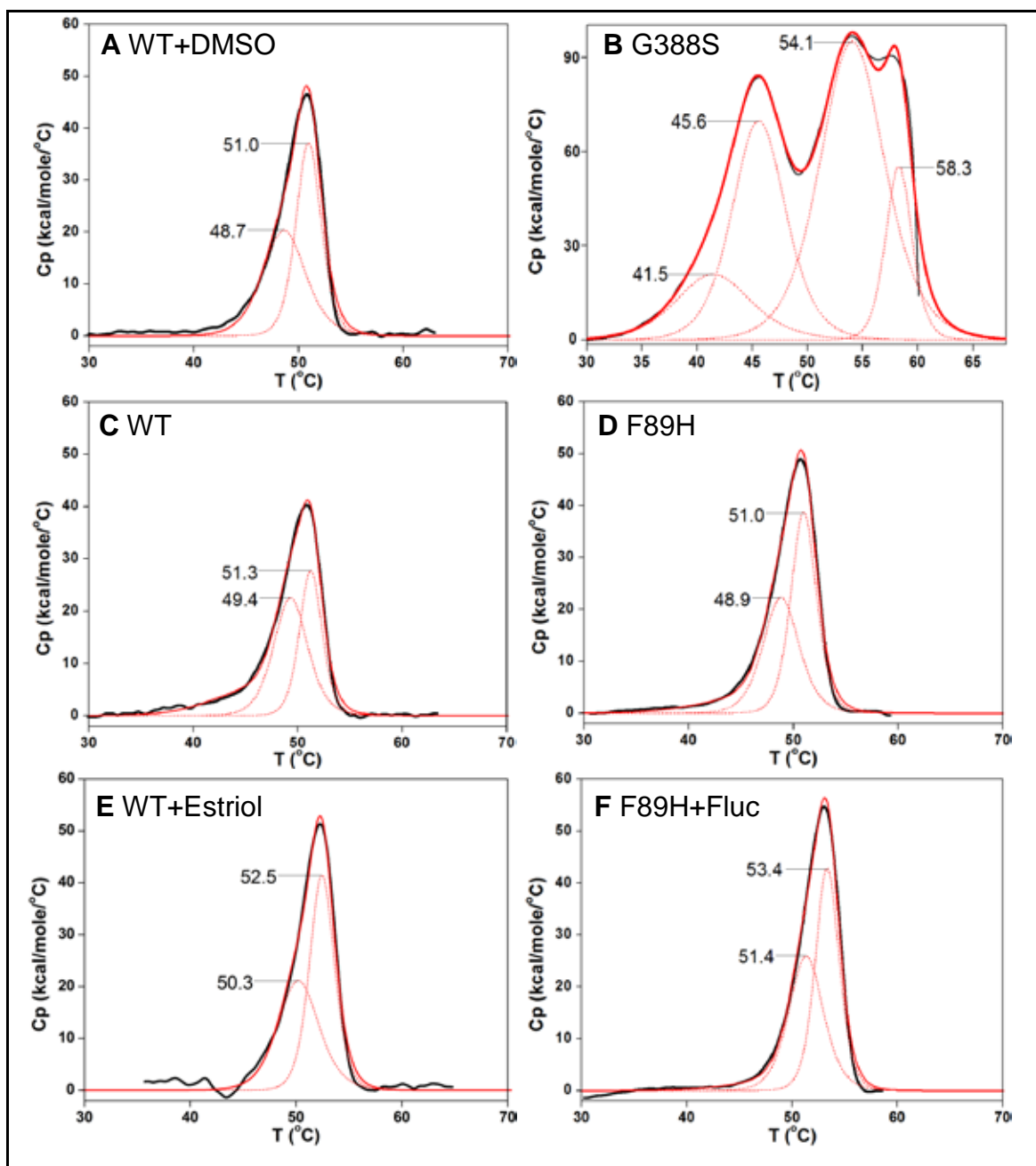


Figure 4.4: Protein unfolding transition thermograms for ligand-free and inhibitor-bound CYP51B1. The overall fitting (solid red line) of raw data (solid black line) for protein unfolding events are illustrated by step-wise heat changes with respective midpoint transition events (T_m), shown by dashed red lines, obtained by fitting raw data to a non-two-state model available from the OriginLab DSC software (OriginLab Corp., Northampton MA, USA) and as described in section 2.2.10.3. All protein samples were diluted to 1 mg/mL in 100 mM KPi buffer pH 7.5. **A)** WT + 0.5% DMSO, **B)** G388S, **C)** WT, **D)** F89H, **E)** WT + 0.2 mM estriol, **F)** F89H + 0.1 mM fluconazole (Fluc).

Table 4.1: Melting temperatures or transition midpoints (T_m) for WT and mutant CYP51B1 enzymes. The 4 values reported for the G388S mutant reflect T_m values 1-4 consecutively.

CYP51B1	Ligands	T_{m1} (°C)	T_{m2} (°C)	ΔT_m (°C)
WT	Ligand-free	49.40 ± 0.65	51.30 ± 0.16	-
	0.2 mM Estriol	50.25 ± 0.81	52.47 ± 0.12	0.85/1.17
	0.1 mM Fluconazole	52.39 ± 0.61	54.14 ± 0.19	2.99/2.84
	2 mM 4-PI	49.29 ± 0.71	51.19 ± 0.16	0.11/0.11
	0.05 mM EPBA	52.36 ± 0.55	54.15 ± 0.19	2.96/2.85
	0.5% DMSO	48.65 ± 0.59	50.98 ± 0.08	0.75/0.32
F89H	Ligand-free	48.85 ± 0.54	51.01 ± 0.12	-
	0.1 mM Fluconazole	51.35 ± 0.73	53.36 ± 0.16	2.50/2.44
L100F	Ligand-free	47.85 ± 0.61	49.94 ± 0.20	-
	0.1 mM Fluconazole	52.42 ± 0.61	54.25 ± 0.20	4.57/4.29
G388S	Ligand-free	45.51 ± 2.50	54.12 ± 0.15	-
		45.62 ± 0.29	58.30 ± 0.10	-
R391K	Ligand-free	49.39 ± 0.53	51.24 ± 0.16	-
	0.1 mM Fluconazole	51.97 ± 0.67	53.94 ± 0.12	2.58/2.70
	2 mM 4-PI	49.24 ± 0.90	51.34 ± 0.12	0.15/0.10

4.5 Analysis of Ferric-Heme Coordination by Electron Paramagnetic Resonance (EPR)

4.5.1 EPR of CYP51B1 Ligand-Free and Bound Forms

The effects of ligands to the P450 ferric heme was of interest for the CYP51B1 mutants studied here, and particularly for those at the cysteinyl loop (G388S and R391K CYP51B1). The coordination of heme iron on binding azole drugs and the spin state of ferric heme before and after azole drug coordination was investigated using EPR. The rhombic LS EPR signals of hexa-coordinate ferric heme WT CYP51B1 were established previously by Mclean *et al.* (2006) for ligand-free WT CYP51B1 and for its complexes with fluconazole and 4PI, indicating a near-homogeneous LS hexa-coordinated heme iron with an aqua distal ligand and a cysteine thiolate proximal ligand in the resting state, with 3 major g values of $g=2.44$, $g=2.25_y$ and $g=1.91_x$ indicative of a $S = \frac{1}{2}$ nuclear spin state (McLean *et al.* 2006). These values were in good agreement with g values obtained from this study, as illustrated for the EPR spectrum of WT CYP51B1 shown in Figure 4.5, with g values of 2.43, 2.25 and 1.91. Other Mtb and bacterial P450 proteins also exhibited similar major LS g -values, e.g. CYP121 (2.47, 2.25, 1.90) (McLean *et al.* 2002), CYP144 (2.42, 2.25, 1.93) (Driscoll *et al.* 2011) and P450cam (2.46, 2.26, 1.91) (Lewis 2007).

However, Mtb CYP125 revealed heterogeneous LS EPR signals, as seen by the splitting of the g values at $g_z=2.40/2.42$, $g_y=2.25$ and $g_x=1.94/1.93$, which was attributed to different heme conformations or different angles of the heme axial ligands at cryogenic temperatures (10 K) (McLean *et al.* 2009).

These 3 main CYP51B1 WT LS g values in Figure 4.5 also compared well to the mutant ligand-free enzymes. Along with the 3 major LS signature g values, additional minor HS P450 signature g values at 7.55 and 8.00 for the F89H and G388S CYP51B1 mutants were indicative of a proportion of HS thiolate-ligated, penta-coordinated ferric heme in the dominantly LS hexa-coordinated mixture. Also, an unusual minor HS species with a g value at 5.75 (F89H) and 5.86 (G388S) was seen for both these mutants in their ligand-free forms, suggesting the presence of a small amount of a HS penta-coordinated thiol-ligated species of ferric heme, which disappeared upon binding toazole ligands (discussed later on and in Figure 4.7 B, C).

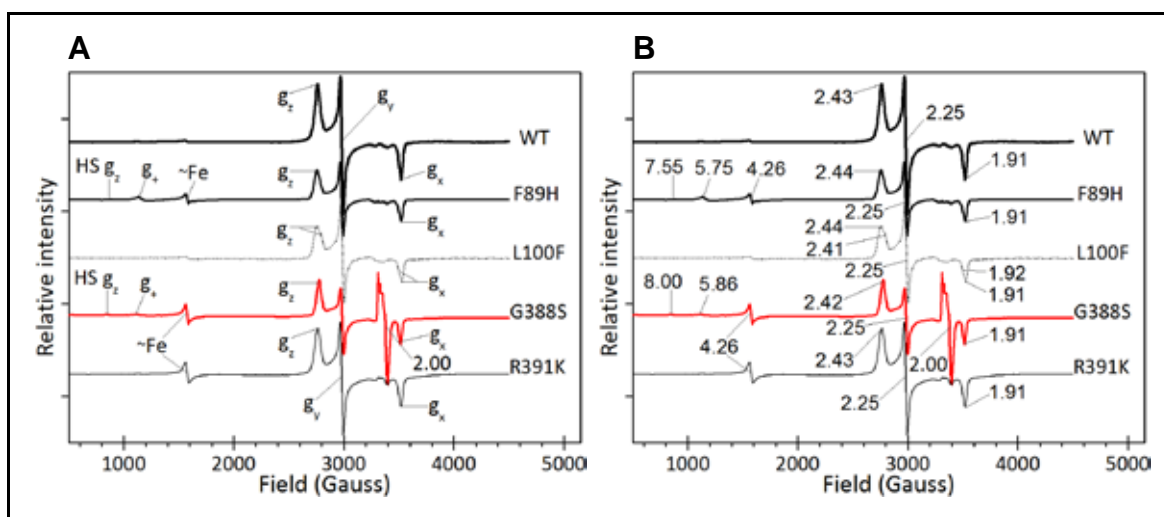
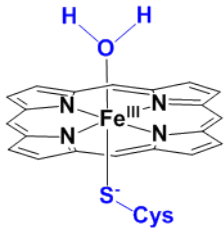
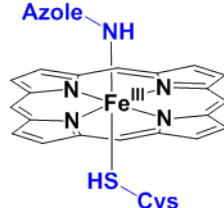

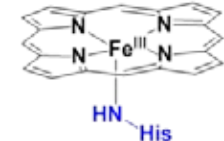


Figure 4.5: EPR spectra of ligand-free mutants and WT CYP51B1. WT and mutant CYP51B1 enzymes exhibited rhombic EPR signals typical of LS hexa-coordinated ferric heme with water and cysteinate as the axial ligands, and with major g values of 2.42-2.44 g_z , 2.25 g_y , and 1.91-1.92 g_x . Minor P450 HS species were detected in F89H and G388S mutants with g values at 7.55 and 8.00, respectively, indicative of HS penta-coordinated, thiolate-ligated ferric heme. Minor atypical P450 HS g values at 5.75 and 5.86 (indicated as g_+) were also observed for F89H and G388S, respectively, suggesting the presence of HS penta-coordinated, thiol-ligated ferric heme species. Adventitious iron signatures were detected for F89H, G388S and R391K at a g value of 4.26, with G388S also having a larger signal at g 2.00, possibly due to superoxide radicals resulting from its heme instability and reactions of free heme/heme iron with oxygen. G388S spectra are shown in red for clarity. **Panel A** shows annotated symbols for the major features described in the spectra. **Panel B** indicates the relevant g values for these EPR features.

G388S CYP51B1 also exhibited a large signal at $g \sim 2.00$ that might be due to the formation of superoxide anions or other free radicals which could result from interactions of heme with solvents (e.g. DMSO, acetone or benzene), as reported by Sakurai *et al.* (1990) who found similar $g \sim 2.00$ values on studies with hemin complexes (Sakurai *et al.* 1990). In the case of G388S, such signals could originate from free radicals due to heme and/or iron released from the enzyme (and possibly from radicals caused by such heme or heme iron interactions with DMSO solvent). Minor free ferric iron signals were also observed at $g = 4.26$ for G388S, F89H and R391K CYP51B1. Similar g values were also reported by Mowat *et al.* in studies of mutants of the lactate dehydrogenase flavocytochrome b_2 , which were assigned to free ferric iron and free copper (II) for the WT b_2 enzyme and for a H66C mutant that altered the heme iron proximal ligand. These free metal species were reported with g values of 4.30 and 2.05, respectively (Mowat *et al.* 2000).

Atypical HS heme iron spectra with minor g values at $g \sim 6.00$ observed in F89H and G388S CYP51B1 were also reported in HS non-P450 hemoproteins, e.g. HS myoglobin or hemoglobin, both of which have an imidazole nitrogen ligated to the ferric heme provided by its proximal His ligand (Dawson *et al.* 2001; Perera and Dawson 2004), bis-methionine ligated cytochrome b_{562} (Barker *et al.* 1996) and HS flavocytochrome b_2 (Miles *et al.* 1993; Mowat *et al.* 2000). It was suggested that these $g \sim 6.00$ values could be due to a thiol (Cys-SH) penta-coordinated HS species, and this might also be the explanation for these signals in the CYP51B1 mutants reported in this thesis (Figure 4.7 and Figure 4.8). The different ligation states of ferric heme that give rise to diagnostic EPR signals have been characterized for various heme-containing proteins, and some examples are given in Table 4.2.

Table 4.2: Examples of various ligation and spin states of ferric heme in proteins.

Illustration of ferric heme ligation states	Designation of ferric heme	Description	Examples
 <p>LS Hexa-thiolate</p>	P450 LS hexa-coordinated thiolate	The typical resting state ferric heme configuration of a P450. This is illustrated using a iron-porphyrin skeleton to illustrate the ferriprotoporphyrin IX of the P450s.	<ol style="list-style-type: none"> 1. A product of mutagenesis. LS hexa-coordinated Cys-Fe-Glu in A264E CYP102A1 (Girvan <i>et al.</i> 2009). 2. Ligation to inhibitors (e.g.azole drugs) LS hexa-coordinated thiolate with imidazole or triazole as the distal ligand in e.g. Mtb CYP121, CYP142 and CYP144 (McLean <i>et al.</i> 2006, Driscoll <i>et al.</i> 2010, 2011).
 <p>LS Hexa-thiolate</p>	P450 HS penta-coordinated thiol	The neutral thiol form (protonated cysteinate) of the ferric proximal ligand, also known as the P420 species when in the reduced form with a CO distal ligand. The CYP51B1 ferrous form has a spectral signature at 422-427 nm.	<ol style="list-style-type: none"> 1. Suggestion of a neutral thiol ligation in M80C cytochrome <i>c</i> mutant by resonance Raman analysis of penta-coordinated (Cys80-ligated) mutant (Smulevich <i>et al.</i> 1994). 2. Ligand-free ferrous heme of CYP51B1 is prone to protonation of Cys thiolate ligand (to thiol) – as seen by spectral signature of ferrous heme at 558.5 nm, and by development of P420 band in Fe(II)CO species. (McLean <i>et al.</i> 2006).
 <p>LS Hexa-myo/hemoglobin</p>	LS hexa-coordinated myo/hemoglobin	Myoglobin and hemoglobin are a distinct set of hemoproteins from P450s and have their heme configuration as LS hexa- or HS penta-coordinated states with an imidazole moiety of a histidine molecule as the proximal heme ligand.	<ol style="list-style-type: none"> 1. HS myoglobin or hemoglobin, both of which have an imidazole nitrogen ligated to the ferric heme iron, provided by its proximal His ligand; while the LS species typically has either an O₂ or CO molecule as the distal ligand (Dawson <i>et al.</i> 2001; Perera and Dawson 2004).
 <p>HS Penta-myo/hemoglobin</p>	HS penta-coordinated myo/hemoglobin		

The g values are very sensitive to the nature of the heme axial ligands and to perturbations such as the orientations of the ligands at the ferric heme iron. While WT CYP51B1 and the other mutants were near-homogeneous in their LS resting forms, L100F CYP51B1 showed minor heterogeneity with a splitting of g_z values at 2.44 and 2.41, mirrored by g_x values of 1.91 and 1.92 respectively, similar to the aforementioned heterogeneity observed for Mtb CYP125. In studies using azole inhibitors, the L100F CYP51B1 mutant enzyme's heterogeneity in g values was emphasised upon binding to imidazole type drugs (4PI and clotrimazole), with their respective g values displayed in Figure 4.6. For 4PI, whose structure is less bulkier than either clotrimazole or voriconazole, it might be expected that this inhibitor can adapt to different binding orientations to the heme iron, explaining the distinct g_x values of 1.90, 1.85 and corresponding g_z values of 2.44, 2.55, suggesting two major ligation states of the ferric heme by 4PI in L100F CYP51B1. These could be explained by e.g. (i) different orientations of the 4PI imidazole ligating the ferric heme or (ii) a mixture of 4PI imidazole coordinating directly to the heme iron, or via an interstitial water ligand. The latter situation was observed in studies of Mtb CYP121 in complex with fluconazole (Seward *et al.* 2006). 4PI has a relatively weak affinity for CYP51B1 with a K_d of 390 μM , while bulkier azoles such as clotrimazole and voriconazole bind more tightly with K_d values of 0.05 and 0.31 μM , respectively. It is not immediately clear how the mutations at the B-C loop region situated away from the heme cavity can influence the imidazole-type ligand orientation at the heme iron, as seen by the distinct sets of g values for L100F (Figure 4.6) and F89H (Figure 4.7 C) as compared to mutants at the cysteinyl loop region, G388S and R391K CYP51B1 in Figure 4.7 (B, C), which had 2 and 3 sets of g_x and g_z values in their complexes with clotrimazole, respectively.

Perhaps the L100F mutant can cause heterogeneity due to the side chain of the F100 residue, which may form interactions with the 4PI drug upon its entry/exit to the active site, or possibly with adjacent residues, causing them to interact with the phenyl group of 4PI, or with the three bulky aromatic groups of clotrimazole – a drug which also gives a heterogeneous set of g values on binding the L100F (and other CYP51B1) mutant heme iron. Such interactions could thus cause major binding orientation perturbations for the azoles, as is reflected by the different sets of g values in L100F CYP51B1 on drug binding. Conversely, upon binding to voriconazole, the heterogeneity of the L100F CYP51B1 ferric heme g values was lost, and a single set of g values (2.44, 2.25 and 1.89) was observed. This likely indicates that the nitrogen atom from the triazole moiety of this inhibitor coordinates in a single orientation to the heme iron, perhaps stabilized by bonding

between its substituent groups (e.g. making hydrophobic interactions and H-bonding interactions) and amino acid residues in the heme distal pocket.

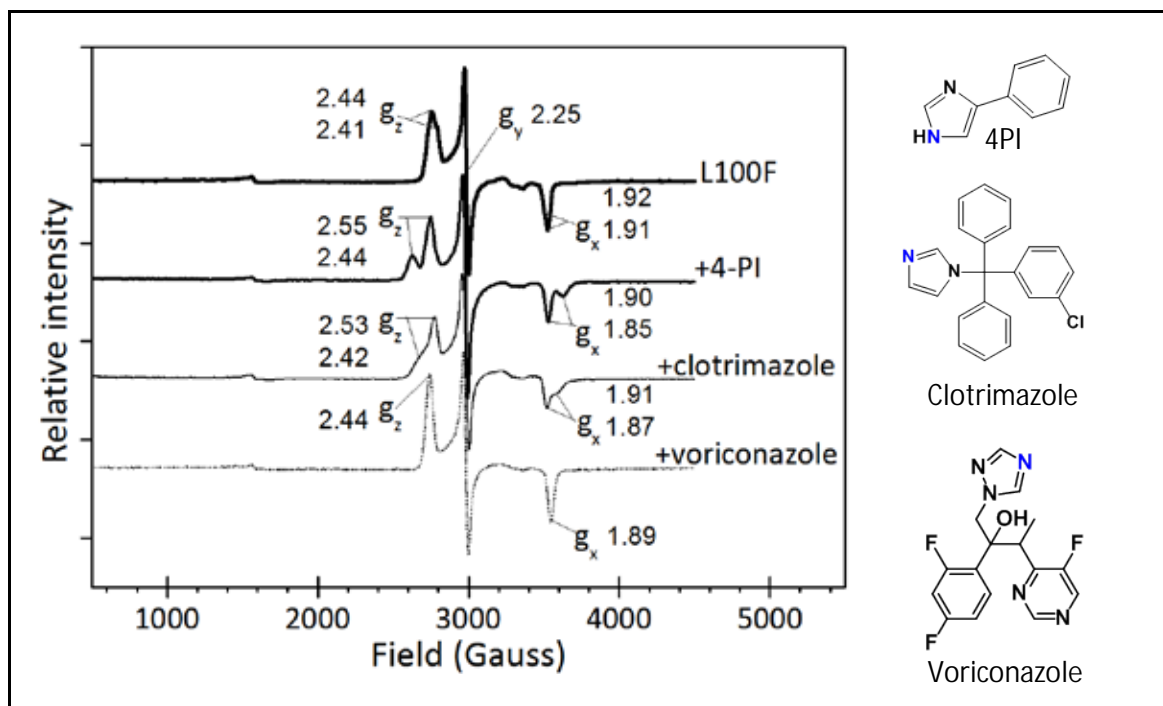


Figure 4.6: EPR spectra of the CYP51B1 L100F mutant enzyme bound to azole-inhibitors. The EPR spectra for L100F CYP51B1 in absence of inhibitor (top) and in complex with the azole inhibitors 4-phenylimidazole (4PI), clotrimazole and voriconazole are shown. The inhibitor structures are also presented, with their heme iron coordinating nitrogen highlighted in blue.

This apparent heterogeneity of heme iron coordination by imidazole drugs was observed in all of the mutants, as demonstrated by the multiple g values for 4PI and clotrimazole complexes with WT, F89H and G388S CYP51B1 enzymes in Figure 4.7. This proposed imidazole-ligand orientation heterogeneity for all these enzymes did not arise from any prolonged incubation with the drugs, as was proven by recording the same g values whether EPR analysis was carried out immediately upon adding the imidazole drugs (followed by flash-freezing in liquid nitrogen) or when the imidazole drugs were added to the enzyme and the mixture left to equilibrate for ~ 2 h before being flash-frozen. The R391K CYP51B1 mutant also demonstrated multiple g values upon coordination to clotrimazole, with g_z values of 2.51, 2.46, 2.43, and corresponding g_x values of 1.87, 1.89, and 1.92. The g_y value was constant at 2.25, and these values were similar to the multiple g value sets found for the clotrimazole-bound F89H CYP51B1 mutant (Figure 4.7 C). The R391K mutation is in the same vicinity as G388S, and both these mutants demonstrated some apparent heme instability, with adventitious iron signatures at g 4.26. This signal was also present in the F89H CYP51B1 mutant, but to a lesser extent. For R391K CYP51B1,

this free iron signature at g 4.26 increased (~ 2 fold) upon binding to clotrimazole. This may be consistent with the decrease in intensity of the R391K CYP51B1 Soret band observed during equilibrium binding studies with fluconazole and miconazole in comparison to L100F CYP51B1, as discussed in the last chapter (Figure 3.25). Possibly, R391K heme binding is destabilized somewhat on addition of this drug and/or its solvent. The atypical, minor HS species observed in F89H and G388S CYP51B1 were eliminated upon binding to the azole inhibitors, consistent with the formation of LS hexa-coordinated ferric heme on binding a strong 6th ligand. As a matter of fact, all of the enzymes (except WT and L100F CYP51B1) demonstrated heme cofactor instability to a certain extent, as evidenced by their adventitious iron signature at g 4.26.

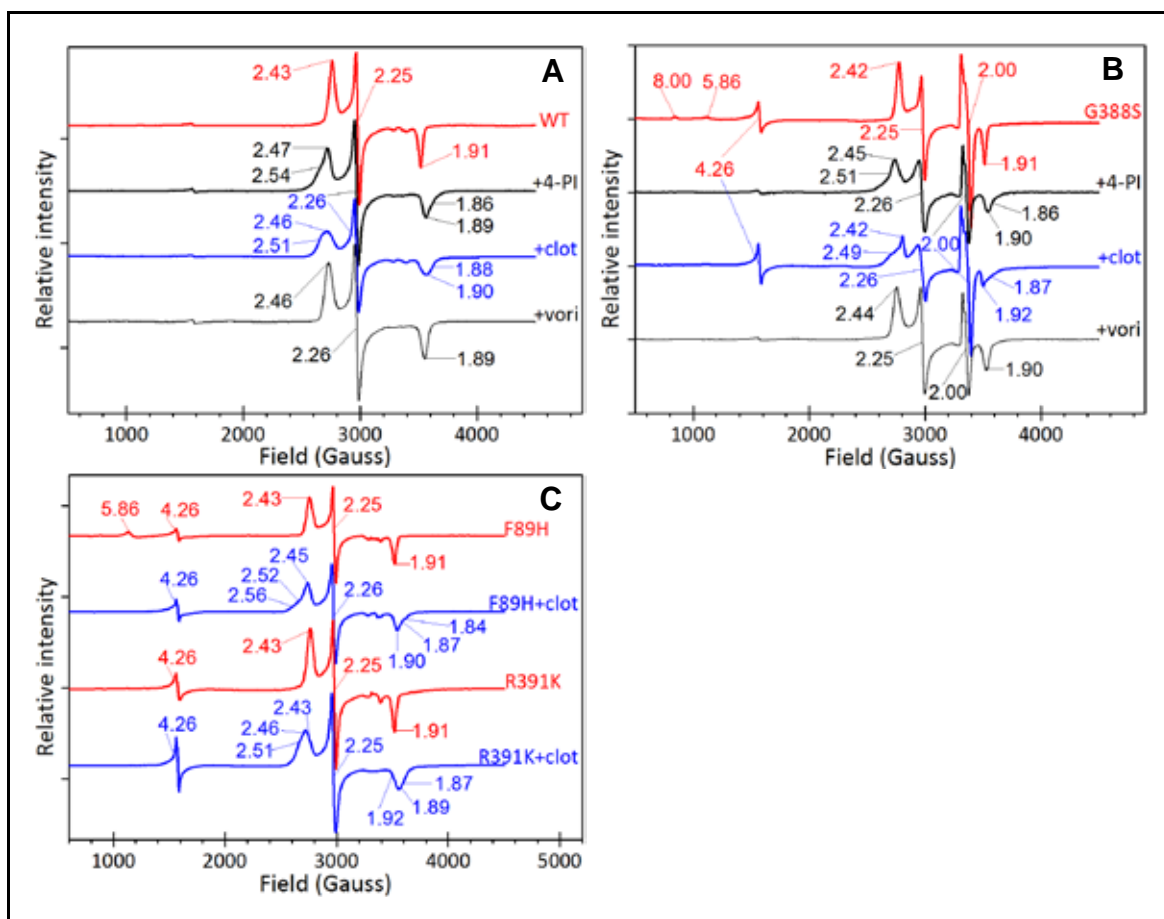


Figure 4.7: EPR spectra of WT and mutant CYP51B1 enzymes in resting and azole-bound forms. A) WT and B) G388S EPR X-band spectra are shown for ligand-free enzyme (red line) and for enzyme bound to inhibitors: 4-phenylimidazole (thick black line), clotrimazole (blue line) and voriconazole (thin black line), along with the respective g values. C) Spectra of F89H and R391K mutants are shown in the ligand-free (red) and clotrimazole-bound (blue) states. Heterogeneity of g_x and g_z values is consistently observed in both these mutants upon binding to the imidazole drug clotrimazole.

The other major g values, signifying LS hexa-coordinated ferric heme, were also present, although some heterogeneity in this heme ligation state was observed in WT CYP51B1 and all mutant enzymes except L100F CYP51B1 (Figure 4.6). These heterogeneous g values and the major atypical HS $g \sim 6.00$ signal may be explained by the following models: (i) the aqua distal ligand to the ferric heme could have been displaced or perturbed by another molecule. Such a molecule might be sulfite or another breakdown product of dithionite. Interactions of such ligands were spectrally demonstrated by previous work with P450cam, as discussed in the previous chapter (section 3.9, Figure 3.17) and with regards to transient spectral signatures at 463-464 nm (Sono and Dawson 1982). Direct coordination by e.g. sulfite would be expected to produce a LS heme iron, however; (ii) the ferric heme could be in a thiol (protonated thiolate) penta-coordinated form to explain the prominent HS signal; (iii) since the $g \sim 6.00$ signal is more often recognised as a non-P450 HS signal for His-axial ligation to a ferric heme, e.g. in myoglobin and hemoglobin, it could be the case that the nearby His392 (Figure 3.15), which is phylogenetically conserved in the P450s, could replace the cysteine as the ferric heme proximal ligand. This would likely be a temporary event, as demonstrated by the slow reversibility of this HS species over 24 h. However, there has been no compelling proof for such a Cys/His switch in other P450s.

Model (iii) was somewhat strengthened by studies of CO binding to the L100F CYP51B1 ferrous heme following the ***second round** (post redox >24 h) of EPR analysis. These studies failed to show any spectral changes to either the P450 or P420 forms, perhaps supporting the idea of a proximal ligand switch. However, it should be borne in mind that both hemoglobin and myoglobin do bind to CO in their ferrous state to give a Soret feature at ~ 420 nm. Thus, no firm proof of the nature of this HS species is available as yet, although its slow reversibility to the LS thiolate-coordinated form is possibly most consistent with the notion of a protonated cysteinate, which slowly reconverts to thiolate.

After the first EPR analysis (following redox cycling) and upon thawing, no protein precipitation was noticed in the enzymes, but similar oxidised ferric Soret band features were noticed at 411-415 nm, as described in the previous chapter. After the first round of EPR analysis, these enzyme samples were left to thaw on ice overnight (~ 24 h). A significant amount of precipitated protein was observed after this time, and this was separated by centrifugation. The supernatant was once again flash frozen and the second EPR analysis was done (***second round**). From Figure 4.8, decreases in the HS ($g \sim 6.00$) and free radical ($g \sim 2.00$) signals were observed (black spectra). The percentages of LS and HS $g \sim 6.00$ species post redox cycling and after 24 h were estimated from integration of

the EPR spectra. Immediately after the redox cycle, 80% of HS $g \sim 6.00$ species were formed relative to 20% LS species. This 80% HS species collapsed back after 24 h of incubation on ice to achieve an $\sim 50/50$ balance of both HS and LS species. This relatively slow duration for the reversibility of this atypical P450 HS species indicated that this event cannot be a biological event (which might be expected to happen at about the same rate of as catalysis by the enzyme) but is probably instead a chemically reversible event that occurs gradually over much longer periods, again possibly pointing to the controversial notion of whether this HS $g \sim 6.00$ is a signature for either a proximally His-ligated ferric heme or a P450 penta-coordinated neutral thiol-ligated form.

4.6 CYP51B1 Crystallisation

Highly purified WT CYP51B1 and mutant forms (except for G388S) post SEC purification were all subjected to crystal trials using a protocol published by Podust and co-workers (Podust *et al.* 2001a; Podust *et al.* 2007; Podust *et al.* 2004). While initial crystal trials for enzyme either in absence of ligands or in the presence of fluconazole and voriconazole yielded only precipitate, crystals were observed in the presence of 4PI and when bound to an azole-structure mimic (EPBA: α -ethyl-N-4-pyridinyl-benzeneacetanamide) which was employed in earlier CYP51B1 structural studies (Podust *et al.* 2007). This yielded reddish/dark brown protein crystals in different crystal shapes, and less than 0.5 mm in size after a week's incubation at 20 °C (Figure 4.9). However, crystals could not be obtained for the F89H CYP51B1 mutant. Only after employing the microseeding method, as described in section 2.2.11, F89H ligand-free and azole-bound protein crystals were obtained. Crystals were thus obtained for all the mutants, either in ligand-free or 4PI-/EPBA-bound forms, although no crystal formation was observed for triazole-bound samples. Crystals which were large and robust enough to survive the crystal handling and plunge-flash freezing in liquid N₂ technique were sent for X-ray diffraction data collection at the Diamond Synchrotron near Oxford. Given the lack of successful co-crystallisation, efforts were made to obtain fluconazole-, voriconazole- and clotrimazole-bound crystals by the ligand soaking method, which entailed soaking the protein crystals with a saturated solution of the azole drugs (dissolved in DMSO) in the mother liquor. Unfortunately, structure solution revealed that the soaking technique did not lead to replacement of either 4PI or EPBA with the larger azole drugs.

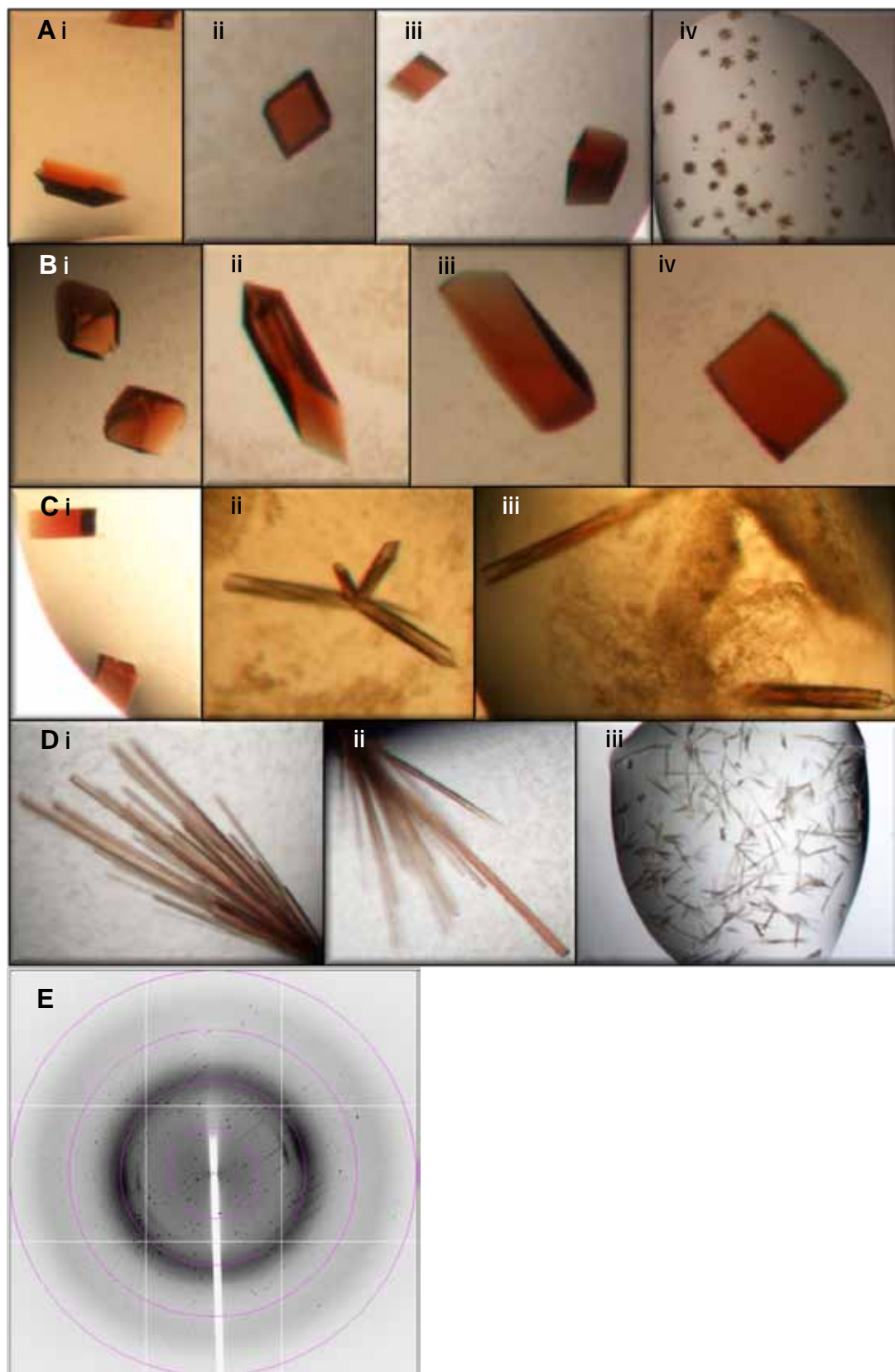


Figure 4.9: Protein crystals obtained and a representative diffraction pattern for CYP51B1 WT and mutant forms. A-D) Formation of various co-crystals under different conditions and after a week of incubation at 20-21 °C. **Ai**) WT-4-phenylimidazole (4PI), **Aii-iii**) WT-ethyl-pyridinyl-benzeneacetanamide (EPBA), **Aiv**) WT-EPBA microcrystals used in microseed stock preparation. **Bi-ii**) F89H-4PI, **Biii-iv**) F89H-EPBA. **Ci**) L100F-EPBA. **Cii-iii**) R391K-4PI. **Di-ii**) R391K-EPBA, **Diii**) R391K-EPBA microcrystals used in microseed stock preparation. **E**) Diffraction pattern of R391K-4PI (**Ciii**) mutant, solved at 1.8 Å.

4.7 CYP51B1 Crystal Structure Features in Ligand-Bound Forms

WT and mutant CYP51B1 crystal structures were solved and refined using standard methods, and the final structures were visualised using the PyMol molecular display program (PyMol™ DeLano Scientific). Structures of WT-4PI, F89H-4PI, F89H-EPBA, L100F-EPBA and R391K-EPBA CYP51B1 are exhibited in Figure 4.10, depicting the mutated residues studied in this thesis. Crystallography statistics data for solved structures can be found in Appendix H. All structures were C-alpha aligned and superimposed to show structural perturbations which may have occurred due to different ligands binding to the heme, or which are due to the point mutations at the B-C loop (F89 to H89 and L100 to F100) and at the heme proximal loop (R391 to K391).

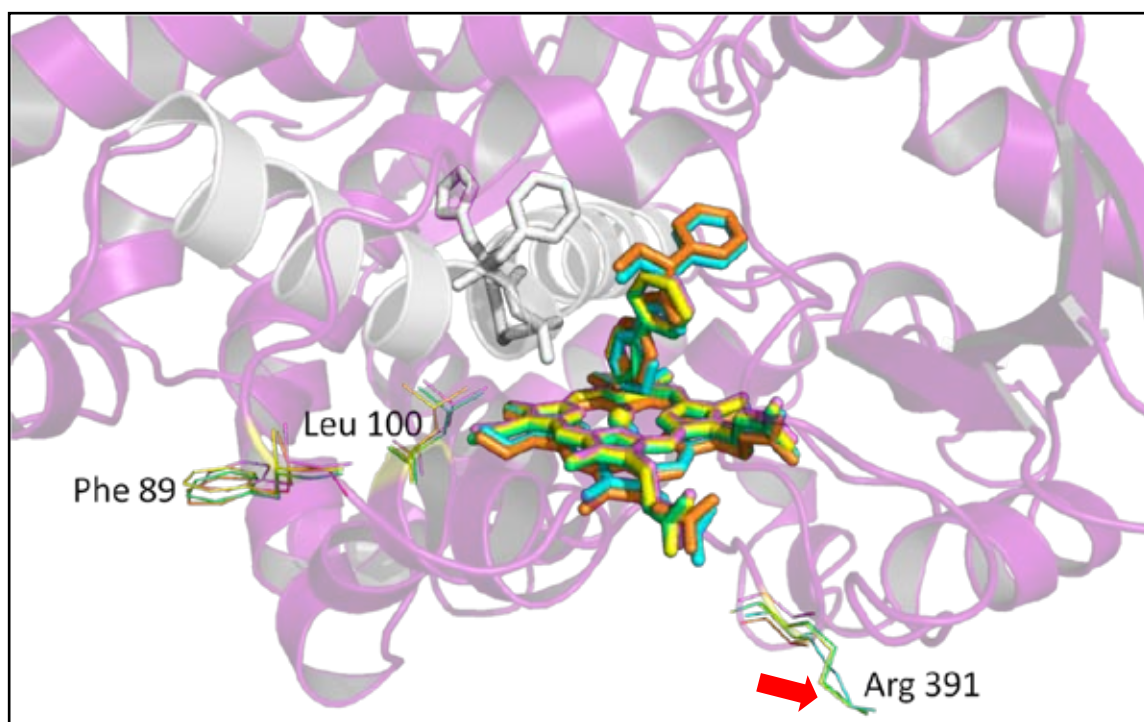


Figure 4.10: Crystal structures of CYP51B1 mutants. An overlay of final structures obtained for various CYP51B1 mutants in complex with 4-phenylimidazole (4PI) and α -ethyl-N-4-pyridinyl-benzeneacetanamide (EPBA). The WT fluconazole-bound model (pdb: 1ea1, 2.21Å) was used as the template structure to solve ligand-bound crystal structures of WT, F89H, L100F and R391K CYP51B1 enzymes according to the difference Fourier technique. The longest helix, the α I (white), runs through the molecule with its characteristic kink in the middle. The model is oriented such that the viewer looks into the heme binding site via the B-C loop opening, where Phe89 was mutated to His and Leu100 was mutated to Phe. The structures of both F89H and L100F CYP51B1 bound to EPBA were solved at 2.0 Å (cyan) and 1.8 Å (orange), respectively, while F89H-4PI (yellow) was solved at 1.4 Å. The CYP51B1 mutant R391K at the cysteinyl loop was solved both bound to 4PI (green) and to EPBA, with both structures solved at 1.8 Å. WT CYP51B1 bound to 4PI was solved at 1.4 Å (purple). The structures were superimposed and C-alpha aligned to produce the model above, where the heme macrocycle, ligands and mutated residues are illustrated as sticks and lines. Note that the guanidinium side chain of residue Arg 391 is disordered (see red arrow) in WT structures.

The kink in the middle of the I-helix (α I) is accentuated by interactions of the two side groups of Phe256 and His259 residues with adjacent residues or ligands. Phe256 and His259 are separated by Ala and Gly residues (i.e. a FAGH sequence). Glycine residues are known to confer flexibility to secondary structural elements and to have a low propensity to form α -helical structures, and are usually found in loop structures (Lepesheva *et al.* 2003). The observed conformational flexibility of the α I confers either the open or closed configuration of CYP51B1, allowing ligand entry, docking or exit. This conformational flexibility is not observed for structures of CYP51 from human and protozoa, at this position. In addition, Gly residues in CYP51B1 (e.g. Gly84 and Gly175) were identified as important residues needed to maintain flexibility at loop regions and catalytic activity of this enzyme with 24, 25-dihydrolanosterol (Lepesheva *et al.* 2003).

From the previous chapter, the R391K CYP51B1 mutant was shown to have a slower rate of ferrous-thiolate protonation compared to WT CYP51B1 and to the other mutants (Table 3.1 and Figure 3.14 E). This may be attributed to the missing arginine guanidinium side chain in the R391K mutant. The guanidinium side chain of Arg391 might have two roles at the cysteinyl loop region of CYP51B1, i.e. (i) by forming multiple H-bonds with adjacent amino acid side chains and/or (ii) by establishing an efficient proton transfer system during thiolate-thiol transitions of the reduced enzyme. The WT-4PI (Figure 4.12, in purple) and L100F-EPBA (in cyan) crystal structures from this work revealed that the Arg391 side chain was disordered (red arrow), which might suggest that facilitating proton transfer to/from the proximal cysteine thiolate/thiol ligand is a more likely role for this residue. However, it should also be remembered that Lys391 is also a potential proton donor/acceptor.

CYP51B1 exhibits a disordered α I region in the ligand-free form, and a profound distortion of the α I was observed in both estriol- and inhibitor ligand (4PI or fluconazole)-bound forms (Podust *et al.* 2004). This deformation, combined with the extended conformation of the B-C loop region, creates a wide access channel to the active site, as shown in Figure 4.1. Comparisons of the crystal structures of ligand-free and estriol-bound forms of CYP51B1 show that the α C (the location of the L100F mutation) undergoes a helix-to-coil transition on estriol dissociation and that the loss of the α C structure results in a more extensive opening to the heme pocket (Podust *et al.* 2004). Binding of azoles or estriol triggers substantial (4PI) or partial (fluconazole or estriol) α C ordering. Azole binding does not affect the conformation of the B-C loop, but estriol binding releases the loop from its surface position and enables it to adopt a more closed conformation (Munro

et al. 2007b). The structures of WT and F89H mutant CYP51B1 enzymes at the B-C loop regions are illustrated in Figure 4.11. Interestingly, this F89H mutation on the B-C loop drastically affects the average mobility of this region, inducing severe disorder, as shown by the near-absent electron density in this region of the F89H-4PI mutant structure (Figure 4.11 **B**), as compared to the relative order of the corresponding segment of the WT-4PI complex structure (Figure 4.11 **A**). It needs to be noted that, even in the WT CYP51B1 structures available, both those determined in this thesis and others available in the literature, the BC loop has significantly higher mobility with respect to the core structure. Nevertheless, the introduction of a F89H mutation leads to increased flexibility in this region which results in total loss of ordered electron density (Figure 4.11).

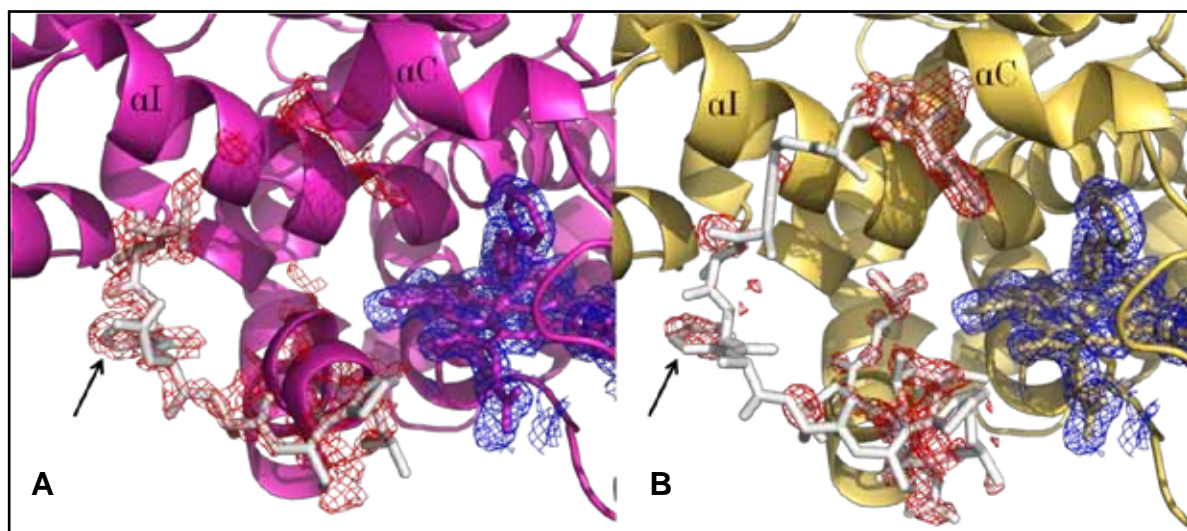


Figure 4.11: Dynamics of the highly mobile CYP51B1 B-C loop. **A**) B-C loop of the CYP51B1 WT-4PI structure solved at 1.5 Å indicates limited disorder and a corresponding weak electron density (as compared to the strong blue electron density of the heme) at the B-C loop **B**) A similar view of the F89H-4PI CYP51B1 solved at 1.4 Å. In this case, no significant electron density could be observed for the BC loop region. Electron density was contoured at 1 σ . A black arrow indicates the 89 position.

Conserved residues in the C-terminal heme-binding site are thought to be important for maintenance of P450 tertiary structure (Munro *et al.* 2007b; Ortiz de Montellano 2005), and to contribute to heme binding. The CYP51B1 Gly388 is heavily conserved at this position throughout the CYP51 family and across other P450s, as shown by multiple sequence alignment (MSA) of this region by Kelly *et al.* (Kelly *et al.* 2001) and Podust *et al.* (2001b). The cysteinate ligand to the heme iron is absolutely conserved and is critical to P450 oxygenase function, and resides in the cysteinyl loop region (the β -bulge) preceding the α L (Figure 1.10 **B**). This segment shields the C394 ligand from solvent and enables it to accept hydrogen bonds from peptide NH groups (Munro *et al.* 2007b).

The electron density at the heme proximal region for both the WT (magenta) and the R391K CYP51B1 (green) mutant show few differences (Figure 4.12), implying that the lysine mutation has little effect on the local protein structure or dynamics. Furthermore, electron density for the guanidine moiety of Arg391 (black arrow in Figure 4.12 A, B) is missing in WT structures, indicating its high mobility. This suggests that no stable H-bond network is formed between the Arg391 side chain and surrounding residues. The inability of the G388S CYP51B1 enzyme to form crystals was likely due to its heterogeneous nature, existing in both unstable apoprotein and holoenzymes forms, and also in different oligomeric states with various melting temperatures, as described in section 4.4.

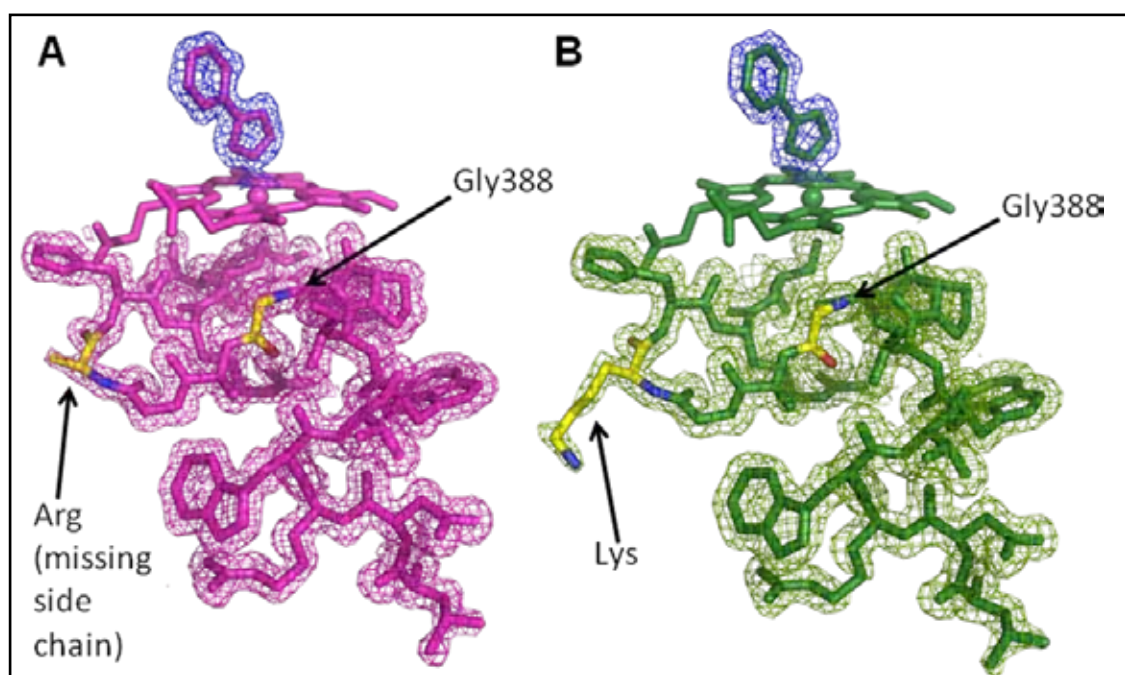


Figure 4.12: Comparison of WT and R391K mutant structures. A) The arginine residue at 391 in the WT-4PI CYP51B1 structure (1.5 Å) was modelled up to the C_β atom, due to the absence of electron density for the Arg391 side chain. B) The R391K mutation results in little structural change. No apparent major perturbations were observed for the CYP51B1 R391K mutation at the conserved loop. Arg391 and Gly388 are shown as colour coded sticks (yellow-C, blue-N, red-O). The electron density (blue) around the 4PI distal ligand to the heme macrocycle is also shown.

In order to illustrate the regions of CYP51B1 which are highly mobile within the crystal structure, the structure was colour coded according to B-factors (from least mobile-dark blue to highly mobile-red) for the F89H-4PI mutant enzyme structure (Figure 4.13 A). The corresponding B-factor graph in Figure 4.13 (B) gives a relative numerical value to the mobile regions of WT CYP51B1, as earlier published by Podust *et al.* (2004).

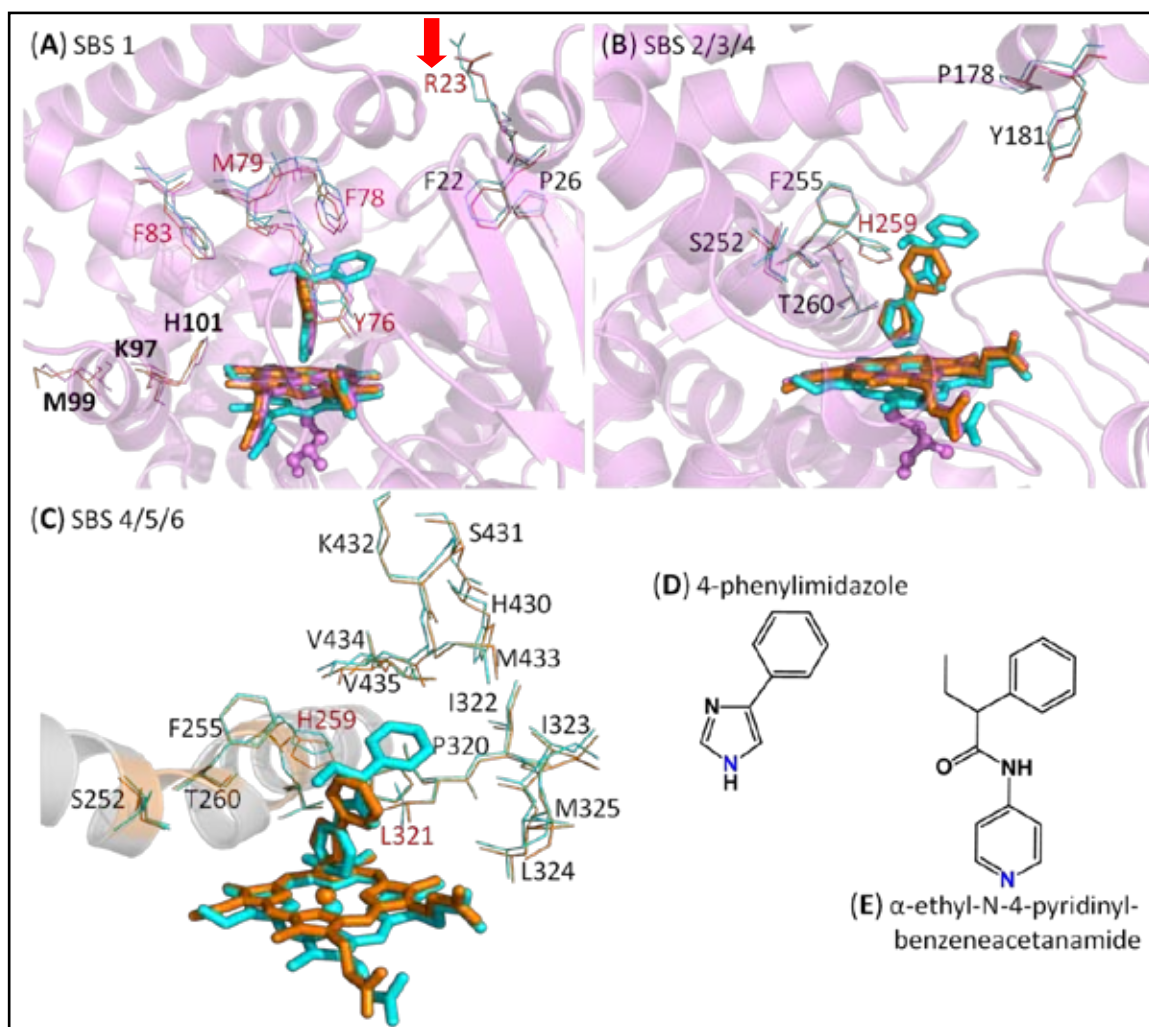


Figure 4.14: Structural differences induced by 4PI and EPBA ligation in CYP51B1. Three models, 1.5 Å WT-4PI (purple), 1.4 Å F89H-4PI (orange) and 2.0 Å F89H-EPBA (cyan), were superimposed. The hemes are shown in the same colour scheme. The proximal cysteine 394 ligand is shown in purple stick and ball representation. **A)** Substrate binding site 1 (SBS 1) residues at the B-C loop, α B' and α C are shown in line structures. The side chains for M99, K97 and H101 (labelled in bold, black text) on the α C are disordered in the EPBA-bound enzyme structure, suggesting that ligand-induced disorder occurs, while Y76, F78, M79, F83 and R23 (labelled in red) showed slight perturbations, depending on the nature of the ligand. **B)** SBS 2 (on α F), SBS 3 (on α G) and SBS 4 (on α I) residues showed little change, except for H259 (labelled in red) on the α I, which directly interacts with the ligand. This is also shown in **(C)** where the imidazole side group of H259 and the isobutyl side group of L321 are involved in binding the benzene ring of EPBA. **D** and **E** illustrate the chemical structures of 4PI and EPBA.

In the case of EPBA, the same two residues at SBS 1 (Tyr76) and at SBS 4 (His259), and other residues at SBS 1 (Phe78 and Met79) and SBS 6 (Leu321) are involved in ligand binding. The His259 residue is one of the two residues (the other being Phe256) associated with the kink in the α I of CYP51B1. The F89H CYP51B1 mutant structures solved in complex with 4PI and EPBA were superimposed. Interestingly, ligand identity can significantly affect the mobility of SBS 1 residues at the B-C loop regions. This is demonstrated by the absence of electron density for Met99, Lys97 and His101 (bold black

text in Figure 4.14 A) when CYP51B1 is bound to EPBA in the F89H-EPBA, L100F-EPBA and R391K-EPBA CYP51B1 structures, by comparison to the relative order of the same residues in 4PI-bound mutant and WT CYP51B1 enzymes.

4.8 Summary and Critical Assessment

This chapter complements the biochemical results from chapter 3 by confirming that the overall secondary structures of mutant CYP51B1 enzymes are not affected by single-point mutations at important sites in the enzyme associated with azole drug-resistance in *C. albicans* CYP51. All of the CYP51B1 variants generated in this study are α -helix rich, as shown by the features at 209 nm and 224 nm from far UV CD analysis. The deeper major trough at 224 nm, when observed without the minor trough at 209 nm, is one signature for an unfolded random coil protein structure. This major trough (224 nm) was observed concurrently with a minor trough at 209 nm for G388S CYP51B1, consistent with this protein being extensively folded. However, the G388S CYP51B1 far UV CD spectrum showed differences to that for other mutant and WT CYP51B1 enzymes, which can possibly be attributed to its heterogeneous mixture of holoenzyme and apoprotein forms. This heterogeneous nature of the G388S mutant was also detected by MALLS analysis, which showed different oligomeric states that likely arise from aggregation of the apoprotein with other apoprotein or holoprotein molecules. These various G388S enzyme states were also indicated by the more complex protein unfolding patterns defined by DSC analysis of ligand-free G388S CYP51B1 (with at least four distinct T_m values). These calorimetric and dynamic light scattering results were in contrast to those for WT and other mutant CYP51B1 enzymes. For instance, a clear two stage unfolding was observed for WT CYP51B1 with T_m values of ~ 49 °C and ~ 51 °C, and monomeric states of WT CYP51B1 and the other mutant enzymes were observed by MALLS analysis.

The ligation state of the ferric heme iron of WT and mutant CYP51B1 enzymes was also probed by EPR, and this indicated some important differences in coordination states and other properties. Although the typical LS set of g values in ligand-free CYP51B1 enzymes and the sets obtained for azole inhibitor-bound forms were highly similar to data published on CYP51B1 previously by McLean *et al.* (2006), there were two novel EPR features observed for the mutant CYP51B1 enzymes in different ligand-bound forms. The most prominent novel feature was the g 2.00 signal observed in the G388S CYP51B1 enzyme, indicating adventitious metal (free iron in this case) that was likely due to the instability of heme cofactor binding in this mutant. In addition, atypical P450 HS signatures


at $g \sim 6.00$ (5.74, 5.80, 5.84 and 5.86 in different CYP51B1 enzymes) were novel observations made for both F89H and G388S CYP51B1 enzymes in their ligand-free states, and for all the CYP51B1 variants post redox-cycling. This atypical HS $g \sim 6.00$ value in both F89H and G388S CYP51B1 diminished upon distal heme iron ligation by a N atom from the triazole moiety of azole drugs. It appears likely that the signal arises from a penta-coordinated, cysteine thiol-ligated HS state of the ferric heme, as illustrated in Table 4.2. The disappearance of the HS signal on distal ligation by a triazole drug would then be a consequence of the spin-state shift to LS. For the post redox-cycled CYP51B1 variants that all exhibit the HS $g \sim 6.00$ value, the most likely explanations may be that a sulfur-containing molecule derived from dithionite influences the distal ligand environment, or that the proximal thiolate ligand becomes protonated to thiol. The restoration of a LS thiolate-ligated form that occurs on extended incubation of redox cycled CYP51B1 enzymes suggests that the latter explanation is more credible. Possibilities for the identities of CYP51B1 ligands in the redox-cycled HS state were considered in light of previously published data for ferric heme proteins having similar EPR $g \sim 6.00$ values and with a histidine proximal ligand (Dawson *et al.* 2001; Perera and Dawson 2004), a HS methionine proximal ligand (Miles *et al.* 1993) or *bis*-methionine axial ligands (Barker *et al.* 1996). However, there is no firm structural data to indicate that a histidine can occupy either a distal or proximal ligand position in a wild-type P450 enzyme, and thus a model of cysteine thiol as proximal ligand in pentacoordinated redox-cycled CYP51B1 enzymes appears most likely.

Co-crystals were derived from all the mutant CYP51B1 enzymes (except for the G388S mutant enzyme) in complex with 4PI and EPBA inhibitors. Diffraction data were collected for F89H-4PI, F89H-EPBA, ligand-free F89H, WT-4PI, WT-EPBA, L100F-EPBA, R391K-4PI and R391K-EPBA crystals (Appendix H). Analysis of the crystal structures of R391K CYP51B1 bound to 4PI and EPBA revealed that this mutation did not influence the highly conserved cysteinyl loop structure. Mutations at the B-C loop region (as evident from the F89H and L100F CYP51B1 structures) revealed that mobility at this putative entry/exit channel was increased when compared to the already elevated levels of the WT CYP51B1.

Previous P450 structural studies have suggested that conformational flexibility is key to the position of azole drug-resistance-conferring mutations found in *C. albicans* CYP51A1. These mutations map mainly to flexible P450 regions (including the F-G and B-C helical sections and their intervening loops) rather than to the active site, and this

suggests that resistance may be achieved by altered conformational dynamics in CYP51, as opposed to disruption of the substrate binding site (Munro *et al.* 2007b).

In this study, it was confirmed that selected mutations do not cause disruption to the active site, as observed from solved crystal structures of the F89H mutant bound to 4PI and EPBA, and for the L100F CYP51B1 mutant bound to EPBA. In contrast, the mobility of various structural elements lining possible entry-exit routes to the active site can be influenced by the mutations, possibly affecting the kinetics of binding (k_{on}) and dissociation (k_{off}) for the various ligands. Such altered ligand binding/debinding kinetics may be the key to affording azole drug-resistance e.g. as shown for the largely unique G388S variant which exists in a mixture of apo- and holoenzyme species, having highly positive redox potentials and demonstrating much faster thiolate protonation than the other variants of CYP51B1 studied here. These mutations at important SRS and SBS regions on CYP51B1 could also potentially have less effect on substrate affinity than on azole affinity so as not to compromise physiological function at the same time keeping in mind that the point mutants of CYP51B1 do not necessarily reflect the true 'fluconazole-resistant' CYP51A1 (CYP51ca) from fluconazole-resistant *C. albicans* due to other circumstances i.e. variations in amino acid sequences of CYP51, effect of other mechanisms of drug-resistance in *C. albicans* (mutations in the drug efflux pump genes) and the *in vitro* experiments of CYP51B1 which may not reflect true *in vivo* conditions. Findings in this study serve as a quantitative guide in elucidating the mechanisms of fluconazole drug-resistance at the aforementioned regions of CYP51B1 at the molecular enzymology level.



*Chapter 5 | Molecular Biology Studies of
CYP123 and CYP136*

- 5.1 Pseudogenes, Paralogues or New Enzymes*
- 5.2 Gene and Protein Engineering*
 - 5.2.1 CYP123*
 - 5.2.2 CYP136*
- 5.3 Expression Systems*
 - 5.3.1 CYP123*
 - 5.3.2 CYP136*
- 5.4 Purification with Native and Tagged Proteins*
- 5.5 Chaperone Proteolysis*
- 5.6 MALLS and CD Analysis*
- 5.7 Discussions from Bioinformatics Analysis*
- 5.8 Summary and Future Work*

5 MOLECULAR STUDIES OF CYP136 AND CYP123

5.1 Pseudogenes, Paralogues or New Enzymes

Several reports have highlighted important connections between CYP51 from various different pathogenic organisms and human macrophages, with respect to human diseases e.g. *Leishmania infantum* (Hargrove *et al.*, *J. Biol. Chem.*, in press) and *Mycobacterium tuberculosis* (McLean *et al.* 2010). In the case of Mtb, the physiological role of CYP51B1 has yet to be established. However, there is strong evidence for the functions of other Mtb P450 enzymes in sterol metabolic pathways, i.e. CYP125 (A 27-hydroxylase of cholesterol and cholest-4-en-3-one from the host, which was also shown to further oxidise 27-hydroxycholest-4-en-3-one to cholest-4-en-3-one-27-oic acid) (McLean *et al.* 2009; Ouellet *et al.*, 2010) and CYP142 (a cholesterol-27-hydroxylase) (Driscoll *et al.* 2010). Both these enzymes are involved in oxidation of host cholesterol to facilitate its catabolism by Mtb, and there may be additional roles in detoxification of 4-cholesten-3-one and/or production of immunomodulatory 27-hydroxycholesterol. Although Mtb appears not to have a sterol biosynthetic pathway, CYP125 and CYP142 are clearly important for infection and survival in the host, and it is highly likely that CYP51B1 also has an important role (e.g. for infectivity or re-infection of Mtb in humans), along with these enzymes and possibly other orphan Mtb P450 enzymes, which are present in high numbers in this human pathogen (only ~6 of the 20 Mtb P450s have assigned functions). On this pretext, and also as a consequence of the presence of dual functional copies of CYP51 in *Aspergillus* spp. (also human pathogens) (Mellado *et al.* 2001; Warrilow *et al.* 2010), work was done in this chapter to investigate the hypothesis that Mtb too could possibly have dual or multiple copies of the sterol demethylases. However, to date, whether these other P450s are functional enzymes and/or a product of evolution (paralogues) has yet to be proven, and was addressed in this chapter with studies on Mtb CYP123 and CYP136.

Genetic evidence to support the hypothesis that Mtb possesses additional sterol demethylases comes from the proximity of some P450 genes to *CYP51B1* (*Rv0764c*), e.g. the *CYP123* gene (*Rv0766c*) which is situated upstream on the same operon dedicated to intermediary metabolism and respiration and in a gene cluster rich in predicted oxidoreductases (Tuberculist webserver: <http://tuberculist.epfl.ch/>) (Cole 1999). In addition, the presence of an adjacent ferredoxin redox partner (Fd1 – 68 a.a.) (product of *Rv0763c*) and a nearby *Rv0688c* gene coding for the novel FAD-associated reductase (Fdr - 406 a.a.), both of which were proven to facilitate electron transfer from NADPH to CYP51B1 in Chapter 3 (Figure 3.11), also highlights the proximity of redox proteins that

could drive both CYP51B1 and CYP123 function. These genetic observations thus strengthen the possibility that proximal potential sterol demethylase(s) could share these redox partners to enable electron transfer in the C-14 demethylation of sterol substrates (or related activities on similar substrates), probably using sterols provided by the host (possibly in the host macrophage during Mtb infection/latency). CYP123 (402 a.a., product of *Rv0766c*) and CYP126 (414 a.a., product of *Rv0778*) share 32% amino acid sequence identity, while CYP123 and CYP51B1 (451 a.a.) share 20% amino acid sequence identity (ClustalW2: <http://www.ebi.ac.uk/Tools/msa/clustalw2/>). Both values are below the 40% “cut-off” limit that would currently qualify them as members of the same family of P450 enzymes, however. These five genes (*CYP51B1*, *CYP123*, *CYP126*, *Fd1* and *Fdr*) are situated in the same locus dedicated to intermediary metabolism and respiration, suggesting that they might have important roles in maintaining cell viability, although *CYP51B1*, *CYP123* and *Fdr* have been categorised as non-essential for growth (in rich media) in the Mtb H37Rv pathogenic strain, while essentiality data for *CYP126* and *Fd1* are not available (Lamichhane *et al.* 2003; Sasseti 2003). Interestingly, both *Fdr* and CYP123 have recently been found in the cell membrane fractions of Mtb H37Rv using proteomics analysis (Malen *et al.* 2010; Mawuenyega *et al.* 2005), suggesting a possible role for these proteins in membrane biochemistry, or perhaps in maintaining cell wall integrity. In another study, the *Fd1* (*Rv0763c*) gene was found to be differentially expressed during Mtb infection in mice (McLean *et al.* 2007; Etienne *et al.* 2002), suggesting an important role for this gene during infection.

In addition to *CYP123*, another gene coding for a putative P450 (CYP136, 492 a.a., product of *Rv3059*) is situated ~2500 bp downstream of the genes coding for CYP51B1 and CYP123. CYP136 has been assigned as a possible sterol demethylase (possibly the second in Mtb) by virtue of BLASTp results showing its similarity to a CYP51 (29% amino acid identity) from *Plesiocystis pacifica* (marine slime bacterium) and its having FASTA scores of >25% amino acid identity to the CYP51 lanosterol 14- α demethylase from *Rattus norvegicus* (brown rat) and *Mus musculus* (house mouse) (tuberculist webserver: <http://tuberculist.epfl.ch/>). While there is a possibility that the *CYP123* and *CYP136* genes code for P450s with functions divergent from CYP51B1 as a product of gene evolution from an ancient progenitor (e.g. *CYP51B1*), and would thus be termed paralogues, it appears unlikely that they are dysfunctional pseudogenes, since their DNA coding sequence translates into full length protein sequences in both cases (Appendix B). In a related pathogenic bacterium, *Mycobacterium leprae*, 12 P450 (*CYP*) pseudogenes were found, along with only one functional P450 gene (coding for CYP164A1) (Warrillow *et al.* 2009). The fact

that leprosy (caused by *M. leprae* infection) is less contagious than TB might explain the high number of P450 pseudogenes in *M. leprae* and the apparent absence of pseudogenes among the 20 P450 genes in Mtb (Pubmed Health), assuming that several of the P450s in Mtb have key roles in bacterial infection and establishment of the disease state. Hence, the possibility raised here is that these previously uncharacterized Mtb *CYP123* and *CYP136* genes have the potential to code for new enzymes with novel functions (possibly related to sterol metabolism) that are unique to Mtb. Therefore, the main objective of the research in this chapter was to put in place the molecular biology groundwork for CYP123 and CYP136 proteins in order to optimise their expression, and also to understand their biochemical features and whether they are functionally related to CYP51B1.

The multiple sequence alignment (MSA) in Figure 5.1 shows amino acid sequences of the N-terminal sequence regions for CYP51 from *A. fumigatus*, *C. albicans*, *H. sapiens*, Mtb and *T. brucei*, and for CYP136 and CYP123 of Mtb. The first ~30-60 non-polar/hydrophobic amino acid residues at the N-terminal for the eukaryotic CYP51s indicates the membrane anchor region, which is absent from CYP51B1 and CYP123. CYP51A1 from *C. albicans* contains ~40% hydrophobic residues in its N-terminal sequence, CYP51 from human has ~43%, while CYP136 has only ~25%. This predicts that, even though it has an extended N-terminal region compared to none detected in CYP51B1 and CYP123, CYP136 (full MSA comparison in Appendix D) has the potential to be a soluble cytoplasmic protein.

<i>A. fumigatus</i> -CYP51a	-----MVPMLWLTAYMAVAVLTAILLNVVYQLFFRLWN-----RTE	36
<i>A. fumigatus</i> -CYP51b	MGLIAFILDGICKHCSTQSTWVLVIGLLSILAVSVIINVLQQLLFKN-----PHE	51
<i>C. albicans</i> -CYP51A1	---MAIVETVIDGINYFLSLSVTQQISILLGVPFVYNLVWQYLYSLR-----KDR	47
<i>H. sapiens</i> -CYP51	MLLLGLLQAGGSVLGQAMEKVTGGNLLSMLLIACAFTLSLVYLIRLAAGHLVQLPAGVKS	60
Mtb-CYP51B1	-----MSAVA	5
<i>T. brucei</i> -CYP51	-----MLLEVAIFLLTALALYSFYFVKSFNVTR-----PTD	31
Mtb-CYP136	MATIHPPAYLLDQAKRRFTPSFNFPGMSLVEHMLLNTKFPKLLAEP-----PGSGLK	55
Mtb-CYP123	-----MT	2
<i>A. fumigatus</i> -CYP51a	PPMVFWVWPYLGSTISYGIDPYKFFACREKYG-DIFTFILLGQKTTVYLGVQGNFILN	95
<i>A. fumigatus</i> -CYP51b	PPVVFHWFPFIGSTISYGIDPYKFFDCRAKYG-DIFTFILLGKKTIVYLGTKGNDFILN	110
<i>C. albicans</i> -CYP51A1	APLVFYWIPWFGSAASYGQPYEFFESCQRKYG-DVFSFMLLGKIMTVYLGPKGHEFVFN	106
<i>H. sapiens</i> -CYP51	PPYIFSPIPFLGHAIAFGKSPIEFLENAYEKYG-PVFSFTMVGKTFYLLGSDAAALLFN	119
Mtb-CYP51B1	LPRVSGGHDEHGLEEFRTDPIGLMQRVRDECG-DVGTFQLAGKQVLLSGSHANEFVFR	64
<i>T. brucei</i> -CYP51	PPVYPVTVPI LGHI IQFGKSP LGFMQE CKRQLKSGIFTINIVGKRVTIVGDPHEHSRFFL	91
Mtb-CYP136	PVVG DAGLPILGHMIEMLRGGPDYLMFLYKTKG-PVVF GDSAVLPGVAALGPDA AQVIYS	114
Mtb-CYP123	VRVGDPELVLDPYDYDFHEDPYPYRRLRDEAP-LYRNEERNFWAVSRHHDVLQGF RDST	61

Figure 5.1: Amino-terminal sequence alignment of CYP51s, CYP123 and CYP136.

The N-terminal sequence for Mtb CYP51B1 has been highlighted in black to indicate it as the soluble “benchmark” without a hydrophobic amino acid N-terminal membrane anchor region, which is present in other CYP51 isoforms from fungi, human and protozoa. The Mtb CYP136 does have an extended N-terminal region, and was suggested to resemble a mitochondrially-localised protein using TargetP software (<http://www.cbs.dtu.dk/services/TargetP/>).

5.2. Gene and Protein Engineering

5.2.1 CYP123

Molecular biology steps were performed to excise the *CYP123* gene (1.209 kb) from the initial pGEMT vector, using either NdeI/BamHI or NdeI/HindIII restriction enzymes, and the relevant *CYP123* gene fragments were cloned into different pET vector expression systems: pET15 (using NdeI/BamHI), pET20b (NdeI/BamHI and NdeI/HindIII), pET24b (NdeI/HindIII) and pET28b (NdeI/HindIII). Examples of the relevant *CYP123* gene fragments resolved on agarose gels are shown in Figure 5.2.

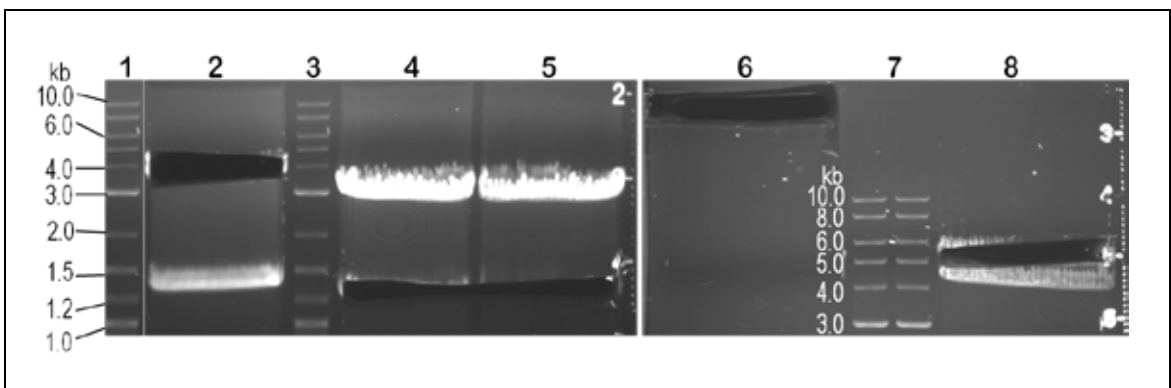


Figure 5.2: Plasmid and gene isolation for *CYP123* vector construction. Plasmids were digested with NdeI and HindIII restriction enzymes at 37°C for 5 h to excise gene inserts, and samples were loaded onto a 1% agarose gel as follows: L2 – 250 ng pET20b (3.7 kb, 36 ng/μL post gel extraction - quantified by Nanodrop) with the *CYP51B1* gene excised from the gel (~1.5 kb); L4 and L5 – 450 ng pGEMT loaded per well (~3.5 kb, 45 ng/μL) with the *CYP123* gene excised from gel (1.2 kb); L6 – 100 ng pET24b loaded (circular, undigested plasmid vector, 28 ng/μL); L8 – 100 ng pET28b (~6 kb, 20 ng/μL) with protein-encoding gene excised from gel (~4.5 kb). L1, L3 and L7 are 2-log bp DNA ladders.

The *CYP123* gene cloned using NdeI/HindIII restriction sites resulted in a stop codon immediately at the end of the P450. By mutating out the “T” nucleotide from the stop codon, just before the HindIII recognition site, an in frame fusion to a C-terminal His₆-tag was created for CYP123, as illustrated in Figure 5.3. The same NdeI/HindIII cloning and mutation strategy was used to produce CYP123 with both a C-terminal and a N-terminal His-tag in the pET28b expression vector.


```

>cyp123pET28b_Nterm&CtermHis6tag

ATGGGCAGCAGCCATCATCATCATCACAGCAGCGGCCTGGTGCCGCGCGGCAGCCA
Tatgaccgtccgcgctcgggtgaccccgaaactggtcctggacccctacgactacgactttcac
gaagaccgtaccggtattatcgtcggctgcgggacgagggccccgctgtaccgtaacgag
gaacgcaatttctgggcggtgtcgcggcaccacgacgtgctgcaaggcttccgggacagc
acggcggtgtcgaatgcctatggggatccctggatccgtcctcacgacttctgagggc
taccgggtaatgtcgaatgctggccatggacgacccccgcacatctgaggatgctgacctt
gtgtccaagggttccccacggcggtatccgtgaaactcgagccgaggtgctcgaactt
gcccgcattcacctggattcggccctgcaaacgaaagtctcgattcgtagcagaattc
gctggcaagctgccgatggatgtgatttcagagctgataggcgtgcccgacaccgaccgg
gcccgcattccgcgctggccgatgagggtgctgcaccgcgaggacggcgtggccgatgtg
ccccgcggcgatggcggcgtcgaatcgaatcgaatcgaatcgaatcgaatcgaatcgaatc
gaattccggcgggcgcccgcaacaatctgacgtcggcactgctggcagccgagctcgac
ggcgaccggcttccgaccaggaaatcatggcgttctctgtttctcatgggtgatcgccggc
aacgagaccaccaccaagctactggccaatgcccgtctactgggcccaccaccacctggc
cagctggcccgcgtattcggccgaccactcccggattccgatgtgggtggaggaaacctg
cgctacgacacgtccagccagattctggcccgcaccgtcgcgcacgatctcacgttgtac
gacaccacgatccccgaggggtgaggtgttgctgctgctaccgggatcggccaacctgac
gaccgggtgttcgacgacccggacgactatcgcatcggccgcgaaatcggctgcaacta
gtcagtttcggcagcgggtgccacttctgtctgggggtcacctggcccggatggaagcc
cgggtggccctgggcgcgctgctgctgctgctgctgctgctgctgctgctgctgctgctg
gtcgtgcgcgctccattccagcaacgtgcgcggtatttggccatctgcccgatcagcgtgca
gcccaggaaAGCTTTCGGCCGCACTCGAGCACCACCACCACCACCACCCTGAGATCCGGCTGCTAA
...aggTaaAGCTTGC...

HindIII site:      5'... AAGCTT ...3'
                   3'... TTCGAA ...5'

PCR primers:
Forward = 5' ATCAGCGTGCAGGCCAGGAAGCTTG 3'
Reverse = 5' CAAGCTTCCTGGCCTGCACGCTGAT 3'

```

Figure 5.3: Primer design for reading frame correction for the *Rv0776c* (*CYP123*) gene constructs. Reading frame correction to facilitate C-terminal His₆-tag fusion was done for pET vector *Rv0776c* gene constructs with C-terminal HindIII sites and His-tags. Nucleotides in lower case are the *Rv0776c* gene DNA, yellow highlighted nucleotides are the HindIII recognition site, nucleotides in UPPER CASE are pET28b vector DNA, and underlined nucleotides in the *Rv0776* sequence are those complementary to the reverse primer. A PCR single nucleotide deletion mutation (■) was made following ligation/insertion to correct the reading frame shift and to enable a C-terminal His₆-tag fusion to CYP123.

5.2.2 CYP136

The *CYP136* gene was inserted into pET15b cut with NdeI/BamHI restriction sites and expression trials were performed systematically in various expression hosts with/without N and/or C-terminals His₆-tags, as described in section 2.2.3. However, the predominantly insoluble expression of *CYP136* in a pET15b system (as described in more detail later) led to further work involving cloning of this gene into pET11a and pET20b, as shown in Figure 5.4. This was followed by cloning *CYP136* into the novel pCOLDTMTF vector. This is shown in Figure 5.5, which describes the insertion of *CYP136* into the

multiple cloning site of this vector. The pCOLDTMTF plasmid will also be termed pCOLD^{tf} in this thesis. This vector is claimed to facilitate solubilization of otherwise insoluble proteins by fusing them to a N-terminal His₆-tagged trigger factor (tf) chaperone. Thus, a His₆-tf-*CYP136* gene fusion was generated, and expressed under control of a T7 lac promoter system.

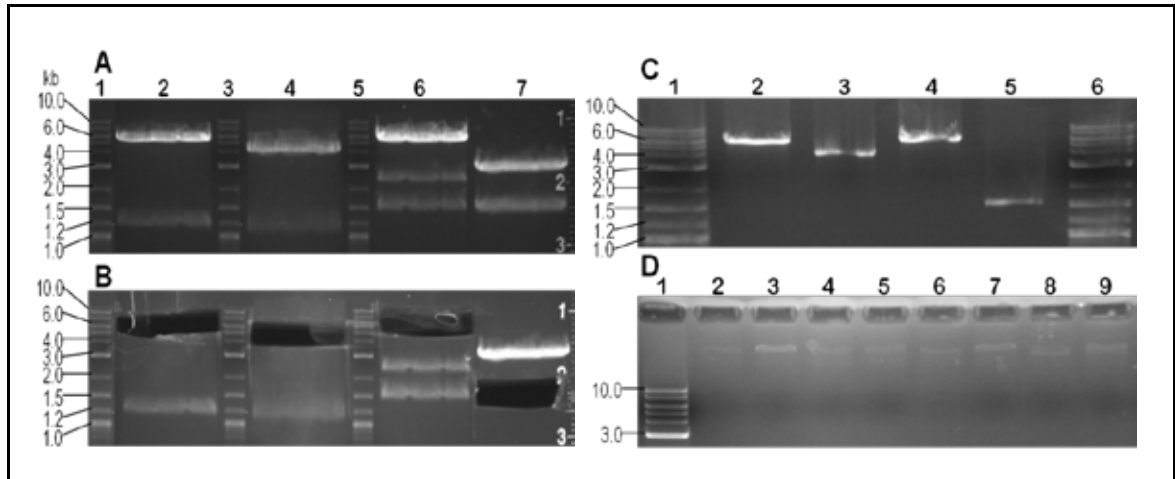


Figure 5.4: Plasmid and DNA isolation for *CYP136* vector construction. Plasmid DNA samples (50 μ L/well) were loaded onto a 1.1% agarose gel post NdeI/BamHI digestion at 37°C for 5 h, and quantified using a Nanodrop instrument. **A-B)** L1, L3 and L5 are 2-log bp DNA ladders, L2 – 220 ng/ μ L pET11a (~6 kb) + *CYP125* (~1.2 kb), L4 – 200 ng/ μ L pET20b (~4 kb) + *CYP51B1* (~1.2 kb), L6 – 520 ng/ μ L pCOLDTMTF (~6 kb) + *DGCR8* (~1.5+2.3 kb), L7 – 430 ng/ μ L pGEMT (~3 kb) + *CYP136* (~1.5 kb). Plasmids and *CYP136* gene were excised from **B** for a DNA gel extraction procedure, after which 5 μ L (out of 30 μ L) of each sample were loaded onto a 0.8% agarose gel shown in **C**, with L1 and L6 – 2-log bp DNA ladder, L2 – pET11a (70 ng/ μ L), L3 – pET20b (22 ng/ μ L), L4 – pCOLDTMTF (44 ng/ μ L) and L5 – *CYP136* (18 ng/ μ L). After DNA concentration normalisation to ~18 ng/ μ L, a ligation protocol was carried out using the NEB Quick Ligation Kit. Post-ligated plasmid DNA was screened for successful ligation on a 0.8% agarose gel **D**. **D)** Each well was loaded with 10 μ L samples. L1 – 2-log bp DNA ladder, L2-4 – pET11a, L5-7 – pET20b, L8-9 – pCOLDTMTF. L2, L5 and L8 – controls, i.e. plasmid vectors only without *CYP136* gene insert, L3, L6 and L9 – plasmids with gene insert (1:3 ratio), and L4 and L7 – plasmids with gene insert (1:6 ratio). Successful ligation can be observed by large sized DNA bands in almost all the lanes, and also by faint bands in the control lanes (L2, 5 and 8), indicating recircularised plasmid DNA. Successful ligation products from L3, L7 and L9 were transformed into NB super-competent cells for vector DNA production (midiprep scale), followed by confirmation of gene insertion by outsourced (Geneservice or MWG Eurofins) DNA sequencing. The *DGCR8* sample used encodes a human microRNA synthesising enzyme, and was used as a control in this study.

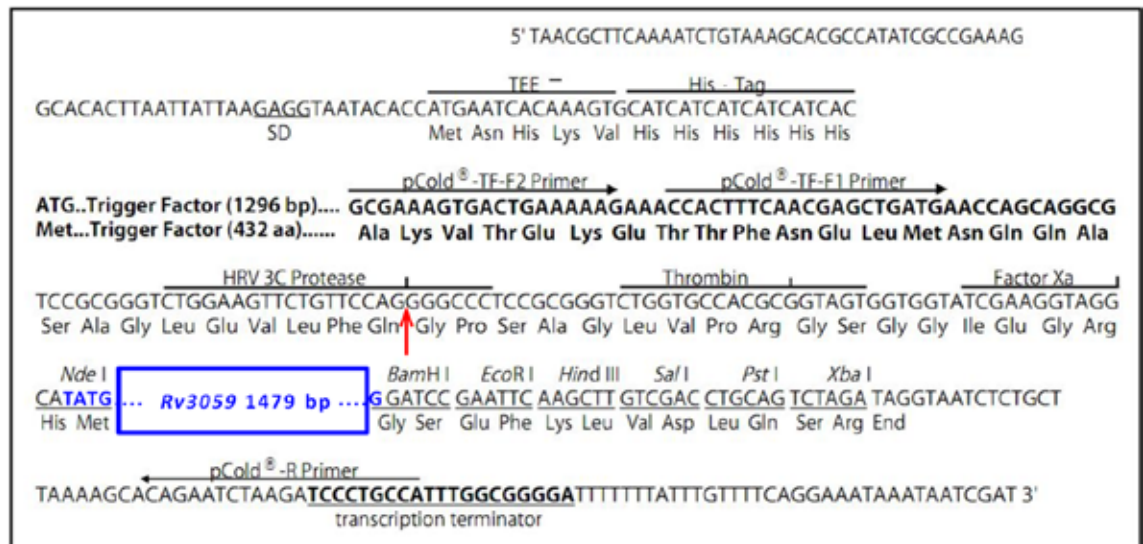


Figure 5.5: Multiple cloning sites in pCOLDTMTF vector and position of *Rv3059* gene. The *Rv3059* gene (blue) coding for CYP136 was inserted at NdeI/BamHI restriction sites downstream of the trigger factor (tf) chaperone with an N-terminal His₆-tag. Expression for this fused protein, i.e. tf (48.2 kDa) and CYP136 (56.2 kDa), was done at 14 °C overnight in strain HMS174(DE3). The red arrow points to the HRV3C protease restriction site used to cleave the His₆-tagged tf chaperone from the CYP136 protein. DNA sequencing to confirm the presence of the *Rv3059* gene insert was done using pCOLD-TF-F1 and pCOLD-R primers (Takara Bio Inc.). SD – Shine Dalgarno sequence. Figure was adapted from pCOLDTMTF multiple cloning site catalogue from Takara Bio Inc.

5.3 Expression Systems

5.3.1 CYP123

Following successful plasmid construct engineering of *CYP123* and *CYP136*, expression trials were carried out for chosen constructs using different expression hosts, according to their availability and their expression properties. **pET15b+*CYP123*** was transformed into HMS174 (DE3), BL21 (DE3) and Rosetta2 (DE3) followed by expression trials in TB medium, induced with 0.4-1.0 mM IPTG at 24 °C for 16 hours. Apparently, no *CYP123* expression was detected in BL21 (DE3) and HMS174 (DE3), but it was expressed in the insoluble fraction using Rosetta2 (DE3) - which aims to improve translation by expressing tRNAs for seven rare codons. In the soluble fraction of these cells, a protein band of similar molecular weight to CYP123 (42.6 kDa) was apparently *E. coli* TU elongation factor (43 kDa) which was constitutively expressed in large amounts, and identified by mass spectrometry using MALDI, and by Western blot His-tagged protein assays.

There was a similar occurrence for non-tagged pET20b+CYP123 and pET24b+CYP123 constructs expressed in Rosetta2 (DE3) (Figure 5.6), with *E. coli* TU

elongation factor again identified by MALDI. CYP123 expression remained insoluble, although the expression temperature was decreased to 18-20 °C and the IPTG concentration varied between 0.1-0.5 mM. The other two *CYP123* constructs, pET20b and pET24b, were trialled without the C-terminal His-tags incorporated, using BL21 (DE3), HMS174 (DE3) and Rosetta2 (DE3) expression strains, but without any change in CYP123 solubility. Figure 5.6 describes the protein expression using **non-tagged pET20b** and **pET24b CYP123** constructs, and with Rosetta2 (DE3) at 18 °C.

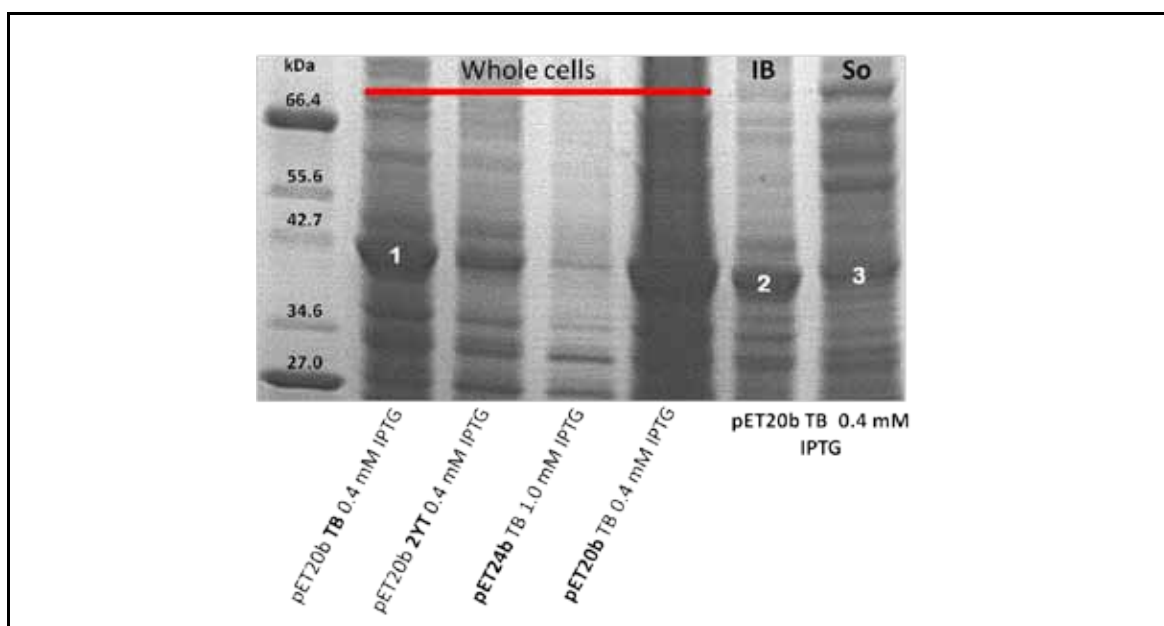


Figure 5.6: Expression of *CYP123* in non-tagged pET20b and pET24b constructs with Rosetta2 (DE3) expression host. Optimisation of *CYP123* expression was carried out under various conditions in pET20b and pET24b using Rosetta2 (DE3) and with various parameter changes, i.e. different media (TB and 2YT) and concentrations of IPTG (0.4 and 1.0 mM). The combination of pET20b in TB medium and induction with 0.4 mM IPTG resulted in greatest *CYP123* expression. Protein identification for the numbered bands was performed by MALDI and the results were: **1** – WC (whole cells) – Mtb CYP123 (42.6 kDa). **2** – Insoluble (IB, inclusion bodies) – Mtb CYP123 42.6 kDa. **3** – Soluble (So) – *E. coli* TU elongation factor (43 kDa).

CYP123 constructs with C-terminal His₆-tags in pET24b, and single (C-terminal) and double (C- and N-terminal) His₆-tags in pET28b were prepared as a result of the above negative results, but due to time limitations of this project and the concurrent expression trials of CYP136, systematic expression trials for CYP123 using these constructs were not carried out, but should be done in future in attempts to produce soluble and active CYP123 protein.

5.3.2 CYP136

As mentioned in section 5.2.2, CYP136 was expressed in the insoluble fraction in a pET15b construct using BL21 (DE3), HMS174 (DE3), OrigamiB (DE3) and Rosetta2 (DE3) as expression hosts. Figure 5.7 (B) shows the resolution of the soluble and insoluble cellular fractions on a PVDF membrane (post Western transfer). The corresponding immunoblot (Figure 5.7 A) identifies the 56.2 kDa His-tagged CYP136 protein in the insoluble fraction (odd numbered lanes). No significant amounts of *CYP136* expression were observed in Rosetta2 (DE3). Exhaustive measures were taken to increase CYP136 solubility using the other two constructs, pET11a and pET20b, including those taken for CYP123, and additionally using four different types of media (LB, TB, 2YT and autoinduction media) and supplementation with the heme precursor (δ -ala) during general cell growth and post-induction expression stages.

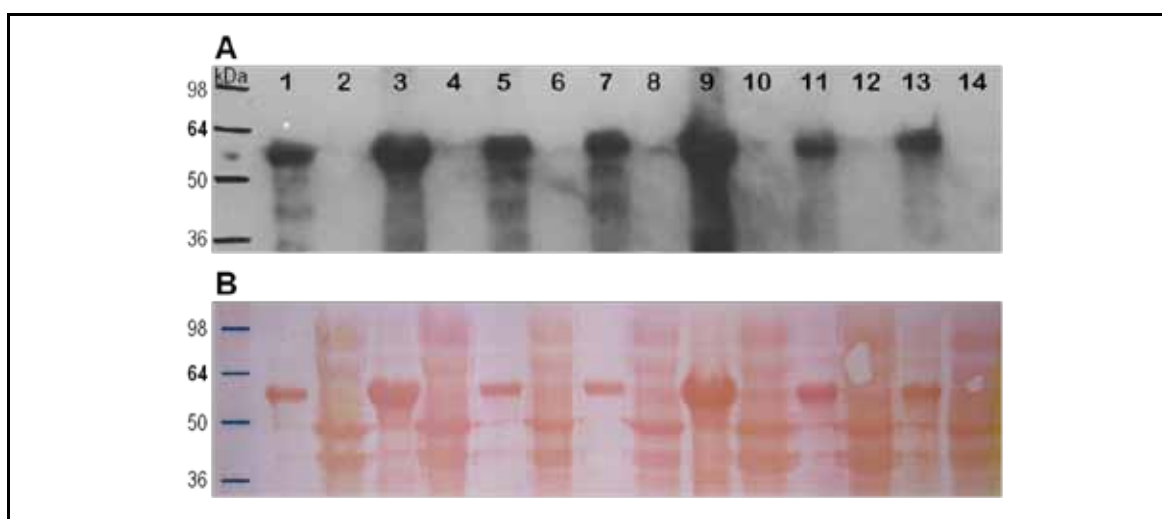


Figure 5.7: Expression of His₆-tagged CYP136 in pET15b construct with various expression hosts. SDS-PAGE gel Western transfer onto PVDF membrane was done overnight (16 h) at 10 mV. **A)** An exposure time of 30 s was done to obtain the above immunoblot for His₆-tagged CYP136tf from pET15b. **B)** Post immunoblot, the PVDF membrane was stained with Ponceau S in 7% acetic acid. Terrific broth was used as the culture medium and cells were grown at 37 °C and then at 18 °C following IPTG induction of *CYP136* expression (Lanes 1, 2, 5, 6, 9, 10, 13, 14), and at 25°C (Lanes 3, 4, 7, 8, 11, 12). Cells were induced with 0.1 mM IPTG (Lanes 1-12) and 0.01 mM IPTG (Lanes 13, 14). Even-numbered lanes are soluble fractions while the rest are insoluble inclusion bodies. Three expression hosts were used: BL21 (DE3) Lanes 1-4, HMS174 (DE3) Lanes 5-8, and Origami B (DE3) Lanes 9-14.

CYP136 was consistently expressed as an insoluble protein, and the light yellowish nature of the pellets from expression of CYP136 using the pET15b construct in HMS174 (DE3) was likely also indicative of poor heme cofactor incorporation (Figure 5.8). To address insolubility issues and cofactor incorporation, the pCOLDt expression vector

was used together with δ -ala for CYP136 protein production. At this stage, no detergent was included in the extraction buffer (which might have aided solubilisation of this protein), and a regular aqueous buffer system was employed (as with CYP51B1) in order to try to maintain a native conformation of this enzyme, and with a view towards future crystallogensis trials that were planned for CYP136.

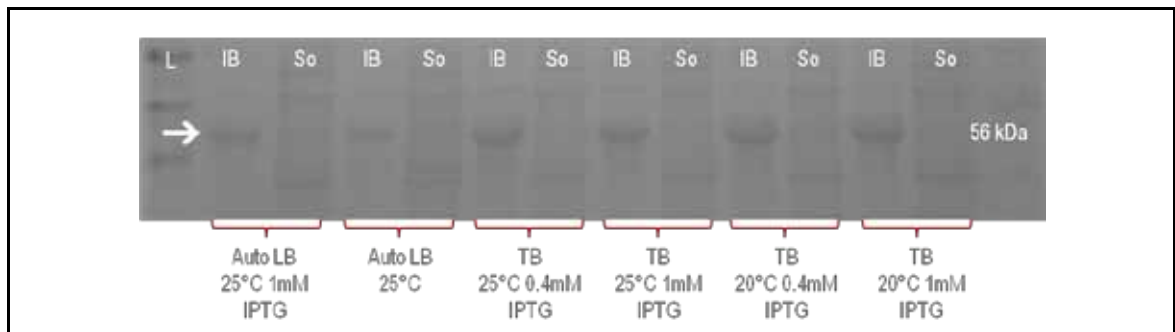


Figure 5.8: Expression of CYP136 in pET15b with a HMS174 (DE3) expression host. The white arrow points to the 56 kDa band for His₆-tagged CYP136, found predominantly in pale white inclusion bodies (IB), and with no significant amounts of CYP136 seen in the soluble fraction (So).

As can be seen in Figure 5.9, evidence for production of soluble CYP136tf fusion protein (104.4 kDa) was detected by SDS-PAGE analysis followed by MALDI protein identification confirmation. However, the fusion protein remained colourless, even though it appeared soluble in PBS, pH 8.0 with 10% glycerol.

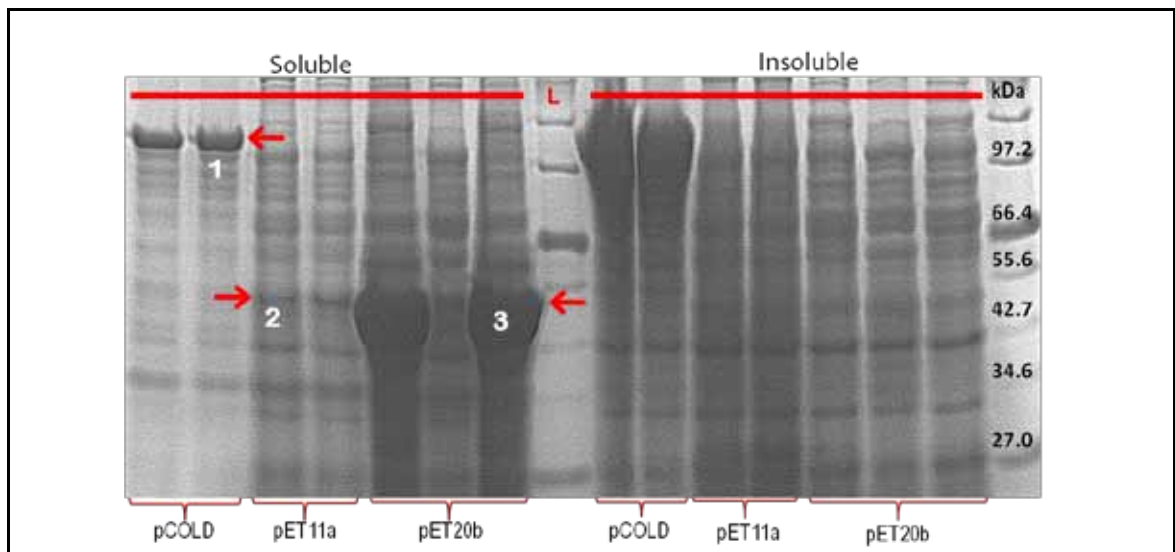


Figure 5.9: Expression of CYP136 in various vectors with a HMS174 (DE3) expression host. Numbered bands were sent for protein identification by MALDI and the results were: **1** – Mtb CYP136 (56.2 kDa) and *E. coli* trigger factor (48.2 kDa). **2** – Mtb CYP136 (56.2 kDa). **3** – *E. coli* trigger factor (48.2 kDa), *E. coli* ATP synthase (55.2 kDa) and Mtb CYP136 (56.2 kDa). Soluble and insoluble cellular fraction lanes are indicated at the top of the gel.

5.4 Purification of Native and Tagged Proteins

Following establishing that CYP136 could be produced in a soluble form when fused to trigger factor, the next stage of experimentation was to attempt to reincorporate heme into CYP136 apoprotein by introducing mild chaotropic agents (e.g. urea or guanidinium chloride) in order to encourage partial unfolding of the apoprotein and to facilitate heme binding. Thereafter, to perform dialysis to remove chaotropic agents from the apoprotein-heme solution mixture in order to promote refolding with the heme incorporated. The first step to this end was done by removing the N-terminal His₆-tagged tf chaperone. Therefore, purification of CYP136tf was carried out according to the Ni-NTA affinity chromatography protocol in section 2.2.5. CYP136tf was expressed well in the soluble fraction, but was colourless, as shown by the yellow arrow in lane 2 (L2) of Figure 5.10. CYP136tf was then subjected to purification from this fraction. Truncated versions of the CYP136tf fusion were also eluted in the 100 mM imidazole elution step, as confirmed by MALDI protein identification. Truncation of CYP136tf during purification may be attributed to the presence of protease activity in the expression strains, and also perhaps due to instability of the fusion protein itself, despite the use of protease inhibitors in both extraction and purification buffers. The pooled eluted fraction (L6) with 250 mM imidazole was concentrated, dialysed and was used for tf chaperone proteolysis experiments at the HRV3C protease restriction site (separating CYP136 and trigger factor) as indicated by the red arrow in Figure 5.5.

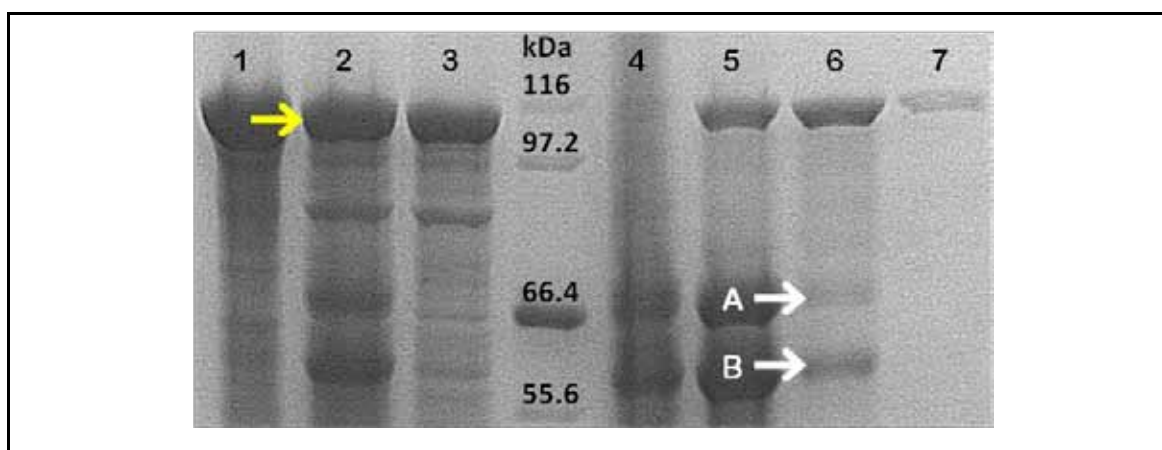


Figure 5.10: Purification protocol for His₆-tagged CYP136 fused to trigger factor chaperone expressed from the pCOLDt_f vector. L1 and L2 show the insoluble and soluble fractions, respectively. The soluble fractions were pooled and loaded onto a Ni-NTA column equilibrated with 50 mM Kpi, 0.1 mM NaCl, 10% glycerol buffer, pH 7.5 with 10 mM imidazole. L3 is the flow-through fraction. L4-7 are the protein fractions eluted with 50, 100, 250 and 500 mM imidazole in the above-mentioned buffer, respectively. The yellow arrow indicates the target protein band of 104.4 kDa. Bands A and B (white arrows) were sent for MALDI protein identification and were both found to contain peptides from both *E. coli* trigger factor and CYP136, suggesting that these bands are from proteolytically cleaved segments of CYP136tf. The protein sample from L6 was used for further analysis.

5.5 Chaperone Proteolysis

CYP136tf was incubated with HRV3C protease (Novagen) at various protease-to-fusion protein ratios, i.e. 1:5, 1:25, 1:50, 1:100 and 1:200 at 4 °C for 16 h, and mixtures were loaded onto a Ni-NTA column to separate His-tagged tf chaperone from CYP136. Assuming the digestion was successful at the site shown in Figure 5.5, three bands should be seen in the post digested mixture, with sizes ~56 kDa (CYP136), ~48 kDa (tf) and 22 kDa (HRV3C). Samples were loaded onto an SDS-PAGE gel, shown in Figure 5.11 (A). Interestingly, Lanes 2-6 of Figure 5.11 (A) showed three bands at 56 kDa (indicative of CYP136), ~25 kDa (indicative of HRV3C protease) and an unidentified fragment at <20 kDa. The non-tagged, cleaved CYP136 was in the Ni-NTA flow through fraction. Assuming that both tf and CYP136 were of similar size and not resolved on the SDS-PAGE gel (hence only one intense 56 kDa protein band, indicated by the yellow arrow), digested protein from L6 (1:200 ratio) was concentrated by ultrafiltration and a Western blot transfer was carried out, followed by an immunoblot (Figure 5.11 B). In lane 1 of Figure 5.11 B, there is a single band giving a fluorescence signal at ~22 kDa (white arrow). This is likely due to His-tagged HRV3C which has passed through the column. It is expected that residual His-tagged HRV3C along with His-tagged tf are also retained on the column following HRV3C treatment. Cleaved CYP136 is expected to be in the flow-through, but does not have a fluorescence signal since it now lacks a His-tag. In lane 2 of Figure 5.11 B, one major band is present. The fluorescent signal (yellow arrow) arises from His-tagged tf which is released from the column on washing with the imidazole buffer. MALDI protein identification of the band in L6 Figure 5.11 (A) (yellow arrow) showed that it contained peptide fragments from both CYP136 and tf proteins. Closer inspection of the gel indicates that there may be two closely migrating bands, and thus that the CYP136 and tf proteins may have similar electrophoretic mobility.

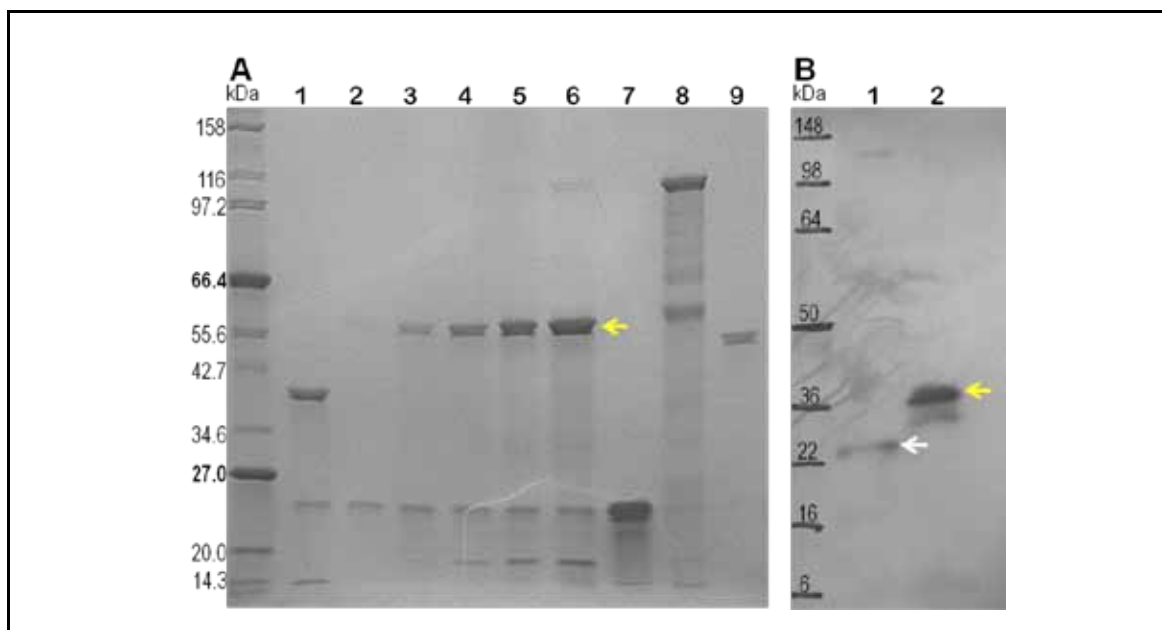


Figure 5.11: Trigger factor chaperone proteolysis trials by HRV3C protease. A) SDS-PAGE analysis (12% gel) of post-HRV3C protease-digested CYP136tf fractions with different volume ratios of HRV3C:CYP136tf of 1:5 (L2), 1:25 (L3), 1:50 (L4), 1:100 (L5) and 1:200 (L6) (40 units of HRV3C in each case). L0 – Protein marker, L1 – HRV3C digested supplier’s HRV3C cleavage control protein (14 kDa and 39.1 kDa fragments), L7 – HRV3C protease (22 kDa), L8 – undigested CYP136tf (104.4 kDa) and L9 – undigested control protein (53.1 kDa). B) Immunoblot analysis of samples. L1 shows post-digested 1:200 fraction flow-through from Ni-NTA column, with white arrow pointing to unbound His-tagged HRV3C at 22 kDa. There is no fluorescence signal for a His-tagged tf or for full length CYP136tf. L2 shows the 1:200 fraction protein which was bound to Ni-NTA following column elution using the imidazole-containing buffer. The yellow arrow points to a His-tagged protein fluorescence signal indicative of a truncated tf from the same fraction.

A scale-up HRV3C protease digestion of the CYP136tf fusion protein was carried out in 50 mL volumes at a 1:200 protease-to-fusion protein ratio, using the same parameters as the above optimised experiment (again with 40 units of HRV3C enzyme added) and according to the Novagen HRV3C user protocol (TB420 Rev. A0804). Once the protease digestion was terminated, the protein mixture was loaded onto a Ni-NTA column, after ensuring that the pH of the solution was 8.0. The column flow-through, which should contain the cleaved non-His-tagged CYP136, was loaded onto an SDS-PAGE gel and a single resulting band at approximately 56 kDa molecular weight was observed (yellow arrow in L3 of Figure 5.12), indicative of isolated CYP136, which still appeared colourless and probably heme-depleted. However, according to MALDI protein identification, this protein band was again a mixture of peptides from both CYP136 and tf. Subsequent immunoblot analysis showed no fluorescence signal at ~56 kDa, indicating that the CYP136 protein was proteolytically cleaved from its tf chaperone (which has a His-tag at its N-terminal). As discussed above, it appears that tf and CYP136 have similar electrophoretic mobility, resulting in MALDI identification of both proteins.

From these observations, it appears that HRV3C digestion is successful, but that the similar SDS-PAGE mobility of tf and CYP136 resulted in their lack of resolution on the gel, as detected by MALDI. The lack of red colour in the samples also suggested strongly that the CYP136 sample was in an apoprotein form. The absence of any protein bands in L4-L7 in Figure 5.12 possibly suggests that the supposedly 'free and soluble' CYP136 may have precipitated out of solution and therefore was not collected in the soluble fraction (but could be trapped within the Ni-NTA agarose) of the column flow-through upon cleavage from the tf chaperone. However, another possibility is that contaminant protease activity and/or aggregation/precipitation of protein samples post-HRV3C treatment resulted in CYP136 loss, explaining lack of its detection in Lane 2 and Lanes 4-7.

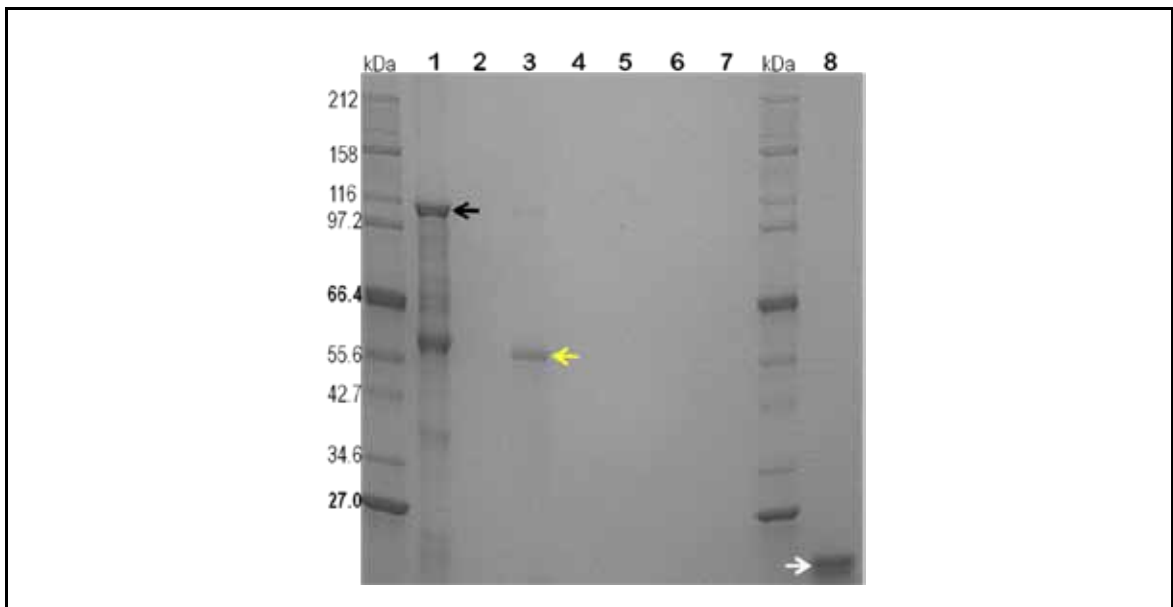


Figure 5.12: Scale-up of trigger factor chaperone proteolysis from CYP136. L1 – CYP136tf (104.4 kDa, black arrow) before digestion with HRV3C protease. L2 – diluted (50-fold) mixture of CYP136tf and HRV3C protease post-digestion. L3 – fraction bound onto Ni-NTA agarose which was identified as containing both CYP136 and tf peptides (yellow arrow) from MALDI protein analysis. L4–L7 – concentrated Ni-NTA flow-through. L8 – HRV3C protease (10 μ L from 40 units stock – 22 kDa, white arrow).

The fact that an insoluble protein can be solubilised when expressed with a molecular chaperone does not mean that, once dissociated from its chaperone, the target protein will remain in solution (Hoffmann *et al.* 2010; Ranson *et al.* 1998). This has been observed by other researchers with proteins which aggregated or which proved to be incorrectly folded when they were dissociated from the molecular chaperone trigger factor. For instance, D-glyceraldehyde-3-phosphate dehydrogenase (GAPDH), cysteine proteinase

and lysozyme (Huang *et al.* 2002; Huang *et al.* 2000). Also, antichaperone activity of trigger factor, promoting protein aggregation or retarding protein export from the ribosome, has also been reported under different buffer systems, high chaperone concentrations and/or with over-expressed trigger factor with target proteins such as lysozyme, creatine kinase, GAPDH and protein disulfide isomerase (PDI) (Huang *et al.* 2002; Lee and Bernstein 2002).

Trigger factor (48 kDa) is an early stage chaperone that assists proper protein folding during ribosomal translation of mRNAs into polypeptide chains. It is an ATP-independent cold shock chaperone, unlike the DnaK (69 kDa) and GroEL/GroES (~800 kDa) molecular chaperonin systems, which are ATP-dependent heat shock-induced chaperones (Hoffmann *et al.* 2010). Some proteins need a full system of molecular chaperonins to be correctly processed into functional enzymes, while (at the other extreme) some proteins can be folded into their correct native 3-dimensional functional forms without the assistance of any molecular chaperones (Hoffmann *et al.* 2010). In Mtb, there are a host of established molecular chaperones and one of the Mtb heat shock (HSP) molecular chaperones, the alpha-crystallin family 2 gene (*Acr2*, 16.3 kDa), was reported to be important for virulence and to be upregulated during heat shock, oxidative stress and macrophage uptake, all of which conditions are representative of TB infection (Qamra *et al.* 2005; Stewart *et al.* 2002; Yuan *et al.* 1998). In addition, another HSP molecular chaperone gene in Mtb, *GroEL* (*cpn60*), was found in duplicate copies in this bacterium and to be highly conserved in all bacteria. It is essential for protein folding in this pathogen and both copies of this gene product elicit strong immune responses in humans (Goyal *et al.* 2006; Qamra *et al.* 2005). It appears likely that CYP136 requires at least one of these abundant chaperonin systems when expressed in Mtb, and in order to correctly aid its folding into the native functional enzyme conformation, and to enable heme binding. When expressed heterologously in the fast-growing *E. coli*, the host chaperones may not be so efficient in aiding folding of a functional CYP136, and trigger factor fusion may also be insufficient to form a holoprotein CYP136.

5.6 MALLS and CD Analysis

Due to likely CYP136 aggregation upon dissociation from the tf chaperone, further spectroscopic analyses were carried out on the intact CYP136tf fusion protein. Purified CYP136tf was found to exist in two different oligomeric states from hydrodynamic studies. Figure 5.13 shows two peaks from MALLS analysis with protein absorption measurements at 280 nm. The MALLS signals consist of a minor peak (7.3%) with an average Mw of 221.5 kDa and a major peak (92.7%) with an average Mw of 57.1 kDa. The Mw of the minor species is likely indicative of a dimeric state of CYP136tf, resulting from the two 104.4 kDa protein molecules dimerizing with each other in solution. This is likely to result from tf being predominantly in a dimeric state in order for it to maintain its chaperonin functionality before it binds to target proteins to assist protein folding (Liu *et al.* 2005). The lower Mw of the major peak observed (57.1 kDa) may represent one (or more) truncated forms of the CYP136-tf fusion protein. This would be consistent with earlier results in this chapter, and specifically regarding the presence of two protein bands at ~56 kDa and 66 kDa that were observed together with the full length fusion protein CYP136tf (see Figure 5.10).

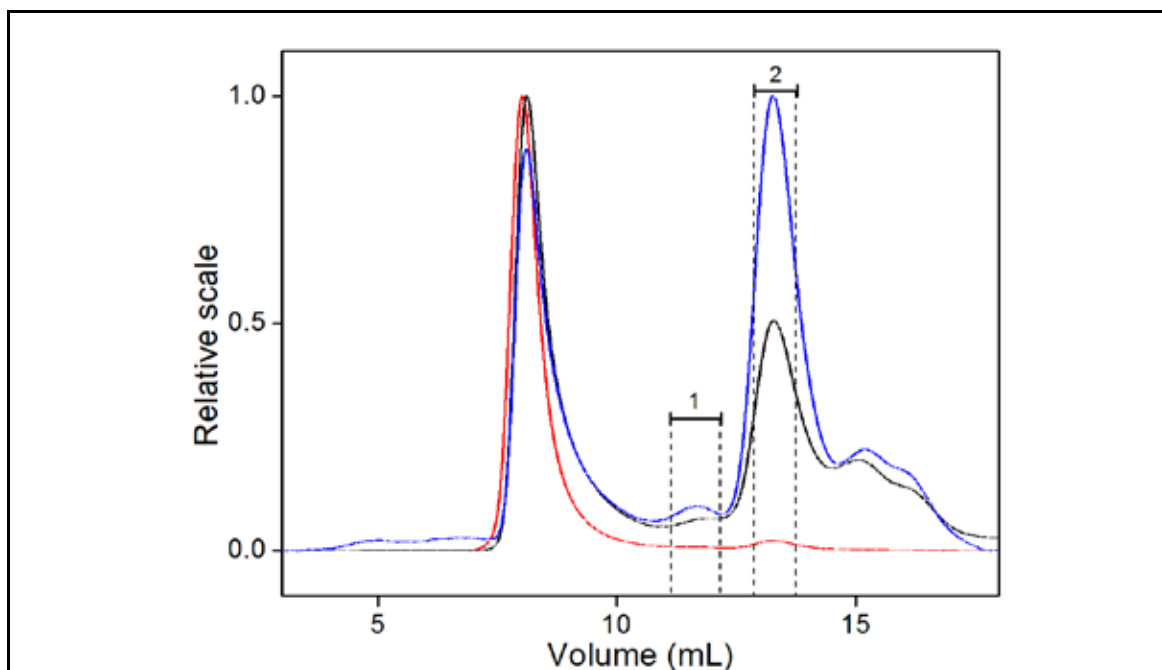


Figure 5.13: Light scattering results from analysis of the CYP136-trigger factor chaperone fusion protein. Red line – light scattering; black line – absorbance at 280 nm; blue line – diffraction index. Fraction 1 (7.3%) has an average Mw of 221.5 kDa and Fraction 2 (92.7% of the total of fractions 1 and 2) has an average Mw of 57.1 kDa. The total size of CYP136tf is 104.4 kDa. CYP136 alone is 56.23 kDa. Fraction 1 is most likely CYP136tf in its dimeric form, while fraction 2 is either the proteolytically separated CYP136 apoprotein or trigger factor chaperone, or both truncated proteins mixed together. Assuming tf remains dimeric on proteolytic separation from CYP136, the band is perhaps more likely to represent CYP136.

Secondary structural analysis by CD spectrophotometry in Figure 5.14 indicated that the full length CYP136tf fusion protein was α -helix rich, similar to tf itself (Hoffmann *et al.* 2010) and as would be expected for a correctly folded P450 protein. Since tf exists in a dimeric state in solution, as reported previously (Liu *et al.* 2005), the larger Mw (CYP136tf) species from MALLS analysis is likely to be the fusion protein dimer. Since the folded state of CYP136 is uncertain, the $\theta_{221\text{ nm}}$ signals from the CD analysis of CYP136tf might be mainly due to the secondary structural composition of tf in its dimeric state, while the attached CYP136 at the C-terminal end of tf might be partially or extensively unfolded. Alternatively, since a folded P450 is mainly alpha helical (like tf), this might contribute to the magnitude of the observed far UV CD spectrum without altering significantly the overall shape of the spectrum. Further quantitative analysis of the contributions of the individual tf and CYP136 components to the CD spectra are necessary before a firm conclusion can be drawn. However, the greater intensity of the CYP136tf CD spectrum (compared to that for a similar quantity of the folded CYP51B1 protein, see Figure 5.14) does suggest that a substantial amount of CYP136 may be folded correctly (albeit likely lacking heme) in the CYP136tf protein.

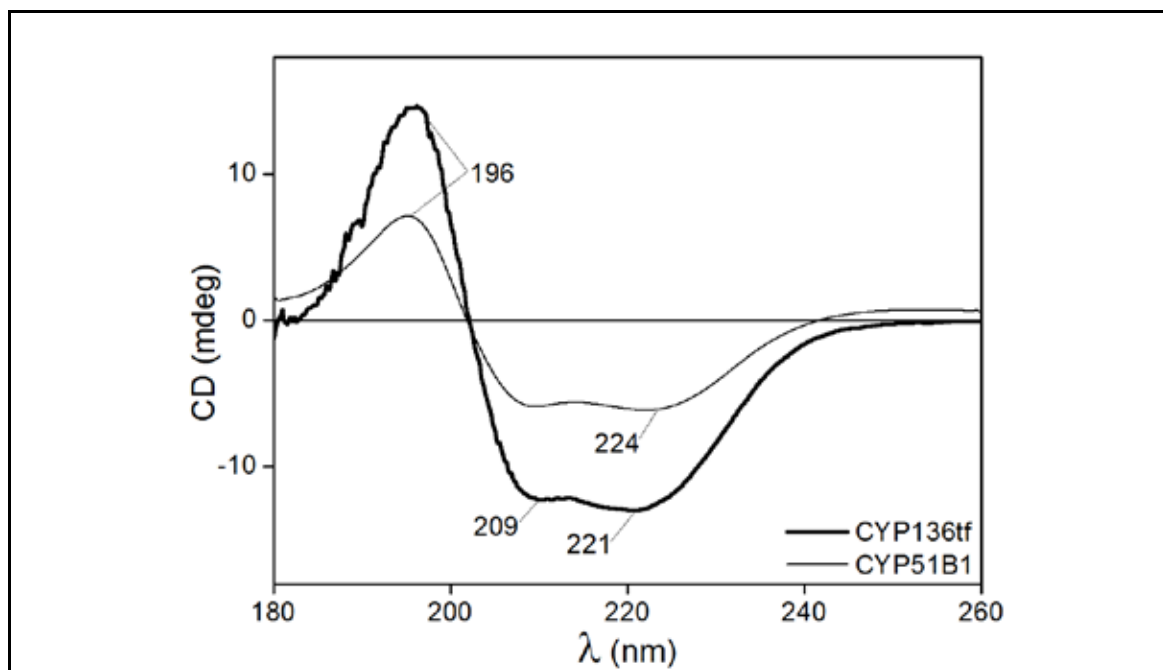


Figure 5.14: Far UV CD spectra of CYP136tf and CYP51B1. Both proteins were calculated to be 1.0 mg/mL from measurement of A_{280} (CYP136tf) and A_{419} (CYP51B1). 100 μ L of 1.0 mg/mL samples were used for each run, and both were aliquots from concentrated protein stocks. The strong negative CD signals at $\theta_{221-0226}$ nm are unique signatures for α -helix rich proteins, and both tf and CYP51B1 are predominantly α -helical. The intense CD spectrum of the CYP136tf protein possibly results from the composite contributions of folded tf and CYP136 proteins. However, it is also possible that at least part of the CYP136 enzyme is unfolded, and that CD signals (or absence thereof) for unfolded portions of this enzyme are buried underneath the dominant contributions from folded parts of CYP136 and fully folded tf protein. While it is feasible that there is a small degree of error in protein concentration estimates based on absorption measurements, this is unlikely to explain the large difference in CD intensity between the two proteins. Thus, the CD data suggest that CYP136 (at least when bound to tf) is in an extensively folded state.

5.7 Discussions from Bioinformatics Analysis

With regards to the possibility that CYP136 is a membrane associated protein (due to its extended N-terminal region), this prediction was supported to some extent using ExPASy protein prediction tools online, e.g. TargetP for subcellular localisation (Emanuelsson *et al.* 2000), TopPred for topology prediction of membrane proteins (Von Heijne 1992) and TopCons also for α -helical membrane protein topology prediction based on consensus, and suggested to be 80% superior to TopPred (Hennerdal and Elofsson 2011) (TargetP: <http://www.cbs.dtu.dk/services/TargetP/>, TopPred: <http://mobyli.pasteur.fr/cgi-bin/portal.py?#forms::toppred> and TopCons: <http://topcons.cbr.su.se/>). By PredictProtein (<http://www.predictprotein.org/>) (Rost *et al.* 2004), CYP136 is predicted to be localised in the Mtb cytoplasm. However, if CYP136 is considered to be a eukaryotic protein, then it is predicted (albeit with low confidence levels, i.e. 4/5) to be mitochondrially-localised, based on a predicted mitochondrial targeting

peptide in its N-terminal amino acid sequence. This outcome does point to an N-terminal extension in CYP136, which could have some role in membrane tethering in Mtb. In contrast, human CYP51 is predicted to be in the secretory pathway (higher confidence i.e. 2/5, with lowest confidence score being 5/5 and highest confidence score at 1/5) based on a signal peptide present in its N-terminal sequence (TargetP). It is known that human CYP51B1 is a membrane anchored enzyme with a N-terminal membrane spanning helix. Thus, these predictions should be treated with some caution.

CYP136 has a relatively lower number of hydrophobic residues at the N-terminal (first ~70 residues, as demonstrated in Figure 5.15 and Appendix E) compared to typical membrane-bound proteins, e.g. *C. albicans* CYP51A1 and human CYP51 (TopPred and TopCons). Essentially, the prediction results generated by both TopPred and TopCons were in agreement with other protein prediction softwares e.g. SCAMPI, PRODIV, PRO and OCTOPUS (Bernsel *et al.* 2009) (Figure 5.15). The “reliability” score for the predicted transmembrane (TM) portion at the N-terminal region for CYP136 (Figure 5.15 **A**) is superior to that predicted for CYP51B1, where the latter is a soluble protein without any TM region at the N-terminal sequences (as indicated by the lowest reliability score at the ~1-70 amino acid residues for the TM region prediction in CYP51B1) (Figure 5.15 **B**). These bioinformatics results essentially indicate that CYP136 could be a membrane-associated protein in Mtb, although it is probably unlikely to have a formal membrane anchor peptide.

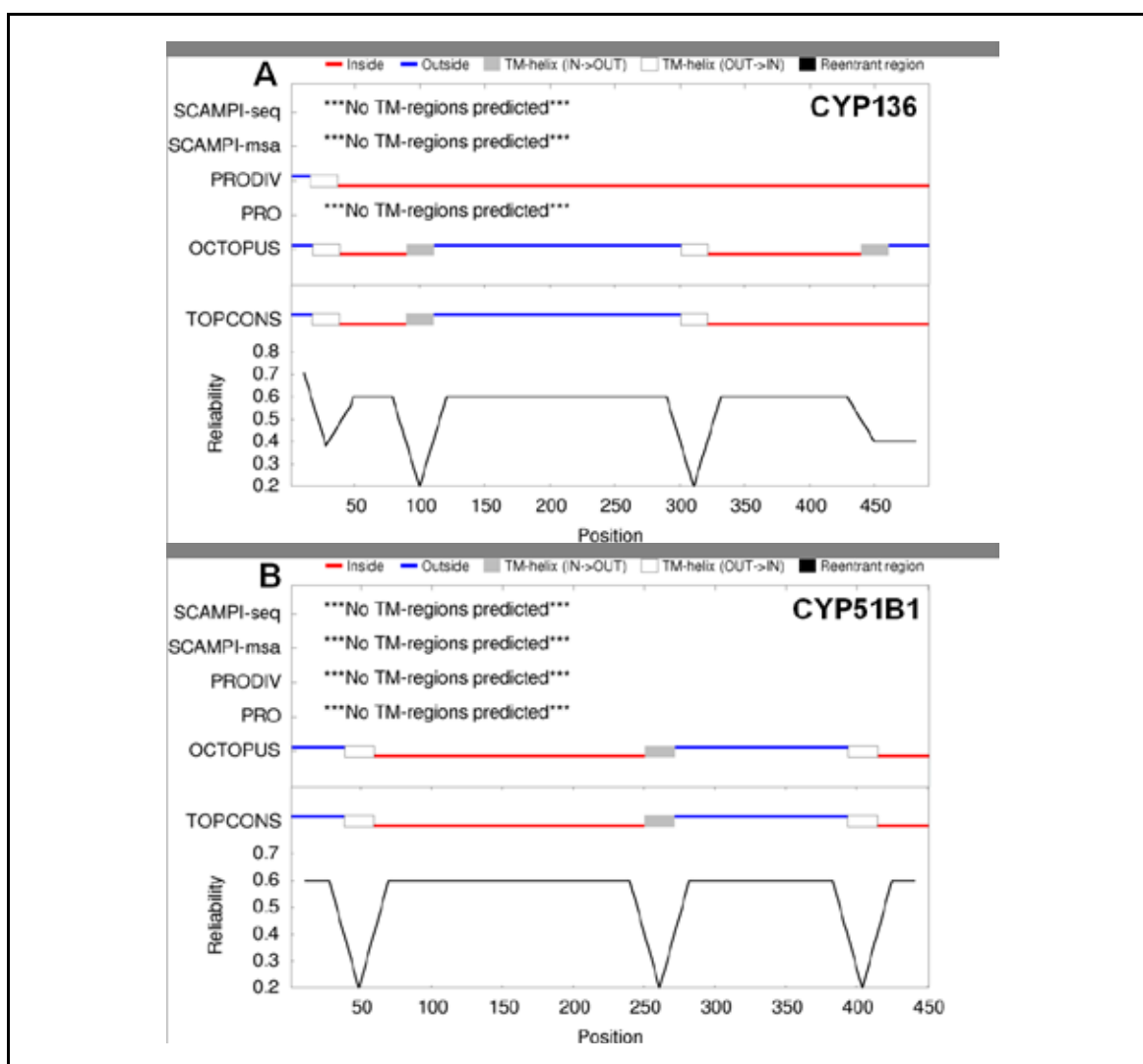


Figure 5.15: Transmembrane protein predictions for CYP136 and CYP51B1. The above graphs were generated by TopCons (<http://topcons.cbr.su.se/>) (Hennerdal and Elofsson 2011) for the amino acid sequences of CYP136 and CYP51B1 from Mtb. The residues were compared with other membrane proteins by consensus pattern recognition of membrane proteins across six different membrane protein prediction programs, and the generated data from 50% of these programs suggested that CYP136 (A) has a TM region at the N-terminal end (1-50 a.a.), with a higher reliability score (y-axis) at the N-terminal end as compared to the prediction for CYP51B1 in B at the same region. CYP51B1, which is an established soluble P450, is predicted to have three TM regions in its sequence. However, these have reliability scores of < 0.3 , indicating very low confidence that these predictions are correct. Therefore, according to reliability scores, CYP136 may have only one probable TM region which is situated at the N-terminal end, making it a probable membrane-associated protein in Mtb. As discussed above, these annotations should be taken with caution, although it remains clear that CYP136 does have a hydrophobic N-terminal, which could possibly result in membrane attachment in the bacterium.

5.8 Summary and Future Work

Conclusions which can be drawn from results of this chapter on CYP123 are (i) that CYP123 is located close to CYP51B1 on the Mtb genome, possibly indicating their involvement in related processes or similarity in substrate selectivity; (ii) CYP123 may be a P450 that has evolved from CYP51B1 (or vice versa) and/or has sterol demethylase function, but this still needs extensive investigation before a conclusion can be drawn; and (iii) due to its location in the same operon as CYP51B1, this gives CYP123 a reasonable probability of association with sterol metabolism pathway(s). Although CYP123 has only 20% amino acid sequence identity to CYP51B1, this does not eliminate the possibility that it may share a similar substrate specificity profile to CYP51B1. This proposal is supported by studies of two other CYPs involved in sterol biosynthesis in humans i.e. CYP46A1 and CYP11A1 (Irina Pikuleva, CASE Western Reserve University, personal communication). These two proteins have >25% amino acid sequence identity but are able to catalyse oxidation of the same substrate (cholesterol). The main structural difference between these two proteins is in the size and conformations of their active sites (Mast *et al.* 2008; Mast *et al.* 2011). Such observations may support the proposal that CYP123 could share the same substrate(s) or substrate type(s) as for CYP51B1, or even for CYP126 (substrate still unknown, but crystal structure resolved, Le van Duyet, University of Manchester, personal communication) which share 32% amino acid identity with CYP123. The *CYP123* gene is up-regulated at high temperatures, which also may indicate the importance of CYP123 activity in the infective state of Mtb. Further work to investigate expression of *CYP123* and characterisation of the CYP123 protein is necessary to arrive at more definitive conclusions on structure/function of the enzyme, as discussed earlier in this chapter. Due to the time constraints of this PhD, further experiments on CYP123 were not possible, although novel expression constructs (in vectors pET28b and pET24b) were prepared and stored in -80°C for future *CYP123* expression trials. Regarding CYP136, conclusions which can be made are (i) that it is a potential membrane associated protein; (ii) that it may be expressed in an apoprotein form in *E. coli*; and (iii) that the *in vivo* folding of CYP136 in Mtb may require the association of one or more chaperonin systems, of which Mtb has several (Goyal *et al.* 2006) – this conclusion being supported due to CYP136's apparent aggregation once proteolytically cleaved from its soluble fusion to the tf chaperone.

It is clear that several aspects of Mtb's sterol metabolic biochemistry have yet to be resolved. Major findings from our group (and others) have identified enzymes from the P450 superfamily (i.e. CYP125, CYP142, CYP124 and CYP51B1) that are involved in sterol and steroid oxidation reactions. However, it appears to be the case that their

substrates are not synthesised by Mtb, but are likely instead derived from the host organism (Bellamine *et al.* 1999; Cole *et al.* 1998; Driscoll *et al.* 2010; Johnston *et al.* 2009; McLean *et al.* 2009; Ouellet *et al.* 2010). Further studies have also identified non-P450 proteins in Mtb which are also related to sterol and steroid biosynthesis. Among these are protein kinase G (Walburger *et al.* 2004), PE_PGRS protein products of the *Rv0746* and *Rv1651c* genes (Delogu *et al.* 2006), cholesterol oxidase (Brzostek *et al.* 2007), the product of *Rv0760c*, a Mtb homologue of delta 5-3-ketosteroid isomerase (Cherney *et al.* 2008), and the product of *Rv1106c*, a Mtb 3-beta-hydroxysteroid dehydrogenase (Yang *et al.* 2007). This highly significant number of genes involved in sterol/steroid biosynthesis/breakdown in Mtb, even though Mtb itself is devoid of its own sterol/steroid biosynthetic pathway, cannot be ignored in the context of the importance of sterol metabolism to Mtb. Many of these genes are found near-exclusively in eukaryotes, and may have arrived in Mtb by lateral gene transfer (Rezen *et al.* 2004; Yoshida *et al.* 2000). These genes, some of which are up-regulated during infection of host macrophages, must surely play important roles (together with host's sterol biosynthetic enzymes) and are probably involved in utilising substrates from the host's sterol metabolism pathway(s) to enable Mtb to derive energy from the host and/or to modulate host biochemistry/immune response. Until all the 4012 proteins (TubercuList) from Mtb's genome are characterised, which will take several decades (Cole 1999), definitive roles for all the P450s (including CYP51B1, CYP123 and CYP136) and these other potential sterol metabolising enzymes must remain speculative. However, given the importance of defining the role of sterol metabolism in Mtb and its function in pathogenicity, it is likely that this area will be well researched and may provide important leads in developing new antitubercular drugs.



Chapter 6 | Conclusions and Future Work

- 6.1 Azole-Resistance in CYP51*
- 6.2 Importance of Studying CYP123 and CYP136 from Mtb*
- 6.3 P450s in Mtb and Host Cholesterol Relationship*

6 CONCLUSIONS AND FUTURE WORK

6.1 Azole-Resistance in CYP51

For the first time, results from the work described in this thesis presents quantitative biochemical characterisation of CYP51B1 enzymes containing mutations mapped from fluconazole-resistant variants of the membranous CYP51A1 from *C. albicans*. Although CYP51B1 (from *Mtb*) and CYP51A1 (from *C. albicans*) share only 26% amino acid sequence identity, they have both been shown to catalyse 14 α -demethylase reactions on sterol substrates (Bellamine *et al.* 1999). The prospect of elucidating mechanisms of azole drug resistance in CYP51 mutant enzymes (using spectroscopic, kinetic and crystallographic methods) are much greater for the soluble CYP51B1 enzymes by comparison to using detergent-solubilised CYP51A1, and given the difficulties in expression and isolation of high quality CYP51A1 proteins. Previous studies of CYP51A1 have used detergents and chaotropic agents, e.g. the recent report of Warrillow *et al.* (2010a, b) on CYP51A1 of *C. albicans* and *A. fumigatus* binding to azole drugs, and such studies have not been able to provide serious quantitative or structural data on mutant enzymes and their interactions with azoles. The choice of mutants presented in this chapter was based on their frequency in azole-resistant clinical cases in CYP51A1 and on their location in the CYP51B1 structure. Y132H (F89H in CYP51B1) and G464S (G388S) are two mutants with the highest frequency found in clinical fluconazole-resistant *C. albicans* strains. Both these mutants have been sporadically studied by Kelly *et al.* (1999a, b) in CYP51A1 (or CYP51ca) with little quantitative drug-binding data. Both F89H (Y132H in CYP51A1) and L100F (a reverse mutant, restoring a CYP51A1 WT residue in CYP51B1) are located at SRS 1 flexible hinge regions, while G388S (G464S) and R391K (R467K) are at the highly conserved β -bulge of the cysteinyl loop. The S348F (S405F) mutant is situated at the conserved C-terminal region between an N-terminal helix and beta sheets. The S348F mutation resulted in a misfolded and inactive CYP51B1 enzyme. All the mutants (except for G388S and S348F) showed full heme incorporation and expression levels comparable of that of WT CYP51B1, as judged by the amount of their heterologous expression in absence of added δ -ala heme precursor, and by their comparable Rz ratios for pure enzyme and their heme *b* content relative to WT CYP51B1. The G388S mutant, however, was expressed as a soluble protein at \sim 30x lower levels than WT CYP51B1 and, with the addition of δ -ala, could be purified with \sim 64% heme-bound holoenzyme present. Spectrophotometric characterisation showed that all mutants (F89H, L100F, G388S and R391K) retained their P450 nature by binding CO in the ferrous-heme state, and through

formation of a ferrous-CO complex with maxima at ~450 nm, which decayed to the P420 form over time.

Mutants in the cysteinyl loop region displayed interesting, yet contrasting, behaviours during kinetic and equilibrium reduction studies with dithionite. G388S CYP51B1 demonstrated fast reduction of ferric heme to ferrous-heme and a 9-fold faster protonation of the cysteinate proximal ligand compared to WT CYP51B1. This was consistent with the dominant ferrous-thiol species observed during redox potentiometry experiments, and with the relatively fast collapse (0.88 min^{-1}) of the P450 ferrous-CO adduct to the P420 thiol form. G388S CYP51B1 exhibited a very positive redox potential (-102 mV) in the substrate-free form, even higher than that reported for WT CYP51B1 in complex with estriol, and thus reflecting a higher electron affinity than the estriol-bound WT enzyme. Its inability to form a P450 ferrous-CO species with redox partners and estriol is its distinguishing property, and instead G388S formed exclusively the P420 ferrous-CO species. In WT CYP51B1, the P450 species was stabilized (i.e. an equilibrium between P450 and P420 forms was obtained) with redox partners (FprA, Fdr and Fd2) providing the electrons in the presence of estriol, while in the other mutants this P450 species was stabilised to a certain extent in the presence of estriol. Indeed, the effect of mutating the extensively conserved Gly residue mutation at the Gly-rich cysteinyl loop (by incorporation of the hydroxyl side chain-containing Ser residue in G388S) not only destabilised the binding of the heme cofactor, but also enhanced the rate of the catalytically active P450 species formation on reduction with dithionite (and of the collapse of the ferrous-CO P450 form to P420) and, more relevantly, no P450 formation was detected when the G388S mutant was reduced by an enzyme-based system (NADPH, FprA and/or Fdr, Fd1 and/or Fd2), likely as a consequence of the relatively fast rate of heme thiolate protonation with respect to heme reduction using this non-optimised electron transport system. In view of the unusual behaviour of the G388S mutant, there might seem to be two possible catalytic outcomes for this mutant (once CYP51B1's physiological substrate is confirmed and an efficient redox partner system established). These two routes might be (1) a productive and relatively fast 14α -demethylation reaction on a *bona fide* substrate (avoiding heme thiolate protonation due to efficient turnover of substrate) and (2) a non-productive route with decay of iron-oxo intermediates via one of the three shunt pathways (forming superoxide, peroxide or water) and the abortive release of any bound substrate. Given the presence of some thiolate-bound heme in the G388S mutant, it might be expected that this mutant would be functional in catalysis. However, its altered heme iron potential would likely compromise its ability to reduce and activate dioxygen, and thus

further impact on its catalytic competence. All of the CYP51B1 variants generated in this study are α -helix rich, as shown by the features at 209 nm and 224 nm from far UV CD analysis. However, the G388S CYP51B1 far UV CD spectrum showed differences to that for other mutant and WT CYP51B1 enzymes, which can possibly be attributed to its heterogeneous mixture of holoenzyme and apoprotein forms. This heterogeneous nature of the G388S mutant was also detected by MALLS analysis, which showed different oligomeric states that likely arise from aggregation of the apoprotein with other apoprotein or holoprotein molecules. These various G388S enzyme states were also indicated by the more complex protein unfolding patterns defined by DSC analysis of ligand-free G388S CYP51B1 (with at least four distinct T_m values). These calorimetric and dynamic light scattering results were in contrast to those for WT and other mutant CYP51B1 enzymes. For instance, a clear two stage unfolding was observed for WT CYP51B1 with T_m values of $\sim 49^\circ\text{C}$ and $\sim 51^\circ\text{C}$, and monomeric states of WT CYP51B1 and the other mutant enzymes were observed by MALLS analysis.

While, for G388S CYP51B1, the rate constants for both its ferric-to-ferrous heme iron reduction and heme thiolate protonation were increased by the mutation, in R391K, the thiolate protonation rate was decreased by 2-fold as compared to WT CYP51B1. This might suggest that the Arg391 residue is involved in proton transfer to the heme thiolate to facilitate P420 formation, and that its replacement by a lysine affects structure in this region and makes for less efficient thiolate protonation (which is possibly a beneficial outcome for the enzyme). This structural difference was shown in Figure 4.13 by the absence of the guanidinium side chain density of Arg391 in WT CYP51B1, but with electron density for the side chain of Lys391 clearly present in the R391K mutant CYP51B1 structure. Thus, the R391K CYP51B1 exhibited slower heme thiolate protonation, providing an extended duration of the catalytically active ferrous-thiolate form for substrate monooxygenation. Whilst the G388S mutant's heme cofactor was apparently weakly bound to the protein (i.e. full heme incorporation was not achieved, and "leakage" of heme was observed during purification) and was not apparently further stabilised (or destabilised) by azole drug binding, the R391K mutant showed good heme incorporation. However, upon R391K binding to a strong inhibitor ligand (e.g. azoles), the stability of its heme may have been perturbed, as discussed previously and illustrated by the fall in heme Soret band intensity for the azole complex seen in Figure 3.25. An alternative explanation might be that the extinction coefficient at 419 nm is lower for the azole complexes for this mutant in comparison to WT CYP51B1 and other mutants discussed in section 3.5.1. The G388S and R391K mutations may thus have profound impacts on enzymatic activity in both these

cysteinyll loop mutant P450s, and these mutants have not been examined before in CYP51A1. The ligation state of the ferric heme of WT and mutant CYP51B1 enzymes was also probed by EPR spectroscopy, and this indicated some important differences in ligation states and other properties. Although the typical LS set of g values in ligand-free CYP51B1 enzymes and the sets obtained for azole inhibitor-bound forms were highly similar to data published on WT CYP51B1 previously by McLean *et al.* (2006), there were two novel EPR features observed for the mutant CYP51B1 enzymes in different ligand-bound forms. The most prominent novel feature was the g 2.00 signal observed in the G388S CYP51B1 enzyme, indicating adventitious metal (free iron in this case) that was likely due to the instability of heme cofactor binding in this mutant. In addition, atypical P450 HS signatures at $g \sim 6.00$ (5.74, 5.80, 5.84 and 5.86 in different CYP51B1 enzymes) were novel observations made for both F89H and G388S CYP51B1 enzymes in their ligand-free states, and for all the CYP51B1 variants post redox-cycling. This atypical HS $g \sim 6.00$ value in both F89H and G388S CYP51B1 diminished upon distal heme iron ligation by a N atom from the triazole moiety of azole drugs. It appears likely that the signal arises from a HS penta-coordinated (protonated) thiol-ligated state of the ferric heme, as illustrated in Figure 4.7. The disappearance of the HS signal on distal ligation by a triazole drug would then be a consequence of the spin-state shift to LS. For the post redox-cycled CYP51B1 variants that all exhibit the HS $g \sim 6.00$ value, the most likely explanations may be that a sulphur-containing molecule derived from dithionite influences the distal ligand environment, or that the proximal thiolate ligand becomes protonated to thiol. The restoration of a LS thiolate form that occurs on extended incubation of redox cycled CYP51B1 enzymes suggests that the latter explanation is more credible. Possibilities for the identities of CYP51B1 ligands in the redox-cycled HS state were considered in light of previously published data for ferric heme proteins having similar EPR $g \sim 6.00$ values and with a histidine proximal ligand (Dawson *et al.* 2001; Perera and Dawson 2004), a HS methionine proximal ligand (Miles *et al.* 1993) and *bis*-methionine axial ligands (Barker *et al.* 1996). However, there is no firm structural data to indicate that a histidine can occupy either a distal or proximal ligand position in a wild-type P450 enzyme, and thus a model of cysteine thiol as proximal ligand in pentacoordinated redox-cycled CYP51B1 enzymes appears most likely.

With regards to the mutants at the B-C loop region generated in this work, i.e. the L100F “reverse mutant” of CYP51B1 (a “model” for WT CYP51A1) and WT CYP51B1 (modelling the F145L fluconazole-resistant mutant of CYP51A1), biochemical characterisation data were somewhat consistent with the data for the CYP51A1 enzyme, as

noted by the ~3-4-fold higher K_d values for the L100F mutant enzyme compared to WT CYP51B1 for the binding of fluconazole in both equilibrium binding (Table 3.5) and stopped-flow kinetic binding (Table 3.6) analysis, and as summarised in Table 6.1. The F89H and L100F CYP51B1 mutants in the SRS 1 flexible hinge region demonstrated similar heme iron redox potentials compared to WT CYP51B1 in the ligand-free state. Their capacity to form P450 species (albeit slightly weaker in the case of L100F CYP51B1) with redox partners and using dithionite reduction methods suggested that both these mutants are probably capable of catalysing sterol 14 α -demethylase reactions with the combination of Mtb enzymes used (FprA/Fdr and Fd2). However, in previous studies, the F89H mutant of CYP51B1 was reported to have no enzymatic activity (with 24, 25-dihydrolanosterol) using *E. coli* flavodoxin and ferredoxin reductases (Bellamine *et al.* 2004). With respect to fluconazole binding, the “resistance” to fluconazole was reflected in the relatively higher fluconazole K_d values of all the CYP51B1 mutants compared to that for L100F CYP51B1 (a mutant that is comparable with WT CYP51A1) in the following fluconazole-resistance descending (higher K_d to lower K_d) order in Table 6.1:

Table 6.1: Mutant CYP51B1 fluconazole resistance and susceptibility based on K_d values from SF and EB measurements.

K_d measurement	CYP51	Fluconazole resistant $\hat{=}$ fluconazole susceptible
SF K_d values (Kinetic)	Mtb CYP51B1 variants	F89H > WT > G388S > R391K > L100F
	Corresponding <i>C. albicans</i> CYP51A1	Y132H > F145L > G464S > R467K > WT
EB K_d values (Static)	Mtb CYP51B1	WT > G388S > R391K > F89H > L100F
	Corresponding <i>C. albicans</i> CYP51A1	F145L > G464S > R467K > Y132H > WT

Except for the **F89H** (**Y132H** in CYP51A1) mutant data from SF studies, the order of K_d values for other enzymes were consistent using the SF and EB methods. The varying K_d values using kinetic and equilibrium binding methods for **F89H** (**Y132H**) may be explained by this mutation being located at the highly mobile B-C loop entry channel of this enzyme, and reflect that this region is conformationally mobile. For instance, adaptation of the structure on binding of azoles could lead to the closure of the exit channel, thus explaining the lower K_d values obtained from EB studies compared to the apparent K_d values inferred from transient kinetic analysis. L100F, which mimics WT

CYP51A1, showed relative susceptibility to fluconazole in both methods, consistent with the productive antifungal activity of fluconazole in targeting CYP51A1 from *C. albicans*.

In fact (as seen in both Tables 3.5 and 3.6), this difference in K_d values across the various ligands is consistent between EB and SF analysis methods (with larger K_d values in SF studies), likely highlighting an important mechanistic feature of CYP51B1, and one which may have important ramifications for understanding mechanisms of azole drug resistance. The simplest explanation for these differences is likely related to the different time scales over which these measurements are made. The optical binding titrations likely provide accurate estimates of binding affinity for the enzyme-ligand systems at equilibrium. The stopped-flow studies may instead capture a pre-equilibrium state in which the P450 molecules have not arrived at their final conformationally adapted states following azole drug binding. Several P450s are known to undergo conformational changes (particularly involving mobile loop regions involved in ligand entry/exit), and to crystallise in different conformational states for ligand-free and substrate/inhibitor-bound forms (e.g. CYP3A4, CYP121 and CYP126) (Ekroos and Sjogren 2006; Seward *et al.* 2006). The weaker azole K_d values determined by SF methods might thus result from data that report on azole-heme ligation that occurs prior to completion of CYP51B1 structural adaptations to accommodate the inhibitors. If, for instance, these adaptations favour active site closure and a diminished “escape” rate for the azole, then the apparent k_{off} from stopped-flow studies may be inflated, leading to a K_d value elevated in comparison to the EB measurements. Such a phenomenon might be explored further by further rapid kinetic studies aimed at monitoring protein structural changes on azole binding.

Efforts to confirm these suggestions were made by Trp fluorescence analysis, but these experiments failed to yield convincing data to support the model, due to limited changes in protein fluorescence between ligand-free and fluconazole-bound forms of CYP51B1. Due to the time constraints of this PhD project, further studies in this area were curtailed. However, it is likely that alternative fluorescence-based techniques (e.g. using fluorophore(s) attached to exposed or engineered Cys residues, or by using fluorophore-tagged substrate mimics or fluorophore-tagged azole drugs during binding measurements using stopped-flow-fluorescence techniques) could be used to measure the kinetics of conformational rearrangements in WT CYP51B1 and mutants. These approaches could thus be used to confirm structural adaptations of CYP51B1 enzymes post azole-ligation, and to explain the systematic differences in K_d values obtained from SF and EB analyses in this project.

The studies of CYP51B1 variants were concluded by protein crystallography. Co-crystals were derived from all of the mutant CYP51B1 enzymes, (except for the G388S mutant enzyme) in complex with 4PI and EPBA inhibitors. Diffraction data were collected for F89H-4PI, F89H-EPBA, ligand-free F89H, WT-4PI, WT-EPBA, L100F-EPBA, R391K-4PI and R391K-EPBA crystals (Appendix H). Analysis of the crystal structures of R391K CYP51B1 bound to 4PI and EPBA revealed that this mutation did not influence the highly conserved cysteinyl loop structure. Mutations at the B-C loop region (as evident from the F89H/L100F CYP51B1 structures) revealed that mobility at this putative entry/exit channel was increased when compared to the already elevated levels of the WT CYP51B1.

Previous P450 structural studies have suggested that conformational flexibility is key to the position ofazole drug-resistance-conferring mutations found in *C. albicans* CYP51A1. These mutations map mainly to flexible P450 regions (including the F-G and B-C helical sections and their intervening loops) rather than to the active site, and this suggests that resistance may be achieved by altered conformational dynamics in CYP51, as opposed to disruption of the active site (Munro *et al.* 2007b). In this study, it was confirmed that selected mutations do not cause disruption to the active site, as observed from solved crystal structures of the F89H mutant bound to 4PI and EPBA, and for the L100F CYP51B1 mutant bound to EPBA. In contrast, the mobility of various structural elements lining possible entry-exit routes to the active site can be influenced by the mutations, possibly affecting on-and off-rates of the various ligands. Such altered ligand binding/debinding kinetics may be key to affordingazole drug resistance, and could potentially also have less effect on substrate affinity than onazole affinity, so as not to compromise physiological function.

6.2 Importance of Studying CYP123 and CYP136 from Mtb

The presence of 20 P450s in Mtb has initiated intensive study in various research groups to de-orphanise novel Mtb P450s in order to assign their possible substrates and ultimately to expose their *in vivo* roles. In attempts to assign function for other orphan Mtb P450s, and in view of the fact that increasing numbers of CYPs from Mtb were found to be related to cholesterol metabolism in recent years (Driscoll *et al.* 2010; McLean *et al.* 2010; McLean *et al.* 2007), CYP123 and CYP136 were chosen here as the next two Mtb CYPs to be subjected to this de-orphanising procedure, and based on their genomic context and proximity to the sterol demethylase CYP51B1. Cholesterol is essential for TB infectivity

and re-infection in human macrophages, and thus defining Mtb P450s involved in various aspects of cholesterol metabolism is important. From preliminary studies in chapter 5, it can be concluded that, since *CYP123* is located almost adjacent to *CYP51B1* on the Mtb genome, these P450s may be involved in related processes or exhibit similarity in substrate selectivity. Also, *CYP123* may be a P450 that has evolved from *CYP51B1* (or vice versa) and/or has sterol demethylase function. However, this still needs extensive investigation before any firm conclusion can be drawn. Due to its location in the same operon as *CYP51B1*, this gives *CYP123* a reasonable probability of association with sterol metabolism pathway(s), although it should be noted that a complete cholesterol biosynthetic pathway is absent in Mtb itself. While *CYP123* has only 20% amino acid sequence identity to *CYP51B1*, this does not eliminate the possibility that they may share a similar substrate specificity profile. This proposal is supported by studies of two other CYPs involved in sterol biosynthesis in humans, i.e. *CYP46A1* and *CYP11A1* (Irina Pikuleva, CASE Western Reserve University, personal communication). These two proteins have only >25% amino acid sequence identity, but are able to catalyse oxidation of the same substrate (cholesterol). The main structural differences between these two proteins are in the size and conformations of their active sites (Mast *et al.* 2008; Mast *et al.* 2011). Such observations may support the proposal that *CYP123* could share the same substrate(s) or substrate type(s) as for *CYP51B1*, or even for *CYP126* (substrate presently unknown, but crystal structure resolved, Le van Duyet, University of Manchester, personal communication), which shares 32% amino acid identity with *CYP123*. The *CYP123* gene is up-regulated at high temperatures, which also may indicate the importance of *CYP123* activity in the infective state of Mtb. Further work to investigate expression of *CYP123* and to characterise the *CYP123* protein is necessary to arrive at more definitive conclusions on structure/function of the enzyme, as discussed earlier in this chapter. Due to the time constraints of this PhD, further experiments on *CYP123* beyond cloning and expression analysis were not possible, although novel expression constructs (in vectors pET28b and pET24b) were prepared and stored at -80 °C for future *CYP123* expression/enzyme production trials.

Regarding *CYP136*, conclusions which can be made are that (i) it is a potential membrane associated protein; (ii) it may be expressed in an apoprotein form in *E. coli*; and (iii) the *in vivo* folding of *CYP136* in Mtb may require the association of one or more chaperonin systems, of which Mtb has several (Goyal *et al.* 2006). The final conclusion is supported by the apparent finding that *CYP136* aggregates once it is proteolytically cleaved from its soluble fusion to the tf chaperone.

6.3 P450s in Mtb and Host Cholesterol Relationship

It is clear that several aspects of Mtb's sterol metabolic biochemistry have yet to be resolved. Major findings from our group (and others) have identified enzymes from the P450 superfamily (i.e. CYP125, CYP142, CYP124 and CYP51B1) that are involved in sterol and steroid oxidation reactions. These functions are (at least) partially illustrated in Figure 6.1 for CYP51B1, CYP125 and CYP142.

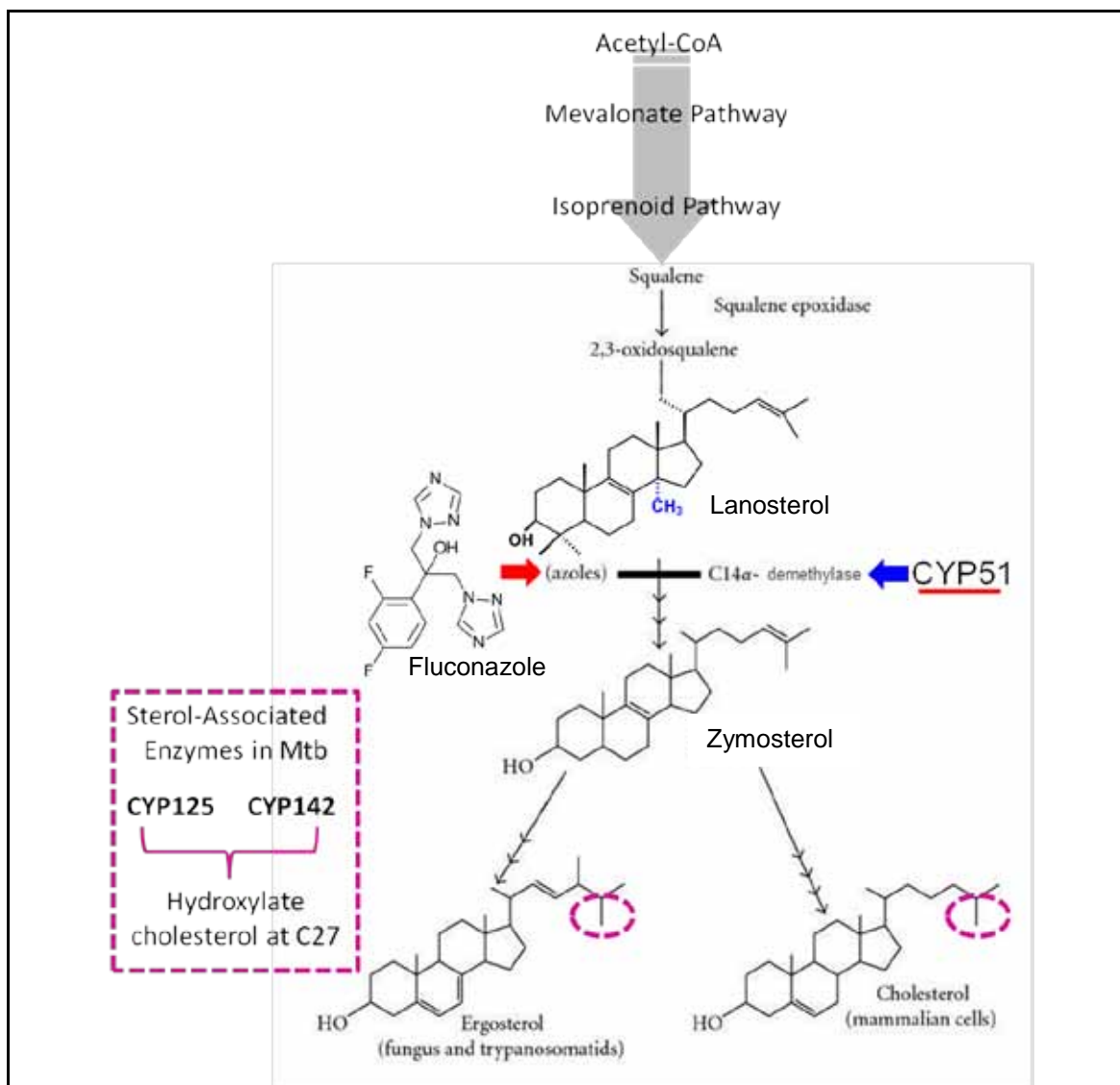


Figure 6.1: The sterol biosynthetic pathway. The common sterol biosynthetic pathway as found in humans, animals, plants, protozoa and fungi is shown. This originates from acetyl-CoA as the precursor for the mevalonate pathway, followed by the isoprenoid pathway for the synthesis of squalene - which is the precursor for the first sterol i.e. lanosterol and 24,25-dihydrolanosterol (mammals, protozoa and fungi) and obtusifoliol (plants) and for further sterol and steroid biosynthesis. Mtb CYP125 and CYP142 have been shown to hydroxylate cholesterol at C27 (dotted purple circle). CYP51B1 demethylates C14 (highlighted in blue) of the lanostane backbone upstream of the CYP125 and CYP142 sites of catalysis. Azoles antifungal drugs (fluconazole structure shown) are well-known inhibitors for CYP51. This sterol biosynthetic pathway is essentially absent in Mtb.

However, it appears to be the case that their substrates are not synthesised by Mtb, but are likely instead derived from the host organism (Bellamine *et al.* 1999; Cole *et al.* 1998; Driscoll *et al.* 2010; Johnston *et al.* 2009; McLean *et al.* 2009; Ouellet *et al.* 2010). Further studies have also identified non-P450 proteins in Mtb which are also related to sterol and steroid biosynthesis. Among these are protein kinase G (Walburger *et al.* 2004); the PE_PGRS protein products of the *Rv0746* and *Rv1651c* genes (Delogu *et al.* 2006); cholesterol oxidase (Brzostek *et al.* 2007), the product of *Rv0760c*; a Mtb homologue of delta 5-3-ketosteroid isomerase (Cherney *et al.* 2008); and the product of *Rv1106c*, a Mtb 3-beta-hydroxysteroid dehydrogenase (Yang *et al.* 2007). This highly significant number of genes involved in sterol/steroid biosynthesis/breakdown in Mtb, even though Mtb itself is devoid of its own sterol/steroid biosynthetic pathway, cannot be ignored in the context of the importance of sterol metabolism to Mtb. Many of these genes are found near-exclusively in eukaryotes, and may have arrived in Mtb by lateral gene transfer (Rezen *et al.* 2004; Yoshida *et al.* 2000). These genes, some of which are up-regulated during infection of host macrophages, must surely play important physiological roles (together with host's sterol biosynthetic enzymes) and are probably involved in utilising substrates from the host's sterol metabolism pathway(s) in order to enable Mtb to derive energy from the host and/or to modulate host biochemistry/immune response. Until all the 4012 proteins (TubercuList) from Mtb's genome are characterised, which will take several decades (Cole 1999), definitive roles for all the P450s (including CYP51B1, CYP123 and CYP136) and these other potential sterol metabolising enzymes must remain speculative. However, given the importance of defining the role of sterol metabolism in Mtb and its function in pathogenicity, it is likely that this area will be well researched and may provide important leads in developing new antitubercular drugs.

Overall, the two main objectives of this research which are **(1)** to describe the effects of point mutations in Mtb CYP51B1 (corresponding to reoccurring fluconazole-resistant single mutations situated at important structural regions of CYP51B1 as mapped from the *C. albicans* ERG11 gene coding for CYP51ca) have on its function and structure and **(2)** to understand the underlying mechanism of azole drug-resistance in CYP51ca from *C. albicans* by using the soluble CYP51B1 from Mtb as a template have been met. Ongoing analyses of substrate turnover activity for CYP51B1 variants with various substrates and redox partners are still underway so as to conclude both objectives and to enable high quality publishable results. It remains important to elucidate the functional nature, substrate specificity and redox partner enzymes for CYP51B1 variants studied in this thesis, and ultimately also for both CYP123 and CYP136. Experiments with lanosterol and

dihydrolanosterol have been carried out for these CYP51B1 variants with Mtb redox partners and are awaiting HPLC-MS product identification analysis at the time of submission of this thesis. Results from this thesis are important in understanding the nature of azole-resistance in CYP51A1 (using CYP51B1 as a model) and have exploited a multifaceted approach using biochemical, biophysical and structural data to obtain a comprehensive understanding of the mechanism and function of this enzyme. The experience and knowledge I have obtained during my doctoral training has enabled me to appreciate a multi-disciplinary approach in addressing important medical issues. At the same time, I have become aware that sound fundamental science is important to understand the bigger problem and that, most of the time, no single PhD project could completely address global multi-drug resistant TB and antifungal drug resistance issues. However, the results presented in this thesis provide important contributions towards global collaborative efforts in dealing with MDR/XDR TB, and in particular towards understanding the properties of the Mtb CYP51B1 enzyme and the factors influencing azole inhibition of this enzyme and its homologue (CYP51A1) in *C. albicans*.

7 REFERENCES

- Achkar JM, Fries BC. 2010. Candida infections of the genitourinary tract. *Clinical Microbiology Reviews* 23(2):253-273.
- Acimovic J, Fink M, Pompon D, Bjorkhem I, Hirayama J, Sassone-Corsi P, Golicnik M, Rozman D. 2008. CREM modulates the circadian expression of CYP51, HMGCR and cholesterol synthesis in the liver. *Biochemical and Biophysical Research Communications* 376(1):206-210.
- Ahmad A, Khan A, Akhtar F, Yousuf S, Xess I, Khan LA, Manzoor N. 2011a. Fungicidal activity of thymol and carvacrol by disrupting ergosterol biosynthesis and membrane integrity against *Candida*. *European Journal of Clinical Microbiology and Infectious Diseases* 30(1):41-50.
- Ahmad Z, Pandey RE, Sharma S, Khuller GK. 2008. Novel chemotherapy for tuberculosis: chemotherapeutic potential of econazole-and moxifloxacin-loaded PLG nanoparticles. *International Journal of Antimicrobial Agents* 31(2):142-146.
- Ahmad Z, Peloquin CA, Singh RP, Derendorf H, Tyagi S, Ginsberg A, Grosset JH, Nuermberger EL. 2011b. PA-824 exhibits time-dependent activity in a murine model of tuberculosis. *Antimicrobial Agents and Chemotherapy* 55(1):239-245.
- Ahmad Z, Sharma, S. and Khuller, G.K. 2006. Azole antifungals as novel chemotherapeutic agents against murine tuberculosis. *FEMS Microbiology Letters* 261(2):181-186.
- Al Sogair S, Hay RJ. 2000. Fungal infection in children: *Tinea capitis*. *Clinics in Dermatology* 18(6):679-685.
- Al-Abdalall AHA. 2010. Pathogenicity of fungi associated with leguminous seeds in the Eastern Kingdom of Saudi Arabia. *African Journal of Agricultural Research* 5(10):1117-1126.
- Andrews JR, Shah NS, Gandhi N, Moll T, Friedland G. 2007. Multidrug-resistant and extensively drug-resistant tuberculosis: implications for the HIV epidemic and antiretroviral therapy rollout in South Africa. *Journal of Infectious Diseases* 196(3):S482-90.
- Andries K, Verhasselt P, Guillemont J, Gohlmann HWH, Neefs JM, Winkler H, Van Gestel J, Timmerman P, Zhu M, Lee E. 2005. A diarylquinoline drug active on the ATP synthase of *Mycobacterium tuberculosis*. *Science* 307(5707):223-227.
- Aoyama Y. 2005. Recent progress in the CYP51 research focusing on its unique evolutionary and functional characteristics as a diversozyme P450. *Frontiers in Bioscience* 10:1546-1557.
- Aoyama Y, Horiuchi T, Gotoh O, Noshiro M, Yoshida Y. 1998. CYP51-Like gene of *Mycobacterium tuberculosis* actually encodes a P450 similar to eukaryotic CYP51. *Journal of Biochemistry* 124(4):694-696.
- Aoyama Y, Kudo M, Asai K, Okonogi K, Horiuchi T, Gotoh O, Yoshida Y. 2000. Emergence of fluconazole-resistant sterol 14-demethylase P450 (CYP51) in *Candida albicans* is a model demonstrating the diversification mechanism of P450. *Archives of Biochemistry and Biophysics* 379(1):170-171.
- Aoyama Y, Noshiro M, Gotoh O, Imaoka S, Funae Y, Kurosawa N, Horiuchi T, Yoshida Y. 1996. Sterol 14-demethylase P450 (P45014DM*) is one of the most ancient and conserved P450 species. *Journal of Biochemistry* 119(5):926-933.
- Aoyama Y, Yoshida Y. 1991. Different substrate specificities of lanosterol 14-alpha-demethylase (P-45014DM) of *Saccharomyces cerevisiae* and rat-liver for 24-methylene-24,25-dihydrolanosterol and 24,25-dihydrolanosterol. *Biochemical and Biophysical Research Communications* 178(3):1064-1071.
- Aoyama Y, Yoshida Y. 1992. The 4-beta-methyl group of substrate does not affect the activity of lanosterol 14-alpha-demethylase (P-45014DM) of yeast – difference between the substrate recognition by yeast and plant sterol 14-alpha-demethylases. *Biochemical and Biophysical Research Communications* 183(3):1266-1272.
- Aoyama Y, Yoshida Y, Hata S, Nishino T, Katsuki H. 1983. Buthiobate – a potent inhibitor for yeast cytochrome P450 catalysing 14-alpha-demethylation of lanosterol. *Biochemical and Biophysical Research Communications* 115(2):642-647.
- Aoyama Y, Yoshida Y, Sonoda Y, Sato Y. 1987. Metabolism of 32-hydroxy-24,25-dihydrolanosterol by purified cytochrome-P-45014DM from yeast – evidence for contribution of the cytochrome to whole process of lanosterol 14-alpha-demethylation. *Journal of Biological Chemistry* 262(3):1239-1243.
- Aoyama Y, Yoshida Y, Sonoda Y, Sato Y. 1989a. Deformylation of 32-oxo-24,25-dihydrolanosterol by the purified cytochrome-P-45014DM (lanosterol 14-alpha-demethylase) from yeast evidence confirming the intermediate step of lanosterol 14-alpha-demethylation. *Journal of Biological Chemistry* 264(31):18502-18505.
- Aoyama Y, Yoshida Y, Sonoda Y, Sato Y. 1989b. Role of the 8-double bond of lanosterol in the enzyme substrate interaction of cytochrome P-45014DM (lanosterol 14-alpha-demethylase). *Biochimica et Biophysica Acta* 1001(2):196-200.
- Aoyama Y, Yoshida Y, Sonoda Y, Sato Y. 1989c. The 3-hydroxy group of lanosterol is essential for orienting the substrate in the substrate site of cytochrome-P-45014DM (lanosterol 14-alpha-demethylase). *Biochimica et Biophysica Acta* 1006(2):209-213.
- Aoyama Y, Yoshida Y, Sonoda Y, Sato Y. 1991. Role of the side-chain of lanosterol in substrate recognition and catalytic activity of lanosterol 14-alpha-demethylase (cytochrome-P-450(14DM)) of yeast. *Biochimica et Biophysica Acta* 1081(3):262-266.

- Aoyama Y, Yoshida Y, Sonoda Y, Sato Y. 1992. Structural-analysis of the interaction between the side-chain of substrates and the active-site of lanosterol 14-alpha-demethylase (P-450(14DM)) of yeast. *Biochimica et Biophysica Acta* 1122(3):251-255.
- Bach RD. 2010. The rate-limiting step in P450 hydroxylation of hydrocarbons a direct comparison of the "somersault" versus the "consensus" mechanism involving Compound I. *Journal of Physical Chemistry A* 114(34):9319-9332.
- Bach RD, Dmitrenko O. 2006. The "somersault" mechanism for the P-450 hydroxylation of hydrocarbons. The intervention of transient inverted metastable hydroperoxides. *Journal of the American Chemical Society* 128(5):1474-1488.
- Barker PD, Nerou EP, Cheesman MR, Thomson AJ, Oliveira PD, Hill HAO. 1996. Bis-methionine ligation to heme iron in mutants of cytochrome b-562: 1. Spectroscopic and electrochemical characterization of the electronic properties. *Biochemistry* 35(42):13618-13626.
- Barnes PD, Marr KA. 2006. Aspergillosis: Spectrum of disease, diagnosis, and treatment. *Infectious Disease Clinics of North America* 20(3):545.
- Bartley GE, Yokoyama W, Young SA, Anderson WHK, Hung S-C, Albers DR, Langhorst ML, Kim H. 2010. Hypocholesterolemic effects of hydroxypropyl methylcellulose are mediated by altered gene expression in hepatic bile and cholesterol pathways of male hamsters. *Journal of Nutrition* 140(7):1255-1260.
- Berry EA, Trumpower BL. 1987. Simultaneous determination of hemes-A, hemes-B, and hemes-C from pyridine hemochrome spectra. *Analytical Biochemistry* 161(1):1-15.
- Bernsel A, Viklund H, Hennerdal A, Elofsson A. 2009. TOPCONS: consensus prediction of membrane protein topology. *Nucleic Acids Research* 37:W465-W468.
- Bellamine A, Lepesheva GI, Waterman MR. 2004. Fluconazole binding and sterol demethylation in three CYP51 isoforms indicate differences in active site topology. *Journal of Lipid Research* 45(11):2000-7.
- Bellamine A, Mangla AT, Dennis AL, Nes WD, Waterman MR. 2001. Structural requirements for substrate recognition of *Mycobacterium tuberculosis* 14-alpha-demethylase: implications for sterol biosynthesis. *Journal of Lipid Research* 42(1):128-136.
- Bellamine A, Mangla AT, Nes WD, Waterman MR. 1999. Characterization and catalytic properties of the sterol 14 alpha-demethylase from *Mycobacterium tuberculosis*. *Proceedings of the National Academy of Sciences of the United States of America* 96(16):8937-8942.
- Betts JC, McLaren A, Lennon MG, Kelly FM, Lukey PT, Blakemore SJ, Duncan K. 2003. Signature gene expression profiles discriminate between isoniazid-, thiolactomycin-, and triclosan-treated *Mycobacterium tuberculosis*. *Antimicrobial Agents and Chemotherapy* 47(9):2903-2913.
- Brennan PJ, D.C. 2007. The cell-wall core of *Mycobacterium tuberculosis* in the context of drug discovery. *Current Topics in Medicinal Chemistry* 7(5):475-488.
- Brzostek A, Dziadek B, Rumijowska-Galewicz A, Pawelczyk J, Dziadek J. 2007. Cholesterol oxidase is required for virulence of *Mycobacterium tuberculosis*. *FEMS Microbiology Letters* 275(1):106-112.
- Bueid A, Howard SJ, Moore CB, Richardson MD, Harrison E, Bowyer P, Denning DW. 2010. Azole antifungal resistance in *Aspergillus fumigatus*: 2008 and 2009. *Journal of Antimicrobial Chemotherapy* 65(10):2116-2118.
- Cai HL, Guengerich FP. 2001. Reaction of trichloroethylene and trichloroethylene oxide with cytochrome P450 enzymes: Inactivation and sites of modification. *Chemical Research in Toxicology* 14(4):451-458.
- Canas-Gutierrez GP, Angarita-Velasquez MJ, Restrepo-Florez JM, Rodriguez P, Moreno CX, Arango R. 2009. Analysis of the CYP51 gene and encoded protein in propiconazole-resistant isolates of *Mycosphaerella fijiensis*. *Pest Management Science* 65(8):892-899.
- Cecil JA, Wenzel RP. 2009. Voriconazole: a broad-spectrum triazole for the treatment of invasive fungal infections. *Expert Review of Hematology* 2(3):237-254.
- Centers for Disease Control and Prevention (CDC). 2006. Emergence of *Mycobacterium tuberculosis* with extensive resistance to second-line drugs-worldwide, 2000-2004. *Morbidity and Mortality Weekly Report* 55(11):301-305.
- Cernicka J, Subik J. 2006. Resistance mechanisms in fluconazole-resistant *Candida albicans* isolates from vaginal candidiasis. *Int J Antimicrob Agents* 27(5):403-8.
- Chatterjee D. 1997. The mycobacterial cell wall: structure, biosynthesis and sites of drug action. *Current Opinion in Chemical Biology* 1(4):579-588.
- Chen C-K, Leung SSF, Guilbert C, Jacobson MP, McKerrow JH, Podust LM. 2010. Structural characterization of CYP51 from *Trypanosoma cruzi* and *Trypanosoma brucei* bound to the antifungal drugs Posaconazole and Fluconazole. *PLoS Neglected Tropical Diseases* 4(4):e651.
- Cherney MM, Garen CR, James MNG. 2008. Crystal structure of *Mycobacterium tuberculosis* Rv0760c at 1.50 angstrom resolution, a structural homolog of Delta(5)-3-ketosteroid isomerase. *Biochimica et Biophysica Acta-Proteins and Proteomics* 1784(11):1625-1632.
- Cohen BE. 2010. Amphotericin B membrane action: role for two types of ion channels in eliciting cell survival and lethal effects. *Journal of Membrane Biology* 238(1-3):1-20.
- Cole S. 1999. TubercuList. <http://tuberculist.epfl.ch/> and <http://genolist.pasteur.fr/TubercuList/> Version 2.3 ed. Paris: Ecole Polytechnique Fédérale de Lausanne. Accessed in June 2008-June 2011.

- Cole ST, Alzari PM. 2005. TB - A new target, a new drug. *Science* 307(5707):214-215.
- Cole ST, Brosch R, Parkhill J, Garnier T, Churcher C, Harris D, Gordon SV, Eiglmeier K, Gas S, Barry CE. 1998. Deciphering the biology of *Mycobacterium tuberculosis* from the complete genome sequence. *Nature* 393(6685):537-44.
- Conner KP, Woods CM, Atkins WM. 2011. Interactions of cytochrome P450s with their ligands. *Archives of Biochemistry and Biophysics* 507(1):56-65.
- Cooper AM. 2009. Cell-mediated immune responses in Tuberculosis. *Annual Review of Immunology* 27(1):393-422.
- Cox HS, McDermid C, Azevedo V, Muller O, Coetzee D, Simpson J, Barnard M, Coetzee G, van Cutsem G, Goemaere E. 2010. Epidemic levels of drug resistant Tuberculosis (MDR and XDR-TB) in a high HIV prevalence setting in Khayelitsha, South Africa. *PLoS One* 5(11):e13901.
- Crick DC, Seabratra Mahapatra, and Patrick J. Brennan. 2001. Biosynthesis of the arabinogalactan-peptidoglycan complex of *Mycobacterium tuberculosis*. *Glycobiology* 11(9):107-118.
- Cronin S, Chandrasekar PH. 2010. Safety of triazole antifungal drugs in patients with cancer. *Journal of Antimicrobial Chemotherapy* 65(3):410-416.
- D'Arcy A, Frederic VA, Marsh M. 2007. An automated microseed matrix-screening method for protein crystallization. *Acta Crystallographica Section D-Biological Crystallography* 63(4):550-554.
- Davydov R, Makris TM, Kofman V, Werst DE, Sligar SG, Hoffman BM. 2001. Hydroxylation of camphor by-reduced oxy-cytochrome P450cam: Mechanistic implications of EPR and ENDOR studies of catalytic intermediates in native and mutant enzymes. *Journal of the American Chemical Society* 123(7):1403-1415.
- Davydov R, Perera R, Jin SX, Yang TC, Bryson TA, Sono M, Dawson JH, Hoffman BM. 2005. Substrate modulation of the properties and reactivity of the oxy-ferrous and hydroperoxo-ferric intermediates of cytochrome P450cam as shown by cryoreduction-EPR/ENDOR spectroscopy. *Journal of the American Chemical Society* 127(5):1403-1413.
- Dawson JH, Pond AE, Roach MP, Perera R, Dasgupta A, Thomas MR, Boxer SG. 2001. Modelling ferrous, ferric and ferryl heme states using His93Gly myoglobin and related heme iron systems. *Journal of Inorganic Biochemistry* 86(1):39-39.
- Debeljak N, Fink M, Rozman D. 2003. Many facets of mammalian lanosterol 14 alpha-demethylase from the evolutionarily conserved cytochrome P450 family CYP51. *Archives of Biochemistry and Biophysics* 409(1):159-171.
- Delogu G, Sanguinetti M, Pusceddu C, Bua A, Brennan MJ, Zanetti S, Fadda G. 2006. PE_PGRS proteins are differentially expressed by *Mycobacterium tuberculosis* in host tissues. *Microbes and Infection* 8(8):2061-2067.
- Delye C, Bousset L, Corio-Costet MF. 1998. PCR cloning and detection of point mutations in the eburicol 14 alpha-demethylase (CYP51) gene from *Erysiphe graminis* f. sp. *hordei*, a "recalcitrant" fungus. *Current Genetics* 34(5):399-403.
- Denisov IG, Grinkova YV, McLean MA, Sligar SG. 2007. The one-electron autoxidation of human cytochrome P450 3A4. *Journal of Biological Chemistry* 282(37):26865-26873.
- Denisov IG, Mak PJ, Makris TM, Sligar SG, Kincaid JR. 2008. Resonance Raman characterization of the peroxo and hydroperoxo intermediates in cytochrome P450. *Journal of Physical Chemistry A* 112(50):13172-13179.
- Denisov IG, Makris, T.M., Sligar, S.G. and Schlichting, I. 2005. Structure and chemistry of cytochrome P450. *Chemical Reviews* 105(105):2253-2277.
- Dorko E, Viragova S, Pilipcinec E, Tkacikova L. 2003. Candida - Agent of the diaper dermatitis? *Folia Microbiologica* 48(3):385-388.
- Driscoll MD, McLean KJ, Cheesman MR, Jowitt TA, Howard M, Carroll P, Parish T, Munro AW. 2011. Expression and characterization of *Mycobacterium tuberculosis* CYP144: Common themes and lessons learned in the *M. tuberculosis* P450 enzyme family. *Biochimica et Biophysica Acta-Proteins and Proteomics* 1814(1):76-87.
- Driscoll MD, McLean KJ, Levy C, Mast N, Pikuleva IA, Lafite P, Rigby SEJ, Leys D, Munro AW. 2010. Structural and biochemical characterization of *Mycobacterium tuberculosis* CYP142: Evidence for multiple cholesterol 27-hydroxylase activities in a human pathogen. *Journal of Biological Chemistry* 285(49):38270-82.
- Ducati RG, Ruffino-Netto A, Basso LA, Santos DS. 2006. The resumption of consumption - a review on tuberculosis. *Mem Inst Oswaldo Cruz* 101(7):697-714.
- Dugdale DC, Vyas JM, Zieve D. 2009. Disseminated tuberculosis. <http://www.nlm.nih.gov/medlineplus/ency/article/000624.htm>. Version updated on 12th July 2010. National Institutes of Health. Accessed in January 2011.
- Dunford AJ, McLean KJ, Sabri M, Seward HE, Heyes DJ, Scrutton NS, Munro AW. 2007. Rapid P450 heme iron reduction by laser photoexcitation of *Mycobacterium tuberculosis* CYP121 and CYP51B1 - Analysis of CO complexation reactions and reversibility of the P450/P420 equilibrium. *Journal of Biological Chemistry* 282(34):24816-24824.

- Edlayne G, Simone A, Felicio JD. 2009. Chemical and biological approaches for mycotoxin control: a review. *Recent Patents on Food, Nutrition and Agriculture* 1(2):155-161.
- Ehrt SaS, D. 2007. *Mycobacterium tuberculosis* virulence: lipids inside and out. *Nature Medicine* 13(3):284-285.
- E Kroos M, Sjogren T. 2006. Structural basis for ligand promiscuity in cytochrome P450 3A4. *Proceedings of the National Academy of Sciences of the United States of America* 103(37):13682-13687.
- Emanuelsson O, Nielsen H, Brunak S, von Heijne G. 2000. Predicting subcellular localization of proteins based on their N-terminal amino acid sequence. *Journal of Molecular Biology* 300(4):1005-1016.
- Emsley P, Lohkamp B, Scott WG, Cowtan K. 2010. Features and development of Coot. *Acta Crystallographica Section D-Biological Crystallography* 66(4):486-501.
- Etienne G, Villeneuve C, Billman-Jacobe H, Astarie-Dequeker C, Dupont MA, Daffe M. 2002. The impact of the absence of glycopeptidolipids on the ultrastructure, cell surface and cell wall properties, and phagocytosis of *Mycobacterium smegmatis*. *Microbiology* 148(10):3089-3100.
- Favre B, Didmon M, Ryder NS. 1999. Multiple amino acid substitutions in lanosterol 14 α -demethylase contribute to azole resistance in *Candida albicans*. *Microbiology* 145(10):2715-25.
- Fischer F, Raimondi D, Aliverti A, Zanetti G. 2002. *Mycobacterium tuberculosis* FprA, a novel bacterial NADPH-ferredoxin reductase. *European Journal of Biochemistry* 269(12):3005-3013.
- Furge LL, Guengerich FP. 2006. Cytochrome P450 enzymes in drug metabolism and chemical toxicology. *Biochemistry and Molecular Biology Education* 34(2):66-74.
- Gantt SL, Denisov IG, Grinkova YV, Sligar SG. 2009. The critical iron-oxygen intermediate in human aromatase. *Biochemical and Biophysical Research Communications* 387(1):169-173.
- Garcia-Effron G, Mellado E, Alcazar-Fuoli L, Buitrago MJ, Cuenca-Estrella M, Rodriguez-Tudela JL. 2005. Role of *Aspergillus fumigatus* 14- α sterol demethylase (Cyp51b) gene on cell growth and viability, antifungal susceptibility and sterol composition. Abstracts of the Interscience Conference on Antimicrobial Agents and Chemotherapy 45:440.
- Gatfield J, Pieters J. 2000. Essential role for cholesterol in entry of mycobacteria into macrophages. *Science* 288(5471):1647-1650.
- Gibson GG, Skett P. 2001. Introduction to drug metabolism. Nelson Thornes Publishers, Cheltenham, United Kingdom. p.243.
- Gill P, Moghadam TT, Ranjbar B. 2010. Differential scanning calorimetry techniques: applications in biology and nanoscience. *Journal of Biomolecular Techniques* 21(4):167-93.
- Girvan HM, Levy CW, Williams P, Fisher K, Cheesman MR, Rigby SEJ, Leys D, Munro AW. 2010. Glutamate-haem ester bond formation is disfavoured in flavocytochrome P450 BM3: characterization of glutamate substitution mutants at the haem site of P450 BM3. *Biochemical Journal* 427(3):455-466.
- Girvan HM, Toogood HS, Littleford RE, Seward HE, Smith WE, Ekanem IS, Leys D, Cheesman MR, Munro AW. 2009. Novel haem co-ordination variants of flavocytochrome P450 BM3. *Biochemical Journal* 417(1):65-76.
- Golden MP, Vikram HR. 2005. Extrapulmonary tuberculosis: an overview. *American Family Physician* 72(9):1761-8.
- Goldman GH, Ferreira MED, Marques ED, Savoldi M, Perlin D, Park S, Martinez PCG, Goldman MHS, Colombo AL. 2004. Evaluation of fluconazole resistance mechanisms in *Candida albicans* clinical isolates from HIV-infected patients in Brazil. *Diagnostic Microbiology and Infectious Disease* 50(1):25-32.
- Gorren ACF, Schrammel A, Schmidt K, Mayer B. 1997. Thiols and neuronal nitric oxide synthase: Complex formation, competitive inhibition, and enzyme stabilization. *Biochemistry* 36(14):4360-4366.
- Gotoh O. 1992. Substrate recognition sites in cytochrome-P450 family-2 (CYP2) proteins inferred from comparative analyse of amin-acid and coding nucleotide-sequences. *Journal of Biological Chemistry* 267(1):83-90.
- Gotoh O, Tagashira Y, Morohashi K, Fujikuriyama Y. 1985. Possible steroid binding-site common to adrenal cytochrome-P450SCC and prostatic steroid binding-protein. *FEBS Letters* 188(1):8-10.
- Goyal K, Qamra R, Mande SC. 2006. Multiple gene duplication and rapid evolution in the groEL gene: Functional implications. *Journal of Molecular Evolution* 63(6):781-787.
- Green MT. 2009. C-H bond activation in heme proteins: the role of thiolate ligation in cytochrome P450. *Current Opinion in Chemical Biology* 13(1):84-88.
- Green MT, Dawson JH, Gray HB. 2004. Oxoiron(IV) in chloroperoxidase compound II is basic: Implications for P450 chemistry. *Science* 304(5677):1653-1656.
- Grover ND. 2010. Echinocandins: A ray of hope in antifungal drug therapy. *Indian Journal of Pharmacology* 42(1):9-11.
- Groves JT, McClusky GA. 1976. Aliphatic hydroxylation via oxygen rebound – oxygen-transfer catalyzed by iron. *Journal of the American Chemical Society* 98(3):859-861.
- Guengerich FP. 2006. Cytochrome P450s and other enzymes in drug metabolism and toxicity. *American Association of Pharmaceutical Scientists Journal* 8(1):e101-e111.
- Guengerich FP. 2008. Cytochrome P450 and chemical toxicology. *Chemical Research in Toxicology* 21(1):70-83.

- Guengerich FP, Isin EM. 2008. Mechanisms of cytochrome P450 reactions. *Acta Chimica Slovenica* 55(1):7-19.
- Guengerich FP, Rendic S. 2010. Update information on drug metabolism systems-2009, Part I. *Current drug metabolism* 11(1):1-3.
- Guengerich FP, Tang ZM, Cheng QA, Salamanca-Pinzon SG. 2011. Approaches to deorphanization of human and microbial cytochrome P450 enzymes. *Biochimica et Biophysica Acta-Proteins and Proteomics* 1814(1):139-145.
- Guengerich FP, Tang ZM, Salamanca-Pinzon SG, Cheng QA. 2010. Characterizing proteins of unknown function: Orphan cytochrome P450 enzymes as a paradigm. *Molecular Interventions* 10(3):153-163.
- Guo N, Liu JB, Wu XP, Bi XM, Meng RZ, Wang XL, Xiang H, Deng XM, Yu L. 2009. Antifungal activity of thymol against clinical isolates of fluconazole-sensitive and -resistant *Candida albicans*. *Journal of Medical Microbiology* 58(8):1074-1079.
- Gupta AK. 2001. Uncommon localization or presentation of tinea infection. *Journal of the European Academy of Dermatology and Venereology* 15(1):7-8.
- Harrison C. 2010. Antifungal drugs targeting histone acetylation. *Nature Reviews Drug Discovery* 9(9):680-681.
- Hayaishi O, Katagiri M, Rothberg S. 1957. Studies on oxygenases – Pyrocatechase. *Journal of Biological Chemistry* 229(2):905-920.
- He XJ, Yamauchi H, Suzuki K, Ueno M, Nakayama H, Doi K. 2007. Gene expression profiles of drug-metabolizing enzymes (DMEs) in rat liver during pregnancy and lactation. *Experimental and Molecular Pathology* 83(3):428-434.
- Hoehamer CF, Cummings ED, Hilliard GM, Rogers PD. 2010. Changes in the proteome of *Candida albicans* in response to azole, polyene, and echinocandin antifungal agents. *Antimicrobial Agents and Chemotherapy* 54(5):1655-1664.
- Hui Bon Hoa G, McLean MA, Sligar SG. 2002. High pressure, a tool for exploring heme protein active sites. *Biochimica et Biophysica Acta* 1595(1-2):297-308.
- Hintz MJ, Peterson JA. 1980. The kinetics of reduction of cytochrome -P-450CAM by the dithionite anion monomer. *Journal of Biological Chemistry* 255(15):7317-7325.
- Hennerdal A, Elofsson A. 2011. Rapid membrane protein topology prediction. *Bioinformatics* 27(9):1322-1323.
- Hoffmann A, Bukau B, Kramer G. 2010. Structure and function of the molecular chaperone trigger factor. *Biochimica et Biophysica Acta-Molecular Cell Research* 1803(6):650-661.
- Huang GC, Chen JJ, Liu CP, Zhou JM. 2002. Chaperone and antichaperone activities of trigger factor. *European Journal of Biochemistry* 269(18):4516-4523.
- Huang GC, Li ZY, Zhou JM, Fischer G. 2000. Assisted folding of D-glyceraldehyde-3-phosphate dehydrogenase by trigger factor. *Protein Science* 9(6):1254-1261.
- Isin EM, Guengerich FP. 2008. Substrate binding to cytochromes P450. *Analytical and Bioanalytical Chemistry* 392(6):1019-1030.
- Jackson CJ, Lamb DC, Marczylo TH, Parker JE, Manning NL, Kelly DE, Kelly SL. 2003. Conservation and cloning of CYP51: a sterol 14 alpha-demethylase from *Mycobacterium smegmatis*. *Biochemical and Biophysical Research Communications* 301(2):558-563.
- Jackson CJ, Lamb DC, Marczylo TH, Warrilow AGS, Manning NJ, Lowe DJ, Kelly DE, Kelly SL. 2002. A novel sterol 14 alpha-demethylase/ferredoxin fusion protein (MCCYP51FX) from *Methylococcus capsulatus* represents a new class of the cytochrome P450 superfamily. *Journal of Biological Chemistry* 277(49):46959-46965.
- Johnston JB, Kells PM, Podust LM, de Montellano PRO. 2009. Biochemical and structural characterization of CYP124: A methyl-branched lipid omega-hydroxylase from *Mycobacterium tuberculosis*. *Proceedings of the National Academy of Sciences of the United States of America* 106(49):20687-20692.
- Johnston JB, Ouellet H, de Montellano PRO. 2010. Functional redundancy of steroid C-26-monooxygenase activity in *Mycobacterium tuberculosis* revealed by biochemical and genetic analyses. *Journal of Biological Chemistry* 285(47):36352-36360.
- Jones MG. 2007. The first filamentous fungal genome sequences: *Aspergillus* leads the way for essential everyday resources or dusty museum specimens? *Microbiology* 153(1):1-6.
- Jung C. 2011. The mystery of cytochrome P450 Compound I. A mini-review dedicated to Klaus Ruckpaul. *Biochimica et Biophysica Acta-Proteins and Proteomics* 1814(1):46-57.
- Kahn RA, Bak S, Olsen CE, Svendsen I, Moller BL. 1996. Isolation and reconstitution of the heme-thiolate protein obtusifoliol 14 alpha-demethylase from *Sorghum bicolor* (L.) Moench. *Journal of Biological Chemistry* 271(51):32944-32950.
- Takeya H, Miyazaki Y, Miyazaki H, Nyswaner K, Grimberg B, Bennett JE. 2000. Genetic analysis of azole resistance in the Darlington strain of *Candida albicans*. *Antimicrobial Agents and Chemotherapy* 44(11):2985-2990.
- Kamai Y, Maebashi K, Kudoh M, Makimura K, Naka W, Uchida K, Yamaguchi H. 2004. Characterization of mechanisms of fluconazole resistance in a *Candida albicans* isolate from a Japanese patient with chronic mucocutaneous candidiasis. *Microbiology and Immunology* 48(12):937-43.

- Kellner DG, Hung SC, Weiss KE, Sligar SG. 2002. Kinetic characterization of Compound I formation in the thermostable cytochrome P450 CYP119. *Journal of Biological Chemistry* 277(12):9641-9644.
- Kelly SL, Lamb DC, Kelly DE. 1999a. Y132H substitution in *Candida albicans* sterol 14 alpha-demethylase confers fluconazole resistance by preventing binding to haem. *FEMS Microbiology Letters* 180(2):171-175.
- Kelly SL, Lamb DC, Cannieux M, Greetham D, Jackson CJ, Marczylo T, Ugochukwu C, Kelly DE. 2001. An old activity in the cytochrome P450 superfamily (CYP51) and a new story of drugs and resistance. *Biochemical Society Transactions* 29(2):122-128.
- Kelly SL, Lamb DC, Loeffler J, Einsele H, Kelly DE. 1999b. The G464S amino acid substitution in *Candida albicans* sterol 14 alpha-demethylase causes fluconazole resistance in the clinic through reduced affinity. *Biochemical and Biophysical Research Communications* 262(1):174-179.
- Kendall SL, Rison, S.C., Movahedzadeh, F., Frita, R. and Stoker, N.G. 2004. What do microarrays really tell us about *M. tuberculosis*? *Trends in Microbiology* 12(12):537-544.
- Kim JH, Campbell BC, Mahoney N, Chan KL, Molyneux RJ, Balajee A. 2010. Augmenting the activity of antifungal agents against aspergilli using structural analogues of benzoic acid as chemosensitizing agents. *Fungal Biology* 114(10):817-824.
- Kim MJ, Kim HR, Hwang SS, Kim YW, Han SK, Shim YS, Yim JJ. 2009. Prevalence and its predictors of extrapulmonary involvement in patients with pulmonary tuberculosis. *Journal of Korean Medical Science* 24(2):237-241.
- Koul A, Arnoult E, Lounis N, Guillemont J, Andries K. 2011. The challenge of new drug discovery for tuberculosis. *Nature* 469(7331):483-490.
- Krishnan-Natesan S, Chandrasekar PH, Alangaden GJ, Manavathu EK. 2008. Molecular characterisation of cyp51A and cyp51B genes coding for P450 14 alpha-lanosterol demethylases A (CYP51Ap) and B (CYP51Bp) from voriconazole-resistant laboratory isolates of *Aspergillus flavus*. *International Journal of Antimicrobial Agents* 32(6):519-524.
- Kubica G. 1976. *Mycobacterium tuberculosis* culture revealing this organism's colonial morphology. <http://www.infectiousdiseaseneews.com/article.aspx?id=33881> U.S.A: Centers for Disease Control and Prevention. Accessed in June 2011.
- Kudo M, Ohi A, Aoyama Y, Nitahara Y, Chung SK, Yoshida Y. 2005. Effects of Y132H and F145L substitutions on the activity, azole resistance and spectral properties of *Candida albicans* sterol 14-demethylase P450 (CYP51): A live example showing the selection of altered P450 through interaction with environmental compounds. *Journal of Biochemistry* 137(5):625-632.
- Kumar R, Rai S, Kant S, Anand K, Dar L, Singh U. 2010. HIV prevalence and MDR TB among DOTS attendees in a rural area of Haryana, India. *International Journal of Infectious Diseases* 14:E148-E149.
- Kumbhar PP, Dewang PM. 2001. Eco-friendly pest management using monoterpenoids. I. Antifungal efficacy of thymol derivatives. *Journal of Scientific & Industrial Research* 60(8):645-648.
- Kupfer R, Liu SY, Allentoff AJ, Thompson JA. 2001. Comparisons of hydroperoxide isomerase and monooxygenase activities of cytochrome P450 for conversions of allylic hydroperoxides and alcohols to epoxyalcohols and diols: Probing substrate reorientation in the active site. *Biochemistry* 40(38):11490-11501.
- Lamb DC, Kelly DE, Baldwin BC, Kelly SL. 2000. Differential inhibition of human CYP3A4 and *Candida albicans* CYP51 with azole antifungal agents. *Chemico-Biological Interactions* 125(3):165-175.
- Lamb DC, Kelly DE, Kelly SL. 1998. Molecular diversity of sterol 14 alpha-demethylase substrates in plants, fungi and humans. *FEBS Letters* 425(2):263-265.
- Lamb DC, Kelly DE, White TC, Kelly SL. 2000. The R467K amino acid substitution in *Candida albicans* sterol 14 alpha-demethylase causes drug resistance through reduced affinity. *Antimicrobial Agents and Chemotherapy* 44(1):63-67.
- Lamb DC, Lei L, Warrilow AGS, Lepesheva GI, Mullins JGL, Waterman MR, Kelly SL. 2009. The first virally encoded cytochrome P450. *Journal of Virology* 83(16):8266-8269.
- Lamb DC, Skaug T, Song HL, Jackson CJ, Podust LM, Waterman MR, Kell DB, Kelly DE, Kelly SL. 2002. The cytochrome p450 complement (CYPome) of *Streptomyces coelicolor* A3(2). *Journal of Biological Chemistry* 277(27):24000-24005.
- Lamichhane G, Zignol M, Blades NJ, Geiman DE, Dougherty A, Grosset J, Broman KW, Bishai WR. 2003. A postgenomic method for predicting essential genes at subsaturation levels of mutagenesis: Application to *Mycobacterium tuberculosis*. *Proceedings of the National Academy of Sciences of the United States of America* 100(12):7213-7218.
- Lamping E, Ranchod A, Nakamura K, Tyndall JDA, Niimi K, Holmes AR, Niimi M, Cannon RD. 2009. Abc1p is a multidrug efflux transporter that tips the balance in favor of innate azole resistance in *Candida krusei*. *Antimicrobial Agents and Chemotherapy* 53(2):354-369.
- Lawson RJ, Leys D, Sutcliffe MJ, Kemp CA, Cheesman MR, Smith SJ, Clarkson J, Smith WE, Haq I, Perkins JB. 2004. Thermodynamic and biophysical characterization of cytochrome P450 BioI from *Bacillus subtilis*. *Biochemistry* 43(39):12410-12426.

- Leibovici V, Alkalay R, Hershko K, Ingber A, Westerman M, Leviatan-Strauss N, Hochberg M. 2008. Prevalence of *Candida* on the tongue and intertriginous areas of psoriatic and atopic dermatitis patients. *Mycoses* 51(1):63-66.
- Lepesheva GI, Hargrove TY, Anderson S, Kleshchenko Y, Furtak V, Wawrzak Z, Villalta F, Waterman MR. 2010a. Structural insights into inhibition of sterol 14 alpha-demethylase in the human pathogen *Trypanosoma cruzi*. *Journal of Biological Chemistry* 285(33):25582-25590.
- Lepesheva GI, Hargrove TY, Kleshchenko Y, Nes WD, Villalta F, Waterman MR. 2008. CYP51: A major drug target in the cytochrome P450 superfamily. *Lipids* 43(12):1117-1125.
- Lepesheva GI, Park H-W, Hargrove TY, Vanhollebeke B, Wawrzak Z, Harp JM, Sundaramoorthy M, Nes WD, Pays E, Chaudhuri M. 2010b. Crystal structures of *Trypanosoma brucei* sterol 14 alpha-demethylase and implications for selective treatment of human infections. *Journal of Biological Chemistry* 285(3):1773-1780.
- Lepesheva GI, Podust LM, Bellamine A, Waterman MR. 2001. Folding requirements are different between sterol 14 alpha-demethylase (CYP51) from *Mycobacterium tuberculosis* and human or fungal orthologs. *Journal of Biological Chemistry* 276(30):28413-28420.
- Lepesheva GI, Virus C, Waterman MR. 2003. Conservation in the CYP51 family. Role of the B' helix/BC loop and helices F and G in enzymatic function. *Biochemistry* 42(30):9091-9101.
- Lepesheva GI, Waterman MR. 2007. Sterol 14alpha-demethylase cytochrome P450 (CYP51), a P450 in all biological kingdoms. *Biochimica et Biophysica Acta* 1770(3):467-477.
- Lepesheva GI, Waterman MR. 2011. Structural basis for conservation in the CYP51 family. *Biochimica Et Biophysica Acta-Proteins and Proteomics* 1814(1):88-93.
- Lewis DF. 2004. 57 varieties: the human cytochromes P450. *Pharmacogenomics* 5(5):305-318.
- Lewis DFV. 1996. *Cytochromes P450: Structure, function and mechanism*. London, United Kingdom: Taylor & Francis. p.348.
- Lewis DFV. 2001. *Guide to cytochrome P450: Structure and function*. London, United Kingdom: Taylor & Francis. p.215.
- Lewis, DG. 2007. Characterization of *Mycobacterium* sp. P450 systems. PhD thesis, The University of Leicester. p.359.
- Lee HC, Bernstein HD. 2002. Trigger factor retards protein export in *Escherichia coli*. *Journal of Biological Chemistry* 277(45):43527-43535.
- Leys D, Mowat CG, McLean KJ, Richmond A, Chapman SK, Walkinshaw MD, Munro AW. 2003. Atomic structure of *Mycobacterium tuberculosis* CYP121 to 1.06 Å reveals novel features of cytochrome P450. *Journal of Biological Chemistry* 278(7):5141-5147.
- Li LJ, Chen W, Xu H, Wan Z, Li RY, Liu W. 2010. Antifungal activity of ibuprofen against aspergillus species and its interaction with common antifungal drugs. *Chinese Medical Journal* 123(19):2701-2705.
- Li Y; Weiss WFIV; Roberts, CJ. 2009. Characterization of high-molecular-weight nonnative aggregates and aggregation kinetics by size exclusion chromatography with inline multi-angle laser light scattering. *Journal of Pharmaceutical Sciences* 98(11):3997-4016.
- Lipp HP. 2011. Posaconazole: clinical pharmacokinetics and drug interactions. *Mycoses* 54(1):32-38.
- Liu CP, Perrett S, Zhou JM. 2005. Dimeric trigger factor stably binds folding-competent intermediates and cooperates with the DnaK-DnaJ-GrpE chaperone system to allow refolding. *Journal of Biological Chemistry* 280(14):13315-13320.
- Liu TT, Lee REB, Barker KS, Lee RE, Wei L, Homayouni R, Rogers PD. 2005. Genome-wide expression profiling of the response to azole, polyene, echinocandin, and pyrimidine antifungal agents in *Candida albicans*. *Antimicrobial Agents and Chemotherapy* 49(6):2226-2236.
- Llerena C, Fadul SE, Garzon MC, Mejia G, Orjuela DL, Garcia LM, Alvarez HB, Ruiz FJ. 2010. Drug-resistant *Mycobacterium tuberculosis* in children under 15 years. *Biomedica* 30(3):362-370.
- Lo HJ, Wang JS, Lin CY, Chen CG, Hsiao TY, Hsu CT, Su CL, Fann MJ, Ching YT, Yang YL. 2005. Efg1 involved in drug resistance by regulating the expression of ERG3 in *Candida albicans*. *Antimicrobial Agents and Chemotherapy* 49(3):1213-1215.
- Loffler J, Kelly SL, Hebart H, Schumacher U, Lass-Flörl C, Einsele H. 1997. Molecular analysis of CYP51 from fluconazole-resistant *Candida albicans* strains. *FEMS Microbiology Letters* 151(2):263-268.
- Long R, Light B, Talbot JA. 1999. Mycobacteriocidal action of exogenous nitric oxide. *Antimicrobial Agents and Chemotherapy* 43(2):403-405.
- Macdonald IDG, Smith WE, Munro AW. 1996. Inhibitor fatty acid interactions with cytochrome P-450 BM3. *FEBS Letters* 396(2-3):196-200.
- Machida M, Gomi K, editors. 2010. *Aspergillus: Molecular Biology and Genomics*. Ed.(1). Norfolk, United Kingdom. Caister Academic Press. p.238.
- Malen H, Pathak S, Softeland T, de Souza GA, Wiker HG. 2010. Definition of novel cell envelope associated proteins in Triton X-114 extracts of *Mycobacterium tuberculosis* H37Rv. *BMC Microbiology* 10(132):1-11.
- Manavathu EK, Kallakuri S, Arganoza MT, Vazquez JA. 1999. Amino acid variations of cytochrome P-450 lanosterol 14 alpha-demethylase (CYP51A1) from fluconazole resistant clinical isolates of *Candida albicans*. *Revista Iberoamericana de Micología* 16(4):198-203.

- Mansfield BE, Oltean HN, Oliver BG, Hoot SJ, Leyde SE, Hedstrom L, White TC. 2010. Azole drugs are imported by facilitated diffusion in *Candida albicans* and other pathogenic fungi. *PLoS Pathogens* 6(9).
- Marais BJ. 2008. Tuberculosis in children. *Pediatric Pulmonology* 43(4):322-329.
- Marichal P, Koymans L, Willemsens S, Bellens D, Verhasselt P, Luyten W, Borgers M, Ramaekers FCS, Odds FC, Bossche HV. 1999. Contribution of mutations in the cytochrome P450 14 alpha-demethylase (Erg11p, Cyp51p) to azole resistance in *Candida albicans*. *Microbiology* 145(10):2701-2713.
- Martel CM, Parker JE, Bader O, Weig M, Gross U, Warrilow AGS, Kelly DE, Kelly SL. 2010a. A clinical isolate of *Candida albicans* with mutations in ERG11 (encoding sterol 14 alpha-demethylase) and ERG5 (encoding C22 desaturase) is cross resistant to azoles and amphotericin B. *Antimicrobial Agents and Chemotherapy* 54(9):3578-3583.
- Martel CM, Parker JE, Bader O, Weig M, Gross U, Warrilow AGS, Rolley N, Kelly DE, Kelly SL. 2010b. Identification and characterization of four azole-resistant ERG3 mutants of *Candida albicans*. *Antimicrobial Agents and Chemotherapy* 54(11):4527-4533.
- Martel CM, Parker JE, Warrilow AGS, Rolley NJ, Kelly SL, Kelly DE. 2010c. Complementation of a *Saccharomyces cerevisiae* ERG11/CYP51 (sterol 14 alpha-demethylase) doxycycline-regulated mutant and screening of the azole sensitivity of *Aspergillus fumigatus* isoenzymes CYP51A and CYP51B. *Antimicrobial Agents and Chemotherapy* 54(11):4920-4923.
- Martinez M, Lopez-Ribot JL, Kirkpatrick WR, Bachmann SP, Perea S, Ruesga MT, Patterson TF. 2002. Heterogeneous mechanisms of azole resistance in *Candida albicans* clinical isolates from an HIV-infected patient on continuous fluconazole therapy for oropharyngeal candidosis. *Journal of Antimicrobial Chemotherapy* 49(3):515-524.
- Mason HS, Fowles WL, Peterson E. 1955. Oxygen transfer and electron transport by the phenolase complex. *Journal of the American Chemical Society* 77(10):2914-2915.
- Massone C, Propst E, Kopera D. 2006. Rosacelike dermatitis with *Candida albicans* infection. *Archives of Dermatology* 142(7):945-946.
- Mast N, Annalora AJ, Lodowski DT, Palczewski K, Stout CD, Pikuleva IA. 2011. Structural basis for three-step sequential catalysis by the cholesterol side chain cleavage enzyme CYP11A1. *Journal of Biological Chemistry* 286(7):5607-5613.
- Mast N, Whitet MA, Bjorkhem I, Johnson EF, Stout CD, Pikuleva IA. 2008. Crystal structures of substrate-bound and substrate-free cytochrome P450 46A1, the principal cholesterol hydroxylase in the brain. *Proceedings of the National Academy of Sciences of the United States of America* 105(28):9546-9551.
- Mawuenyega KG, Forst CV, Dobos KM, Belisle JT, Chen J, Bradbury EM, Bradbury ARM, Chen X. 2005. *Mycobacterium tuberculosis* functional network analysis by global subcellular protein profiling. *Molecular Biology of the Cell* 16(1):396-404.
- Mayhew SG. 1978. Redox potential of dithionite and SO₂ – from equilibrium reactions with flavodoxins, methyl viologen and hydrogen plus hydrogenase. *European Journal of Biochemistry* 85(2):535-547.
- McLean KJ, Belcher J, Driscoll MD, Fernandez CC, Le Van D, Bui S, Golovanova M, Munro AW. 2010. The *Mycobacterium tuberculosis* cytochromes P450: physiology, biochemistry and molecular intervention. *Future Medicinal Chemistry* 2(8):1339-1353.
- McLean KJ, Carroll P, Lewis DG, Dunford AJ, Seward HE, Neeli R, Cheesman MR, Marsollier L, Douglas P, Smith WE. 2008. Characterization of active site structure in CYP121 a cytochrome P450 essential for viability of *Mycobacterium tuberculosis* H37Rv. *Journal of Biological Chemistry* 283(48):33406-33416.
- McLean KJ, Cheesman MR, Rivers SL, Richmond A, Leys D, Chapman SK, Reid GA, Price NC, Kelly SM, Clarkson J. 2002a. Expression, purification and spectroscopic characterization of the cytochrome P450 CYP121 from *Mycobacterium tuberculosis*. *Journal of Inorganic Biochemistry* 91(4):527-41.
- McLean KJ, Clift D, Lewis DG, Sabri M, Balding PR, Sutcliffe MJ, Leys D, Munro AW. 2006a. The preponderance of P450s in the *Mycobacterium tuberculosis* genome. *Trends in Microbiology* 14(5):220-228.
- McLean KJ, Dunford AJ, Neeli R, Driscoll MD, Munro AW. 2007a. Structure, function and drug targeting in *Mycobacterium tuberculosis* cytochrome P450 systems. *Archives of Biochemistry and Biophysics* 464(2):228-240.
- McLean KJ, Dunford AJ, Sabri M, Neeli R, Girvan HM, Balding PR, Leys D, Seward HE, Marshall KR, Munro AW. 2006b. CYP121, CYP51 and associated redox systems in *Mycobacterium tuberculosis*: Towards deconvoluting enzymology of P450 systems in a human pathogen. *Biochemical Society Transactions* 34(6):1178-1182.
- McLean KJ, Girvan HM, Munro AW. 2007b. Cytochrome P450/redox partner fusion enzymes: biotechnological and toxicological prospects. *Expert Opinion on Drug Metabolism and Toxicology* 3(6):847-63.
- McLean KJ, Lafite P, Levy C, Cheesman MR, Mast N, Pikuleva IA, Leys D, Munro AW. 2009. The structure of *Mycobacterium tuberculosis* CYP125 molecular basis for cholesterol binding in a P450 needed for host infection. *Journal of Biological Chemistry* 284(51):35524-35533.
- McLean KJ, Leys D, Marshall KR, Lewis G, Warman AJ, Scrutton NS, Munro AW. 2003a. Cytochrome P450 redox systems in *Mycobacterium tuberculosis*. Anzenbacher PHJ, Ed. p.249-251.

- McLean KJ, Marshall KR, Richmond A, Hunter IS, Fowler K, Kieser T, Gurcha SS, Besra GS, Munro AW. 2002b. Azole antifungals are potent inhibitors of cytochrome P450 mono-oxygenases and bacterial growth in mycobacteria and streptomycetes. *Microbiology* 148(10):2937-2949.
- McLean KJ, Munro AW. 2008. Structural biology and biochemistry of cytochrome P450 systems in *Mycobacterium tuberculosis*. *Drug Metabolism Reviews* 40(3):427-446.
- McLean KJ, Sabri M, Marshall KR, Lawson RJ, Lewis DG, Clift D, Balding PR, Dunford AJ, Warman AJ, McVey JP. 2005. Biodiversity of cytochrome P450 redox systems. *Biochemical Society Transactions* 33(4):796-801.
- McLean KJ, Scrutton NS, Munro AW. 2003b. Kinetic, spectroscopic and thermodynamic characterization of the *Mycobacterium tuberculosis* adrenodoxin reductase homologue FprA. *Biochem Journal* 372(2):317-327.
- McLean KJ, Warman AJ, Seward HE, Marshall KR, Girvan HM, Cheesman MR, Waterman MR, Munro AW. 2006c. Biophysical characterization of the sterol demethylase P450 from *Mycobacterium tuberculosis*, its cognate ferredoxin, and their interactions. *Biochemistry* 45(27):8427-43.
- Meissle M, Mouron P, Musa T, Bigler F, Pons X, Vasileiadis VP, Otto S, Antichi D, Kiss J, Palinkas Z. 2010. Pests, pesticide use and alternative options in European maize production: current status and future prospects. *Journal of Applied Entomology* 134(5):357-375.
- Mellado E, Diaz-Guerra TM, Cuenca-Estrella M, Rodriguez-Tudela JL. 2001. Identification of two different 14-alpha sterol demethylase-related genes (cyp51A and cyp51B) in *Aspergillus fumigatus* and other aspergillus species. *Journal of Clinical Microbiology* 39(7):2431-2438.
- Mellado E, Garcia-Effron G, Alcazar-Fuoli L, Melchers WJG, Verweij PE, Cuenca-Estrella A, Rodriguez-Tudela JL. 2007. A new *Aspergillus fumigatus* resistance mechanism conferring *in vitro* cross-resistance to azole antifungals involves a combination of cyp51A alterations. *Antimicrobial Agents and Chemotherapy* 51(6):1897-1904.
- Mellado E, Garcia-Effron G, Buitrago MJ, Alcazar-Fuoli L, Cuenca-Estrella A, Rodriguez-Tudela JL. 2005. Targeted gene disruption of the 14-alpha sterol demethylase (cyp51A) in *Aspergillus fumigatus* and its role in azole drug susceptibility. *Antimicrobial Agents and Chemotherapy* 49(6):2536-2538.
- Miles CS, Manson FDC, Reid GA, Chapman SK. 1993. Substitution of a heme-iron axial ligand in a flavocytochrome-*b*₂. *Biochimica et Biophysica Acta* 1202(1):82-86.
- Mingot JM, Penalva MA, Fernandez-Canon JM. 1999. Disruption of phacA, an *Aspergillus nidulans* gene encoding a novel cytochrome P450 monooxygenase catalyzing phenylacetate 2-hydroxylation, results in penicillin overproduction. *Journal of Biological Chemistry* 274(21):14545-14550.
- Moore JT, Gaylor JL. 1968. Investigation of component reactions of sterol demethylation - preparation and properties of yeast demethylase activity. *Archives of Biochemistry and Biophysics* 124(1-3):167-175.
- Mowat CG, Miles CS, Munro AW, Cheesman MR, Quaroni LG, Reid GA, Chapman SK. 2000. Changing the heme ligation in flavocytochrome *b*₂: substitution of histidine-66 by cysteine. *Journal of Biological and Inorganic Chemistry* 5(5):584-92.
- Mugnol KCU, Ando RA, Nagayasu RY, Faljoni-Alario A, Brochsztain S, Santos PS, Nascimento OR, Nantes IL. 2008. Spectroscopic, structural, and functional characterization of the alternative low-spin state of horse heart cytochrome *c*. *Biophysical Journal* 94(10):4066-4077.
- Munoz P, Guinea J, Rojas L, Bouza E. 2010. New antifungal agents for the treatment of candidaemia. *International Journal of Antimicrobial Agents* 36:s63-s69.
- Munro AW, Girvan HM, McLean KJ. 2007a. Cytochrome P450 - redox partner fusion enzymes. *Biochimica et Biophysica Acta* 1770(3):345-359.
- Munro AW, Girvan HM, McLean KJ. 2007b. Variations on a (t)heme - novel mechanisms, redox partners and catalytic functions in the cytochrome P450 superfamily. *Natural Product Reports* 24(3):585-609.
- Munro AW, Le Van D, Fernandez CC, Sabri M, Driscoll M, Bui S, Leys D, McLean KJ. 2009. Characterization of P450 redox systems in the human pathogen *Mycobacterium tuberculosis*. Shoun H, Ohkawa H, editors. *Proceedings of the 16th International Conference on Cytochrome P450 - Biochemistry, Biophysics, Biotechnology*. p.57-61.
- Munro AW, McLean KJ, Marshall KR, Warman AJ, Lewis G, Roitel O, Sutcliffe MJ, Kemp CA, Modi S, Scrutton NS. 2003. Cytochromes P450: novel drug targets in the war against multidrug-resistant *Mycobacterium tuberculosis*. *Biochemical Society Transactions* 31(3):625-30.
- Munro AW, Noble MA, Robledo L, Daff SN, Chapman SK. 2001. Determination of the redox properties of human NADPH-cytochrome P450 reductase. *Biochemistry* 40(7):1956-63.
- Musaji N. 2010. Antifungal drug resistance: not all azoles are equal. *Expert Review of Anti-Infective Therapy* 8(5):515-516.
- Myasoedova KN. 2008. New findings in studies of cytochromes P450. *Biochemistry-Moscow* 73(9):965-969.
- Neeli R, Girvan HM, Lawrence A, Warren MJ, Leys D, Scrutton NS, Munro AW. 2005. The dimeric form of flavocytochrome P450BM3 is catalytically functional as a fatty acid hydroxylase. *FEBS Letters* 579(25):5582-5588.
- Nelson DR. 2009. The cytochrome P450 homepage. *Human Genomics* 4(1):59-65.

- Nelson DR, Koymans L, Kamataki T, Stegeman JJ, Feyereisen R, Waxman DJ, Waterman MR, Gotoh O, Coon MJ, Estabrook RW. 1996. P450 superfamily: Update on new sequences, gene mapping, accession numbers and nomenclature. *Pharmacogenetics* 6(1):1-42.
- Newcomb M, Zhang R, Chandrasena REP, Halgrimson JA, Horner JH, Makris TM, Sligar SG. 2006. Cytochrome P450 Compound I. *Journal of the American Chemical Society* 128(14):4580-4581.
- Nierman WC, Pain A, Anderson MJ, Wortman JR, Kim HS, Arroyo J, Berriman M, Abe K, Archer DB, Bermejo C. 2005. Genomic sequence of the pathogenic and allergenic filamentous fungus *Aspergillus fumigatus*. *Nature* 438(7071):1151-1156.
- Nigg AP, Schulze-Koops H, Wirth S, Weiss M, Bogner JR. 2008. Tuberculous spondylitis (Pott's disease). *Infection* 36(3):293-294.
- NIH. 1996. Tuberculosis. National Institute of Health (NIH), National Institute of Allergy and Infectious Diseases (NIAID). <http://www.niaid.nih.gov/topics/tuberculosis/Pages/default.aspx>. Accessed in June 2008.
- NIH. 2007. NIAID Research agenda, multidrug-resistant and extensively drug-resistant tuberculosis. National Institute of Health. p.16. Document web address as accessed in January 2011: <http://www.niaid.nih.gov/topics/tuberculosis/Research/Documents/mdrxdrresearchagenda.pdf>.
- Niimi M. 2010. Characterization of the multi-drug efflux systems of pathogenic fungi using functional hyperexpression in *Saccharomyces cerevisiae*. *Nippon Ishinkin Gakkai Zasshi* 51(2):79-86.
- Nolan KB. 1986. Spectroscopic models for cytochrome-P-450 derivatives – hyperporphyrin spectra in thiolatoiron(III)-porphyrin complexes. *Journal of the Royal Society of Chemistry* (10):760-762.
- Ogura H, Nishida CR, Hoch UR, Perera R, Dawson JH, de Montellano PRO. 2004. EpoK, a cytochrome P450 involved in biosynthesis of the anticancer agents epothilones A and B. Substrate-mediated rescue of a P450 enzyme. *Biochemistry* 43(46):14712-14721.
- Omura T. 2010. Structural diversity of cytochrome P450 enzyme system. *Journal of Biochemistry* 147(3):297-306.
- Omura T, Sato R. 1962. A new cytochrome in liver microsomes. *Journal of Biological Chemistry* 237(4):1375.
- Ortiz de Montellano PR. 2005. *Cytochrome P450 Structure, Mechanism, and Biochemistry*. Ortiz de Montellano PR, Ed. New York, U.S.A.: Kluwer Academic/ Plenum Publishers. p.689.
- Ortiz de Montellano PR. 2010. Hydrocarbon hydroxylation by cytochrome P450 enzymes. *Chemical Reviews* 110(2):932-48.
- Ortiz de Montellano PR, De Voss JJ. 2002. Oxidizing species in the mechanism of cytochrome P450. *Natural Product Reports* 19(4):477-493.
- Oshima R, Fushinobu S, Su F, Zhang L, Takaya N, Shoun H. 2004. Structural evidence for direct hydride transfer from NADH to cytochrome P450nor. *Journal of Molecular Biology* 342(1):207-217.
- Ost TW, Miles CS, Munro AW, Murdoch J, Reid GA, Chapman SK. 2001. Phenylalanine 393 exerts thermodynamic control over the heme of flavocytochrome P450 BM3. *Biochemistry* 40(45):13421-9.
- Ouellet H, Guan SH, Johnston JB, Chow ED, Kells PM, Burlingame AL, Cox JS, Podust LM, Ortiz de Montellano PR. 2010. *Mycobacterium tuberculosis* CYP125A1, a steroid C27 monooxygenase that detoxifies intracellularly generated cholest-4-en-3-one. *Molecular Microbiology* 77(3):730-742.
- Ouellet H, Kells PM, Ortiz de Montellano PR, Podust LM. 2011. Reverse type I inhibitor of *Mycobacterium tuberculosis* CYP125A1. *Bioorganic and Medicinal Chemistry Letters* 21(1):332-337.
- Ouellet H, Lang J, Couture M, Ortiz de Montellano PR. 2009. Reaction of *Mycobacterium tuberculosis* cytochrome P450 enzymes with nitric oxide. *Biochemistry* 48(5):863-872.
- Ouellet H, Podust LM, Ortiz de Montellano PR. 2008. *Mycobacterium tuberculosis* CYP130 - Crystal structure, biophysical characterization, and interactions with antifungal azole drugs. *Journal of Biological Chemistry* 283(8):5069-5080.
- Pande S, Galloway J, Gaur PM, Siddique KHM, Tripathi HS, Taylor P, MacLeod MWJ, Basandrai AK, Bakr A, Joshi S. 2006. Botrytis grey mould of chickpea: a review of biology, epidemiology, and disease management. *Australian Journal of Agricultural Research* 57(11):1137-1150.
- Paoli M, Marles-Wright J, Smith A. 2002. Structure–function relationships in heme-proteins. *DNA and Cell Biology* 21(4):271-280.
- Pasqualotto AC, Thiele KO, Goldani LZ. 2010. Novel triazole antifungal drugs: Focus on isavuconazole, ravuconazole and albaconazole. *Current Opinion in Investigational Drugs* 11(2):165-174.
- Perera R, Dawson JH. 2004. Modeling heme protein active sites with the his93gly cavity mutant of sperm whale myoglobin: complexes with nitrogen-, oxygen- and sulfur-donor proximal ligands. *Journal of Porphyrins and Phthalocyanines* 8(1-3):246-254.
- Perera R, Sono M, Sigman JA, Pfister TD, Lu Y, Dawson JH. 2003. Neutral thiol as a proximal ligand to ferrous heme iron: Implications for heme proteins that lose cysteine thiolate ligation on reduction. *Proceedings of the National Academy of Sciences of the United States of America* 100(7):3641-3646.
- Peto HM, Pratt RH, Harrington TA, LoBue PA, Armstrong LR. 2009. Epidemiology of extrapulmonary tuberculosis in the United States, 1993-2006. *Clinical Infectious Diseases* 49(9):1350-1357.
- Pietila MP, Vohra PK, Sanyal B, Wengenack NL, Raghavakaimal S, Thomas CF, Jr. 2006. Cloning and characterization of CYP51 from *Mycobacterium avium*. *American Journal of Respiratory Cell and Molecular Biology* 35(2):236-242.

- Podust LM, Poulos TL, Waterman MR. 2001a. Crystal structure of cytochrome P450 14 alpha-sterol demethylase (CYP51) from *Mycobacterium tuberculosis* in complex with azole inhibitors. Proceedings of the National Academy of Sciences of the United States of America 98(6):3068-3073.
- Podust LM, Stojan J, Poulos TL, Waterman MR. 2001b. Substrate recognition sites in 14 alpha-sterol demethylase from comparative analysis of amino acid sequences and X-ray structure of *Mycobacterium tuberculosis* CYP51. Journal of Inorganic Biochemistry 87(4):227-235.
- Podust LM, von Kries JP, Eddine AN, Kim Y, Yermalitskaya LV, Kuehne R, Ouellet H, Warriar T, Altekoester M, Lee J-S. 2007. Small-molecule scaffolds for CYP51 inhibitors identified by high-throughput screening and defined by x-ray crystallography. Antimicrobial Agents and Chemotherapy 51(11):3915-3923.
- Podust LM, Yermalitskaya LV, Lepesheva GI, Podust VN, Dalmasso EA, Waterman MR. 2004. Estriol bound and ligand-free structures of sterol 14 alpha-demethylase. Structure 12(11):1937-1945.
- Poulos TL. 2005. Intermediates in P450 catalysis. Philosophical Transactions of the Royal Society A-Mathematical Physical and Engineering Sciences 363(1829):793-806.
- Poulos TL, Finzel BC, Howard AJ. 1987a. High-resolution crystal structure of cytochrome-P-450CAM. Journal of Molecular Biology 195(3):687-700.
- Poulos TL, Howard AJ. 1987b. Crystal structures of metyrapone-inhibited and phenylimidazole-inhibited complexes of cytochrome-P-450CAM. Biochemistry 26(25):8165-8174.
- Prince RC, Bashford CL, Takamiya K, Vandenberg WH, Dutton PL. 1978. 2nd order kinetics of reduction of cytochrome c_2 by ubiquinone cytochrome $b-c_2$ oxidoreductase of *Rhodospseudomonas sphaeroides*. Journal of Biological Chemistry 253(12):4137-4142.
- Qamra R, Mande SC, Coates ARM, Henderson B. 2005. The unusual chaperonins of *Mycobacterium tuberculosis*. Tuberculosis 85(5-6):385-394.
- Ranson NA, White HE, Saibil HR. 1998. Chaperonins. Biochemical Journal 333:233-242. Need part number
- Rendic S, Guengerich FP. 2010. Update information on drug metabolism systems-2009, Part II. Summary of information on the effects of diseases and environmental factors on human cytochrome P450 (CYP) enzymes and transporters. Current Drug Metabolism 11(1):4-84.
- Rezen T, Debeljak N, Kordis D, Rozman D. 2004. New aspects on lanosterol 14 alpha-demethylase and cytochrome p450 evolution: Lanosterol/cycloartenol diversification and lateral transfer. Journal of Molecular Evolution 59(1):51-58.
- Rittle J, Green MT. 2010. Cytochrome P450 Compound I: Capture, characterization, and C-H bond activation kinetics. Science 330(6006):933-937.
- Rittle J, Younker JM, Green MT. 2010. Cytochrome P450: The active oxidant and its spectrum. Inorganic Chemistry 49(8):3610-3617.
- Rivers EC, Mancera RL. 2008. New anti-tuberculosis drugs in clinical trials with novel mechanisms of action. Drug Discovery Today 13(23-24):1090-1098.
- Rost B, Yachdav G, Liu JF. 2004. The PredictProtein server. Nucleic Acids Research 32:w321-w326.
- Rozman D, Fink M, Fimia GM, Sassone-Corsi P, Waterman MR. 1999. Cyclic adenosine 3',5' -monophosphate(cAMP)/cAMP-responsive element modulator (CREM)-dependent regulation of cholesterologenic lanosterol 14 alpha-demethylase (CYP51) in spermatids. Molecular Endocrinology 13(11):1951-1962.
- Rozman D, Sassone-Corsi P, Stromstedt M, Waterman MR. 1997. Expression of the lanosterol 14 alpha-demethylase (CYP51) during spermatogenesis: cAMP-dependent and cAMP-independent regulation. FASEB Journal 11(9):a818-a818.
- Rozman D, Stromstedt M, Waterman MR. 1996. The three human cytochrome P450 lanosterol 14 alpha-demethylase (CYP51) genes reside on chromosomes 3, 7, and 13: Structure of the two retrotransposed pseudogenes, association with a line-1 element, and evolution of the human CYP51 family. Archives of Biochemistry and Biophysics 333(2):466-474.
- Rozman D, Waterman MR. 1998. Lanosterol 14 alpha-demethylase (CYP51) and spermatogenesis. Drug Metabolism and Disposition 26(12):1199-1201.
- Sabri M. 2007. Biochemical characterization of the *Mycobacterium tuberculosis* cytochrome P450 (CYP51B1) and its redox partner (FprA). PhD thesis, The University of Manchester. p.319.
- Sakagami Y. 2010. Antifungal drugs mode of action and recent development. Combating Fungal Infections: Problems and Remedy. Springer-Verlag, Berlin, Germany, Book chapter p.99-107.
- Sakurai H, Tsuchiya K, Sugasaki N, Shibuya M. 1990. Unusual hyperporphyrin spectrum by bis(glutathione dimethyl ester)-heme complex, a model of cytochrome-P-450-thiolate complexes. Biochemical and Biophysical Research Communications 169(1):22-29.
- Sales MDU. 2009. Aspergillosis: from diagnosis to treatment. Jornal Brasileiro De Pneumologia 35(12):1238-1244.
- Salvado M, Garcia-Vidal C, Vazquez P, Riera M, Rodriguez-Carballeira M, Martinez-Lacasa J, Cuchi E, Garau J. 2010. Mortality of tuberculosis in very old people. Journal of the American Geriatrics Society 58(1):18-22.

- Sanglard D, Ischer F, Koymans L, Bille J. 1998. Amino acid substitutions in the cytochrome P-450 lanosterol 14 α -demethylase (CYP51A1) from azole-resistant *Candida albicans* clinical isolates contribute to resistance to azole antifungal agents. *Antimicrobial Agents & Chemotherapy* 42(2):241-53.
- Sanglard D, Ischer F, Parkinson T, Falconer D, Bille J. 2003. *Candida albicans* mutations in the ergosterol biosynthetic pathway and resistance to several antifungal agents. *Antimicrobial Agents and Chemotherapy* 47(8):2404-2412.
- Sasseti CM, Boyd, D.H. and Rubin, E.J. 2003. Genes required for mycobacterial growth defined by high density mutagenesis. *Molecular Microbiology* 48(1):77-84.
- Schenkman JB. 1970. Studies on nature of type-I and type-II spectral changes in liver microsomes. *Biochemistry* 9(10):2081.
- Schenkman JB, Moldeus P, Orrenius S, Kraschni.R, Cinti DL. 1972. Nature o reverse type I (modified type II) spectral change in liver microsomes. *Biochemistry* 11(23):4243.
- Schlichting I, Berendzen J, Chu K, Stock AM, Maves SA, Benson DE, Sweet BM, Ringe D, Petsko GA, Sligar SG. 2000. The catalytic pathway of cytochrome P450cam at atomic resolution. *Science* 287(5458):1615-1622.
- Scullion J. 2003. Tuberculosis and older people. *Nursing Older People* 15(3):23-7.
- Semba RD, Darnton-Hill I, de Pee S. 2010. Addressing tuberculosis in the context of malnutrition and HIV coinfection. *Food and Nutrition Bulletin* 31(4):s345-s364.
- Seward HE, Roujeinikova A, McLean KJ, Munro AW, Leys D. 2006. Crystal structure of the *Mycobacterium tuberculosis* P450 CYP121-fluconazole complex reveals new azole drug-P450 binding mode. *Journal of Biological Chemistry* 281(51):39437-43.
- Shaik S, Hirao H, Kumar D. 2007. Reactivity of high-valent iron-oxo species in enzymes and synthetic reagents: A tale of many states. *Accounts of Chemical Research* 40(7):532-542.
- Shaik S, Kumar D, de Visser SP, Altun A, Thiel W. 2005. Theoretical perspective on the structure and mechanism of cytochrome P450 enzymes. *Chemical Reviews* 105(6):2279-2328.
- Shi WN, Chen ZZ, Chen X, Cao LL, Liu P, Sun SJ. 2010. The combination of minocycline and fluconazole causes synergistic growth inhibition against *Candida albicans*: an in vitro interaction of antifungal and antibacterial agents. *FEMS Yeast Research* 10(7):885-893.
- Sinclair PR, Gorman N, Jacobs JM. 2001. Measurement of heme concentration. *Current Protocols in Toxicology*: John Wiley and Sons, Inc. p831-837.
- Sligar SG. 2010. Glimpsing the critical intermediate in cytochrome P450 oxidations. *Science* 330(6006):924-925.
- Smulevich G, Bjerrum MJ, Gray HB, Spiro TG. 1994. Resonance Raman-spectra and the active-site structure of semisynthetic Met80Cys horse heart cytochrome-C. *Inorganic Chemistry* 33(21):4629-4634.
- Sohaskey CD. 2008. Nitrate enhances the survival of *Mycobacterium tuberculosis* during inhibition of respiration. *Journal of Bacteriology*. 190(8):2981-2986.
- Sono M, Dawson JH. 1982. Formation of low-spin complexes of ferric cytochrome P-450-CAM with anionic ligands – spin state and ligand affinity comparison to myoglobin. *Journal of Biological Chemistry* 257(10):5496-5502.
- Soubani AO, Chandrasekar PH. 2002. The clinical spectrum of pulmonary aspergillosis. *Chest* 121(6):1988-1999.
- Stammler G, Cordero J, Koch A, Semar M, Schlehuber S. 2009. Role of the Y134F mutation in CYP51 and overexpression of CYP51 in the sensitivity response of *Puccinia triticina* to epoxiconazole. *Crop Protection* 28(10):891-897.
- Stergiopoulos I, Van Nistelrooy JGM, Kema GHJ, De Waard MA. 2003. Multiple mechanisms account for variation in base-line sensitivity to azole fungicides in field isolates of *Mycosphaerella graminicola*. *Pest Management Science* 59(12):1333-1343.
- Stewart GR, Wernisch L, Stabler R, Mangan JA, Hinds J, Laing KG, Young DB, Butcher PD. 2002. Dissection of the heat-shock response in *Myobacterium tuberculosis* using mutants and microarrays. *Microbiology* 148(10):3129-3138.
- Stout CD. 2004. Cytochrome P450 conformational diversity. *Structure* 12(11):1921-1922.
- Stromstedt M, Keeney DS, Waterman MR, Paria BC, Conley AJ, Dey SK. 1996a. Preimplantation mouse blastocysts fail to express CYP genes required for estrogen biosynthesis. *Molecular Reproduction and Development* 43(4):428-436.
- Stromstedt M, Rozman D, Waterman MR. 1996b. The ubiquitously expressed human CYP51 encodes lanosterol 14 α -demethylase, a cytochrome P450 whose expression is regulated by oxysterols. *Archives of Biochemistry and Biophysics* 329(1):73-81.
- Stromstedt M, Waterman MR, Haugen TB, Tasken K, Parvinen M, Rozman D. 1998. Elevated expression of lanosterol 14 α -demethylase (CYP51) and the synthesis of oocyte meiosis-activating sterols in postmeiotic germ cells of male rats. *Endocrinology* 139(5):2314-2321.
- Strushkevich N, Usanov SA, Park H-W. 2010. Structural basis of human CYP51 inhibition by antifungal azoles. *Journal of Molecular Biology* 397(4):1067-1078.

- Takahata S, Okutomi T, Ohtsuka K, Hoshiko S, Uchida K, Yamaguchi H. 2005. *In vitro* and *in vivo* antifungal activities of FX0685, a novel triazole antifungal agent with potent activity against fluconazole-resistant *Candida albicans*. *Medical Mycology* 43(3):227-233.
- Tala-Heikkila M. 2002. Is the BCG--*Bacillus Calmette-Guerin* transferred to history? *Duodecim* 118(1):89-90.
- Thompson JD, Higgins DG, Gibson TJ. 1994. Clustal-W – Improving the sensitivity of progressive multiple sequence alignment through sequence weighting, position-specific gap penalties and weight matrix choice. *Nucleic Acids Research* 22(22):4673-4680.
- Tomioka H, Namba K. 2006. Development of antituberculous drugs: Current status and future prospects. *Kekkaku* 81(12):753-774.
- Toth A, Fackelmann J, Pigott W, Tolomeo O. 2004. Tuberculosis prevention and treatment. *The Canadian Nurse* 100(9):27-30.
- Trocha PJ, Sprinson DB. 1976. Location and regulation of early enzymes of sterol biosynthesis in yeast. *Archives of Biochemistry and Biophysics* 174(1):45-51.
- Trzaskos J, Kawata S, Gaylor JL. 1986. Microsomal enzymes of cholesterol biosynthesis – purification of lanosterol 14-alpha-methyl demethylase cytochrome-P-450 from hepatic microsomes. *Journal of Biological Chemistry* 261(31):4651-4657.
- von Heijne G. 1992. Membrane-protein structure prediction – hydrophobicity analysis and the positive-inside rule. *Journal of Molecular Biology* 225(2):487-494.
- Wadsworth C. 2008. Disease carriers bacteria: *Mycobacterium tuberculosis*. <http://www.wadsworth.org/databank/mycotubr.htm>. New York: New York State Department of Health. Accessed in November 2010.
- Walburger A, Koul A, Ferrari G, Nguyen L, Prescianotto-Baschong C, Huygen K, Klebl B, Thompson C, Bacher G, Pieters J. 2004. Protein kinase G from pathogenic mycobacteria promotes survival within macrophages. *Science* 304(5678):1800-1804.
- Wang HP, Kong FR, Sorrell TC, Wang B, McNicholas P, Pantarat N, Ellis D, Xiao M, Widmer F, Chen SCA. 2009. Rapid detection of ERG11 gene mutations in clinical *Candida albicans* isolates with reduced susceptibility to fluconazole by rolling circle amplification and DNA sequencing. *BMC Microbiology* 9(167):1-12.
- Wang J, Xing Z. 2002. Tuberculosis vaccines: the past, present and future. *Expert Reviews of Vaccines* 1(3):341-54.
- Wang M, Roberts DL, Paschke R, Shea TM, Masters BSS, Kim JJP. 1997. Three-dimensional structure of NADPH-cytochrome P450 reductase: Prototype for FMN- and FAD-containing enzymes. *Proceedings of the National Academy of Sciences of the United States of America* 94(16):8411-8416.
- Warrilow AGS, Martel CM, Parker JE, Melo N, Lamb DC, Nes WD, Kelly DE, Kelly SL. 2010a. Azole binding properties of *Candida albicans* sterol 14-alpha demethylase (CaCYP51). *Antimicrobial Agents and Chemotherapy* 54(10):4235-4245.
- Warrilow AGS, Melo N, Martel CM, Parker JE, Nes WD, Kelly SL, Kelly DE. 2010b. Expression, purification, and characterization of *Aspergillus fumigatus* sterol 14-alpha demethylase (CYP51) isoenzymes A and B. *Antimicrobial Agents and Chemotherapy* 54(10):4225-4234.
- Waterman MR, Lepesheva GI. 2002. CYP51 structure/function relationships in different phyla. *Drug Metabolism Reviews* 34(1):8-8.
- Waterman MR, Lepesheva GI. 2005. Sterol 14 alpha-demethylase, an abundant and essential mixed-function oxidase. *Biochemical and Biophysical Research Communications* 338(1):418-422.
- Wells AV, Li PS, Champion PM, Martinis SA, Sligar SG. 1992. Resonance Raman investigations of *Escherichia coli* expressed *Pseudomonas putida* cytochrome-P450 and cytochrome-P420. *Biochemistry* 31(18):4384-4393.
- White TC. 1997. The presence of an R467K amino acid substitution and loss of allelic variation correlate with an azole-resistant lanosterol 14-alpha demethylase in *Candida albicans*. *Antimicrobial Agents and Chemotherapy* 41(7):1488-94.
- WHO. 2007. Tuberculosis fact sheet N°104 - Global and regional incidence. <http://www.who.int/mediacentre/factsheets/fs104/en/>. World Health Organisation. Accessed in March 2008.
- WHO. 2010a. Multidrug and extensively drug-resistant TB (M/XDR-TB): 2010 Global report on surveillance and response. <http://www.who.int/tb/publications/2010/978924599191/en/index.html>. p.71. Accessed in February 2011.
- WHO. 2010b. Tuberculosis fact sheet N°104. <http://www.who.int/mediacentre/factsheets/fs104/en/>. World Health Organization. Accessed in January 2011.
- Williams PA, Cosme J, Sridhar V, Johnson EF, McRee DE. 2000. Mammalian microsomal cytochrome P450 monooxygenase: Structural adaptations for membrane binding and functional diversity. *Molecular Cell* 5(1):121-131.
- Wurtele H, Tsao S, Lepine G, Mullick A, Tremblay J, Drogaris P, Lee EH, Thibault P, Verreault A, Raymond M. 2010. Modulation of histone H3 lysine 56 acetylation as an antifungal therapeutic strategy. *Nature Medicine* 16(7):774-780.

- Xu Y, Chen L, Li C. 2008. Susceptibility of clinical isolates of *Candida* species to fluconazole and detection of *Candida albicans* ERG11 mutations. *Journal of Antimicrobial Chemotherapy* 61(4):798-804.
- Xu J, Saunders CW, Hu P, Grant RA, Boekhout T, Kuramae EE, Kronstad JW, DeAngelis YM, Reeder NL, Johnstone KR. 2007. Dandruff-associated *Malassezia* genomes reveal convergent and divergent virulence traits shared with plant and human fungal pathogens. *Proceedings of the National Academy of Sciences of the United States of America* 104(47):18730-18735.
- Yamanouchi K, Eguchi S, Takatsuki M, Hidaka M, Kamohara Y, Miyazaki K, Hamasaki K, Tajima Y, Kanematsu T. 2010. Management of fungal colonization and infection after living donor liver transplantation. *Hepato-Gastroenterology* 57(101):852-857.
- Yan L, Yang Q, Zhou Y, Duan X, Ma Z. 2009. A real-time PCR assay for quantification of the Y136F allele in the CYP51 gene associated with *Blumeria graminis* f.sp tritici resistance to sterol demethylase inhibitors. *Crop Protection* 28(5):376-380.
- Yang XX, Dubnau E, Smith I, Sampson NS. 2007. *Rv1106c* from *Mycobacterium tuberculosis* is a 3 beta-hydroxysteroid dehydrogenase. *Biochemistry* 46(31):9058-9067.
- Yano JK, Koo LS, Schuller DJ, Li HY, Ortiz de Montellano PR, Poulos TL. 2000. Crystal structure of a thermophilic cytochrome P450 from the archaeon *Sulfolobus solfataricus*. *Journal of Biological Chemistry* 275(40):31086-31092.
- Yoshida Y, Aoyama Y, Noshiro M, Gotoh O. 2000. Sterol 14-demethylase P450 (CYP51) provides a breakthrough for the discussion on the evolution of cytochrome P450 gene superfamily. *Biochemical and Biophysical Research Communications* 273(3):799-804.
- Yoshida Y, Noshiro M, Aoyama Y, Kawamoto T, Horiuchi T, Gotoh O. 1997. Structural and evolutionary studies on sterol 14-demethylase P450 (CYP51), the most conserved P450 monooxygenase .2. Evolutionary analysis of protein and gene structures. *Journal of Biochemistry* 122(6):1122-1128.
- Yuan Y, Crane DD, Simpson RM, Zhu YQ, Hickey MJ, Sherman DR, Barry CE. 1998. The 16-kDa alpha-crystallin (Acr) protein of *Mycobacterium tuberculosis* is required for growth in macrophages. *Proceedings of the National Academy of Sciences of the United States of America* 95(16):9578-9583.
- Zager EM, McNERNEY R. 2008. Multidrug-resistant tuberculosis. *BMC Infectious Diseases* 8(10):1-5.
- Zanno A, Kwiatkowski N, Vaz ADN, Guardiola-Diaz HM. 2005. MT FdR: a ferredoxin reductase from *M. tuberculosis* that couples to MT CYP51. *Biochimica et Biophysica Acta-Bioenergetics* 1707(2-3):157-169.
- Zanoni BC, Phungula T, Zanoni HM, France H, Feeney ME. 2011. Impact of tuberculosis cotreatment on viral suppression rates among HIV-positive children initiating HAART. *AIDS* 25(1):49-55.
- Zarn JA, Bruschweiler BJ, Schlatter JR. 2003. Azole fungicides affect mammalian steroidogenesis by inhibiting sterol 14 α -demethylase and aromatase. *Environmental Health Perspectives* 111(3):255-261.
- Zhang Y, Post-Martens K, Denkin S. 2006. New drug candidates and therapeutic targets for tuberculosis therapy. *Drug Discovery Today* 11(1-2):21-27.
- Zhang Y, Scorpio A, Nikaido H, Sun ZH. 1999. Role of acid pH and deficient efflux of pyrazinoic acid in unique susceptibility of *Mycobacterium tuberculosis* to pyrazinamide. *Journal of Bacteriology* 181(7):2044-2049.
- Zhang YQ, Gamarra S, Garcia-Effron G, Park S, Perlin DS, Rao R. 2010. Requirement for ergosterol in V-ATPase function underlies antifungal activity of azole drugs. *PLoS Pathogens* 6(6):e1000939.
- Zwiers LH, Stergiopoulos I, Van Nistelrooy JGM, De Waard MA. 2002. ABC transporters and azole susceptibility in laboratory strains of the wheat pathogen *Mycosphaerella graminicola*. *Antimicrobial Agents and Chemotherapy* 46(12):3900-3906.

8 APPENDICES

Appendix A – Summary of CYP51B1 WT and Mutants Experimental Analysis

Table 8.1: Summary of experimental analysis on WT and fluconazole-resistant CYP51B1 mutants performed in this PhD thesis.

Analysis	Ligands/ comments	WT	F89H	L100F	G388S	R391K
CD	Far UV					
	Near UV-Vis					
MALLS	Ligand-free					
	Clotrimazole					
DSC	Ligand-free					
	4PI, 2 mM					
	Fluc, 0.1 mM					
	Estriol					
	DMSO					
	EPBA					
Thiolate-thiol	PDA					
CO binding quantitative	P450 collapse rate					
NO binding qualitative	Fe(III)+NO					
CO trap +estriol +CO ($k=\ln(2)/t_1$) k =rate of P450 formation t_1 =half life of P450	FprA + Fdr + Fd2***	at 7.5 min	...at 15 min	... at 6 min	P420 only	...at 13 min
	FprA + Fdr + Fd1	at 4.5 min				
	FprA+ Fdr	at 6 min			No estriol added P420 only	
	FprA + Fd1	no P450 until Fd2+Fdr was added**				
	FprA + Fd2	no P450 until Fdr was added***			P420 only	P420 only
	FprA + Fd1 + Fd2 + Fdr**	at 7.5 min				
Redox potentiometry	Ligand-free (mV)					
Crystallisation screens - trials	Ligand-free					
	Co-crystals					
Structure	Ligand-free					
	EPBA	2.3 Å	2.0 Å	1.8 Å		1.8 Å
	4PI	1.5 Å	1.4 Å			1.7 Å
Redox cycle	Anaerobic					
	Nanodrop					
EPR	Post-redox					
	Ligand-free					
	Clotrimazole					
	4PI					
	Voriconazole					
Estriol+Fe(III) → +Na ₂ S ₂ O ₄	Estriol-Fe(II) adduct					

Pyridine hemochromogen	Ligand-free					
Stopped-flow analysis	Fluconazole					
	Voriconazole					
	Clotrimazole					
	Econazole					
	Miconazole					
	PDA-Fluc					
	PDA-Estriol					
Equilibrium titrations	4-PI					
	EPBA					
	Fluconazole					
	Voriconazole					
	Clotrimazole					
	Econazole					
	Miconazole					
	Ketoconazole					
Estriol						

	= Experiments completed for all mutants and WT
	= Experiments completed for some mutants
	= Experiments not carried out

Appendix B – Brief Genomics and Proteomics Summary of CYP51B1, CYP123 and CYP136

Table 8.2: Potential P450 drug target proteins from Mtb worked on 2008-2011 in this thesis.

	CYP51B1	CYP136	CYP123
Gene name	<i>Rv0764c</i>	<i>Rv3059</i>	<i>Rv0766c</i>
Gene length	1356 bp	1479 bp	1209 bp
Protein length	451 a.a.	492 a.a.	402 a.a.
Location on H37Rv	858.04 kb	3419.49 kb	860.07 kb
Molecular Mass	50877 Da	56227 Da	45421 Da
Isoelectric point	5.70	7.00	5.31
Function – functional comments	Sterol 14-alpha demethylase	Unknown – intermediary metabolism and respiration	Unknown – intermediary metabolism and respiration
Gene essentiality	non essential gene by Himar1-based transposon mutagenesis in H37Rv and CDC1551 strains (Sasseti et al., 2003 and Lamichhane et al., 2003).	non essential gene by Himar1-based transposon mutagenesis in H37Rv and CDC1551 strains (Sasseti et al., 2003 and Lamichhane et al., 2003).	non essential gene by Himar1-based transposon mutagenesis in CDC1551 strain (Lamichhane et al., 2003) and potential drug target (McLean et al., 2006)
Comments/ Transcriptome	Involved in sterol biosynthesis. Unknown precise biological substrate. Catalyses C14-demethylation of lanosterol, 24,25-dihydrolanosterol and obtusifoliol. First reaction is critical for yeast ergosterol biosynthesis. It transforms lanosterol into 4,4'-dimethyl cholesta-8,14,24-triene-3-beta-ol.	Similar to other cytochrome P450-dependent oxidases	mRNA identified by DNA microarray analysis and up-regulated at high temperatures (Stewart et al., 2002). DNA microarrays show lower level of expression in H37Rv than in <i>phoP</i> (<i>Rv0757</i>) mutant (Walters et al., 2006).
BLASTp results	14-alpha sterol demethylase CYP51	>25% amino acid identity to CYP51 from <i>Plesiocystis pacifica</i> (marine slimebacteria), lanosterol 14-alpha demethylase from <i>Rattus norvegicus</i> (rat) and <i>Mus musculus</i> (mouse)	Heme-thiolate proteins. 31% amino acid identity to CYP126
Coding sequence	atgagcgtgtgactacccgggttccgggtggccacgacgaacacggc cacctcaggagttccgaccgatccgatcgggctgatgcaacgggtccg gacgaatgacggagacgtcgttacctccagctggcgggaagcaggtcgt gctgctgtccggctcgcacgccaacgaattcttctccgggcgggcgacga cgacctggaccaggccaaggcataccgttcacgacccgatcttcggcga ggcgctggtgttcgacgccagcccgaacggcgtaaagagatgctgcaca atgccgcgtacgcccggcgagcagatgaagggccacgctgccaccatcgaa	atggcgacgatccaccccgccatacctccttgaccaagccaagcgtcgc ttcacgccgtcgtcaacaacttccggcatgagcttgcgaacacatgct gctgaacaccaaattccggagaagaactcgcgaaccgccgaggca gccccgtcaagccggtcgtcggtagcgcgggctgccatccttgggcac atgatcgagatgttcgcccggaccggactatctgatgttcctgtacaaga cgaagggtccggtcgtattcggcgactcagctgtcgtccgggtgtcgcag cactgggcctgacgcccggcgaggtcatctactccaaccgcaacaaggact	atgaccgtccgctcggtagccccaactggtcctggaccctacgactac gactttcacgaagaccgtaccgtattatcgtcggctcgggacgaggcc ccgctgtaccgtaacgaggaacgaatttctggcgggtcgcggcaccac gacgtgctcaaggctcgggacagcagcggcgtgtcgaatgcctatggg gtatccctggatccgtctcagcacttctgaggcgtaccgggtaatgtcga tgctggccatggacaccccacatctcgggatgctaccttgggtcca agggttcacccacggcgatccgtgaactcgagccgaggtgctcgaa

	<p>gatcaagtccgacggatgatcgccgactggggtagggccggcgagatcga tctgctggacttcttccgagctgacctctacacctctccggcctgcctga tcggcaagaagtccgacgacctcgcagggcgattcccaagctctatc acgagttggagcgcggcaccgaccactagcctacgtcaccgctatctgc cgatcgagagcttccgtcggcgcgacaagcccgaatggtctggggcac tggttcggacatcatgaacggcggatcgcaacccaccaccgacaag agcgaccgtgacatgctcagctgctcctcgcctgaaggtgagaccggc actccccggttctcggccgacgagatcaccggcatggtcctcctgatgatt cgccggccatcacaccagctcgggtacggcttcgtggacgctgatcgagtt gatgacctcgcgacgctacgcgccgtgacgacgaactcagcagc tgtacggcgacggcctgctgagtttccatgcgctgcgacgattccgc agctggaaaacgtctgaaagagacgctgcctgcacccctcctgctgatca tctcatcgagtgccaaggcgagttcaggtgcaagccaccggattc atgagggcgtatggtggcgccctccccggcgtatccaaccggatccccg aagactccccgatccccagacttctgcccagcagatacagcagccgc ggcaggaagatctgctcaaccgctggagctggattccgttcggcgccggcc ggcatcgttgcgtggggggcgcttccatcatcgatcaaaagcattct ctcggtgttgcgcgagatgagttgagatggcgcaaccgccaagaagc tatcgtaacgaccattcaagatggtggtcagttggccagcccgttgcg tgcgctaccgcccgaacgggagtttaa</p>	<p>actcgacgagggtgggtgccctgatcgccctcttccaccgccc tgatgctgctcgaactcgaagacacatgttccaccgacggatcatgcagga ggcgttcgctccggctcagggctcggcgtacctcagcagatggacagggg cgtctcgggggtgctcggcagcactggctcgaacgacgacgcttct tgtctaccggccatgaaggcgtcagcctgacatgctcgtgatgcttca tggggcacgaacccggcaccgatcacgaactggcaccgaaggtgaacaag gcttcacgattaccaccgtgcccggcaacgctgatccgaccagcgtg ccaccgtcacctgggtggcagggactcgcagcagcagctgctggaaaa ctactcaccgcccaggtcaaaagcgcggcgaagcgtcggggcaacgacc tgctgacgggtgtgtccagaccgaagacgacgacggcaaccgggtctccg acgccacatcgtcaaccacatgatcttctgatgatggcccccacgatac ctcagcgtcaacggccacgacgatggcctaccagctggcccaccggg aatggcagcagcgtgcccgcgacgaatcgaccggcagcagcagggcc gctcgacatcgaatccttagagcagctggatcgtcagctggtgatgaa cgagtcgatccggttggtagcggcgtccagtgggcagcagcaggg tgcgcgataccgaactgctgggctactacctaccaaggccaccaacgtga tcgcataccagggatgaatcatcgctcgggaaactggacagaccgc tgacattcgaccggaacggtttaccgagcggcgcacagcagcacaagcgg caccgctatgcttcacgcttccggcggcggcgtgcacaagtgatcggg atggtgttgcacaatggagataaagacatcctgcaccggctgctgcgc gctaccggctggagctgtcccgtcccactaccagccccgctgggactaca gtgccatgccatcccgatggacgggatccgatgctgctgctccaggt ag</p>	<p>cttggccgattcacctggattcggccctgcaaacgaaagtctcattcgt agcagaattcgtggcaagctgcccgatggatgtgattcagagctgataggc gtccccgacaccgaccggcccgcacccgctggccgatgctgggtgc tgaccgagggacggcgtggccgatgtccccccggcggatggcggc gtcgatcgagctgatgagatattacgctgacctgatcggaattccggcg gcccggcgaacaactctgacgtcggcactgctggcagccgagctcgacg gcgaccggcttccgaccaggaatcatggcgttctgttctcatggtgatc ggcccaacagacaccaccaagctactggccaatgcccgtctactggggc cgcccaccacctggcagctggccgctgattcggcaccactcccggga ttccgatgtgggtggaggaaacctgcgctacgacacgtccagccagattc tggcccgcaccgtcgcgacgatctcagttgtacgacaccagatccccg agggtgaggtgtgctgctaccgggatcgccaaccgtgacaccgg gtgttcgacgaccggcagactatcgatcgccgcgaaatcggtgcaa actagtcagttcggcagcgggtcccacttctgctgctggggctcactggcc cggatggaagcccgggtggcctggggcgcgctgctgctcgatccgcaa ctcgaagtcgacgacgacaacgtcgtcgcgctcattccagcaactgctg cggatttcccctgcccgatcagcgtgagggccaggtaa</p>
<p>Protein sequence</p>	<p>MSAVALPRVSGHDEHGHLEEFRTDPIGLMQ RVRDECGDVGTFQLAGKQVLLSGSHANEFF FRAGDDDLQAKAYPFMTPIFGEGVVFDA ERRKEMLHNAALRGEQMKGHAATIEDQVRR MIADWGEAGEIDLLDFFAELTIYTSSACLIGK KFRDQLDGRFAKLYHELERTDPLAYVDPYL PIESFRRRDEARNGLVALVADIMNGRIANPPT DKSDRDMLDVLIAMKAETGTPRFSADIEITGM FISMMFAGHHTSSGTASWTLIELMRHRDAYAA VIDELDELYDGRSVSFHALRQIPQLENVLE TLRLHPPLIILMRVAKGEFEVQGHRIHEGLV AASPAINRIPEDFPDPHDFVPARYEQPRQED LLNRWTWIPFAGRHRCVGAFAIMQIKAFS VLLREYEFEMAQPPEYSYRNDHDKMVVQLAQP ACVRYRRRTGV</p>	<p>MATIHPPAYLLDQAKRRFTPSFNNFPGMSLVE HMLLNTKFPEKLAEPGGSLKPVVGDAGL PILGHMIEMLRGGPDYLMFLYKTKGPVVF SAVLPGVAAALGPDAAQVIYSNRNKDYSQQG WVPVIGPFFHRGLMLLDFFEEHMFHRRIMQEA FVRSRLAGYLEQMDRVVSRVADDWVND RFLVYPAMKALTDIASMVFMGHEPGTDHEL VTKVNKAFTITRAGNAVIRTSVPPFTWWRGL RARELLENYFTARVKERREASGNDLLTVLCQ TEDDDGNRFSADIVNHMIFLMAAHDSTSTS TATTMAYQLAAHPEWQQRCDSDRHGDGP LDIESLEQLESLLVMNESIRLVTPVQWAMRQ TVRDTELLGYYLPKGTNVIAYPGMNHRLPEI WTDPLTFDPERFTEPRNEHKRHRYAFTPGG GVHKCIGMVFDQLEIKTILHRLRRYRLELSR PDYQPRWDYSAMPIMDGMPIVLRPR</p>	<p>MTVRVGDPELVLDPYDYDFHEDPYPYRRLR DEAPLYRNEERNFWAVSRHHDVLQGRDST ALSNAYGVSLDPSRSTSEAYRVMMSMLAMDDP AHLRMRTLVSFGFTPRRIRELEPQVLELARIH LDSALQTESFDFVAEFAGKLPMDVISELIGVP DTRARIRALADAVLHREDGVADVPPPAMA ASIELMRYADLIAEFRRRPANNLTSALLAAEL DGDRLSDQEIMAFLLMVIAGNETTTKLLAN AVYWAAHHPGQLARVAFDHSRIPMWVEETL RYDTSSQILARTVAHDLTLYDTTPEGEVLLLL PGSANRDDRVDPPDDYRIGREIGCKLVSFG SGAHFCLGAHLARMEARVALGALLRRIRNYE VDDDNVVRVHSSNVRGFAHLPISVQAR</p>

Appendix C – DSC Data for CYP51B1 Variants

Table 8.3: Melting temperatures or transition midpoints (T_m), enthalpy or calorimetric heat change (ΔH) and van't Hoff heat change (ΔH_v) values.

CYP51B1	Ligands	T_m ($^{\circ}\text{C}$)	ΔH (kcal/mol) $\times 10^3$	ΔH_v (kcal/mol/ $^{\circ}\text{C}$) $\times 10^3$
WT	Ligand-free	49.40 \pm 0.65	10.0 \pm 5.43	19.20 \pm 3.16
		51.30 \pm 0.16	7.90 \pm 4.12	30.20 \pm 5.84
	Estriol	50.25 \pm 0.81	-10.9 \pm 4.61	16.3 \pm 1.57
		52.47 \pm 0.12	12.9 \pm 4.55	27.6 \pm 4.06
	Fluconazole	52.39 \pm 0.61	10.9 \pm 6.55	22.1 \pm 3.62
		54.14 \pm 0.19	8.28 \pm 5.06	33.4 \pm 7.69
	4-PI	49.29 \pm 0.71	8.60 \pm 4.42	19.0 \pm 2.55
		51.19 \pm 0.16	6.87 \pm 3.76	30.8 \pm 6.52
	EPBA	52.36 \pm 0.55	9.98 \pm 5.23	22.0 \pm 2.96
		54.15 \pm 0.19	8.14 \pm 4.26	31.2 \pm 6.07
DMSO	48.65 \pm 0.59	11.1 \pm 3.16	15.2 \pm 1.06	
	50.98 \pm 0.08	11.9 \pm 3.04	26.5 \pm 2.91	
F89H	Ligand-free	48.85 \pm 0.54	10.2 \pm 4.15	18.1 \pm 2.19
		51.01 \pm 0.12	12.5 \pm 3.52	26.3 \pm 2.78
	Fluconazole	51.35 \pm 0.73	11.3 \pm 6.87	19.5 \pm 3.5
		53.36 \pm 0.16	12.8 \pm 5.42	29.0 \pm 4.57
L100F	Ligand-free	47.85 \pm 0.61	-10.3 \pm 7.31	-18.7 \pm 4.51
		49.94 \pm 0.20	-11.5 \pm 5.38	-26.5 \pm 5.32
	Fluconazole	52.42 \pm 0.61	11.3 \pm 7.81	22.7 \pm 4.84
		54.25 \pm 0.20	12.4 \pm 5.83	30.6 \pm 5.41
G388S	Ligand-free	45.51 \pm 2.50	19.0 \pm 16.0	8.69 \pm 1.69
		45.62 \pm 0.29	45.1 \pm 16.9	12.5 \pm 1.84
		54.12 \pm 0.15	74.6 \pm 6.09	10.9 \pm 0.77
		58.30 \pm 0.10	17.6 \pm 3.61	27.7 \pm 3.19
R391K	Ligand-free	49.39 \pm 0.53	9.78 \pm 5.01	20.7 \pm 2.96
		51.24 \pm 0.16	9.32 \pm 3.96	29.5 \pm 4.40
	Fluconazole	51.97 \pm 0.67	11.7 \pm 5.45	18.1 \pm 2.09
		53.94 \pm 0.12	10.8 \pm 4.58	29.4 \pm 4.65
	4-PI	49.24 \pm 0.90	9.28 \pm 5.32	16.6 \pm 2.46
		51.34 \pm 0.12	11.6 \pm 4.44	26.8 \pm 3.68

Appendix D – Multiple Sequence Alignment of CYP51 Enzymes, CYP123 and CYP136

A. fumigatus-CYP51a	-----MVPMLWLTAYMAVAVLTAILLNNAVYQLFFRLWN-----RTE	36
A. fumigatus-CYP51b	MGLIAFILDGICKHCSTQSTWLVVGLLSSILAVSVIINVQLQLLQFN-----PHE	51
C. albicans-CYP51A1	---MAIVETVIDGINVFLSLSVTQQISILLGVPVYVNLVWQYLYSLR-----KDR	47
H. sapiens-CYP51	MLLLGLLQAGSGLVQGAMEKVTGGNLLSMLLIACAFVLSLVYLRLRAAGHLVQLPAGVKS	60
Mtb-CYP51B1	-----MSAVA	5
T. brucei-CYP51	-----MLLEVAIFLLTALALYSFYFVKSFNVTR-----PTD	31
Mtb-CYP136	MATIHPPAYLLDQAKRRFTPFSNNFPGMSLVHEMLLNTKFKPKLAAPP-----PGSLGK	55
Mtb-CYP123	-----MT	2
A. fumigatus-CYP51a	PPMVFWHPVPLGSTISYGDIPYKFFFAKREKYG-DIFTFILLGQKTTVVLGVQNEFILN	95
A. fumigatus-CYP51b	PPVVFHWPFFIGSTISYGDIPYKFFFDKRAKYG-DIFTFILLGKKTTVVLGKGNDFILN	110
C. albicans-CYP51A1	APLVFYWIPWFGSAASYGQQPYEFFESCROKYG-DVFSFMLLGGKIMTVVLGPKGHEFVN	106
H. sapiens-CYP51	PPYIFSPIFPLGHAIAFGKSPIEFLENAYEKYK-PVFSFTMVGKFTTYLLGSDAALLFN	119
Mtb-CYP51B1	LPRVSGGHEHGHLEEFRTDPIGLMQVRVDECG-DVGTFLQAGKQVLLSGSHANEFFFR	94
T. brucei-CYP51	PPVYVPTVPLGHIIQFGKSPGLGFMQCKRQLKSGIFTINIVGKRVTVIGDPHEHSRFLP	61
Mtb-CYP136	PVVGDAGLPLGHMIEMLRGGPDYLMFLYKTKG-PVVFGDSAVLPGVAALGPDAQAQVIYS	114
Mtb-CYP123	VRVGDPELVLDPDYDFHEDPYPYRRLRDEAP-LYRNEERNFVAWSRHHVLDVQGRDST	61
A. fumigatus-CYP51a	GKLDVNAEEVYSPLTTPVFGSDVYDCPNKSLMEQKFKIKYGLTQSALESHVPLIEKEV	155
A. fumigatus-CYP51b	GKLRDVCABEVYSPLETTVPVGRHVYDCPNAKLMQKFKVYGLTSDALRSYVPLITDVE	170
C. albicans-CYP51A1	AKLSDVSAEADYKHLTTPVFGKGVYDCPNRSLMEQKFKAFKALTTDSFKRYVPKIREEI	166
H. sapiens-CYP51	SKNEDLNAEDVYSRLTTPVFGKGVAYDVPNFVLEQKMLKSLGNI AHFKQHVSI IEKET	179
Mtb-CYP51B1	AGDDDLQAKAYP-FMTPIFGEGVVFDA SPERKE--MLHNAALRGEQMKGHAATIEDQV	121
T. brucei-CYP51	PRNEVLSPREVYS-FMVPVFGEGVAYAAPYPRMREQLNFLAEELTIAKFNQVPAIQHEV	150
Mtb-CYP136	NRNKDYSQ-QGWVPVIGPFFHRGLMLLDFEHHMFHR-RIMQEA FVRSRLAGYLEQMDRVV	172
Mtb-CYP123	ALSNAYGVSLEDPSSRTSEAYRVMSMLAMDDPAHLRMRITLVSKGFTPRRIRLEPQVLELA	121
	: : : : :	
A. fumigatus-CYP51a	LDYLRDSPNFQSS---GRVDISAAMAEITIFTAARALQGGQEVRSKLTAEFADLYHDL	211
A. fumigatus-CYP51b	ESFVKNSPAQGHK---GVDFVCKTIAETITTYASRSLQKGEVRSKFDSTFAELYHNL	226
C. albicans-CYP51A1	LNIFYVDESFLKKEKTHGVANVMKTPQETITFTASRSLFGDEMRRIFDR-SFAQLYSDDL	225
H. sapiens-CYP51	KEYFES---WGES---GEKNVFEALSLEIILTASHCLHGKEIRSQJNE-KVAQLYADLD	231
Mtb-CYP51B1	RRMIADWG-----EAGEIDLDFFAELTIYTSASACLIGKFFRDQLDG-RFAKLYHELE	173
T. brucei-CYP51	RKFMANWD---KDEGEINLLEDCEMINTACQCLFGEDELKRLDARRFAQLLAKME	205
Mtb-CYP136	SRVVADDWVVN---DARFLVYPMKALTDIASMVMFGHEPCTDHELVTKVKNKATFIT	227
Mtb-CYP123	RIHLDS-----ALQTESFDFVAEFAGKLPMDVISELIGVPTDRARIRALADAVL	171
	: : : : :	
A. fumigatus-CYP51a	KGFTPIINFMLP---WAPLPHNKRDAAHARMRSIYVDIITQRRL-DGEKDSQKSDMIWNL	267
A. fumigatus-CYP51b	MGFAPINFMLP---WAPLPHNKRDAAKRLTETMEI IKARRQ-AGSK-KDSEDMVWNL	281
C. albicans-CYP51A1	KGFTPIINFVFP---NLPLPHYWRDAQAQKISATYMKIKSRRE-RGIDPNRDLIDSL	281
H. sapiens-CYP51	GGFSHAALLPG---WLPLPSFRRRDRAHREIKDI FYKAIQKRRQ-SQEK--IDDLQTL	285
Mtb-CYP51B1	RGTDPLAYVDP---YLPESFRRRDEARNGVALVADIMNGRIA-NPPTDKSRRDMLDVL	229
T. brucei-CYP51	SSLIPAAVFLPILLKPLPQSARCHEARTELOKILSEII IARKEE EVNKDSSSTDLLSGL	265
Mtb-CYP136	TRAGNAVIRTS---VPPFTWRRGLRARELLENYFTARVKERRE-----ASGNLTLV	277
Mtb-CYP123	HREDGVADVPP-----PAMAASIELMRYADLIAEFRR-----RPANNL TSA	213
	: : : : *	
A. fumigatus-CYP51a	MNCTYKNGQQ-VPDKEIAHMMITLLMAGQHSSSSI SAWIMLRASQPKVLEELYQEQLAN	326
A. fumigatus-CYP51b	MSCVYKNGTP-VPDEEIAHMMIALMAGQHSSSSTASWIVLRLATRPDI MEELYQEQRV	340
C. albicans-CYP51A1	IHSTYKDGVK-MTDQEIANLLIGILMGGQHTSASTSAWFLHLGKPHLQDVIIYQEVVEL	340
H. sapiens-CYP51	LDATYKDRP-LTDDVAGMLIGLLLAGQHTSSTTSAWGFPLARDKTLQKCYLQKTV	344
Mtb-CYP51B1	IAVABTGTFRFSADEITGMFISMFFAGHHTSGTASWTLIELMRHRDAYAAVIDLELD	289
T. brucei-CYP51	LSAVYRDGTP-MSLHEVCGMIVAAMFAGQHTSITTTTSMHLHMPANVKHLEALRKEI	324
Mtb-CYP136	CQTEDEDDGNR-FSDAIVNHMI FLMAAHDSTSTATTATMAYLAAHPEWQQRCDSDRH	336
Mtb-CYP123	LLAAELDGR-LSDQEIAMFLFLMVIAGNETTKLLANAVYAAHHPGQLARVFAD---	268
	* : : : : . : : : . : : : .	
A. fumigatus-CYP51a	LGPAGPDGSLPPLQYKDLKLPFHQHVIRETLRHSSSIHSMRKKVSPLPVPGTPYMI	386
A. fumigatus-CYP51b	LG----SDLPPLTYDNLQKLDLHAKVIKETLRLHAPIHSI IRAVKNPMAVDGTSYVIPT	395
C. albicans-CYP51A1	LKEKG---GDLNLDLTYEDLQKLPVNNITKETLRMHMPLHSIFRKYVNTPLRIPETNYIVPK	398
H. sapiens-CYP51	CG----ENLPLTYDQLKDLNLLDRCIKETLRLRPPIMIMMRMARTPQTAVG--YTIPP	397
Mtb-CYP51B1	YG----DGRSVSFHALRQIPQLENVLKETLRLHPLLILMRVAKGEFEVQG--HRIHE	341
T. brucei-CYP51	EFP----AQLNYNVMDEMPFAERCARESI RRDPLMLMRKVMADVKVGS--YVVKP	376
Mtb-CYP136	GD-----GPLDIESLEQLESLDLVMNESIRLVTVPQWAMRQTVRDTLELLG--YYLPK	386
Mtb-CYP123	-----HSRIPMWVEETLRYDTSSQILARTVAHDLTYD--TTIPE	306
	: : : : * : : : *	
A. fumigatus-CYP51a	GRVLLASPGVTALSDEHFPNAGCWDPHRWENQATKE---QENDKVVYGYGAVSKGTSS	442
A. fumigatus-CYP51b	SHNVLSSPGVTARSEHFPNPLEWNPWRWENIAAAS---AEDDEKVDYGYGLVSKGTSS	451
C. albicans-CYP51A1	GHYVLVSPGYAHTSERYFDNPEDFDPTRWDTAAKANSVSNSSSEVDYGFVKVSKGVSS	458
H. sapiens-CYP51	GHQVCVSPVTNQRKDSWVERLDFNPDYLDQNPAS-----GEKF	437
Mtb-CYP51B1	GDVLAASPAISNRIPEDFPDPHFVFPARYEQPRQED-----LLNRW	382
T. brucei-CYP51	GDIIACSPLLSHHDEAFPEPRRWDPERDEK-----VEG	410
Mtb-CYP136	GTNVIAYPGMNHLRPEIWTDPDTPDFRFTPEPRNEH-----KRHY	427
Mtb-CYP123	GEVLLLLPGSANRRDDRVDDPDDYRIGREIG-----C	338
	: : * : : : *	
A. fumigatus-CYP51a	PYLPFGAGRHRICIGEFAYVNLGVILATIVRHLRFLNVDGKKGVPETDYSSLFSGPMKPS	502
A. fumigatus-CYP51b	PYLPFGAGRHRICIGEFAYLQGTITAVLRLFRFRNLPGVDGIPDTPDYSSLFSGPLGRS	511
C. albicans-CYP51A1	PYLPFGGGRHRICIGEFAYVQLGTITLTFVYVNLRTWIDG--YKVPDPDYSMMVLPTEPA	516
H. sapiens-CYP51	AYVFPGAGRHRICIGENFAYVQIKTIWSTMLRLYEFDLIDG--YFPTVNYTTMIHTPENP-	494
Mtb-CYP51B1	TWLPFGAGRHRICVGAFAIMQIKAFVLLREYEFEMAQP--PESYRNDHSMKVVQLAQPA	441
T. brucei-CYP51	AFIGFGAVHCKIGQKFGLLQVKTILATAFRSYDFQLLRD--EVPDPDYHTMVVGTASQ	468
Mtb-CYP136	AFTPGGGVHKICIGMVFQLEIKTILHLLRRYRLELSRP-DYQPRWDYSAMP IPMDMG	486
Mtb-CYP123	KLVSFGGAHFCLAGHARMEARVALGALLRRIRNYEVD--DNVVRVHSSNVRGFAHLP	396
	** * * * : : : :	
A. fumigatus-CYP51a	IIGWEKRSKNTSK	515
A. fumigatus-CYP51b	FVEFEKRESATKA	524
C. albicans-CYP51A1	EIIWEKRETCMF-	528
H. sapiens-CYP51	VIRYKRRSK----	503
Mtb-CYP51B1	CVRYRRRTGV---	451
T. brucei-CYP51	CRVKYIRKAAAA	481
Mtb-CYP136	IVLPR-----	492
Mtb-CYP123	ISVQAR-----	402

Appendix E – Membrane Protein Topology Prediction of CYP123, CYP136 and CYP51B1 from Mtb

by TopPred: <http://mobyle.pasteur.fr/cgi-bin/portal.py?#forms::toppred>

Ref: von Heijne, G. (1992) Membrane Protein Structure Prediction: Hydrophobicity Analysis and the 'Positive Inside' Rule. *J. Mol. Biol.* **225**, 487-494.

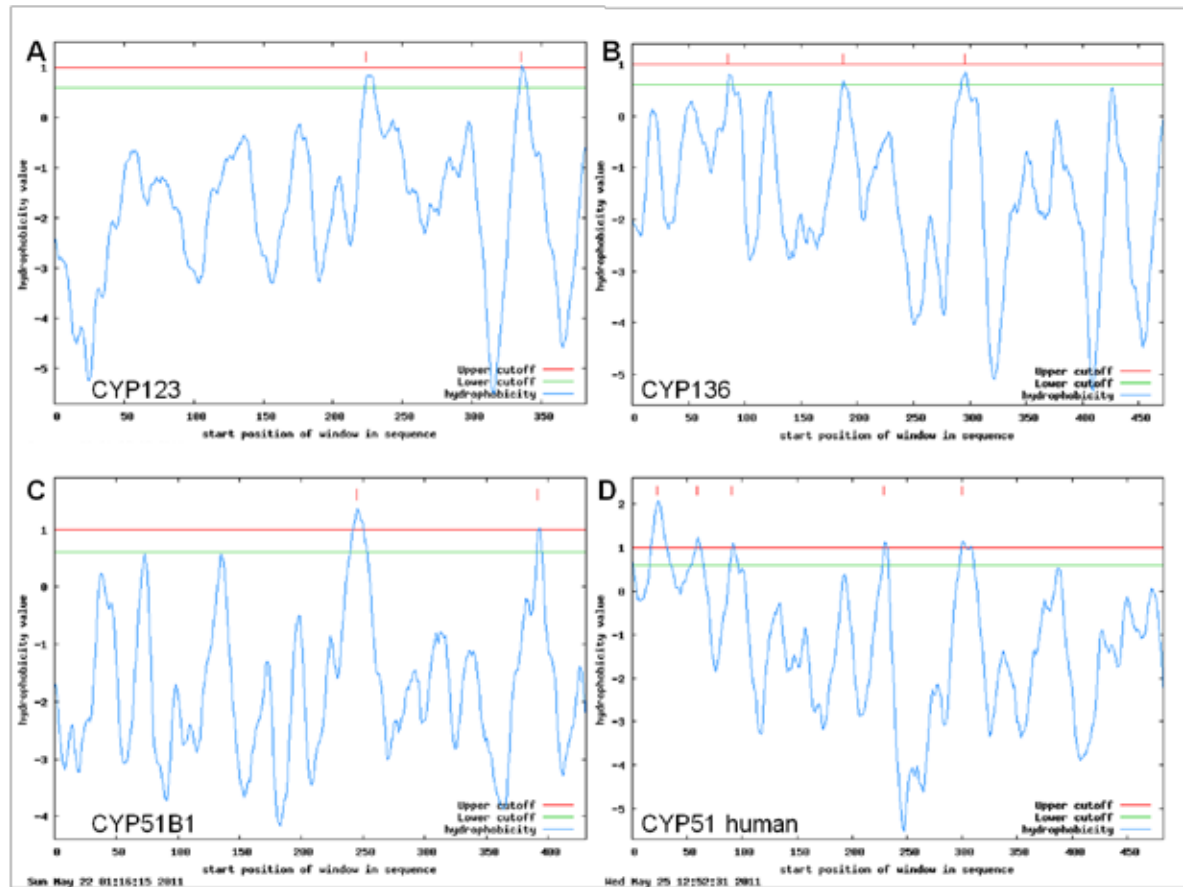


Figure 8.1: Topology prediction of membrane proteins. The graphs represent the amino acid topology prediction of CYP123 (A), CYP136 (B), CYP51B1 (C) and CYP51 from human (D). The graphs identify hydrophobic sections and can thus be used to predict whether the protein is membrane-bound, membrane-associated or cytosolic. In the case of human CYP51, a N-terminal hydrophobic membrane anchor is predicted.

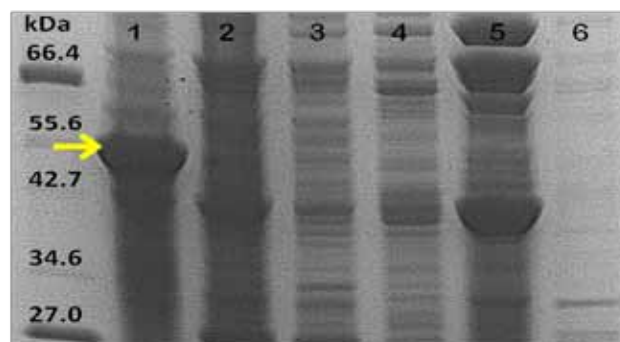


Figure 8.2: Purification results for native non-His₆-tagged CYP136 from pET20b vector. Lanes 1 and 2 are the soluble and insoluble fractions, respectively. The soluble fraction was loaded onto a Q-Sepharose column. Lanes 3 and 4 are the flow-through and wash fractions, respectively. Elution was done step-wise using high-salt buffer A. Lanes 5 and 6 are eluted fraction with 50% and 100% high salt buffer respectively. CYP136 (56.2 kDa) was only found in the insoluble fraction identified by the yellow arrow.

Appendix F – EPR g Values for CYP51B1

WT	$g_z = 2.43$	(2756G)	
	$g_y = 2.25$	(2974G)	
	$g_x = 1.91$	(3510G)	
WT + clotrimazole	$g_z = 2.51$	(2669G)	
	$g_z = 2.46$	(2721G)	
	$g_z = 2.43$	(2757G)	
	$g_y = 2.26$	(2965G)	
	$g_x = 1.88$	(3562G)	
several unresolvable components			
WT + 4-phenylimidazole	$g_z = 2.47$	(2717G)	74%
	$g_y = 2.26$	(2965G)	
	$g_x = 1.89$	(3556G)	
	$g_z = 2.54$	(2638G)	26%
	$g_y = 2.26$	(2965G)	
	$g_x = 1.86$	(3606G)	
WT + voriconazole	$g_z = 2.46$	(2727G)	
	$g_y = 2.26$	(2965G)	
	$g_x = 1.89$	(3547G)	
F89H	$g_z = 7.55$	(882G)	
minor high spin species	$g_{\perp} = 5.75$	(1165)	
minor high spin species	$g_z = 2.44$	(2751G)	
	$g_y = 2.25$	(2974G)	
	$g_x = 1.91$	(3510)	
F89H + clotrimazole	$g_z = 2.56$	(2617G)	
	$g_z = 2.52$	(2574G)	
	$g_z = 2.45$	(2736G)	
	$g_y = 2.26$	(2969G)	
	$g_x = 1.90$	(3532G)	
	$g_x = 1.87$	(3590G)	
	$g_x = 1.84$	(3634G)	
R391K	$g_z = 2.43$	(2756G)	
	$g_y = 2.25$	(2974G)	
	$g_x = 1.91$	(3510G)	
R391K + clotrimazole	$g_z = 2.51$	(2669G)	
	$g_z = 2.46$	(2722G)	
	$g_z = 2.43$	(2755G)	
	$g_y = 2.25$	(2967G)	
	$g_x = 1.92$	(3497G)	
	$g_x = 1.89$	(3545G)	
	$g_x = 1.87$	(3576G)	
G388S	$g_z = 8.00$	(840G)	
minor high spin species	$g_{\perp} = 5.86$	(1143G)	
minor high spin species	$g_z = 2.42$	(2771G)	
	$g_y = 2.25$	(2974G)	
	$g_x = 1.91$	(3507G)	
free iron at $g = 2.00$			
G388S + clotrimazole	$g_z = 2.49$	(2698G)	
	$g_z = 2.42$	(2752G)	
	$g_z = 2.39$	(2801G)	
	$g_y = 2.26$	(2964G)	
	$g_y = 2.24$	(2990G)	
	$g_x = 1.92$	(3492G)	
More g_x unresolved in broad tail.			
Maybe a little $g_{\perp} = 5.86$, but not much.			
G388S + 4-phenylimidazole	$g_z = 2.45$	(2737G)	72%
	$g_y = 2.26$	(2965G)	
	$g_x = 1.90$	(3533G)	
	$g_z = 2.51$	(2668G)	28%
	$g_y = 2.26$	(2965G)	
	$g_x = 1.86$	(3604G)	
G388S + voriconazole	$g_z = 2.44$	(2751G)	
	$g_y = 2.25$	(2965G)	
	$g_x = 1.90$	(3527G)	
Plus all samples contain a small amount of adventitious 'rhombohedral' ferric iron at $g = 4.26$ (1576G)			
L100F	$g_z = 2.44$	(2747G)	
	$g_z = 2.41$	(2785G)	
	$g_y = 2.25$	(2980G)	
	$g_x = 1.92$	(3485G)	
	$g_x = 1.91$	(3515G)	
L100F + 4-phenylimidazole	$g_z = 2.55$	(2629G)	
	$g_z = 2.44$	(2750G)	
	$g_y = 2.25$	(2982G)	
	$g_x = 1.90$	(3530G)	
	$g_x = 1.85$	(3630G)	
L100F + clotrimazole	$g_z = 2.53$	(2658G)	
	$g_z = 2.42$	(2764G)	
	$g_y = 2.25$	(2978G)	
	$g_x = 1.91$	(3510G)	
	$g_x = 1.87$	(3575G)	
L100F + voriconazole	$g_z = 2.44$	(2744G)	
	$g_y = 2.25$	(2983G)	
	$g_x = 1.89$	(3545G)	

Appendix G – Choice of Model Parameters in the DSC Software

Fitting of differential scanning calorimetry data to a Non-two-state model 2 with zero ΔC_p . (Reference: Lesson 1 and 5 of the DSC Data Analysis in Origin® Tutorial Guide Version 5.0 October 1998, MicroCal™, pg 45.)

Origin provides four models with which to fit a curve to your data. All four models use the Levenberg-Marquardt non-linear least-square method, but differ in the number of parameters involved, as shown below:

Model Parameters

Model 1: 2-State with zero ΔC_p	T_m, H
Model 2: Non-2-State with zero ΔC_p	T_m, H, H_v
Model 3: 2-State with non-zero ΔC_p	T_m, H, C_p, BL_0, BL_1
Model 4: Dissoc with non-zero ΔC_p	$T_m, H, C_p, BL_0, BL_1, n$

T_m is the thermal midpoint of a transition; H is the calorimetric heat change (DH); H_v is the van't Hoff heat change (DH_v); C_p is the $D C_p$ for each transition; BL_0 and BL_1 define the slope and intercept of the low-temperature baseline segment; and n is the number of sub-units.

All of the models except model 4 can be used to fit to one or more transitions. In the case of multiple transitions, each transition has its own complete parameter set; e.g., if model 1 is used to fit two overlapping transitions there will be two independent parameter sets [T_{m1}, H_1] and [T_{m2}, H_2]. These specify the thermal midpoint (T_m) and the heat change (DH) at the T_m for each transition. The BL_0 and BL_1 parameters are an exception to this rule. These parameters appear only once in the model; they are not repetitive for each transition.

While all four models use a calorimetric heat change (DH), only the **non-2-state model** (model 2) has a van't Hoff heat change (DH_v). The calorimetric heat H is determined only by the area under a transition peak, while the van't Hoff heat H_v is determined only by the shape of the transition peak. The sharper the transition, the larger is H_v , and vice versa. The relationship between H and H_v can sometimes provide insights not accessible from H alone. For example, if a protein is composed of two identical domains which unfold independently with the same T_m and H , then the ratio of H/H_v will be 2.0, while it would be 1.0 if the protein had only a single domain. If, on the other hand, the protein dimerised and the dimer underwent only a single coupled transition then the H/H_v ratio would be 0.5. It is clear from this that the calorimetric heat H refers to *heat change per mole* while H_v is *heat change per unfolding unit* (called the *cooperative unit*). Thus the ratio H/H_v can, in simple cases, be thought of as *the number of cooperative units per mole*.

(Note: It is important to realize that the ratio of calorimetric to van't Hoff heat depends on concentration normalization, since calorimetric heat is always expressed on a *per mole* basis. Thus for the protein dimer example considered above, the ratio will be 0.5 if concentration normalization is carried out on a *per mole of monomer* basis while it will be 1.0 if concentration is entered in terms of *moles of dimer* present.)

Appendix H – Crystallographic Data Statistics of CYP51B1 Variants

Table 8.4: Crystallography Statistics of CYP51B1 Wild Type and Mutants.

Crystal	WT		F89H		L100F	R391K	
Ligands	4PI	EPBA	4PI	EPBA	EPBA	4PI	EPBA
Space group	P2 ₁ 2 ₁ 2 ₁	P2 ₁ 2 ₁ 2 ₁	P2 ₁ 2 ₁ 2 ₁	P2 ₁ 2 ₁ 2 ₁	P2 ₁ 2 ₁ 2 ₁	P2 ₁ 2 ₁ 2 ₁	P2 ₁ 2 ₁ 2 ₁
Unit cell a,b,c (Å)	45.56/85.24/ 110.36	45.57/85.18 /110.30	46.25/85.02/ 110.12	45.47/85.22/ 110.37	46.54/85.12/ 110.59	46.50/84.88/ 110.05	46.78/84.88/ 110.34
Data Collection							
Resolution (Å)	15.00-1.49	15.00-2.30	20.00-1.43	19.88-2.00	20.00-1.80	20.00-1.71	19.96-1.79
Unique reflections	63070	18539	72969	28025	39240	45115	3286
Completeness (%)	93.10	98.88	100	100	98.87	99.08	98.66
Average I/σI	16.4	8.2	13.4	17.3	15.4	23.5	9.3
Redundancy	4.2	2.9	3.8	5.3	3.1	4.7	2.9
R _{sym} (%)	7.2	12.7	8.7	9.2	7.7	6.8	6.9
Refinement Statistics							
R _{crys} /R _{free} (%)	12.45/17.06	21.7/29.4	16.94/19.84	17.95/23.84	15.72/20.56	14.95/18.80	15.61/20.47
Model Statistics							
Average B-factor (Å ²)	11.633	37.24	16.368	22.896	12.609	12.000	13.565
Ramachandran (allowed) (%)	99.5%	99.0%	99.2 %	99.7%	99.8%	99.3%	99.3%
Rms deviations:							
Bonds (Å)	0.026	0.024	0.028	0.023	0.025	0.025	0.024
Angles (°)	1.905	2.016	2.263	1.880	1.895	1.901	1.834